Stellingen

1. De systematische vergelijking van remote sensing data met geologische veldgegevens levert meer vragen op dan antwoorden. De waarde is echter dat het aanleiding geeft tot het stellen van vragen die anders nooit gesteld zouden worden.

2. Het is niet consistent dat laboratoriumgegevens in geologische publikaties uitgebreid worden gerapporteerd voor evaluatie en interpretatie door de lezer, terwijl geologische veldgegevens vaak op een dusdanig abstractieniveau worden weergegeven dat er geen terugkoppeling naar de oorspronkelijke observaties mogelijk is.

3. De analyse van "airborne" gamma spectrometrische gegevens maakt het mogelijk subtiele samenstellingverschillen in granietlichamen in kaart te brengen die bij directe veldwaarneming onopgemerkt blijven (dit proefschrift).

4. Geologische diensten, universiteiten en exploratiemaatschappijen dienen veldgegevens te beheren op een manier die volledige toegang en efficient hergebruik voor elke denkbare toepassing mogelijk maakt (dit proefschrift).

5. Geïntegreerde beeldrepresentaties van strukturele informatie verkregen uit hoge resolutie satellietbeelden en geochemische informatie verkregen uit "airborne" gamma spectrometrische gegevens kunnen inzicht geven in de vervorming van granietlichamen die optreedt tijdens en na intrusie (dit proefschrift).

6. De geïntegreerde representatie van beeldvormende radar en "airborne" magnetische gegevens is bruikbaar ter ondersteuning van de strukturele interpretatie van schuifzones (dit proefschrift).

7. De verschuiving in kleurwaarde (hue) die optreedt bij beeldfusie heeft weinig of niets te maken met het gebruikte algoritme, maar is vooral afhankelijk van de schaling die wordt toegepast in de uiteindelijke beeldrepresentatie (dit proefschrift).

8. De informatie van kaarten wordt vaak als 100% nauwkeurig beschouwd, terwijl hun nauwkeurigheid vaak niet bekend is. Daarentegen wordt de informatie uit classificaties van remote sensing gegevens met een nauwkeurigheid van 85% vaak met tegenzin gebruikt (Stan Aronoff, 1991).

9. Ruimtepuin vormt in toenemende mate een bedreiging voor de aardobservatie.

10. Er is niets verkeerd aan het vergelijken van appels met peren als dit helpt bij het bepalen van de inhoud van een fruitschaal.

11. Het slagingspercentage van een opleiding is met de toenemende commercialisering van het hoger onderwijs een onbetrouwbare graadmeter voor de kwaliteit.

12. Neurale netwerken zijn ideale instrumenten voor managers die controle willen houden over hun organisatie. Hoe de externe factoren aan de invoerknopen ook veranderen, implementatieregels worden aan de verborgen knopen zodanig aangepast, dat de vooraf aan de uitvoerknopen ingestelde beleidsdoelen behaald worden.

Stellingen behorende bij het proefschrift "Integrated analyses of granite-gneiss terrain from field and multisource remotely sensed data" Ernst Schetselaar, Delft, 19 juni, 2000.

Propositions

1. Attempts to systematically reconcile image patterns from remotely sensed data with geological ground observations raises more questions than answers. The advantage of such exercises is that questions are raised that otherwise would never have been asked.

2. It is inconsistent that in geological publications laboratory data are extensively reported in their authentic form for readership evaluation, while map-related field observations are generally represented at such a high level of abstraction that they can not be related-back to the authentic observations.

3. Enhancement and analysis of airborne gamma-ray spectrometry data may show compositional variations within granitoid intrusions not visible in outcrop (this thesis).

4. Geological surveys, universities and exploration companies should record and manage field data in a manner that permits full access and effective reuse for any future application (this thesis).

5. The integrated image representation of structural information from high-spatial resolution optical imagery with geochemical information from airborne gamma-ray spectrometry data can provide insight in the strain accommodated within plutons, during and after their emplacement (this thesis).

6. The integrated analysis and enhancement of imaging radar and airborne magnetic data can be effective in supporting the structural interpretation of shear zones (this thesis).

7. The hue distortion in fused images is little dependent on the employed merging algorithm, but rather a function of the scaling applied in generating the colour composite image afterwards (this thesis).

8. Maps are frequently treated as if the information is 100% accurate when the accuracy is actually unknown! Yet when classifications derived from remotely sensed data are presented as 85% accurate, there is often resistance to using the information (Stan Aronoff, 1991).

9. Orbital debris is increasingly becoming a threat to Earth observation from space.

10. There is nothing wrong in comparing apples with oranges, if this helps in establishing the contents of a fruit bowl.

11. Given the present commercialization of higher education the percentage of students that successfully pass an educational programme is an unreliable quality estimate.

12. Artificial neural networks are ideal for managers that want to keep control over their organization. Whatever happens with the external factors at the input nodes, implementation rules are repeatedly fine-tuned at the hidden nodes, such that the managerial goals, as predefined at the output nodes, are always achieved.

Propositions related to the dissertation "Integrated analyses of granite-gneiss terrain from field and multisource remotely sensed data" Ernst Schetselaar, Delft, June 19th 2000.

Integrated analyses of granite-gneiss terrain from field and multisource remotely sensed data

A case study from the Canadian Shield

Proefschrift

ter verkrijging van de graad van doctor
aan de Technische Universiteit Delft,
op gezag van de Rector Magnificus prof. ir. K.F. Wakker,
in het openbaar te verdedigen ten overstaan van een commissie,
door het College voor Promoties aangewezen,

op maandag 19 juni 2000 te 16.00 uur

door

Ernst Martinus SCHETSELAAR
doctorandus in de geologie
geboren te Dordrecht

Dit proefschrift is goedgekeurd door de promotor:

Prof. dr. S.B. Kroonenberg

Toegevoegd promotor:

Prof. dr. A.G. Fabbri

Samenstelling promotiecommissie:

Rector Magnificus, voorzitter	
Prof. dr. S. B. Kroonenberg,	Technische Universiteit Delft, promotor
Prof. dr. A. G. Fabbri,	ITC, Enschede, toegevoegd promotor
Prof. dr. C. V. Reeves,	ITC, Delft
Prof. Dr. Ing. habil. R. A. P. Klees,	Technische Universiteit Delft
Prof. dr. C. W. Passchier,	Johannes Gutenberg Universität, Mainz
Dr. C. F. Chung,	Geological Survey of Canada, Ottawa
Dr. G. J. Weltje,	Technische Universiteit Delft

ISBN 90-6164-180-2
ITC dissertatie nummer 73

aan Astrid en Martijn

ACKNOWLEDGEMENTS

The research presented in this thesis was conducted at the International Institute for Aerospace Survey and Earth Sciences in cooperation with the Geological Survey of Canada. The fieldwork component of the research was financially and logistically supported by the mineral development project of Alberta (MDA) and the data set analyzed in this thesis was made available by the Geological Survey of Canada.

I wish to thank my promotors Salomon Kroonenberg and Andrea Fabbri. Salle, your support, inspiration and valuable suggestions were gratefully accepted. You provided worthy insight for the geological interpretation of the remote sensing data set, based on your extensive experience in geological mapping in the Precambrian shield in Colombia and Suriname. Andrea, I greatly appreciated your suggestions on the methodological aspects of my research. Lively and extensive discussions at ITC provided me with the inspiration needed to complete this thesis.

I am grateful to Chang-Jo Chung who involved me in the MDA project and provided valuable guidance and support in the application of classification techniques, which made my visits to the Geological Survey of Canada in Ottawa, pleasant and stimulating learning experiences. I am also grateful to Mike McDonough for his support during the field component of this thesis and his open attitude towards remote sensing techniques, leading to interesting discussions during fieldwork and the publication of two papers. Without his support, the ground validation conducted during my research would not have been possible. I am grateful to Eric de Kemp who as a friend provided moral support and stimulated me with enthusiasm and inspiration for bridging the gap between geological field mapping and the geological application of remote sensing. I also wish to thank his wife Nancy de Kemp for her hospitality during my visits to Ottawa.

I am grateful to Colin Reeves, Sally Barrit, Jean Roy and Hans Erren of the exploration geophysics division of ITC Delft for useful discussions and critically reviewing geophysical aspects of this thesis. Hans Erren is also thanked for his assistance in processing the aeromagnetic data.

Thanks to Willem Langenberg of the Alberta Geological Survey who kindly provided the lithogeochemical data, which allowed me to interpret the gamma-ray spectrometry data. Jan Bednarski of the Geological Survey of Canada in Calgary is thanked for providing orientations of glacial striations. John Grant, Brian Charbonneau and Ray Hetu of the Geological Survey of Canada in Ottawa for their assistance in obtaining the flight line data and additional specifications of the

northeastern Alberta geophysical survey. Andy Rencz is thanked for technical support at the GSC and providing the Landsat TM and ERS-1 data. Wan Bakx and Gerard Reining of the geoinformatics division are thanked for technical support on import and export of image data. Gerrit Huurneman, Wan Bakx and Wim Bakker are thanked for fruitful discussions on the intensity-hue-saturation transform and valuable comments that significantly improved Chapter 5. I also want to thank Rob Harrap, Boyan Brodaric, Tsehaie Woldai, for providing valuable comments on Chapter 4 and Paul Dirks and Eric de Kemp who provided valuable comments in reviewing Chapter 6 and Chapter 7.

I also like to thank Boudewijn de Smeth for his assistance in the preparation of thin sections and Jacques Voncken for his guidance in reflected light microscopy. Anupma Prakash is thanked for technical assistance. My colleagues of the Geological Survey Division are thanked for their patience and fruitful discussions.

The pilots of Loon-air and Glenn Wettlaufer are thanked for close-range oblique aerial views and save take-offs and landings.

I am profoundly grateful to my wife Marja van der Burght, who not only gave me all the moral support I could ever have desired during this research, but even was prepared to share the goods and bads during the second fieldwork in the remote wilderness of northeastern Alberta. I wish to thank my family for encouragement and support and particularly Martijn and Astrid for their patience in asking all the attention they needed from their father during the years in which this thesis was completed.

CONTENTS

ACKNOWLEDGEMENTS v

CHAPTER 1: INTRODUCTION

1.1 Scope 1
1.2 Research rationale 2
1.3 Study area and data set 3
1.4 Thesis outline 4

PART 1: RECONNAISSANCE

CHAPTER 2: A REVIEW OF THE TALTSON MAGMATIC ZONE

2.1 Introduction 10
2.2 Lithological units 15
2.3 Geological structure 20
2.4 Tectono-metamorphic evolution 29

CHAPTER 3: THE NORTHEASTERN ALBERTA DATA SET: ACQUISITION, REGISTRATION AND INTERPRETATION

3.1 Introduction 34
3.2 Spaceborne remotely sensed data 35
3.3 Airborne geophysical data 36
3.4 Acquisition of geological field data 38
3.5 Georeferencing procedures 39
3.6 Geological interpretation 41
3.6.1 Interpretation of aeromagnetic data 43
3.6.2 Interpretation of gamma-ray spectrometry data 52
3.6.3 Interpretation of Landsat TM data 56
3.6.4 Interpretation of ERS-1 data 60
3.6.5 Integrated interpretation 60
3.7 Summary and conclusions 64

PART II: METHODOLOGICAL ASPECTS

CHAPTER 4: DIGITAL FIELD DATA HANDLING: CARTOGRAPHIC ASPECTS AND APPLICATIONS

4.1 Introduction 70
4.2 Geological mapping and field data capture methodology 71

4.3 Implications of digital field data capture to field mapping 74
4.4 A review of field data management and mapping systems 75
4.5 Database structure for geological mapping of the Alberta Shield 77
4.6 Applications facilitated by digital field data handling 79
4.6.1 Cartographic representation of geological field observations 79
4.6.2 Automated map compilation for structural interpretation 85
4.6.3 Automated projection for compiling cross sections 90
4.6.4 Integrated visualization of magnetic inversion models and surface geological data 102
4.7 Summary and concluding remarks 104

CHAPTER 5: OPTIMIZING THE IHS TRANSFORM FOR THE INTEGRATED VISUALIZATION OF REMOTELY SENSED DATA

5.1 Introduction 110
5.2 Tristimulus and chromaticity coordinates 111
5.3 RGB and IHS colour spaces 114
5.4 Application of the IHS transform to the integration of multisource remotely sensed data 117
5.5 A hue-invariant transformation 122
5.6 Implications of using the cylindrical or spherical IHS transform 128
5.7 Summary and conclusions 132

PART III: INTEGRATION STUDIES

CHAPTER 6: INTEGRATION OF MULTISOURCE REMOTELY SENSE DATA FOR MAPPING THE INTERNAL COMPOSITION AND STRUCTURE OF GRANITOID INTRUSIONS: THE ARCH LAKE GRANITE (1.94 Ga.)

6.1 Introduction 138
6.2 Geological observations 141
6.3 Mineralogy and fabric 144
6.4 Interpretation of remotely sensed data 147
6.5 Spectral analysis of gamma-ray spectrometry data 150
6.6 Geochemical and mineralogical associations 153
6.7 Integration of Landsat TM7 and K, eTh, eU grids for structural analysis 156
6.8 Discussion 162
6.9 Summary and conclusions 167

CHAPTER 7: INTEGRATION OF ERS-1, AEROMAGNETIC AND FIELD DATA FOR MAPPING SHEAR ZONES, CHARLES LAKE SHEAR ZONE

7.1 Introduction 172
7.2 Field description of the Charles Lake shear zone 176
7.3 The application of SAR images in mapping geologicalstructure 178
7.4 Ground validation of structural features inferred from ERS-1data1 179
7.5 Ground validation of aeromagnetic data 184
7.6 Comparative analysis of magnetic and ERS-1 lineaments and foliation strike lines 189
7.7 Image enhancement and interpretation methodology 194
7.8 Structural interpretation 198
7.9 Summary and conclusions 203

CHAPTER 8: INTEGRATION OF LANDSAT TM, GAMMA-RAY, MAGNETIC AND FIELD DATA TO DISCRIMINATE LITHOLOGICAL UNITS IN VEGETATED GRANITE-GNEISS TERRAIN

8.1 Introduction 208
8.2 Objectives 209
8.3 Classification algorithms 213
8.4 Classification strategy 216
8.5 Discussion 225
8.6 Summary and conclusions 228

CHAPTER 9: CONCLUSIONS, OUTLOOK AND RECOMMENDATIONS 231

SUMMARY 239

SAMENVATTING 245

REFERENCES 251

BIBLIOGRAPHY 265

CURRICULUM VITAE 271

PLATES

1

INTRODUCTION

1.1 Scope

With the continuously growing availability of geoscience data acquired by remote sensing methods and field surveys, there is an increasing demand to interpret and analyze such multivariate data sets in a spatially consistent and integrated manner. Surveying techniques that are relevant to earth scientists include geological, soil, and geomorphological field mapping, geophysical and geochemical field surveys and a multitude of aerospace remote- sensing methods. These surveying techniques have, over the previous century, proven to be invaluable in complementing conventional geological mapping, identifying targets for mineral and hydrocarbon exploration (Drury, 1992) and there is increasing awareness that they provide invaluable information to monitor the environment (Bennett and Doyle, 1997).

The independent evolution of these surveying techniques has resulted in their establishment as separate disciplines in the earth sciences, as still reflected in the organization of most geological surveys and earth science faculties today. Increasingly, however, the goal of the earth scientist investigating a region of interest, is to integrate and spatially link all the available data to gain insight in the geological phenomena and processes in a study area. The line of reasoning is that each data type potentially provides complementary information and that if such data are adequately integrated, more insight in the geology of an area may be obtained than when each data type is analyzed in isolation.

With the advent of the development of geographic information systems (GIS) and image processing systems (IPS) and their converging functionality in the last decade, the goal of digitally analyzing multiple types of remotely sensed and thematic map data has become feasible. Before the computer era, spatial data integration was done on an analog basis by overlaying transparencies on a common cartographic reference or simply by visually comparing hardcopy images, contour- and geological maps (Bonham-Carter, 1994). In the sixties digital analysis of spatial data sets was initiated by earth scientists in the petroleum industry. These early computer programs facilitated the analysis of sedimentary structures, structural orientation data and drill hole data and provided the tools for automated structural contour- and isopleth mapping (Merriam and Harbaugh, 1964; Fox, 1967; Merriam, 1969; Davis, 1973; Agterberg, 1974). The rapid

developments of GIS functionality since the late eighties has resulted today in a multitude of versatile and easy-to-implement digital processing routines for the analysis of multiple spatial data sets. GIS is gaining importance in the repertoire of field-based earth scientists and is nowadays routinely employed in exploration, natural hazard and environmental applications (Drury, 1992; Bonham-Carter, 1994).

In the sense that GIS is applicable to any activity involving the acquisition and analysis of spatial data, its application in the earth sciences can be considered to be still at its infancy. Digital integration techniques not only apply to situations where all the data relevant to a particular problem have been collected and stored in a GIS, but can also be used as an exploration tool in guiding the mapping and data acquisition itself (Sullivan, 1991). This is particularly relevant in field mapping projects, that being dependent on the accessibility and terrain conditions, are often the most costly activities in exploration and mapping programs. In this context, GIS could be extended from its more traditional application domain, in analyzing and predicting specific phenomena (such as a particular mineral deposit) to a domain where multiple data sets are analyzed to gain insight in the underlying geological processes. In this light, GIS ultimately becomes the vehicle by which geologists complement and enhance their inherent ability to think about the geology of an area in a spatial and integrated manner.

1.2 Research rationale

This thesis presents novel approaches for geologically investigating an area of interest by integrating multiple types of remotely sensed and primary geological field data. Methods of digitally integrating remotely sensed- and ancillary spatially distributed data are increasingly applied by earth scientists (Bonham-Carter, 1994). These integration techniques are, however, even in the modern geological surveys in developed countries, far from being implemented to their full potential. Most of the obstacles are related to the conventional traditions in earth science education and mono-disciplinary organization of earth science institutions:

- Field mapping is often not yet organized and structured in a way to facilitate data integration studies but mainly focuses on compilation of general or thematic geological maps. Usually only the fully compiled geological maps are digitized, while primary observations are left unavailable in the hardcopy notebook of the geologist. Ground validation of the interpretations and analyses obtained from remotely sensed data can therefore not be implemented

in an efficient and systematic manner. In the last decade some mapping projects at geological surveys have started with systematically encoding field observations (Broome *et al.*, 1993). This development has made geological data management, map production and data dissemination more versatile and cost-effective (Broome, 1997). The digital management of field observations, however, is not yet exploited for the interpretation and analysis of multivariate spatial data sets.

- Remotely sensed data are mostly analysed in isolation from field observations and often by personnel that has not been participating in fieldwork activities. The digital analysis of remotely sensed data is as a result rarely implemented for a purpose to which it is very much applicable: guiding the field-based earth scientist to areas where he or she is likely to obtain new information or upgrade previously collected information. Without specific knowledge on the geology and physiography of the study area and interaction with available field data, there is a general lack of geological rationale in the analysis (e.g. the methods are predominantly data-driven instead of being based on both data- and knowledge-driven approaches).

- The field-based earth scientist has often no resources or no time during fieldwork to implement integration methods and usually lacks education and training for analyzing spatial data within a GIS environment.

The rationale of this research is to develop and apply integration strategies aimed at bridging the gap between the insights obtained by geological field mapping and those obtained by analyzing multisource remotely sensed data in a GIS environment. The integration strategies presented in this thesis are intended to overcome the above outlined shortcomings by interactively incorporating field data in knowledge-driven image-enhancement and pattern recognition techniques. In addition field knowledge is used to test the geological significance of the integrated interpretations. This gives insight on to what extent the integration strategies are useful to support geological mapping and should allow identifying promising domains of application.

1.3 Study area and data set

The integration methods presented in this thesis are applied to the Canadian Shield of northeastern Alberta that constitutes the southernmost exposed part of

the Paleoproterozoic Taltson magmatic zone. An extensive integrated data set, comprising remotely sensed image - and airborne geophysical data was acquired over this area under the auspices of the Canada-Alberta agreement on mineral development (Macqueen, 1997). This data set was made available to the author for this research to strengthen the coherence between the tectonic evolution (1A), geophysical survey (1D) and data integration (1F) projects of the MDA programme. The main fieldwork components of the first project involved mapping and radiometric dating of the bedrock units (McDonough *et al.*, 1995), geothermobarometric studies to unravel the tectonometamorphic evolution (Grover *et al.*, 1997), and elucidation of structural controls on sulphide mineralization (McDonough, 1997). The author participated in this multidisciplinary field mapping effort during the 1993 and 1994 field seasons.

A regional airborne gamma ray spectrometer-magnetic-VLF survey was flown and completed in 1994 (Charbonneau *et al.*, 1994). An integrated geoscientific data set, including the above mentioned airborne geophysical survey, Landsat TM, ERS-1, lake geochemistry and mineral showings was compiled and published as an open file on CD-Rom (Chung *et al.*, 1998).

The setting in northeastern Alberta is a densely forested terrain with an overall homogeneous granite-gneiss lithological composition. This provided challenging terrain for investigating the potential of integrating and geologically interpreting multisource remotely sensed data. The integration of remotely sensed data acquired by various platforms is highly relevant in such a setting, because each of the individual data sets are expected to contribute less to geological characterisation in comparison to areas with less vegetation cover and more heterogeneous lithological composition.

1.4 Thesis outline

This thesis consists of three parts, of which the individual chapters were recompiled from five published and two submitted journal articles.

Part I: Reconnaissance

In Chapter 2 the geology of the Taltson magmatic zone is reviewed on the basis of previous studies, recent mapping and field observations of the author. The purpose of this review is to place this research in the context of current geological knowledge and models of the study area. In Chapter 3 the acquisition, data correction and geometric correction procedures to register the data on a common

cartographic projection are described and geological interpretations of each data set are presented with outlines of the major lithological domains and structures. A combined litho-structural interpretation has been conducted by interactively editing domain boundaries and aggregating structural information compiled from the individual interpretations during the display of complementary image data on the background. This exploratory analysis of the multisource remotely sensed data provides the basis for more focussed integration studies presented in Part III.

Part II: Methodological Aspects

In Chapter 4 the computerized capture and handling of geological field observations and its application in geological mapping and data integration are discussed. Its functionality requirements are reviewed with respect to the collection, management and cartographic representation of field observations. The utility and applications of digital field data management in a GIS environment are illustrated with several examples, mainly employed from the case studies presented in Part III.

Chapter 5 presents a method for optimizing the integrated visualization of multiple types of remotely sensed data that is applied to support geological image interpretation in Part III. This novel approach in applying the intensity-hue-saturation (IHS) transform preserves the colour balance of a multispectral data set by uniformly modulating perceptual colour attributes in proportion to the calibrated units of measurement. In addition, this method allows to a priori compromise the percentage of over-range pixels against colour enhancement. The implications of using different IHS transforms for the integrated visualization of remotely sensed data are discussed and processing examples are presented to illustrate the effects of alternative processing methodologies.

Part III: Integration Studies

In Chapter 6 image integration and visualization techniques are applied with the purpose to map and interpret the compositional zonation and structure of one of the Taltson plutonic suits. Gamma-ray spectrometry, magnetic, Landsat TM and previously collected litho-geochemical data are integrated to obtain insight in the magmatic evolution, the mode of emplacement and the nature of post-emplacement deformation. IHS composite images generated from the remotely sensed data with overlays of structural orientation data are interpreted to gain

insight in the spatial association between compositional variations with foliation trajectories, shear zones and faults.

Chapter 7 presents an integration strategy for the structural interpretation of shear zones. The method is applied on the Charles Lake shear zone, the most significant structure of the northeastern Alberta Shield and is based on the integration of ERS-1, vertical derivative magnetic field and a regional map compilation of structural orientation data. Field and laboratory data were used to establish the relationships between structural fabrics and their expression on aeromagnetic and ERS-1 data sets. A knowledge-driven enhancement procedure was implemented to enhance regional strain fabrics in the Taltson basement complex and to interpret those patterns with respect to field observations.

Chapter 8 presents an approach to image classification in mapping lithological units in vegetated terrain by integrating Landsat TM, gamma-ray, magnetic and field data. This classification strategy is applied in a field mapping context in which the field stations obtained by geological mapping were used to train the classifiers. An assessment is made of the extent to which the classifications reproduce traditionally compiled geological maps. The classification is extended to the total study area and discrepancies between the regional geological map and the classified patterns are interpreted with respect to ground cover attenuation factors, internal variations in lithological units and anomalies from subsurface sources.

Chapter 9 presents general conclusions, discusses some of the limitations of the implemented methodologies and gives recommendations for future research.

PART I RECONNAISSANCE

2

A REVIEW OF THE SOUTHERN TALTSON MAGMATIC ZONE*

ABSTRACT

The Precambrian shield of northeastern Alberta constitutes the southernmost exposed portion of the Taltson magmatic zone (TMZ), an Archean to Paleoproterozoic basement complex of ortho- and paragneisses intruded by numerous 1.99 to 1.92 Ga. Paleoproterozoic granitoid suites. The emplacement of the Taltson plutonic suites was broadly synchronous with widespread migmatization and deformation of the basement complex during granulite grade metamorphic conditions. Geochronological evidence indicates that deformation continued while the TMZ was cooling to lower amphibolite grade metamorphic conditions (between about 1.93 and 1.90 Ga.). Tectonic models on the evolution of TMZ remain preliminary and are still under debate. The current models agree, however, on the regional significance of the north-south trending shear zones with a long-lived deformation history. The shear zones have predominantly accommodated the strike-slip components of a transpressional deformation regime during and after events of continental collision (ca. 2.10 - 1.92 Ga.) between the Archean Rae province on the east and the Archean Slave province and Paleoproterozoic Bufallo Head terrane on the west. Lateral escape along these shear zones continued during and after cooling to greenschist facies conditions (at ca. 1.8 Ga.). The review presented in this chapter allows placing the integrated analyses of the remotely sensed and field data in the context of current views on the tectonic evolution of the Alberta Shield.

---

* Parts of this chapter are based on the publication:

McDonough, M.R.M., McNicoll, V.J., Schetselaar, E.M. and Grover, T., 2000, Geochronological and kinematic constraints on crustal shortening and escape in a two-sided oblique-slip collisional and magmatic orogen, Paleoproterozoic Taltson magmatic zone. Canadian Journal of Earth Sciences, (in press).

2.1 Introduction

Northeastern Alberta is underlain by the Taltson magmatic zone (TMZ), a belt of Archean to Paleoproterozoic gneisses predominantly intruded by S-type granites. The TMZ is interpreted to have evolved from a continental magmatic arc to the core of a collisional orogen (Ross *et al.*, 1991; Thériault, 1992; Bostock and van Breemen, 1994; McDonough *et al.*, 1995). The exposed part of the TMZ extends from the Great Slave Lake Shear Zone (GSLSZ) in Northwest Territories to the southern limit of the study area in the northeastern corner of Alberta (Figure 2.1). The TMZ can be traced another 300 km further south beneath Paleozoic cover on the bases of drill hole data and the aeromagnetic anomaly map of western Canada (Ross *et al.*, 1991). The TMZ constitutes, after restoring about 350 km of dextral displacement along GSLSZ, together with the Thelon arc a 2500-km long magmatic belt at the western margin of the Archean Rae province. To the south, underneath the Palaeozoic cover, the magnetic anomalies associated with the TMZ appear to be truncated by the Snowbird Tectonic Zone (STZ) (Ross *et al.*, 1991). The STZ, however, is interpreted as an Archean structure to the northeast where the shear zone can be traced on the surface (Hanmer *et al.*, 1991).

Figure 2.2 shows a map compilation of the exposed TMZ from the regional map compilation of the TMZ in Northwest Territories (after Berman and Bostock, 1997) and northeastern Alberta (after McDonough *et al.*, 1995). The transition from I- to S- type TMZ magmatism between 1.98 and 1.92 Ga. and pre- to postcollisional Nd-isotope signatures have been interpreted to reflect the eastward subduction of oceanic crust and subsequent continental collision between the Archean Rae province on the east and the Paleoproterozoic Buffalo Head terrane (BHT) and Archean Slave province on the west (Ross *et al.*, 1991; Thériault, 1992; Berman and Bostock, 1997). The BHT, entirely underneath Paleozoic cover, has been outlined west of the TMZ on the bases of aeromagnetic anomaly patterns and radiometric age determination of drill core (Ross *et al.*, 1991). The 2.4 - 2.1 Ga. age range of these drill cores overlaps with 2.44-2.27 Ga. granites emplaced within older crust of the Rae province. Together with the similarities in Nd-isotope geochemistry, this has led to the interpretation that the BHT is a rifted crustal fragment of the Rae province (Thériault, 1992; Bostock and van Breemen, 1994).

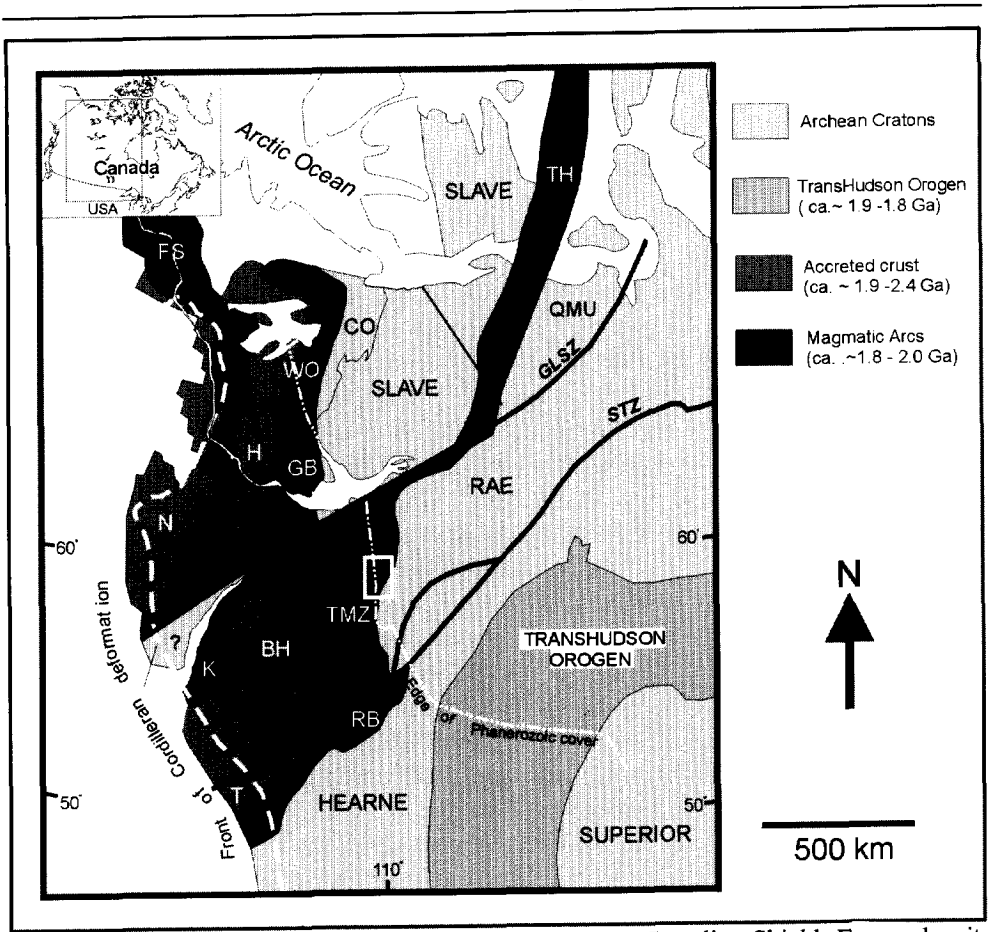

Figure 2.1 Generalized lithotectonic map of the western Canadian Shield. Exposed units after Hoffman (1988); subsurface units after Ross *et al.* (1991). TMZ = Taltson magmatic zone, TH = Thelon arc, GB = Great Bear arc, RB = Rimbey arc, K = Ksituan arc, FS = Fort Simpson arc, WO = Wopmay orogen, CO = Coronation fold and thrust belt, QMU = Queen Maud uplift, BH = Buffalo Head and Chinchaga domains, T = Thorsby, N = Nahanni, H = Hottah, GSLSZ = Great Slave Lake shear zone, STZ = Snowbird tectonic zone. White rectangular box indicates the approximate location of the study area.

Widespread remnants of a supracrustal assemblage (Figure 2.2) and the presence of small enclaves of mafic- and ultramafic rocks within these remnants and the Paleoproterozoic basement in the western Rae margin are also suggestive for an event of rifting (Bostock and van Breemen, 1994).

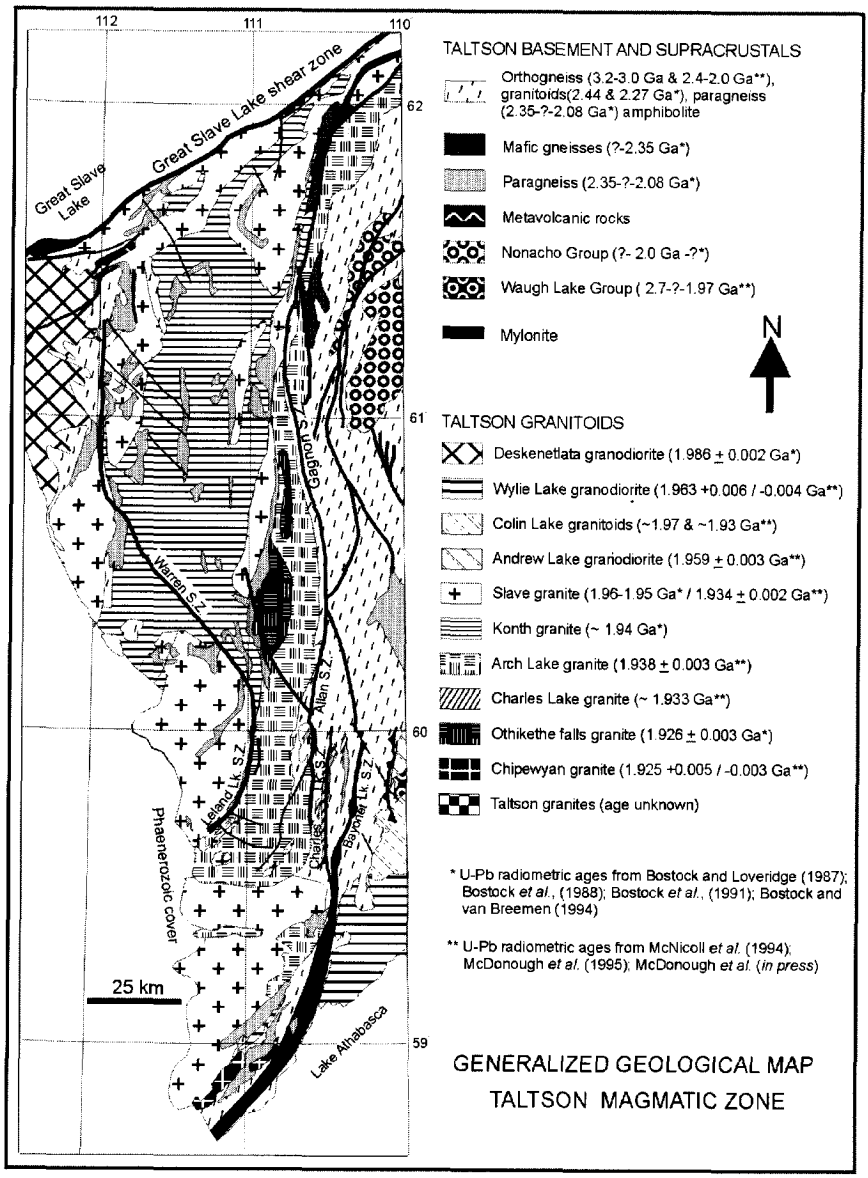

Figure 2.2 Generalized map compilation of the exposed Taltson Magmatic Zone after Berman and Bostock (1997) for the Northwest Territories and after McDonough *et al.* (1995) for Alberta.

In northeastern Alberta the TMZ is composed of an Archean (3.2 – 2.9 Ga.) to Paleoproterozoic (2.4 – 2.0 Ga.) basement complex intruded by numerous Paleoproterozoic (1.96 – 1.92 Ga.) granitoid plutons (McDonough *et al.*, 1995). Contrary to the 1.986 Ga. Deskenatlata suit of the northern TMZ, geochemical classifications (Goff *et al.*, 1986) and recent Nd, O and Pb isotope analysis (De *et al.*, 1997) the granites in the southern TMZ do not have unequivocal I-type characteristics.

The TMZ is cut by two transcurrent ductile-brittle shear zones comprising high-grade to greenschist facies mylonitic rocks. These shear zones have been considered to be genetically related to deformation along the Great Slave Lake Shear Zone (GSLSZ) that accommodated the indentation of the Archean Slave province into the Rae province (Hanmer *et al.*, 1992). According to this model, the north-south striking shear zones in the TMZ have accommodated lateral escape of crustal fragments of the Rae province towards the south (Figure 2.2, Hoffman, 1987; Hanmer *et al.*, 1992).

Mapping on 1:50 000 scale of the northeastern Alberta Shield was conducted in the sixties and seventies by Godfrey and co-workers (Godfrey, 1986 and references contained therein). During three field seasons between 1992 and 1994 the area has been re-mapped on the same scale with focus on the tectonic evolution of the area under the auspices of the Canada-Alberta agreement on mineral development MDA project (Macqueen, 1997). This field mapping project, in which the author participated, resulted in a 1 : 50 000 scale digital map coverage (McDonough *et al.*, *in press*, and references contained therein) of which a generalized compilation is shown in Figure 2.3. The review of the geology of northeastern Alberta provided in this chapter is based on the work of Godfrey, (1986, and references contained therein) and the field observations acquired during the MDA mapping project. It is explicitly stated where the description is based on field observations of the author (unpubl. obs.). U-Pb ages from zircon and monazite are from McNicoll *et al.* (1994), McDonough *et al.* (1995), McDonough *et al.* (2000). The descriptions of metamorphic mineral assemblages and geothermobarometric data are mainly from Grover *et al.*, (1997).

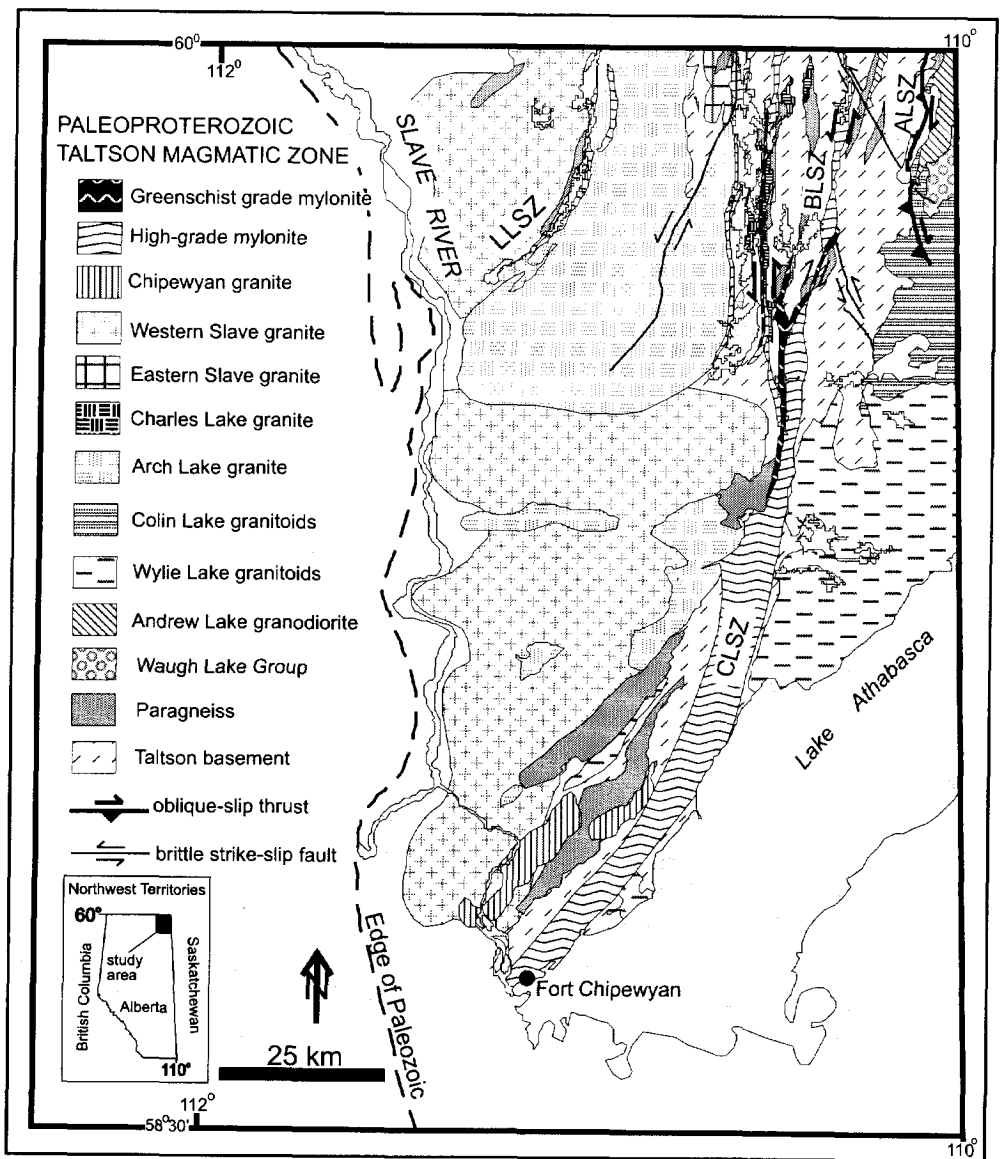

Figure 2.3 Generalized geological map of the Taltson magmatic zone in northeastern Alberta after McDonough *et al.*, 1995 (modified from Godfrey, 1986); ALSZ = Andrew Lake shear zone, BLSZ = Bayonet Lake shear zone, CLSZ = Charles Lake shear zone, LLSZ = Leland Lake shear zone. Inset shows the location of the study area.

2.2 Lithological units

Taltson Basement Complex

The Taltson Basement Complex (TBC) constitutes about 35% of the exposed northeastern Alberta Shield. It is a diverse suit of banded hornblende- and biotite-bearing granitic to tonalitic orthogneisses yielding 3.2 to 2.1 Ga. U-Pb zircon crystallization ages (McNicoll *et al.*, 1994). The gneisses are pervasively intruded by pegmatites and dykes of equigranular leucogranite and contain enclaves of amphibolite and metasedimentary rocks. Amphibolitic rafts are relatively small in dimension with lengths in the order of 5 to 500 meters. Paragneiss enclaves, ranging in length from a few 100 meters up to 40 kilometres are widespread in the TBC and S-type Taltson granites. These paragneisses are interpreted as the supracrustal remnants of the Rutledge River basin (Bostock and van Breemen, 1994).

Detrital zircons of paragneiss enclaves in the Northwest Territories provide an Archean-2.13 Ga. age range while metamorphic ages of monazite are in the range 2.08 to 2.05 Ga. These data suggest that the Rutledge basin closed between 2.13 to 2.08 Ga. (Bostock and van Breemen, 1994). Mineral assemblages in these paragneiss enclaves indicate that peak metamorphic conditions ranged from the upper- to lower granulite facies from west to east across the area. The highest granulite facies assemblage in the west consists of spinel, quartz, garnet, cordierite, K-feldspar and sillimanite whereas the lowest transitional amphibolite-granulite facies assemblage in the east consists of garnet, biotite, cordierite, K-feldspar, sillimanite and quartz. Geothermobarometric calculations together with the stable association of spinel and quartz indicate that maximum temperatures were in excess of 850°C (Grover *et al.*, 1997). Irregular masses and concordant sheets of garnet bearing leucosome in the sedimentary protoliths are abundant, suggesting that the melt formed by biotite dehydration reactions (Berman and Bostock, 1997; Grover *et al.*, 1997). The similar Al-mineralogies between paragneiss and melt, the frequent occurrence of paragneiss in S-type Taltson granites and geochemical evidence all suggest that migmatization was related to widespread granulite-facies metamorphism, anatexis and the formation of the Taltson granites (Goff *et al.*, 1986; Thériault, 1992; Chacko *et al.*, 1994; Berman and Bostock, 1997; Grover *et al.*, 1997).

A retrograde metamorphic overprint is found throughout the TBC but particularly pervasive in shear zones were high-grade gneissic and mylonitic rocks have been reworked into lower amphibolite and greenschist facies mylonites.

Charles Lake granite

Sheets of megacrystic granite (of 0.5-2 km width and 10-30 km length) occur in close association with the metasedimentary rocks within the Charles Lake shear zone. They contain large 5-8 cm. rectangular K-feldspar megacrysts with biotite inclusions in a matrix of dynamically recrystallized quartz, K-feldspar and plagioclase and muscovite, biotite with rare garnet and cordierite. Numerous white to pink leucogranitic dykes with quartz ribbons are co-planar to the mylonitic fabric (Figure 2.4 B). An intensification of strain is commonly observed towards the contacts with the TBC gneisses where the rectangular K-feldspar megacrysts are grain size reduced and recrystallized to rounded porphyroclasts of 1-2 cm diameter in narrow zones of ultramylonite (unpubl. obs.). Zircons analyzed from the Charles Lake granite are highly discordant. Analyses on monazite yield ages in the range 1.918-1.932 Ga. (McDonough *et al.*, 1995). Analysis on biotite inclusions in the K-feldspar megacrysts of two samples, yielded cooling ages of 1.856 ± 0.012 Ga. and 1.799 ± 0.011 Ga., the latter age possibly reflecting thermal resetting (Plint and McDonough, 1995).

Arch Lake granite

The Arch Lake granites are magnetite bearing biotite quartz monzo- to syeno-granites with characteristic rectangular 1 by 3 cm. K-feldspar megacrysts. Locally, xenoliths of TBC orthogneisses and amphibolite are found in the external periphery of the Arch Lake pluton. The Arch Lake granites are to a variable degree affected by ductile deformation. The solid state fabric ranges in intensity from weakly foliated megacrystic granite defined by elongated quartz (Figure 2.4 C) to well foliated augen gneiss and mylonite defined by quartz and feldspar ribbons. This variation in strain is particularly evident towards the marginal shear zones, where the fabric changes within approximately 200 to 300 meters from weakly unfoliated granite, to protomylonite at the pluton margin. Minor elongated masses of mylonitized Arch Lake granite are incorporated in the CLSZ (unpubl. obs.).

A concordant zircon fraction from the Arch Lake granite yields a 1.938 ± 0.001 Ga. crystallization age (McDonough *et al.*, 1995). The Arch Lake suite extends into the Northwest Territories as a 10 to 20 km wide and 200 km long unit along the eastern margin of the megacrystic Konth syenogranite (Figure 2.2) dated at 1.935 ± 0.002 Ga. (Bostock *et al.*, 1987). The ilmenite bearing Konth suit is differentiated from the magnetite bearing Arch Lake suit on the basis of its low magnetic signature (Charbonneau, 1990).

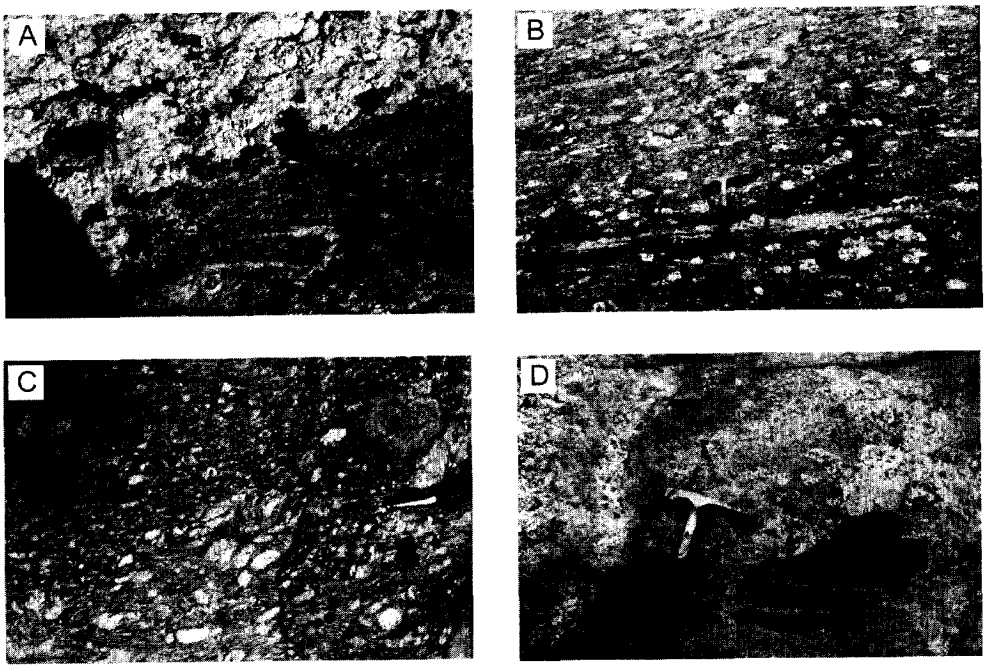

Figure 2.4 Outcrop photographs of lithological units of the southern TMZ. (A) Garnet bearing leucosome in paragneiss enclave; (B) Charles Lake Granite consisting of rectangular K-feldspar megacrysts in a fine grain-size reduced mica rich matrix. Note the foliation parallel dykes of leucogranite; (C) Arch Lake granite displaying fabric of aligned K-feldspar megacrysts; (D) Raft of TBC mafic banded gneiss in Slave Granite. Note mafic clots of biotite-rich restite.

Slave granite

The equigranular, medium to coarse-grained Slave monzogranite is massive to moderately foliated. The Slave monzogranites contain abundant mafic clots consisting of biotite, garnet, hercynite and cordierite (Nielsen *et al.*, 1981; McDonough *et al.*, 1995). Locally, close to the intrusive and tectonic contacts with the TBC, rafts of banded gneisses from the TBC are enclosed in the granite (unpubl. obs., Figure 2.4(D)). Zircons from a Slave granite dyke yielded a U-Pb crystallization age of 1.933 $\pm$ 0.003 Ga. (McNicoll *et al.*, 1994). The Eastern Slave granite crops out west of Charles Lake close to the border with the Northwest Territories (Figure 2.3) and is distinguished as a separate phase (raisin granite),

because of its characteristic texture of K-feldspar phenocrysts in an equigranular matrix (Goff *et al.*, 1986). Two major batholiths of Western Slave granite crop out between Leland Lake shear zone and Slave River and further south between the Slave River and the Charles Lake shear zone (Figure 2.3). The 1.933 Ga. age of crystallization contrasts with the 1.955 $\pm$ 0.002 Ga. crystallization age for the Slave granite in the Northwest Territories (Bostock *et al.*, 1987). This discrepancy in crystallization age possibly suggest that the Slave granite dyke represents a local younger phase or points to the existence of distinct plutonic phases with similar textural and compositional characteristics.

Andrew Lake granodiorite

The Andrew Lake suit, located east of Andrew Lake (Figure 2.3) consists of well foliated to massive megacrystic biotite and hornblende bearing granodiorite to diorite. The Andrew Lake suit is deformed in dip-lineated high-grade mylonites of the Andrew Lake shear zone at its contact with the TBC. A marginal phase of granodiorite containing 15 percent biotite and 1 percent hornblende passes gradually into a quartz monzonite with less then 10 percent biotite (Goff *et al.*, 1986). Zircons of two samples yield U-Pb ages of 1.959 ± 0.003 Ga. and 1.962 +0.016/-0.010 Ga. (McDonough *et al.*, 1995).

Colin Lake granodiorite

The Colin Lake granites range in composition between megacrystic quartz diorite, granodiorite to muscovite bearing granites. A phase of biotite rich megacrystic foliated granodiorite to quartz diorite forms the northern and western margin of the plutonic suit. This marginal phase passes gradually into a homogeneous well foliated megacrystic granodiorite with decreasing biotite content and increasing number of microcline megacrysts (Goff *et al.*,1986). The megacrystic quartz diorite with a zircon U-Pb crystallization age of 1.971 ± 0.004 Ga. (McNicoll *et al.*, 1994) intrudes the metasedimentary rocks of the Waugh Lake group (see below). A white muscovite-bearing phase of the Colin Lake suit, interpreted as late anatectic melts, intrudes the foliated phases and ductile fabrics in the Andrew Lake shear zone. This leucocratic phase has a zircon age of 1.923 ± 0.002 Ga. (McDonough *et al.*, 1995).

Wylie Lake granodiorite

The Wylie Lake suit consists of biotite-hornblende K-feldspar megacrystic granodiorite and a phase of equigranular quartz diorite intruded by lensoidal leucocratic hornblende bearing quartz monzonite (Goff *et al.*, 1986; McDonough *et al.*, 1995) The K-feldspar megacrysts ranges between 5-8 cm length and 2-4 cm width. The northern margin of the Wylie Lake pluton is cut at high angle by sinistral transcurrent shears of the CLSZ whereas the western margin displays a strong ductile strain gradient approaching the main strand on the Charles Lake Shear Zone from the east (McDonough *et al.*, 1995). This suggests that the pluton is pre-kinematic with respect to deformation along the CLSZ. The U-Pb zircon crystallization ages of the Wylie Lake suit is 1.963 +0.006/-0.004 Ga. (McDonough *et al.*, 1995).

Chipewyan granite

The Chipewyan granite is a 30 km long and 6 km wide stock that intruded parallel to dip-lineated gneissic and mylonitic fabrics of the TBC. Locally, however, it intrudes these high-grade fabrics at an angle. The Chipewyan suit itself is generally weakly foliated with local intensification of a greenschist to lowest amphibolite grade fabric along the intrusive contacts with the TBC (McDonough *et al.*, 1995). It is magnetite bearing and ranges in composition between syenogranite to quartzmonzonite (Goff *et al.*, 1986). A 1.925 +0.005/-0.003 Ga. U-Pb zircon crystallization provides a minimum age constraint for the high-grade deformation history of the CLSZ in the southern TBC (McDonough *et al.*, 1995).

Leucogranite

Small bodies of white to pink weakly foliated muscovite bearing leucogranites pervasively intrude the TBC as irregular masses and dykes. This leucogranite is to a variable degree affected by greenschist mylonitization and intrude high-grade mylonite in the Andrew Lake thrust zone (McDonough *et al.*, 1995).

Waugh Lake Group

The Waugh Lake Group forms an enclave of low-grade metamorphic clastic sedimentary and volcanic basin sequence preserved southeast of Andrew Lake (Figure 2.3). The metasediments consist of phyllite, schist, quartzite and a basal

foliated feldspathic pebble conglomerate. The sediments of the Waugh Lake Group have been metamorphosed in the greenschist facies, showing mineral assemblages of quartz, chlorite, biotite and epidote. Sedimentary structures, such as graded bedding and crossbedding have been locally preserved (Godfrey, 1986). Metavolcanic rocks include massive chlorite and chlorite-biotite schists. Relic pyroxene phenocrysts in metavolcanic rocks are altered to epidote and actinolite (Godfrey, 1986). Detrital zircons of the conglomerate beds yield ages in the range 2.3 – 2.0 Ga. and 2.7 Ga. (McNicoll *et al.*, 1994). The Waugh Lake Group is intruded by the Colin Lake granodiorite, which constrains the sedimentation in this basin to have occurred between 2.00 and 1.97 Ga. (McNicoll *et al.*, 1994). The Waugh Lake Group has previously been interpreted to represent a sedimentary cover, deposited on the TBC after peak metamorphic conditions (Baadsgaard and Godfrey, 1967). The recent age-constraints, however, rule out this possibility. The contrast in metamorphic grades between the TBC paragneisses and the Waugh Lake Group has been re-interpreted to reflect the transition from a relative cold footwall to the hot hangingwall of the Andrew Lake thrust zone (see the description of Andrew Lake thrust zone below, McDonough *et al.*, 1995).

2.3 Geological structure

The structural geologic evolution of the TMZ is characterized by multiple ductile, brittle-ductile and brittle deformation events that affected the rocks during regimes of tectonic escape, continental collision and progressive unroofing. The distribution of structures in combination with geochronological constraints suggest that both during and after the Taltson magmatic event, strain was heterogeneously partitioned in zones of shortening accommodated by folding and local thrusting and zones of high non-coaxial strain evolving into regional transcurrent shear zones.

Structural relationships, fabrics and superimposed folding

Most localities within the TBC display a single penetrative planar fabric with a sub-vertical to vertical orientation. The fabric is defined by a gneissic banding of alternating quartzo-feldspathic and mafic layers. Granulite grade mineral assemblages commonly define the fabric in paragneiss (Grover *et al.*, 1997). In thin section the fabric appears to be granoblastic with lobate grain boundaries between garnet, quartz and feldspar to protomylonitic with coarse grained polycrystalline ribbons of quartz, recrystallized feldspar and elongated garnet. In

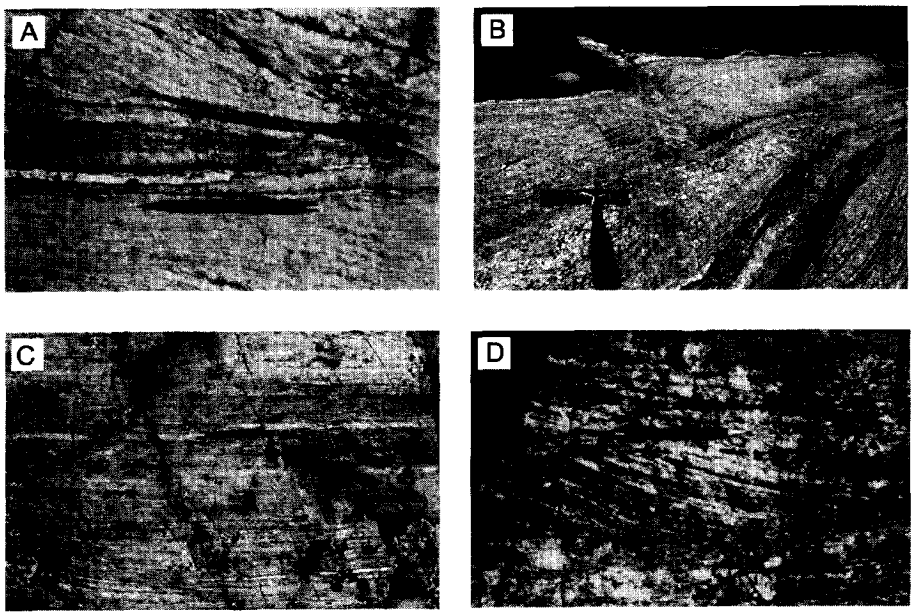

Figure 2.6 Outcrop photographs of shear zones in the TBC. (A) Sinistral deflection of quartzo-feldspathic mylonitic gneiss along discrete lower amphibolite grade shear zone in western splay of Charles Lake shear zone; (B) Apparent dextral offset of pegmatite vein intruding high-grade quartzo-felspathic mylonite along discrete greenschist grade shear zones. The next pegmatite fragment to the lower left, off the photograph, showed an apparent displacement of 10 meters. Note the dextral extensional shear bands in the greenschist shear zone bounding the lower pegmatite fragment. (C) Banded mylonite composed of alternating quartz and feldspar ribbons. (D) Foliation fish in high-grade mylonitic gneisses indicating a sinistral sense of shear.

In outcrop, the fabric varies in intensity from a weakly developed foliation defined by platy blue quartz and the preferred orientation of biotite to augen gneiss. Langenberg and Ramsdale (1980) interpreted this solid state foliation of variable intensity to represent the outlines of gneissic dome structures formed by diapiric ascent.

Marked strain gradients are observed towards the eastern and western pluton margins where 0.5 to 1 km wide zones of mylonitized Arch Lake granite are involved in the LLSZ and CLSZ (McDonough *et al.*, 1995, Figure 2.3). The solid state foliation in the Arch Lake granite is occasionally folded in northerly trending upright open folds with half-wavelengths between 5 to 10 meters.

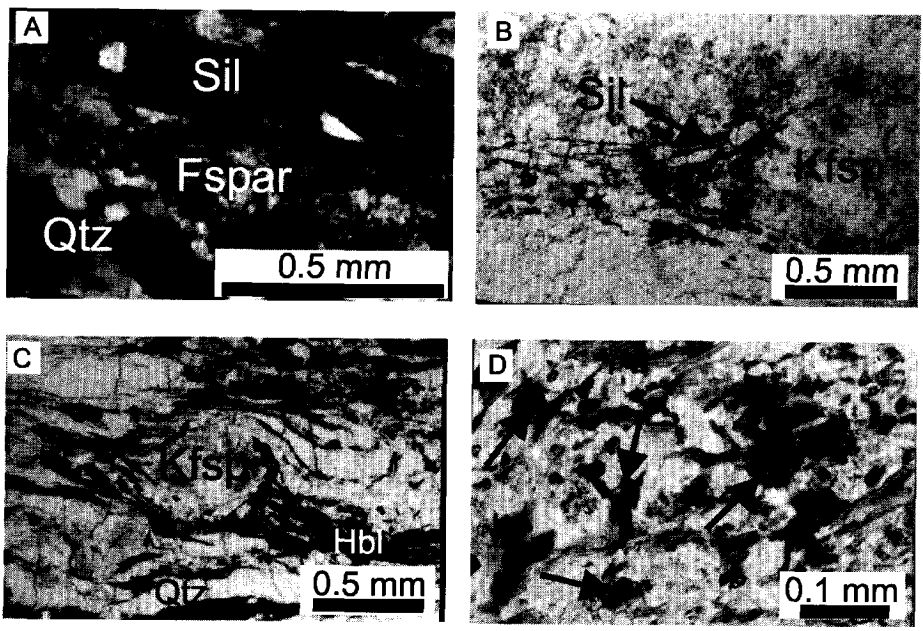

Figure 2.7 Photomicrographs of fabrics in Charles Lake Shear Zone. (A) Cross-polarized view of sillimanite crystal parallel to alternating polycrystalline ribbons of recrystallized feldspar and quartz in high-grade mylonite. Note irregular grain boundaries of quartz, suggesting that they formed in response of grain boundary migration recrystallization; (B) Sillimanite wrapped along K-feldspar porphyroclast in mylonitized paragneiss; (C) Delta-type winged porphyroclast in hornblende bearing granite mylonite, indicating a sinistral sense of shear; (D) Late- to post kinematic biotite overgrowing greenschist- to lower amphibolite grade foliation in Charles Lake granite.

Folds of similar orientation and style deform the intrusive contact between Slave granite and amphibolitic gneisses at the western margin of the TBC (Figure 2.5(D)). Foliation in the Western Slave granite and gneissosity of the TBC are affected by open folding associated with a weakly developed steeply to the west dipping fracture cleavage. This fracture cleavage is parallel in orientation to a locally developed greenschist-grade steeply dipping crenulation cleavage defined by chlorite, muscovite and biotite (unpubl. obs.).

Shear zones

The TMZ is cut by three major ductile to brittle-ductile shear zones. From west to east these are the Leland Lake (LLSZ), Charles Lake (CLSZ) and Andrew Lake (ALSZ) shear zones (Figure 2.3). The LLSZ and CLSZ shear zones are sub-vertical to vertical predominant transcurrent shear zones. The Andrew Lake shear zone is inferred from a number of aligned outcrops of dip-lineated mylonites to form a low angle east vergent thrust zone (McDonough *et al.*, 1993).

Indications for reactivation of the transcurrent shear zones is widespread and displayed in outcrop by: (i) silicification, recrystallization and cataclasis within panels of high-grade mylonite associated with retrograde mineral assemblages of chlorite and epidote, (ii) bending of high-grade mylonite fabrics into localized lower amphibolite grade shear zones of restricted width (20-50 cm) (Figure 2.6 (A)), (iii) pegmatite veins intruding high-grade mylonites that are offset along discrete zones with greenschist grade mineral assemblages (Figure 2.6 (B)).

Leland Lakes shear zone

The Leland Lake shear zone (LLSZ) forms a curvilinear belt of high-grade mylonites, involving TBC units and the western margin of the Arch Lake pluton (Figure 2.3). The shear zone is intruded by the Slave granites such that a 50 to 500 meter wide belt of strike-lineated mylonites has been preserved (McDonough *et al.*, 1995). The mylonites display spectacular striped gneiss fabrics consisting of alternating layers of recrystalized feldspar and quartz ribbons with rare K-feldspar porphyroclasts. Local pull aparts of amphibolitic enclaves suggest large amounts of non-coaxial strain (McDonough *et al.*, 1995).

A granite dyke interpreted to be genetically associated with the Slave granite intrudes high-grade fabrics in the shear zone and yields a U-Pb zircon crystallization age of 1.934 ± 0.002 Ga. (McDonough *et al.*, 1995). Both dextral and sinistral kinematic indicators have been found in the LLSZ (McDonough *et al.*, 1995), between which the relative age relationships have not been established. The regional tectonic escape model proposed by Hanmer et al. (1992) provides one explanation for the bi-directional sense of shear. In this model, a reversal from sinistral to dextral shear sense is interpreted to reflect the transition of a shear zone from the leading- into the trailing boundary of an escaping crustal block (Figure 2.8 (C)). This transition occurs when the locus of escape migrates with the eastward indentation of the Slave province (e.g. Hanmer *et al.*, 1992; McDonough *et al.*, 1995).

The Slave granite that intrudes the LLSZ, locally display a down-dip lineation formed of quartz and feldspar ribbons. From its sparse field observation and lack of diagnostic metamorphic mineral assemblages it is unsure if this lineation is related to the emplacement of the Slave pluton or if it is formed by regional post-emplacement deformation. The high-grade mylonites in the LLSZ are locally reworked in discrete transcurrent shears. These shears consist of greenschist grade mylonite and ultramylonite with C-S fabrics that consistently indicate a sinistral sense of shear (McDonough *et al.*, 1995).

Charles Lake shear zone

The Charles Lake shear zone (CLSZ) constitutes a braided system of anastomosing sub-vertical 0.5 to 1 km wide splays predominantly consisting of strike-lineated mylonite. The CLSZ passes into the strike-lineated Allen (ASZ) and Gagnon (GSZ) shear zones in the Northwest Territories together forming a principle transcurrent shear zone along the western margin of the Rae province (Figure 2.2). Towards the north a dextral splay of the shear zone belt curves towards ENE direction into the lower amphibolite-grade mylonites of the Great Slave Lake shear zone (Hanmer *et al.*, 1992). The magnetic trends of the CLSZ can be traced for about 100 kilometers in southwesterly direction underneath Paleozoic cover on the aeromagnetic map of western Canada until its expression diffuses into alternating positive and negative linear anomaly patterns within the TMZ. The ductilely and cataclastically deformed parent materials mainly comprise orthogneiss of the TBC, Charles Lake granite, and the margins of the Arch Lake and Wylie Lake plutons. Paragneiss enclaves are rarely involved in the CLSZ, providing only local evidence to determine the metamorphic grade of mylonitization. This sparseness of indicative minerals and the continuous shear zone activity during slow protracted cooling to greenschist grade metamorphic conditions (Plint and McDonough, 1995) undoubtedly accounted to the conflicting interpretations in the literature of the metamorphic grade at which mylonitization commenced. Nielsen *et al.* (1981) interpreted the mylonites to have formed at greenschist-grade metamorphic conditions, on the basis of the widespread distribution of chlorite within the mylonite zones. Bostock *et al.*, (1984) and Hanmer *et al.*, (1992) interpreted the Allen and Gagnon Lake shear zones on the basis of their continuity with mylonites of similar grade in the GSLSZ and their mineral assemblage to have formed from lower amphibolite to greenschist grade metamorphic conditions. McDonough *et al.* (1995) and Grover *et al.* (1997) inferred granulite facies conditions during the initiation of mylonitization on the

basis of straight striped fabrics composed of alternating layers of recrystallized feldspar and quartz ribbons (Figure 2.6 (C)) and synkinematic granulite-facies assemblages in protomylonitic paragneiss.

The occurrence of these protomylonitic fabrics in paragneiss, however, are widespread (unpubl. obs.). The field observations of the TBC gneisses, described above, indicate that mild mylonitization at granulite grade, accompanied folding and migmatization throughout the TBC. These fabrics, that were approximately formed at peak metamorphic conditions (Berman and Bostock, 1997; Grover *et al.*, 1997), may alternatively be considered as pre-kinematic with respect to the initial strain localization event that gave rise to the CLSZ.

Thin sections of paragneiss enclaves from the CLSZ, without evidence for retrogression at lower amphibolite to greenschist grade conditions, contain synkinematic sillimanite and muscovite growing parallel to alternating polycrystalline ribbons of recrystallized feldspar and quartz (unpubl. obs., Figure 2.7 (A)) and sillimanite wrapping K-feldspar porphyroclasts (unpubl. obs., Figure 2.7 (B)). Garnet is abundant whereas cordierite and spinel are absent. K-feldspar porphyroclasts show undulous extinction, subgrain boundaries and myrmekite along their foliation parallel faces, suggesting medium- to high-grade deformation conditions (Passchier and Trouw, 1996). The metamorphic grade of this fabric is inferred to be retrograde with respect to the granulite-facies assemblages of K-feldspar, sillimanite, garnet, cordierite and spinel. Although the extent to which these observations are regionally representative remains obscure, they locally indicate that the strain localization that gave rise to the CLSZ, initiated at higher amphibolite-grade metamorphic conditions. The widespread occurrence of epidote and synkinematic hornblende in mylonitized orthogneiss without signs of further retrogression suggest that these mylonites were extensively reworked at lower amphibolite grade conditions. Mylonitized orthogneiss with strong shape-preferred orientation of quartz and flame perthite in K-feldspar porphyroclasts contain synkinematic blue-green amphibole locally wrapping the K-feldspar porphyroclasts (unpubl. obs.; Figure 2.7 (C)) Kinematic indicators, such as shear lenses (Figure 2.5 (D)), sigma and delta type porphyroclasts (Figure 2.7 (C)), shape preferred orientation of quartz and shear bands in amphibolite rafts indicate a sinistral sense of movement in these mylonitized orthogneisses (McDonough *et al.*, 1995), consistent with the sense of shear inferred for the ASZ and GSZ (Bostock, 1988).

A major splay of the Charles Lake shear zone, the Bayonet Lake shear zone (BLSZ; Figure 2.3) forms a 1 to 3 km wide belt of sinistral and dextral high-grade strike-lineated mylonites (McDonough *et al.*, 1995). These high-grade mylonites

are locally reworked into discrete strike-lineated greenschist grade mylonites (McDonough *et al.*, 1995).

Domains of dip-to obliquely-lineated steeply dipping high-grade mylonites and mylonitic gneiss locally flank the strike-lineated domains of CLSZ and BLSZ. West of Lake Athabasca the main foliation, while maintaining steep dip angles, swings about ten degrees eastward, passing into a 10 kilometer wide wedge-shaped domain of oblique- to dip-lineated mylonitic gneisses and mylonites (McDonough *et al.*, 1995, Figure 2.3, Plate 7.1(B)). Kinematic data in this oblique- to dip-lineated domains are scarce but both northwest and southeast directed tectonic transport directions were inferred from oblique subgrain fabrics in quartz (McDonough et al., *in press*). Both oblique- and dip-slip movement predate intrusion of the Chipewyan granites at 1.925 + 0.005/-0.003 Ga. and postdate intrusion of the Wylie granodiorite at 1.963 +0.006/-0.004 Ga. permitting these movements to be synchronous in a transpressional setting. Further north the evidence for extensive retrograde reworking of high-grade fabrics to strike-lineated lower amphibolite to upper greenschist grade mylonite, however, strongly suggest that the CLSZ is multistage. Events of strike-slip movement within the principle splays of the CLSZ outlasted the dip-slip movement recorded in high-grade mylonite zones in broader domains adjacent to the CLSZ and BLSZ (McDonough et al., *in press*, Plate 7.1 (B)).

Andrew Lake shear zone

The poorly exposed Andrew Lake shear zone (ALSZ) was recognized and mapped by McDonough *et al.* (1993). Local zones of dip-lineated mylonites are interpreted as a continuous thrust zone dipping about forty degrees to the southwest. This interpretation is supported by a strong break in the total magnetic field at the western shore of Andrew Lake (Charbonneau, 1997). C/S fabrics and Sigma type porphyroclasts consistently indicate top to the northeast movement during which the TBC was thrusted over the Andrew Lake granodiorite. Slightly oblique down dip stretching lineations indicate thrust displacement with a dextral strike-slip component. The 1.959 + 0.003 Ga. Andrew Lake granodiorite is deformed in the hanging wall of the ALSZ that is intruded by ca. 1.933 Ga. leucogranite (McDonough et al., *in press*).

Greenschist shear zones

Numerous narrow vertical greenschists shear zones ranging in width between a few to ten meters are found in the area between the CLSZ and ALSZ. The shear zones strike north and display ductile deformation of quartz in ribbons and brittle deformation of feldspars. Kinematic indicators predominantly suggest sinistral shear sense. These shear zones, affecting orthogneisses of the TBC, commonly display sinistral C/S fabrics.

Ductile and brittle-ductile sub-vertical to vertical discrete shears cutting the north to northeast striking gneissic and mylonitic foliation display both left-lateral and right-lateral apparent displacement. Occasionally conjugate sets deforming gneissic and mylonite foliation at high angles are found. Epidote and chlorite are the commonly found metamorphic minerals within the discrete zones of brittle and brittle-ductile shear suggesting lower greenschist grade during their activity (McDonough *et al.*, 1995).

2.4 Tectonometamorphic evolution

The crustal evolution of the southern TMZ has previously been interpreted to result from the remobilization of Archean basement during the Trans-Hudson orogeny between ca. 1.90 – 1.80 Ga. (Godfrey and Langenberg, 1978; Nielsen *et al.*, 1981).). Recent U-Pb zircon dating and geothermobarometry data, however, unequivocally demonstrate that peak metamorphic conditions were attained at ca. 1.93 Ga. This metamorphic peak was attained after early arc plutonism and at the culmination of plutonism in increasingly thickened crust within a collisional orogen (Berman and Bostock, 1997; Grover *et al.*, 1997) and support the view that the tectonometamorphic evolution of the TMZ was related to eastward directed subduction followed by continental collision between ca. 2.0 -1.90 Ga. (Hoffman, 1987; Hoffman, 1991; Bostock *et al.*, 1991; Ross *et al.*, 1991; Hanmer *et al.*, 1992). Figure 2.6 shows a recompilation of this model (from Ross *et al.*,1991) in which the kinematic models of Hoffman (1987) and its refinement by Hanmer *et al.*, (1992) have been combined with the structural interpretation of the TMZ in northeastern Alberta (after McDonough *et al.*, 1995).

Before 2.1 Ga. (Figure 2.8 (A)) the Rae margin was the locus of eastward directed subduction associated with emplacement of granites between ca. 2.4 - 2.3 Ga. (Bostock and van Breemen, 1994). The Rutledge River basin received detritus of rocks with a similar range in age.

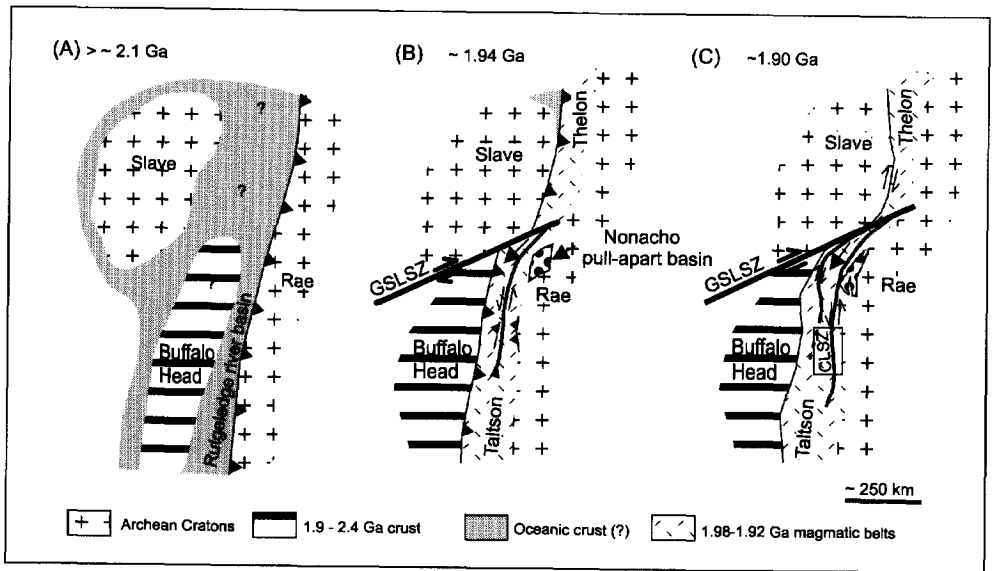

Figure 2.8 Hypothetical model for the tectonic evolution of the Taltson magmatic zone, western Canadian Shield after Hoffman (1988) and Ross *et al.* (1991) including refinements from the interpretations of Hanmer *et al.*, (1991), Bostock and van Breemen (1994) and McDonough *et al.* (1995). Rectangle on Figure 2.8(C) indicates the approximate location of the exposed Alberta Shield.

The time of collision between the subsurface BHT and the Rae province (Figure 2.8 (B)) is enigmatic as its spatial position and drift with respect to the Slave province during the Paleoproterozoic is not well understood (e.g. Ross *et al.*, 1991). The geochronological constraints for closure of the Rutledge River basin at 2.09 Ga. (Bostock and van Breemen, 1994) suggest that the BHT collided with the Rae margin before collision between the Slave and Rae continent at ca. 1.97 Ga. (Hanmer *et al.*, 1992 and references therein). This view apparently contradicts with the model in which widespread S-type plutonism between ca. 1.96 and 1.93 Ga. and granulite-grade metamorphism at ca. 1.93 Ga. was induced by collision with the BHT in a transpressional tectonic setting (Thériault, 1992; McDonough *et al.*, 1995). This temporal discrepancy between basin closure and Slave-Rae collision may be attributed to multiple events of crustal accretion at the western Rae margin (e.g. Berman and Bostock, 1997).

Recently De *et al.*, (*in press*) have questioned the subduction to collision-related magmatic evolution of the TMZ in a plate-marginal setting. On the basis of geochemical and Nd, O, Pb isotopic studies these authors argue that that the

Taltson granitoids lack the mantle contribution required for I-type magmatism in a continental magmatic arc setting. An alternative model is proposed in which it is envisaged that the TMZ and TTZ evolved in a plate-interior setting. In this plate-interior model the western boundary of Laurentia was positioned west of the BHT, whereas the Slave province is considered as an internal crustal block acting as a secondary indentor in analogy to the Tarim Block in central Asia (De *et al.*, *in press*).

The Taltson magmatic event was associated with granulite grade metamorphism culminating at ca. 1.93 Ga. (Grover *et al.*, 1997). This event led to the development of the high-grade gneissic and protomylonitic fabrics and the widespread anatexis of the Archean to Paleoproterozoic basement. Regional crustal shortening during and after anatexis resulted in a belt of high-grade mylonitic and migmatitic gneisses that was reworked into transcurrent shear zones during cooling from granulite grade to greenschist grade metamorphic conditions.

U-Pb zircon age constraints indicate that the broad belts of oblique- to dip-lineated mylonites were formed during the emplacement of the Taltson plutons between ca. 1.96 and 1.92 Ga. (McDonough *et al.*, *in press*), provided that the locally established age-constraints in the ALSZ can be extended to dip-lineated domains elsewhere. The age of movement along high-grade strike-lineated mylonites is constrained by a similar maximum age provided by the 1.963 Ga. U-Pb zircon crystallization age of the pre-kinematic Wylie Lake plutonic suit. The high- to low amphibolite grade strike-lineated mylonites in the CLSZ, suggests that transcurrent movement continued after closure of monazite at ca. 1.93-1.92 Ga. (McDonough et al., *in press*). The strike-slip shear zone locally flanked by zones of convergent shear have tentatively been interpreted to have accommodated deformation in a regime of sinistral transpression as a consequence of oblique collision between the Buffalo Head Terrane and the Rae province (McDonough et al., *in press*).

The CLSZ is continuous with the lower-amphibolite grade Allen- and Gagnon Lake shear zones in the Northwest Territories in which kinematic indicators are consistently sinistral over a strike length of more than 250 km (Bostock, 1988; McDonough *et al.*, 1995). Further north this system changes orientation from a northerly to northeasterly trend as it curves into dextral and sinistral lower-amphibolite facies mylonites that pass into the lower-amphibolite facies mylonite splays of the GLSZ (Hanmer *et al.*, 1992). These shear zones accommodated post-collisional southward escape of crustal fragments in response to the indentation of the Slave province into the Rae province (Hoffman, 1987; Hanmer *et al.*, 1992, Figure 2.8 (C)). The continental Nonacho pull apart (Figure 2.8 (B) & (C))

evolved between ca. 2.00 - 1.91 Ga. (Bostock and van Breemen, 1984). The distribution of the coarse clastic sediments and structural data suggest that the initiation, growth and deformation of this basin was controlled by sinistral strike-slip faulting corroborating the kinematic interpretation of the shear zones in the basement (Aspler and Donaldson, 1985).

Geochronological evidence that dextral shear outlasted sinistral shear in the northern TMZ (Bostock, 1988) has been interpreted to result from the eastward progression of the Slave indentor, during which the leading edge of an escaping crustal block along a sinistral shear zone became the trailing edge along a dextral shear zone (e.g. Hanmer *et al.*, 1992; Figure 2.8 (C)). This model may also account for the dextral and sinistral kinematic indicators in LLSZ (e.g. McDonough *et al.*, 1995), although the relative age relationships between dextral and sinistral shear have not been established.

Hornblende and biotite $^{40}Ar/^{39}Ar$ cooling ages of ca 1.90 Ga. respectively ca. 1.80 Ga. and 1.86 Ga. indicate slow protracted cooling (Plint and McDonough, 1995). K-Ar data provide cooling ages for muscovite and biotite of ca 1.79 Ga. respectively 1.78 Ga. (Baadsgaard and Godfrey (1967). The deformation at greenschist grade is pervasive through the Taltson basement as suggested by widespread sinistral and dextral reworking of high-grade fabrics, discrete ductile and brittle-ductile shears and vertical crenulation cleavage developed in the paragneiss enclaves. These observations indicate a significant tectonic event during lower greenschist grade metamorphic conditions of which the regional tectonic significance is at present poorly understood. The configuration of discrete sinistral and dextral shears suggests NNE-SSW directed bulk extension along steep transcurrent shear zones that reactivated the CLSZ. Mica cooling ages and the fresh overgrowths of biotite in low-grade mylonites in the CLSZ (unpubl. obs.) and east of CLSZ (Baadsgaard and Godfrey, 1967) suggest a low-grade overprint at ca. 1.8 Ga. that is consistent with the widespread greenschist grade retrogression of granulite grade gneisses in northwestern Saskatchewan (Lewry *et al.*, 1985) and the age constraints for minor reactivation of the Grease fault in the Snowbird tectonic zone (Hanmer *et al.*, 1994). A speculative regional interpretation of this event is that the shear zones in the TMZ were reactivated to accommodate the far-field interference of post-collisional (Gibb, 1979) and collisional indentation (Gibb, 1983) of respectively the Slave province-Buffalo-Head terrane and Superior provinces into the Churchill province (Rae and Hearne provinces) after the culmination of the Trans-Hudson orogeny.

3

THE NORTHEASTERN ALBERTA REMOTELY SENSED DATA SET: ACQUISITION, GEOMETRIC REGISTRATION AND GEOLOGICAL INTERPRETATION

ABSTRACT

Aeromagnetic, gamma-ray spectrometry, Landsat TM and ERS-1 data acquired over northeastern Alberta were registered on 100 and 30 meter grids to facilitate their integrated interpretation and analysis. Registration errors between data sets range from nil, between GPS positioned geophysical flight line data, to approximately 200 meters, between ERS-1 data and GPS positioned field stations. Geological interpretations of each data type are presented with outlines of major lithological domains and structures. A combined litho-structural interpretation was compiled by interactively editing domain boundaries during display of complementary images on the background. The integrated appraisal of the data set reveals that the Taltson basement complex, and most of the Taltson granitoids, can be outlined by the combined interpretation of relief shaded aeromagnetic data and a ternary image map of the K, eTh, eU gamma-ray spectrometry grids. Internal lithological variations in the Taltson basement, such as paragneiss enclaves are, however, poorly identified. Some of the outlined units suggest the presence of lithological variations not previously mapped. The Arch Lake megacrystic granite, for example, shows conspicuous internal zonation in thorium broadly in parallel orientation to its margins. Some curvilinear and linear magnetic anomalies do not correspond to geological map units and suggest the presence of distinct intrusive phases in the subsurface. The northerly to northeasterly trending structural grain of the TBC, and the fault and fracture systems transecting it, are evident in the high wave-number magnetic anomaly patterns, ERS-1 and Landsat TM images. Their combined interpretation yields a consistent N to NNE-trending structural grain. Shear zones, broadly parallel to this grain, are expressed as linear lows in the magnetic data and as linear scarps in the ERS-1 scene. The interpretation work presented in the chapter provides an assessment of the complementary geological information content of the data set on the basis of which digital integration strategies in forthcoming chapters have been directed.

3.1 Introduction

The geoscience data acquired over northeastern Alberta comprise different types of remotely sensed imagery, airborne geophysical data and field observations. To facilitate the integrated interpretation and analysis, the multiple types of remotely sensed data first need to be referenced on a cartographic projection and registered on a common grid. Prior to this co-registration procedure, several data specific corrections and reductions apply. Optical remote sensing platforms, such as Landsat Thematic Mapper, acquire image data in a spatially continuous manner that are stored instantly on board of the satellite before being transmitted to ground stations. Although the data are provided in a coherent image format with equidimensional pixels, atmospheric correction, noise removal and radiometric calibration procedures are required before the data can be geometrically corrected (Lillesand and Kiefer, 1994). Synthetic Aperture Radar (SAR) images, such as those acquired by the ERS-1 satellite, are built up from the time delay and strength of the return signals from a radar beam directed towards the Earth's surface. Rigorous processing of the return signals at ground stations is required to represent the data on ground range images (ESA, 1992) (i.e. images with equal size pixel, representing equal portions of the Earth's surface if there is no topographic relief). Airborne geophysical data are acquired in a spatially discontinuous manner at discrete intervals along flight lines spaced from a couple of hundreds meters to kilometers apart. The flight line data (after numerous data specific reductions and corrections) need to be leveled prior to their interpolation on a grid. Geological maps and primary field observations first need to be digitized to facilitate digital representation and integration with the other data types. Geological maps are usually stored in vector format, but the units of a geological map can eventually be rasterized for spatial analysis with remotely sensed data.

Grids obtained from magnetic and gamma-ray spectrometry surveys do not have to be geometrically corrected. This is because in modern geophysical surveys, each flight line sample is geographically positioned with 5 meter or better accuracy by differential GPS (Reeves *et al.*, 1997; Horsfall, 1997).

Landsat TM scenes are geometrically corrected by assigning absolute coordinates to ground control points (GCP's) recognized on both the image and a topographic map. The coefficients of the transformation between the image- and absolute map coordinates of the GCP's are estimated by least square regression analysis. The transformation is used to generate a new grid reference to which all

pixel values of the original grid are resampled (Lillesand and Kiefer, 1994). The geometric correction of imaging radar data is more complex and involves the transformation from slant range geometry to ground range geometry. This transformation requires information on the sensors position, velocity and viewing geometry, the position of the backscatter elements, Doppler frequencies and pulse transit times used for SAR image processing. In addition a digital elevation model is required to correct for layover, foreshortening and shadow. Such distortions are of significant importance in mountainous terrain were their effects are large with respect to the accuracy of selecting GCP's. An elevation difference of 100 meter, for example leads to a planimetric shift of 230 meters at mid-swath in ERS-1 images (Pohl, 1996).

Once the raster representations of each data type are georeferenced, several processing techniques can be applied to enhance the geological interpretation of the data. Whatever techniques are implemented in this interpretation process, it is important to consider multiple data sets not just as a stack of image layers or variables input to image enhancement and multivariate analysis. The interpreter should have sufficient insight in the physics of each method and be aware of the data acquisition geometry, resolution and processing to render the data in image format, and to fully appreciate its potential and limitations for geological interpretation.

In the first part of this chapter the data specifications, reductions, corrections, and the procedures that have been used to register each data type on a cartographic projection are described. In the second part, image renditions of the data set are interpreted with respect to published geological maps, field observations and previously conducted geophysical interpretations of the study area. The qualitative interpretations provide a basis for more focused integrated analysis presented in forthcoming chapters. In general, the integrated appraisal and digital overlay of interpretation layers and raster images, although dependent on subjective judgement, geological insight and skills of the interpreter, is considered effective in reducing field mapping costs and identifying targets for map refinement and exploration.

3.2 Spaceborne remotely sensed data

The specifications of the northeastern Alberta data set are listed in Table 3.1. The spaceborne remotely sensed data acquired over the study area comprise Landsat Thematic Mapper and ERS-1 scenes. The Landsat TM scene (path: 043, row 018, scene center: N59:43:53 / W 111:07:37) was acquired on 7 June, 1993.

Weather conditions were clear during acquisition with less then 10% cloud cover and a sun elevation of fifty degrees above the horizon. The pixels cover approximately a 30 by 30 meters area on the ground.

The ERS-1 .PRI scene (orbit 6871, track 213, scene center N59:40:00/W 110:30:00) was acquired on 7 November 1992 in descending mode with radar energy (in the C-band) incident from the east. The range and azimuth resolutions of the ERS-1 system are respectively 16 and 20 meters (Gerrit Huurneman, pers. comm., 1999). The .PRI scene is a multi-look ground range corrected image resampled to a pixel that correspond to a 12.5 X 12.5 area on the ground (ESA, 1992).

Data set	Acquisition Date	Acquisition resolution	Gridded resolution	Survey/scene area EW x NS
Aeromagnetic		flight lines		
γ-ray spectrometry	7-93	50 m x 1 km	100 / 30 m	80 x 120 km
Landsat TM	7-6-93	30 m	100 / 30 m	180 x 180 km
ERS-1	7-11-92	16 / 20*m	100 / 30 m	100 x 102.5 km

Table 3.1 Specifications of the northeastern Alberta data set. * range and azimuth resolutions of ERS-1 system.

3.3 Airborne geophysical data

The airborne geophysical survey was acquired, corrected and leveled by the Geological Survey of Canada (Charbonneau *et al.* 1994). The survey was flown by the GSC Skyvan aircraft in July 1993 along east-west flight lines spaced 1 km apart with an along flight line sample distance of 50 meters. The survey covers an area of approximately 120 by 80 km approximately coinciding with the exposed Alberta Shield (Figure 2.2). The mean terrain clearance was nominally 125 meters and the average ground speed 190 km/h. Three instruments were carried on board the aircraft to record the total magnetic field, the very low frequency (VLF) electromagnetic field and natural gamma radiation. The total magnetic field was recorded in nanotesla by a Geometrics model G-803 proton precision magnetometer with one (1) nT sensitivity. The magnetic data were corrected for spikes, heading effects and diurnal variations (Charbonneau *et al.* 1994). The in-phase and out-phase components of the VLF electromagnetic field were recorded with a Hertz Totem 2A system VLF instrument in which the receiving coils were tuned to station NLK in Seattle Washington which transmits at a frequency of 24.8 kHz (Charbonneau *et al.*, 1994). The gamma radiation was recorded with a 256

channel spectrometer containing twelve thallium doped sodium iodine detectors with a total crystal volume of 50 liters. The gamma-ray spectrometry data were converted to the K, eTh and eU channels using the following energy windows:

Potassium (K)	1360 - 1560 keV
Uranium (Bi)	1660 - 1860 keV
Thorium (Tl)	2410 - 2810 keV

The count rates in the potassium, uranium and thorium windows were corrected for dead-time, ambient temperature and pressure changes and background radiation due to cosmic radiation, the radioactivity of the aircraft and radon decay products in the air. Additional corrections were made for gamma-ray spectral scattering in the ground, the air and the detectors as well as for deviations of terrain clearance from the planned survey altitude (Charbonneau *et al.* 1994). Factors for converting the corrected airborne count rates to ground concentrations of potassium, uranium and thorium were determined from flights over a calibration range in the Ottawa area (Grasty *et al.*, 1984). These calibration factors are:

1 pct K	=	91.0 counts per second
1 ppm eU	=	9.1 counts per second
1 ppm eTh	=	7.0 counts per second

The total exposure rate in micro Roentgens per hour (μR/h) was computed from the measured ground concentrations of potassium, uranium and thorium (Grasty *et al.*, 1984):

$$\text{Total exposure rate} = 1.505\,\text{K} + 0.625\,\text{eU} + 0.31\,\text{eTh} \qquad [3.1]$$

The flight line samples were leveled by iterative procedures which involved, for the radiometric data, manual adjustments to the backgrounds, re-computation of the ground concentrations, regridding of the data and visual examination of the results (pers. comm. John Grant, 1997). The magnetic data were also leveled by similar iterative procedures while no tie lines were flown during the survey. The data were gridded by interpolation with an inverse distance weighted function (cosine bell) to 100 x 100 meter grid cells on UTM projection, zone 12, North American Datum, 1927 (Clarke 1866 ellipsoid) and stored as 32-bit floating point values. The search area for the gridding algorithm was 11 grid cells along and 23

grid cells across the flight lines. Ratio grids were calculated from the K, eU and Th grids. For all grid cells over water (K < 0.25%) the ratio was set to zero. For all grid cells for which K >= 0.25% each grid cell value is divided by the other grid cell value, provided that both numerator and denominator were statistically significant (standard deviation in count rate > 10 cps). If these values were not statistically significant, the next ring of cells was added in (John Grant, pers. comm., 1997).

3.4 Acquisition of geological field data

Geological field work for the Canada-Alberta Agreement on mineral development MDA was conducted in 1992, 1993 and 1994. Previous mapping on 1:50 000 scale of the Canadian Shield of northeastern Alberta was conducted by Godfrey (1986 and references therein). The recently published maps (McDonough *et al.*, 1993; 1994a; 1994b; 1994c; 1994d; 1995) are compiled from the previously published map sheets and new field mapping which focused on the tectono-magmatic evolution of the Taltson magmatic zone (TMZ) and the kinematic analysis of the shear zones that cross-cut the TMZ.

The tectonic evolution project of the Canada-Alberta agreement on mineral development (project 1A) involved bedrock mapping, rock sampling campaigns for U-Pb zircon and monazite geochronology, geothermobarometry and mineral essays (Macqueen, 1997). The fieldwork was supported by transport with fixed-wing aircraft. The large number of lakes provided access to the traverses by boat or aircraft. Ratio colour composite images of Landsat TM bands and composite images of Landsat TM bands and scanned aerial photographs were used in traverse planning. The spectral information of Landsat TM bands 5, 4 and 3 enabled to distinguish vegetated terrain and outcrops with lichen cover from clean outcrop surfaces. Field stations were positioned with single GPS receivers operating in deep search (due to the forest canopy) and averaging modes. The accuracy of the positioning of field stations by single GPS was verified with topographic maps and aerial photographs and appeared to range from 50 to 100 meters.

All field data were transferred on a weekly basis from notebooks into lap-top computers into Fieldlog 3.4, a computer program designed for the entry, management and cartographic representation of geological field data (Brodaric and Fyon, 1989, see Chapter 4). Interpretation of 1:50 000 scale aerial photographs was conducted in preparation of each field day to outline structural features and lithological variations and outcrop density for traverse planning. A rock geochemical and petrophysical database comprising major and trace elements,

density and magnetic susceptibility measurements from 591 rock samples, collected during previous field surveys (Sprenke *et al.*, 1986; Goff *et al.*, 1986) was made available by the Alberta Geological Survey.

The recently published geological maps were compiled by combining the digitized hydrology and topography, the digitized geology of the previously published maps (Godfrey, 1986 and references therein) and new field observations. The map legend was adapted according to new insights obtained from the recently collected structural and lithological field data and the results of U-Pb zircon geochronology (McNicoll *et al.*, 1994; McDonough *et al.*, 1995).

3.5 Georeferencing procedures

An essential preparatory step in the digital integration of spatial data is the geometric correction and co-registration of all data types on a common cartographic projection. The cartographic base of the airborne geophysical survey (UTM, zone 12, NAD 1927) was used as cartographic base for geometric rectification of the Landsat TM and ERS-1 scenes. The Landsat TM scene was geometrically corrected by an image to map registration procedure. Thirty ground control points were used for the geometric rectification using an affine transformation function and bicubic resampling algorithm. The root mean square error (RMS) obtained from this fit was 1.5 pixels (45 meters). The ERS-1 scene was co-registered relatively to the rectified Landsat TM scene on 30-meter pixels by an affine transformation and bilinear resampling algorithm using 18 control points. The least squares fit of the affine transformation yielded a root mean square error of 2,5 pixels (75 meters). The total RMS error of the geometrically corrected ERS-image with reference to absolute coordinates was estimated by computing the quadratic sum of the two transformation which yields a total RMS of approximately 87 meters (3 pixels). The geometric correction of the ERS-1 scene was verified by overlaying the digitized hydrology on the rectified images. Because no digital elevation model was available no corrections were made for relief. The prevailing low relief with local differences in elevation of 50 meter or less and gentle slopes in the study area minimizes geometric distortions. The good overall agreement of the geometrically corrected ERS-1 scene with digitized hydrography and the relative low RMS error with respect to field station positioning, confirmed that the geometric correction by an affine transformation without topographic corrections was adequate.

The geographic positions of the field stations were either directly derived from single handheld GPS readings or digitized from stations transferred from aerial

photographs on National Topographic Survey (NTS) 1:25 000 maps sheets. Ground positions obtained by absolute positional accuracy of the single handheld GPS receiver operating in average mode appeared to fall within a radius of 4 mm from map-location of evident topographic features on the 1:25 000 NTS maps (100 meters). Estimates for the relative registration accuracy between pair-wise combinations of data are provided in Table 3.2. These are maximum estimates, computed by adding the positional accuracy estimates or root mean square errors of the geometric transformations. In particular, these estimates suggest that data combinations including ERS-1 and field data may be inadequately registered for detailed interpretation work, such as relating foliation strike-lines with individual lineaments. However, the maximum registration errors are within two cells of the lower spatial resolution used. These registration errors are considered to be low enough to compare regional structural trends reflected in image and field data.

The positional accuracy of the geophysical data listed in Table 3.2 refer to the registration of the flight line data by differential GPS positioning of the airborne geophysical survey. The spatially dependent errors of the interpolated geophysical measurements for each of these cells that unsystematically vary over the grid are not taken into account. Variations of the measured geophysical signals and quality of their measurements, quality of data specific reduction and correction procedures, leveling procedures and removal of spatial aliasing between flight lines and the algorithm employed to grid the data, all significantly influence the geometry of the interpolation results. Low radioelement concentrations related to gamma-ray response over large bodies of water showed good correspondence to digitized hydrography on the geometrically corrected Landsat TM image data.

Data set	Absolute accuracy	γ-ray	TM	ERS-1	Field data
Aeromagnetic	5 m	0	50 m	100 m	105 m
γ-Ray	5 m		50 m	100 m	105 m
TM	45 m			75 m	145 m
ERS-1	90 m				190 m
Field data	100 m				

Table 3.2 Estimated absolute and relative registration accuracy of the northeastern Alberta data set (in meters). A maximum estimate of the relative registration accuracy is computed by summation of the positional accuracy estimates of each data component. The relative registration errors with geophysical data refer to point-positioned flight line samples, ignoring the geometrical effects of gridding. The relative registration accuracy of the ERS-1 scene was estimated from the squared sum of the root mean square errors of the TM absolute and the relative image to image registration between the ERS-1 and TM scenes.

Overlays of the hydrography digitized from the topographic maps on the gamma-ray spectrometry grids showed that the unsystematic deviations due to gridding are generally small and within the 100 meter grid resolution of the airborne geophysical data.Tests for airborne geophysical surveys with 400 meter flight line spacing interpolated to 80 meter cell size have shown that grids are accurate to about 2-3 meters, equal to the 2-3 meters positional accuracy of the flight line samples (Denham, 1997).

All raster data were co-registered on 100 x 100 meter and 30 x 30 meter grid cells to provide registered data sets over almost the full spatial resolution range of the various data types. The geophysical grids were densified from 100 meter to 30-meter pixels with a bicubic spline algorithm. This two-step interpolation process was preferred over directly gridding the flight line data to 30 x 30 meter grids. This is because direct gridding flight line data to a resolution that approaches the along line sample interval may introduce artifacts and aliasing problems (Luyendyk, 1997).

3.6 Geological interpretation

In the forthcoming sections an integrated geological interpretation of the northeastern Alberta data set is presented. Although integrated interpretation is highly subjective and dependent on the skills and experience of the interpreter, such integrated interpretation strategies have appeared essential in assessing the complementary geological information that can be derived from multisource remotely sensed data (Nash *et al.*, 1996; Anderson and Nash, 1997). Irrespective of what physical measurements is imaged, qualitative image interpretation is generally subdivided in delineating domains or zones of homogeneous colour or grey tone or coherent texture and curvilinear and linear features (Drury, 1993). The outlined domains usually relate to lithological formations and assemblages. Alternatively they may correspond to subdivisions within map-defined units, overburden or units defined by alteration, strain or metamorphic processes. If the domains outlined by image interpretation correlate well with the units of geological maps, it is useful to label the domains accordingly. This facilitates comparison and highlights discrepancies between image interpreted units and published map compilations. It is important to note, however, that the geological map in the labeling of domains is not regarded as an indisputable source of ground truth. The domain is solely defined on the basis of its image characteristics and is only labeled according to a geological map unit when their outlines broadly correspond. The recognition of geological structures, including faults, shear zones,

folds, foliation and bedding trajectories is usually based on their linear high spatial frequency manifestation. Detailed interpretation of their image signature in terms of wavelength, curvature, periodicity, continuity and amplitude and comparing them to structures outlined by field mapping may allow assigning the linear features to one of the above mentioned categories. Usually, however, direct field verification is needed to unequivocally confirm their tectonic significance.

Lithological domains were outlined that were visually perceived to be homogeneous in colour, tone or texture. These domains were interpreted in the context of field observations including geophysical measurements conducted by previous workers (Sprenke *et al.*, 1986). In addition it was verified to what extent such domains correspond with litho-tectonic assemblages on the regional geological map (Figure 2.3). Table 3.3 provides the abbreviations that were used to label the outlined litho-tectonic domains. Domains that straddled the boundaries of map units were labeled combining the abbreviations of the individual units.

LITHO-TECTONIC ASSEMBLAGE	INTERPRETATION CODE
Western Slave Granite	WSG
Arch Lake Granite	ALG
Wylie Lake Granite	WLG
Collin Lake Granite	CLG
Andrew Lake Granodiorite	ANLG
Chipewyan Granite	CPG
Subsurface Intrusion	SI
Taltson basement complex	TBC
Metasedimentary rocks	MS
Dyke	D
Charles Lake Shear zone	CLSZ
PHANEROZOIC COVER	
Quaternary : glacial till and sand	QC
Paleozoic cover	PLC

Table 3.3 Interpretation codes used for labeling interpreted litho-tectonic domains with respect to the generalized geological map of the northeastern Alberta Shield after McDonough *et al.* (1995).

Such domains are of particular interest for follow-up studies, as they may highlight relative age relationships between intrusive and tectonic events or discrepancies between field and image inferred geological features.

The image fabric, defined here as an image texture in which linear and curvilinear image elements are repeatedly manifested, was outlined in the structural geologic interpretation of the study area. This term, in analogy to its geological connotation, is introduced here to distinguish it from the general term lineament, defined as any individual linear feature of probable geologic origin recognizable from remotely sensed images (Sabins, 1987). The straight isolated linear features that transect the image fabric represent lineaments that themselves are not the constituting elements of the regular arrangement of linear features that forms the image fabric. This distinction appeared useful in the interpretation of the study area. The spatial relationships between the image fabric and lineaments often implied that the last represent relatively young tectonic features with respect to the deformation events that gave rise to the structures reflected in the image fabric.

3.6.1 Interpretation of aeromagnetic data

The most recent interpretation of the magnetic field of northeastern Alberta was conducted by Sprenke *et al.* (1986) who interpreted hand-contoured maps from an aeromagnetic survey flown in 1958 (Geological Survey of Canada, 1963a to 1963d, 1964a to 1964v). Magnetic anomalies were in addition interpreted on the basis of laboratory measurements on the magnetic properties of rock samples (Watkins 1961; Watanabe, 1965; Sprenke, 1972; Sprenke, 1982). Measurements of the Koenigsberger ratio (Q) of the induced over the remanent magnetization of 23 core samples showed that its value was less then 0.2 for 74% of the rock samples. Two samples showed reversed magnetism and an amphibolite sample had high remanent magnetization with a Q ratio of 8.6 (Watkins, 1961).

Sprenke (1982) measured magnetic susceptibilities from 650 standard powder samples. The distributions of these magnetic susceptibility measurements over the major rock units are shown in SI units in Figure 3.1. The granite gneisses of the Taltson basement (unit 10) exhibit an extensive range of relatively high magnetic susceptibilities in comparison to most of the granitoid intrusions (units: 2, 3, 4, 5). Microscopic observations indicate that the magnetite content of granite gneiss and mylonite samples is highly correlated to their magnetic susceptibilities.

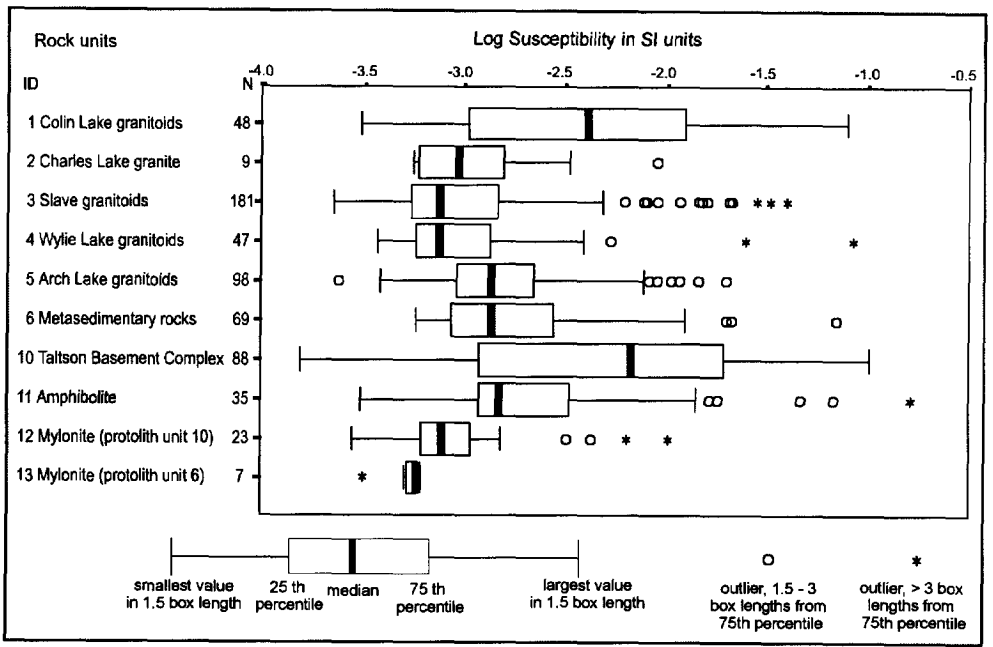

Figure 3.1 Box plots of magnetic susceptibility measurements of major rock units (data of the Alberta Geological Survey).

The low magnetic susceptibilities of the mylonites (units 12 and 13) in comparison to their parent materials (units 6 and 10) are explained by the extensive hematization of magnetite (Watanabe, 1965).

On the basis of the above laboratory observations and interpretations of the total magnetic field contour maps (Geological Survey of Canada, 1963a-1963e; 1964a-1964t) with respect to previously published geological maps (Godfrey; 1986), the main features of the magnetic field of northeastern Alberta were summarized as follows (Sprenke *et al.*, 1986):

1. The magnetic field of northeastern Alberta correlates well with bedrock features seen in outcrop and shows a predominant north to northeast trending fabric. This fabric is interpreted to reflect gneissic foliation and shear planes in fault zones.

2. Linear anomalies are related to regional metamorphism and local shear, whereas circular and curvilinear anomalies are indicative of primary magmatic

conditions in granitoid intrusions.

3. Paragneiss, mylonite and granitoids with low magnetite content are shown as magnetic lows whereas granite gneiss and magnetite rich granitoids correspond to magnetic highs.

4. The magnetic contour map shows a predominant north to northeast fabric that is interpreted to reflect a NW-SE directed stress field.

Although the extensive laboratory work on magnetic rock properties provided a sound basis for geological interpretation, contour maps are in general considered less suitable for regional geological interpretation. Image rendered magnetic data appeal better to the human eye and lend themselves for image enhancement techniques, such as relief shading to reinforce the illusion of three-dimensionality of the data (*e.g.* Reeves *et al.*, 1997). A detailed image interpretation that exploited these enhancement techniques was conducted. Geological domains and structures were outlined on magnetic background, relief and texture of anomaly patterns or on the shape and amplitude of individual anomalies and interpreted with respect to the generalized geological map (Figure 2.3) and field observations where possible.

Plate 3.2 shows a colour-shaded relief image of the total magnetic field. The magnetic anomalies were quantized by histogram equalization in 42 classes after removal of the international reference geomagnetic field (IRGF, datum 1990). The illumination used in the relief shading is directed from WNW (declination = 290°) with an inclination of 30° above the horizon. This illumination direction was considered optimal for enhancement of the northerly to northeasterly trending structural grain of the Taltson basement complex and the internal magnetic fabric within the pre- and synkinematic Taltson plutons.

The first vertical derivative image of the total magnetic field produced by frequency-domain filtering is shown in Figure 3.2. First vertical derivative images, represent the rate of change of the magnetic field with elevation and provide, as relief shading, enhancement of shallow source structural information but without the inherent directional bias of relief shaded representations. Because on vertical derivative magnetic data shallow magnetic sources are enhanced with respect to deeper sources, their image representations generally tend to show a more obvious relationship with geological structures encountered at the surface (Broome, 1990; Anderson and Nash, 1997).

Subsets of the vertical derivative magnetic data were integrated with structural field observations to interpret particular structural styles in more detail (Plates 3.1(B) and 3.1(C)), and for integration with the ERS-1 scene for the structural interpretation of Charles Lake Shear Zone (Plate 7.1).

The favourable geographic location and structural setting of the area facilitate the interpretation of the magnetic field of northeastern Alberta with respect to surface geology. The structures between the major lithological units in the northeastern Alberta Shield are predominantly sub-vertical and the magnetic inclination is 82°. The tectonic setting of the Taltson magmatic zone, as outlined in Chapter 2, constitutes the exhumed roots of a magmatic and mobile belt dominated by steep to sub-vertical structures predominantly extending at constant strike-angles over large distances. In this largely two-dimensional subvertical setting, the dominant susceptibility contrasts can be expected to be oriented sub-horizontally across the planar vertical boundaries of distinct rock masses. Considering that the effects of remanent magnetization, as justified by the low Q-ratio (Watkins, 1961) are relatively small, positive and negative magnetic anomalies tend to occur over rock masses with respectively high and low magnetic susceptibilities that are approximately symmetrical in shape (Colin Reeves, *pers. comm.*).

The symmetrical shapes of the anomalies of the fight line profiles shown in Plate 3.1(A) and their parallel trend to the NNE trending structural grain indicates that such a relationship is applicable to the high wave-number magnetic anomalies in the Taltson basement. Also the close correspondence between the boundaries of the magnetic units with the boundaries of the radioelement domains (compare Plates 3.2 and 3.3) and the boundaries of the lithological assemblages suggests that this generalization provides a useful guideline for interpretation.

The colour-shaded relief image in Plate 3.2 shows a pattern of linear and circular anomalies ranging in magnitude from below -577 nT to above 649 nT. The Archean to Paleoproterozoic Taltson basement is characterized by pronounced N to NNE trending linear and curvilinear magnetic anomalies (TBC1, 2, 3, 4 & 5 on Figure 3.3). The linear anomalies are locally transected by NW- trending lineaments. Field mapping has confirmed that these lineaments correspond to brittle fault zones, and belong to relatively young features of the deformation history (McDonough *et al.*, 1995). One of the two large enclaves of high-grade metasedimentary rocks in the southern TBC (Figure 2.3) is expressed on the magnetic image by a moderately positive broad linear anomaly, lacking internal magnetic relief (MS on Figure 3.3).

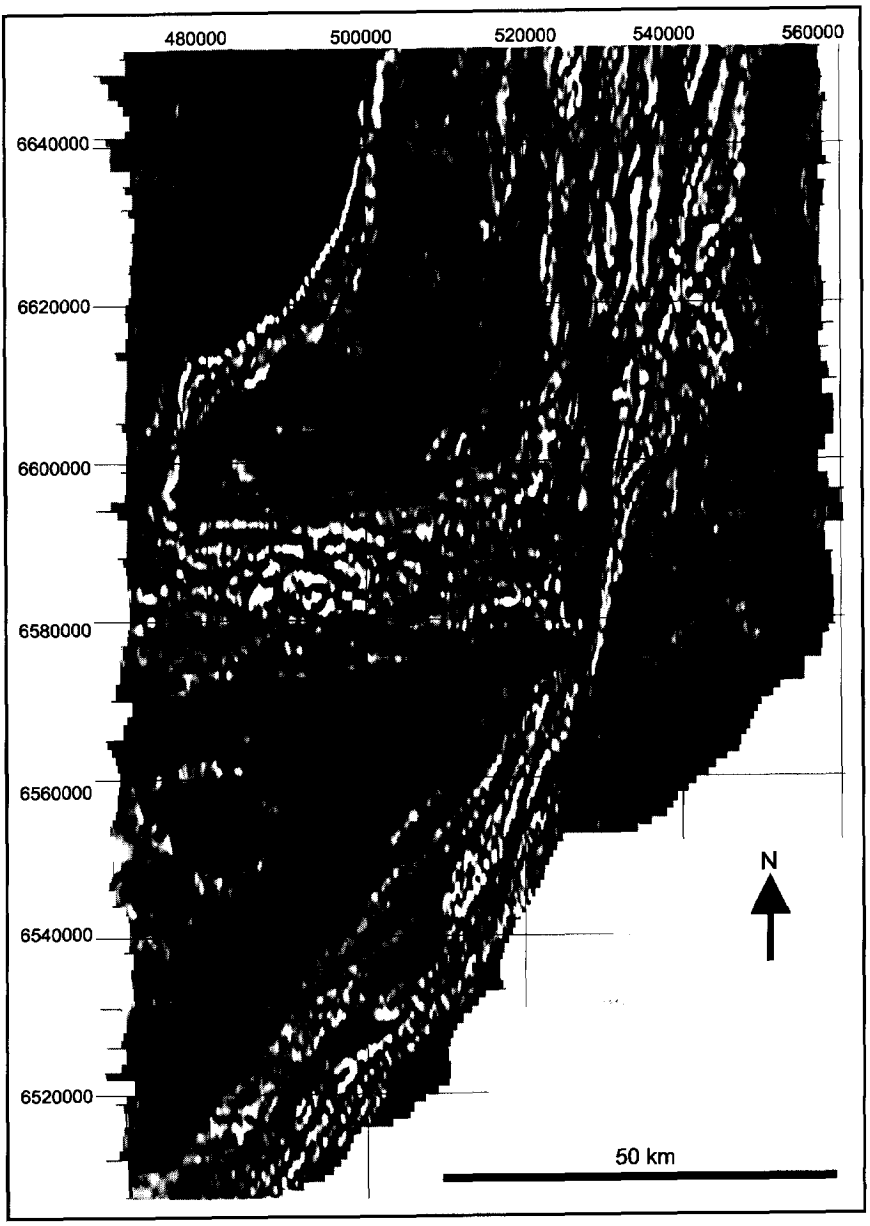

Figure 3.2 Grey-scale image of first vertical derivative magnetic data.

The other large enclave west of it is not clearly expressed on the image, possibly because its magnetic expression interferes with the pronounced low wave-number magnetic gradient between the Slave pluton and the Taltson basement.

The linear and curvilinear anomalies in the Taltson basement correlate well with structural measurements of gneissic and mylonitic foliations. The magnetic fabric has been interpreted to result from intense shear during various stages of the deformation history. The new-growth of magnetite in preferred orientation along the gneissic foliation has been interpreted to occur at granulite facies metamorphic conditions (Sprenke *et al.*, 1986). This interpretation is consistent with the widespread occurrence of lower granulite grade granoblastic and protomylonitic fabrics within the paragneisses of the TBC (Grover *et al.*, 1997, Chapter 2) that in thin section display evidence for metamorphic growth of magnetite. Synkinematic alteration of magnetite to hematite (Sprenke *et al.*, 1986) locally induced magnetic susceptibility contrasts at lower amphibolite- and greenschist-facies metamorphic conditions. These demagnetization and new growth of magnetic minerals may have enhanced the high wavenumber magnetic expression of the TBC (Sprenke *et al.*, 1986).

The regional fold pattern at St. Agnes lake outlined by field mapping (Chapter 2, Langenberg and Ramsden, 1984), broadly corresponds to curvilinear magnetic anomaly patterns. Plate 3.1(B) shows a colour-shaded relief representation of the first vertical derivative magnetic field of this area with an overlay of gneissic foliation trajectories and fold axes. Note that the trend lines of the curvilinear anomalies on Plate 3.1(B) broadly correspond to foliation trajectories of the F2 antiform at St. Agnes Lake. The structural style of this area deviates from the straight N to NE striking foliation trajectories in the TBC. The magnetic anomaly patterns east of the antiform, in combination with structural data suggest the presence of a refolded F1 synform. The exact nature of this fold interference pattern, however, can not be resolved on the basis of the data currently available. The structural mapping and synthesis would have clearly benefited from a higher resolution aeromagnetic survey with reduced flight line spacing in combination with detailed trend surface mapping campaign.

A linear magnetic low (CLSZ on Figure 3.3), about 50 kilometers in length, occurs at the western boundary of the TBC. This anomaly is partly underlain by mylonitized orthogneisses of the TBC and Charles Lake granite. The anomaly is continuous, despite the fact that it underlies ortho- and paragneiss of the TBC and Charles Lake granite protoliths, which as shown in Figure 3.1, have different magnetic susceptibility ranges outside the shear zone. On the basis of its correspondence with the mapped surface trace of the Charles Lake shear zone

(Figure 2.3) and the earlier mentioned evidence for hematization of magnetite in mylonite zones (Watanabe, 1965), the magnetic low must be genetically associated with deformation and/or fluidization processes in the shear zone. The magnetic low bifurcates towards the north into two anomalies with smaller amplitude that enclose a wedge shaped area with positive linear magnetic anomalies. This bifurcation has been confirmed by field mapping (McDonough, 1994(a), Figure 2.3) and is also evident on the ERS-1 scene (Plate 3.5).

The large granitoid plutons, such as the Western Slave-, Colin Lake-, Wylie Lake-, Andrew Lake plutons are associated with magnetic lows with low internal magnetic relief (WSG1, 2, WSG/ALG3, WLG/ CLG, ANLG 1 & 2, Figure 3.3). The magnetite bearing and weakly deformed Chipewyan granite and the circular anomalies between the Arch Lake and Slave pluton are expressed as magnetic highs (WSG/ALG 1,WSG 4, CPG 1, 2 & 3, Figure 3.3)).

The complex magnetic signature of the Arch Lake granite is an exception to the dominant subdued magnetic expression of the Taltson plutons. This plutonic suit displays a high internal magnetic relief with north and northeast trending linear anomalies and a variably low wave-number anomalies from -577 nT in the southwest (in ALG1, Figure 3.3) to 200 nT in the north (in ALG2, Figure 3.3). An explanation for the superposition of high wave-number signature on low wave-number magnetic signature is that it reflects the superposition of shear-induced magnetic susceptibility contrasts on a primary compositional variation of magnetite. This interpretation is strengthened by the broad correspondence to magnetic and thorium highs on the ternary radioelement map (see interpretation of the gamma-ray spectrometry data below and Plate 3.3) and the pre- to synkinematic interpretation of the Arch Lake granite (Chapter 2; McDonough *et al.*, 1995).

Several magnetic lineaments, trending in N, NW and NE directions, cut the Arch Lake pluton and the Slave pluton on the west and the TBC on the east and commonly correspond to linear magnetic lows (Figure 3.3). Many of these lineaments coincide with linear topographic depressions. No rock exposures occur in these topographic lows as they are underlying linear shaped lakes, bogs and swamps. The outcrops on their margins, however, often show evidence of chloritization, silicification, and cataclastic fabrics. These field observations suggest that these lineaments correspond to faults active at lower greenschist grade metamorphic conditions and below (Schetselaar and McDonough, 1996).

In general there is a good correspondence between the magnetic domains and litho-tectonic assemblages.

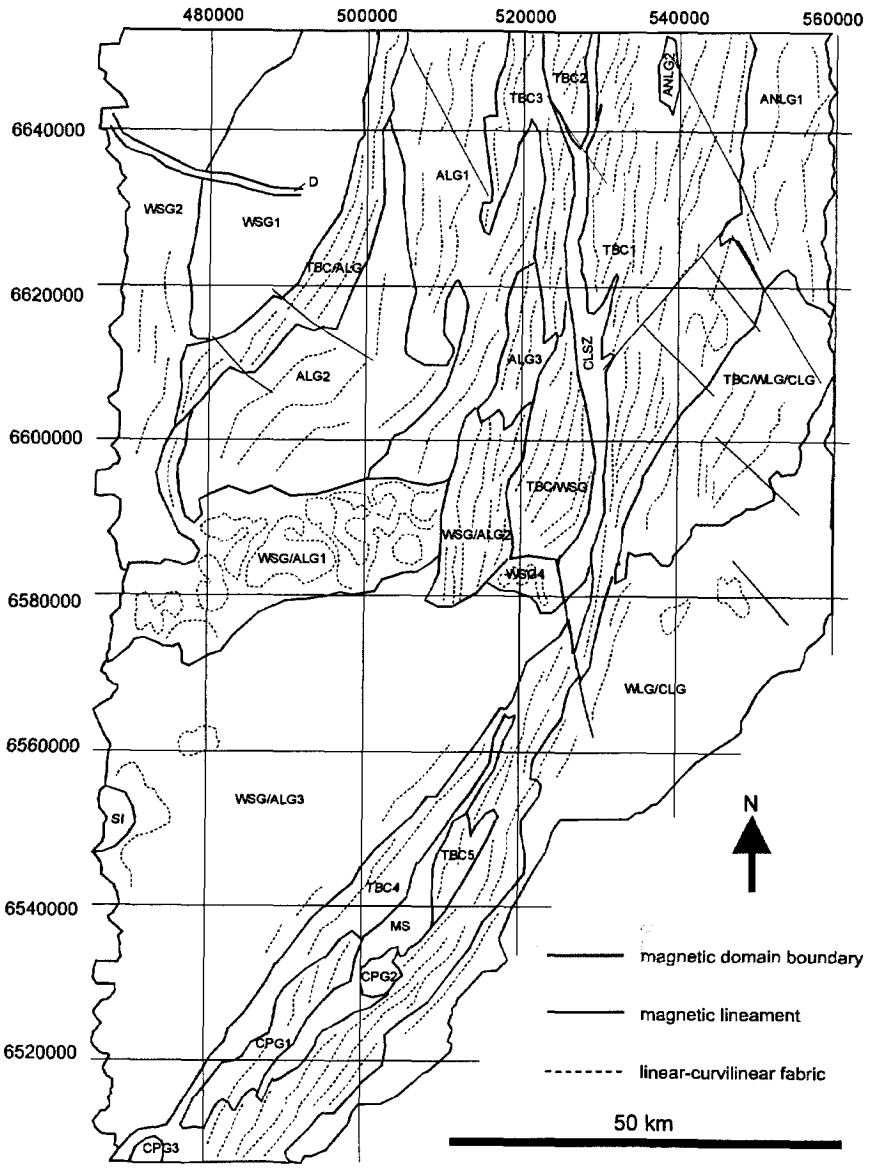

Figure 3.3 Interpretation of colour-relief shaded representation of total field magnetic data (IRGF subtracted) (Plate 3.2). The interpreted geological features are discussed in the text.

Nevertheless several magnetic anomalies on the colour-shaded image do not correspond to geological features on the published geological maps. Moreover magnetic domains occur, of which the outlines do not follow litho-tectonic domains. The following six discrepancies between the generalized geological map pattern and the relief shaded magnetic were identified:

1. The curvilinear anomalies corresponding to the LLSZ together with a weak curvilinear anomaly to the west encloses an elliptical mass of Slave granite (WSG1, Figure 3.3), which can be distinguished as a potassium rich phase on the ternary radio-element image map (Plate 3.3). This structure was interpreted on the bases of its elliptical internal foliation trajectories as a diapiric dome structure. (Tullip dome of Langenberg and Ramsden, 1984). The curvilinear trends of the magnetic anomalies are consistent with the geometry of this dome structure.

2. An isolated ESE trending linear anomaly traverses the Slave pluton (D on Figure 3.3) and is abruptly truncated by the LLSZ. This isolated positive linear anomaly is typical for the magnetic response of a dyke. This feature is not described in the geological literature of northeastern Alberta, possibly because it does not reach the surface. The dyke may correspond to the E-W trending sparrow dykes dated at 1.84 Ga. in the Northwest Territories (Bostock and Loveridge, 1988).

3. Circular and elliptical positive magnetic patterns with high internal relief that are undersampled by the one kilometer flight line spacing, occur at the east-west transition zone between the Arch Lake pluton and the Southern Slave pluton (WSG/ALG1, WSG4, Figure 3.3). The outlines of the elliptical magnetic anomaly patterns straddle the mapped boundaries between the Arch Lake and Slave plutons (Godfrey and Langenberg, 1986). On the basis of their contrasting circular and elliptical outline with respect to the linear anomaly patterns within the Arch Lake granitoids and subdued magnetic signature of the Slave granite this anomalies possible correspond to younger post-kinematic intrusions in the near subsurface. Another circular anomaly (BI, Figure 3.3.) occurs at the western limit of the surveyed area underneath Paleozoic cover. This anomaly has previously been interpreted on the basis of its strong positive magnetization as a basic intrusion (Sprenke *et al.*, 1986). The domain TBC/WSG (Figure 3.3) shows an arrangement of linear magnetic anomalies that is continuous over the mapped boundary between the Western

Slave granitoid and TBC on 1: 50 000 scale geological maps (McDonough *et al.*, 1995) and parallel to gneissic foliation trends. In the field Western Slave granite marginal to the TBC shows many xenoliths and mafic restite within the granite, forming a relic fabric of the TBC within the Slave pluton (Figure 2.4 (D)). East and north of the mapped contact are pervasively intruded by Slave granite like dikes co-planar to the gneissic foliation of the TBC. The linear fabric in this domain may therefore be interpreted as a relic or ghost fabric of TBC gneiss within the Western Slave granite. Alternatively the continuation of linear magnetic anomalies over the mapped Slave granite – TBC boundary, reflect deformation along the CLSZ postdating the emplacement of the Slave granite. Detailed mapping of the fabrics in the Slave granite in this area is required to corroborate one of these alternative interpretations.

4. The domain WSG/ALG2 (Figure 3.3), directly west of the TBC straddles the boundary between the Western Slave- and Arch Lake plutons and traverses two domains with curvilinear to circular magnetic highs (WS/AL-1 and WSG4, Figure 3.3). The strong linear magnetic fabric abruptly truncates the curvilinear fabric of the TBC/WSG domain. This domain coincides to N-striking complex of Slave granite interfingered with Arch Lake granite and TBC gneiss (Godfrey and Langenberg, 1987; lower right corner of Plate 6.1 (C)

5. The Arch-Lake- and Wylie Lake plutons exhibit an increase in magnetic relief towards the LLSZ and CLSZ (domains TBC/ALG and WLG/CLG). The margins of these plutons are involved in the CLSZ. Plate 3.1(C) shows a first vertical derivative image of the contact between the Wylie Lake granitoids and TBC with an overlay of mylonitic and gneissic foliations. The linear anomalies at the contact are parallel to the mylonitic foliation in the Wylie Lake granodiorite and locally transect the contact at high-angle remaining parallel to foliation in the TBC. This suggests that the Wylie Lake suit is prekinematic with respect to mylonitization of its margin, consistent with the maximum age of high-grade mylonitization inferred from the U-Pb zircon crystallization age of the Wylie Lake suit (McDonough *et al.*, 1995).

3.6.2 Interpretation of gamma-ray spectrometry data

A ternary radioelement map, produced from the gamma-ray spectrometry grids is shown in Plate 3.3. The airborne radioelement potassium (K), equivalent

thorium (eTh), and equivalent uranium (eU) grids were linearly stretched, using a two-sided cut-off percentage of 1%. This colour coding scheme is a standard representation scheme for displaying gamma-ray spectrometry data and justified by the fact that the noisiest eU channel is mapped on blue, to which, of the three primary colours, the human eye is the least sensitive (Milligan and Gunn, 1997).

The low gamma-ray responses over water were masked from the data by setting a threshold on the total exposure rate image to 3 μR/h. Comparing the masked areas in Plate 3.3 with the colour composite of Landsat TM3, TM4 and TM5 (Plate 3.4) shows that this threshold effectively masks the major lakes and swamps from the image. By removing the low count rates with high noise levels, the higher gamma-ray counts can be more effectively colour enhanced. An alternative image representation of the radioelement grids (not shown) is based on the relative abundance of K, eTh and eU that can be computed from sum-normalization:

$$K_n = \frac{K}{K + eTh + eU} \qquad [3.2]$$

$$eTh_n = \frac{eTh}{K + eTh + eU} \qquad [3.3]$$

$$eU_n = \frac{eU}{K + eTh + eU} \qquad [3.4]$$

This essentially converts the airborne K, eTh and eU concentrations in percentages of relative radioelement abundance. The computation of sum-normalized radioelement grids, like ratio's (Charbonneau *et al.*, 1997), is useful to reduce variations in gamma-ray response related to attenuation by soil moisture or vegetation cover. Provided that the sum-normalized channels are linearly stretched, the colours of a sum-normalized ternary radioelement map can be directly related to the ternary legend. For example if the dynamic ranges of K, eTh and eU is respectively [0 –3%], [0-30 ppm] and [0-5 ppm], then the following combinations of radioelement concentrations: [3,30,0], [2,20,0] and [1,10,0] will all be represented by maximally saturated yellow on the edge of the triangle, half-way between the K and eTh corners. In addition sum-normalization is useful to

combine the K, eTh and eU channels with other image data, such as the total exposure rate image, its relief shaded representation or Landsat TM data (see Chapter 5). A drawback of sum-normalization, however, is that the contribution to the total exposure rate from the radioactive decay series of K, Th and U is removed. For outlining anomalous concentrations in potassium, equivalent thorium or equivalent uranium, however, it is essential to combine the data with the total exposure rate, so that the contribution of the three radioelements to the total radioactivity is proportional to the intensity of the anomaly. On the other hand, the sum-normalization technique was considered useful to extend radioelement domains of which the continuation appeared to be obscured by attenuation effects. The Th-rich zone on Plate 3.3, for example, that corresponds to the domain ALG3 becomes darker along strike towards the north. This transition coincides with an increase in vegetation cover, as apparent on the colour composite of Landsat TM bands 5, 4 and 3 (Plate 3.4).

Comparing the ternary radioelement image map (Plate 3.3) with the generalized geological map shows that domains of contrasting hue correspond to the large plutonic suites. The Andrew Lake, Colin Lake (ANLG/CLG, Figure 3.4) and Wylie Lake (WLG, Figure 3.4) plutons show similar gamma-ray response consistent with their similar granodioritic composition and textural appearance in the field (Chapter 2, McNicoll *et al.*, 1994). Locally uranium levels reach 10 ppm (UA4, Figure 3.4). The Slave and Arch Lake granites are richer in potassium, reflecting their higher K-feldspar content. The Slave granites (WSG1/2 / 3/ 4 and 5 Figure 3.4) are relatively uranium-rich possibly suggesting that it is the most evolved of the two granitic suits. The Arch Lake pluton shows a complex zonation with a Th-rich, highly radioactive central zone (ALG1 and ALG4 on Figure 3.4) circumvented by a K-rich and Th-poor zone. (WSG/ALG/TBC/QC, Figure 3.4.). The southeastern margin of the Arch Lake pluton is also rich in Th with local U anomalies (ALG3, UA3, Figure 3.4).

At the northern boundary of the surveyed area an elongated U-high (UA1) straddles the margin of the Arch Lake granite, possible suggesting U enrichment of the TBC. Towards the south the thorium enriched central belt becomes discontinuous and Th-rich domains appear progressively offset towards the west (ALG4, Figure 3.4) consistent with the asymmetry in the curvature of the outer margin of the pluton.

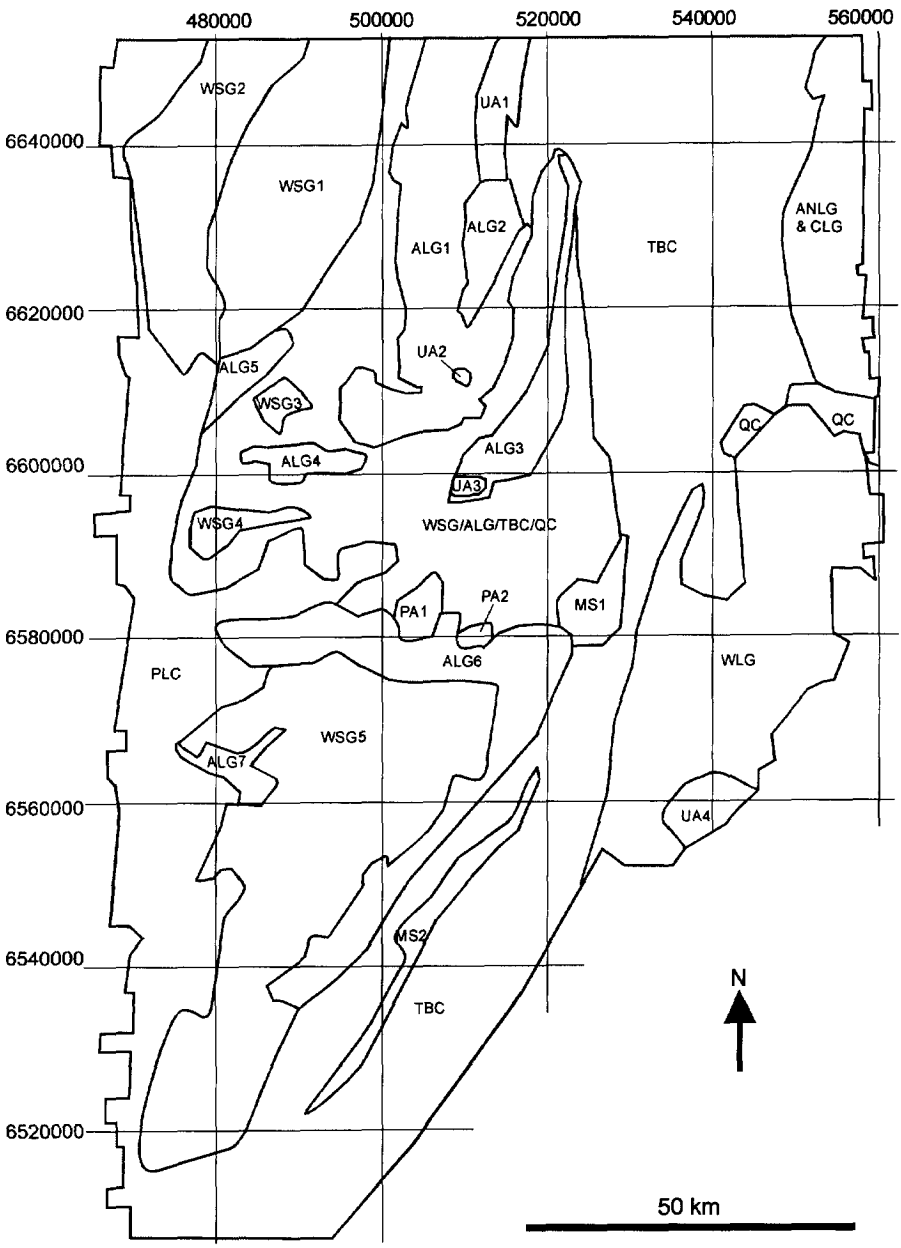

Figure 3.4 Interpretation of Ternary radioelement map (Plate 3.3). Interpreted features are discussed in the text.

Other thorium rich Arch Lake granite domains (ALG5, ALG6 and ALG7), Figure 3.4) are found within and at the margins of the Western Slave Granite pluton (WSG1 and WSG5, Figure 3.4). Further towards the south, it appears difficult to trace the boundary of the Arch Lake pluton with the Western Slave granite and the TBC.

The gamma-ray signatures of the low Th and high K zones and U and K-rich Slave granite interfere with potassium rich glacial sediments deposited in an east-west oriented elongated zone (Bednarski, 1997) between the 658000 and 660000 meter northing grid lines (WSG/ALG/TBC/QC on Figure 3.4).

Potassium anomalies (PA1 and PA2 Figure 3.4) do not correspond to any bedrock features on the regional and 1 : 50 000 scale geological maps and their origin is unknown. Their correspondence to areas of bedrock exposure (Plate 3.4) and the circular shape of anomaly PA1 (Figure 3.4) partly corresponding to one of the circular magnetic anomalies of domain WSG/ALG1, Figure 3.3) may suggest that this anomaly is the surface expression of a local intrusion in the subsurface.

3.6.3 Interpretation of Landsat TM data

A colour composite image of TM bands 5, 4 and 3, respectively assigned to the red, green and blue primaries of the display is shown in Plate 3.4. The colour composite image was created by a linear stretch using two-sided cut-off percentage of one percent. This band combination provide pseudo natural colours showing vegetation in green, water in dark blue and black and outcrops in pink.

In contrast to the good discrimination of lithological assemblages on gamma-ray responses, lithological domains could not be distinguished on the spectral response of the visible and infrared TM bands. The boundaries between some of the units can be recognized, however, on their structural expression.

Various enhancement procedures, such as computation of band ratios, saturation enhancement and vegetation masking techniques, did not provide any results useful for lithological discrimination. This lack of lithological information in the multispectral TM bands is mainly due to the dense vegetation cover including the lichen growth on outcrops. In addition, the granitoid and gneiss units have relative homogeneous bulk mineralogical composition with a general lack of diagnostic absorption features in the TM spectral band ranges. The vegetation cover is shown in various shades of green in which the light green yellow hues correspond to swamps and juvenile forest growth in forest burns, bright green to deciduous forest whereas the darker greens are associated with boreal forest with pre-dominance of pine species.

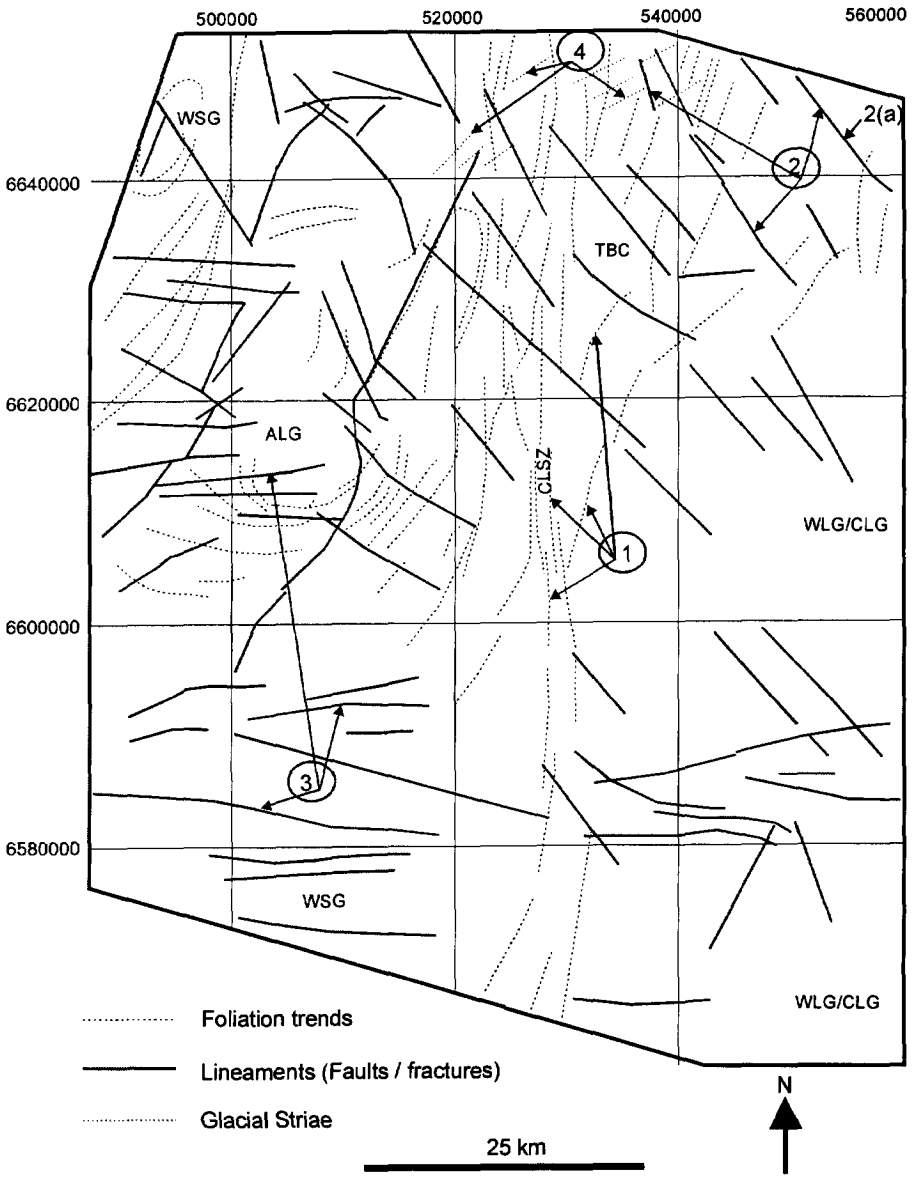

Figure 3.5 Interpretation of Landsat TM band 5 (Plate 3.4). Interpreted features are discussed in the text.

The pink and white hues on the colour composite are associated with clean outcrop surfaces of granitoids and gneisses. Such hues prevail in areas that where affected by forest fires. In these areas the outcrop surfaces are devoid of lichen cover, explaining their low response in TM4. This spectral information appeared useful during geological mapping for delineating areas with clean outcrop surfaces. Even the smaller patches of pink in the colour composite, appeared to be related to local forest burns.

Figure 3.5 shows a lineament interpretation of Plate 3.4. Despite dense vegetation cover, the topographic expression of structures can be recognized, although they are not as evidently expressed as on the SAR ERS-1 image (Plate 3.5). The N to NE-trending scarps (1, Figure 3.5), correspond to linear magnetic anomalies and the regional structural grain within the TBC. This relationship between topography and geological structure is especially clear within the shear zones. Many of the northwest trending lineaments (2, Figure 3.5) also correspond to magnetic lineaments. These lineaments belong to one of the most dominant fracture systems of the Canadian Shield along which the McKenzie Dyke Swarm was emplaced (Lowman, 1994). One of these lineaments (2a, Figure 3.5) has been interpreted as a sinistral brittle fault (McDonough, 1997) displacing the Bayonet Lake and Andrew Lake shear zones.

Another system of E-W trending lineaments, approximately parallel to the flight directions of the airborne geophysical survey and ERS-1 look direction, are best identified on the Landsat TM scene (3 in Figure 3.5). This system corresponds to E-trending brittle faults and joints (Godfrey and Langenberg, 1987). Curvilinear lineaments within the Arch Lake- and Western Slave plutons (WSG and ALG, Figure 3.5), as described in Chapter 2, are related to a weakly developed ductile fabric of quartz and biotite within the granite. This solid state foliation is sub-parallel to the elongated shape of the bedrock exposures within the pluton. The overall elliptical outline of the foliation that is also evident on air photographs and as discussed in Chapter 2, suggest a genetic relationship to the emplacement of the major granitoid plutons west of the TBC. ENE-SWS trending lineaments with relatively short lengths (4, Figure 3.5) correspond on aerial photographs to drumlins and to glacial striations that indicate the glacial transport direction (Bednarski, 1997).

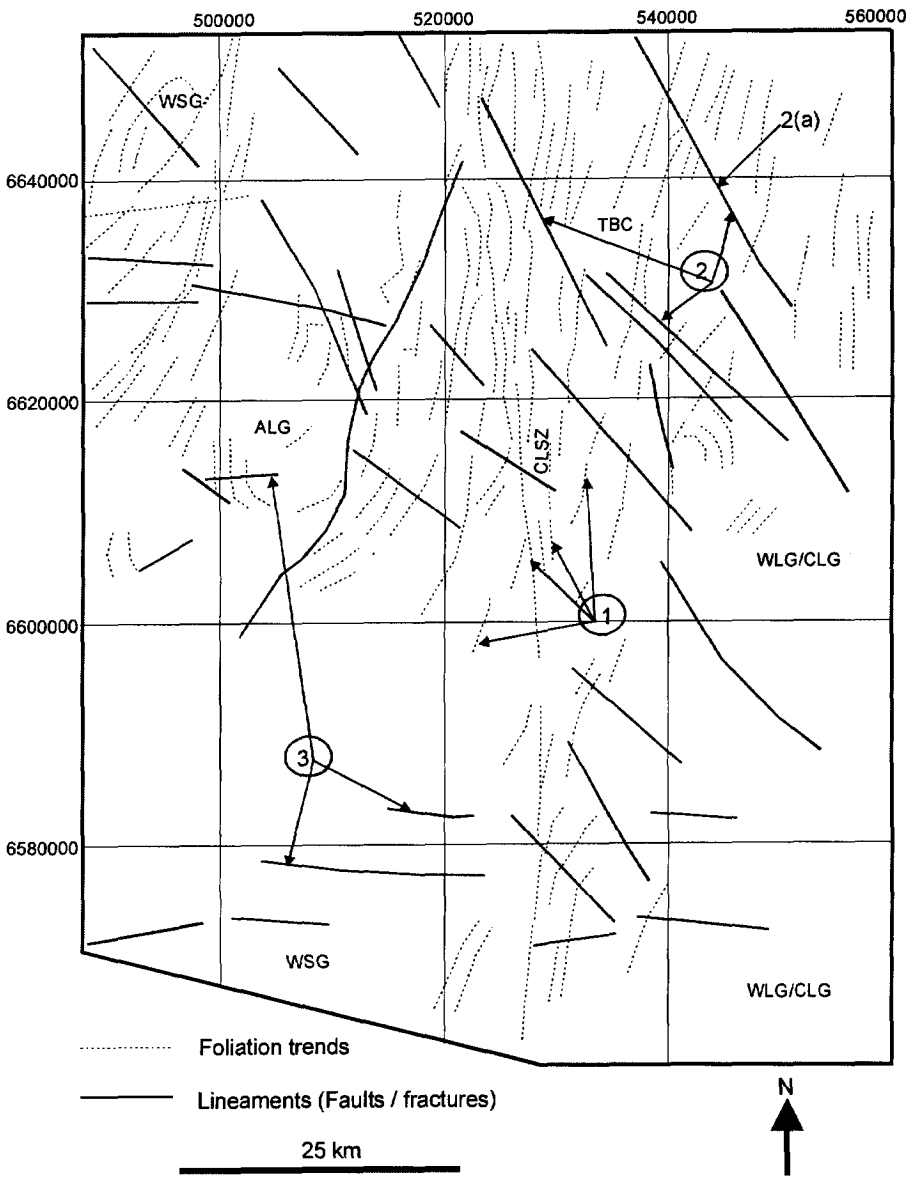

Figure 3.6 Interpretation of ERS-1 scene (Plate 3.5). Interpreted features are discussed in the text.

3.6.4 Interpretation of ERS-1 data

Images generated from synthetic aperture radar (SAR) systems like the European Radar Satellites have the unique capability to image structurally controlled topography (Blom, 1988).

The topographic relief of the Canadian Shield is particularly suited for the use of SAR images due to its prevailing subdued relief and differential erosion by the action of glaciers, etching out structure and lithology (Lowman, 1995). The structures in the study area are favourably oriented for the interpretation of the ERS-1 image (Plate 3.5), because the regional foliation and shear zones trend between northerly and northeasterly directions, approximately perpendicular to the radar energy incident from the east.

The structural interpretation of the ERS-1 image (Figure 3.6) shows the outlines of the major shear zones. The shear zones control topographic relief and are expressed in the terrain as linear topographic highs and lows. These elongated landforms are expressed as linear bright zones flanked by broader zones with darker image tone (1, Figure 3.6). Other linear scarps, correspond to basement-cover contacts between the para- and orthogneisses (2, Figure 3.6). Despite the strong azimuth bias of SAR imaging system, also some of the east trending lineaments are evident on the ERS-1 image (3, Figure 3.6). This may be explained by the radar-smooth water surfaces and bogs in fracture controlled drainage systems. Note that in general the Landsat TM and ERS-1 interpretations show a high degree of similarity, reinforcing the coherence in their structural interpretation. The TM scene shows less directional bias to the north trending structures in comparison to the ERS-1 scene. This explains why the EW trending linear structures and curvilinear patterns within the Slave- and Arch Lake plutons are more evident on the TM scene. The ERS-1 image, on the other hand, provides a more pronounced and detailed view of the N to NE trending foliation within the TBC. This evident image expression of ductile structure is exploited in Chapter 7, where the ERS-1 scene is analyzed in combination with vertical derivative magnetic data and field observations to geometrically characterize the CLSZ.

3.7 Integrated interpretation

The complementary information of the entire data set by analysis of the interrelationships between individual data components has not been exploited. This section briefly discusses interpretation strategies for the integrated appraisal

of multisource remotely sensed data sets. In addition, an attempt to such a combined litho-structural interpretation of the data set is presented.

A simple and practical method, analogous to overlaying transparencies on a light table, consists of overlaying the interpretations to identify matching boundaries that reinforce the interpretation or discrepancies that indicate contradicting interpretations. Conflicts in the interpretations need to be carefully re-analyzed in order to assess their geological significance. After consulting all the available information, including the available geological field knowledge, eventually preference is given to one of the interpretations or further analysis is conducted to resolve the conflict. This requires careful and highly subjective judgement that mainly relies on experience, skills and knowledge of the interpreter. An equally subjective but more interactive approach is to overlay the line interpretation of one data set on the image representation of a complementary data set, such that an interpretation of one data set can be tested and adapted with respect to another data set.

Nash *et al.* (1996), for example, applied overlay techniques for the geological mapping of the Proterozoic Halls Creek mobile belt in Australia. Interpretations of aerial photographs, multispectral satellite data, airborne magnetic and gamma-ray spectrometry data were digitized and co-registered on a common topographic base and were overlain on complementary raster images. The analysis resulted in the recognition of lithological units that were not previously recognized and the identification of mismatches between interpreted boundaries (Nash *et al.* 1996). These digital overlay techniques are obviously more versatile in terms of dynamic cartographic representation and updating functionality with respect to the traditional light table approach. They provide an easily implemented and practical method for comparative analysis of the multisource remote sensed images and its geological interpretation.

One of the major drawbacks of this "digital light table approach", however, is that it is a difficult and subjective task to give preference to one of the interpreted image types in the elimination of mismatches between interpreted boundaries. The image interpretation criteria and confidence in applying those criteria to infer lithological units and structures not only depend on the skills and judgement of the interpreter, but also how these vary, dependent on experience, from the image representation of one data sort to another. The level of confidence in the interpretation may even vary from place to place on a single image representation. This inherent ambiguity and bias in visual interpretation may discourage any integrated interpretation attempts, particularly for those inclined towards more elegant and robust numerical approaches.

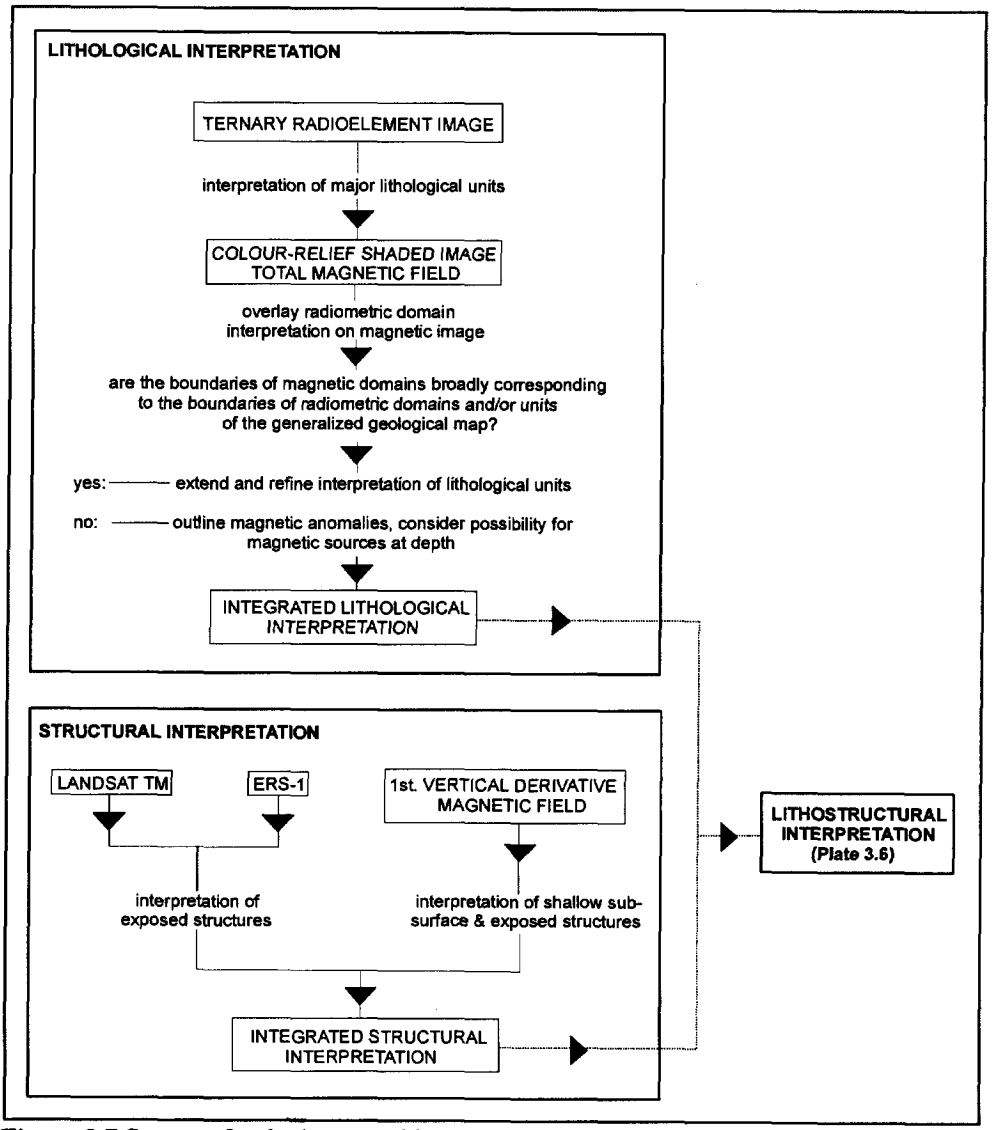

Figure 3.7 Strategy for the integrated interpretation of magnetic, gamma-ray spectrometry, Landsat TM and ERS-1 data shown in Plate 3.6.

The preceding sections indicate, however, that many of the geological features inferred from multisensor remotely sensed data sets are based on recognizing spatial interrelationships between image patterns within one or between multiple images. Such interrelationships may for example be related to intrusive, tectonic and sedimentary processes resulting in apparently truncated, intersected, transected and deflected image patterns. It is well known that these kind of contextual deductions require cognitive learning and hence are extremely difficult to replace by automated techniques. Quoting Drury (1993) on his discussion of automated and visual interpretation approaches: "fingerprints are not detected by computers, they are sought, found and photographed by detectives". Inversion techniques, on a physical bases, applicable to modeling multiple remotely sensed data sets, as far as the author is aware, have not yet been developed. Some work in this direction has been attempted in the joint-inversion of gravity and magnetic data appeared to be extremely difficult (Green and Craig, 1984). In general, inversion on the basis of discrete source geometry suffer from non-uniqueness and interference from adjacent sources (Reeves, 1998).

Statistical pattern recognition techniques applied in a spatial context, such as the image classification techniques presented in Chapter 8, offer the possibility to analyze multiple data types, but are focussed on extracting particular features, such as for example lithological units. Moreover because these multivariate techniques do not take the physics of the different methods into account, they require for each case sound geological and geophysical rationale in substantiating their applicability. In the context of geologically interpreting multivariate remotely sensed data sets, quantitative interpretation methods are considered useful, but their application is limited to corroborating particular aspects of such a synthesis.

The approach for conducting an integrated interpretation with emphasis on near surface and surface geological patterns is shown in Figure 3.7. The interpretation started with outlining lithological domains on the ternary colour composite image (see Figure 3.3), because this image was optimal in differentiating the major plutonic suites and the TBC. The magnetic data were used to extend and refine this interpretation, which not surprisingly appeared to be particularly useful in extending the outline in areas with glacial cover. The surface geological interpretation was further reinforced if such magnetic domains were also corresponding with the units of the generalized geological map. Magnetic domains that were not corresponding to mapped geological units within or outside radioelement domains were outlined with the connotation that they may originate from subsurface magnetic sources not exposed at the surface.

The structural interpretation was based on the image fabrics and lineaments of the magnetic, TM and ERS-1 data. Contrary to intersecting lithological units, lineament intersections do not necessarily indicate interpretation conflicts. Therefore all lineament patterns were represented. Coincidence between magnetic lineaments and lineaments in the satellite image data, reinforce the interpretation that they are the near- surface respectively surface manifestations of the same geological structure.

The combined interpretation, shown in Plate 3.6, permitted to better outline the southern Slave and Arch Lake plutons in comparison to the interpretations of the individual image data. Another asset of the integrated interpretation approach is that one can qualitatively assess the correspondence between image fabrics and lineament systems and their interrelationships. There is, for example, good correspondence between the linear and curvilinear image fabrics of the magnetic, ERS-1 and Landsat TM data.

3.8 Summary and conclusions

The northeastern Alberta data set appears to highlight a large number of geological features in the study area and the correspondence of their interpretation with the generalized geological map pattern suggests that the data set is useful to map regionally significant lithological assemblages and geological structures. The first vertical derivative of the magnetic field was computed with the aim to enhance shallow magnetic sources. This allowed reconciling structural field data with linear and curvilinear anomalies, which resulted in the identification of key areas for structural mapping and interpretation. The 1 km flight line spacing of the geophysical survey, however, is clearly not adequate to map the geological structure in detail (1:50 000 or more detailed mapping scales).

Several image patterns were identified that are in conflict with the generalized geological map providing follow-up targets for further enhancement and analysis. The following summarizes the image interpretations of the northeastern Alberta data set:

1. The gamma-ray spectrometry- and magnetic data proofed superior in delineating the major lithological units in the study area in comparison to the ERS-1 and Landsat TM scenes. The variations in relative concentrations of the Th, U and K radioelements reflect the differences and affinities between the major Taltson plutonic suites. The older Wylie Lake, Colin Lake and Andrew Lake suites in the east are uranium rich and have relatively low K and Th

content. The Arch-Lake and Slave suites have higher levels of potassium rich. Locally within the central and marginal portions of the Arch Lake suit high Th levels (40 ppm) occur. Internal lithological variations within the TBC are not evident on the ternary colour composite. Discrimination of lithological units from the multi-spectral signatures has a very low potential due to vegetation cover, lichen growth on outcrops and the similar bulk mineralogies of the granitoid and gneissic units in the study area. The magnetic data allows differentiating the TBC from the Taltson plutons due to its pronounced magnetic relief.

2. The internal fabric of the Taltson basement complex (TBC), which consists of gneissic banding and mylonitic foliation in shear zones, is evident on Landsat TM data and particularly on ERS-1 data because their signatures are sensitive to structurally controlled topography. These linear topographic features coincide in orientation with the internal magnetic fabric of the TBC consisting of linear positive and negative magnetic anomalies. Considering the steeply dipping geological structures and the subvertical magnetic inclination, it suggests that the high wave-number spectrum of the magnetic data can be used in conjunction with remotely sensed- and field data obtained for structural interpretation. The integration of magnetic data with ERS-1 data with its superior perception of geological structure is therefore considered as the ideal data combination to study the internal structure of the TBC. The potential of integrated mapping of structure is considered particularly interesting with respect to interpreting foliation patterns associated with the geometric and kinematic characterization of Charles Lake shear zones and its associated splays, which is the subject of Chapter 7.

3. The Arch Lake pluton shows a complex zonation pattern in which a thorium rich central zone is circumvented by a thorium low. The margin of the pluton is again thorium rich with local uranium anomalies. The magnetic expression of the Arch Lake pluton is complex, because the pluton is deformed to a variable degree resulting in a high magnetic relief superposed on a low-wavenumber anomaly pattern comprising a central magnetic high and marginal magnetic lows. The zonation, as commonly inferred from gamma-ray spectrometry data, may reflect a magmatic differentiation within the Arch Lake suit. The thorium rich center seems to be offset to the south along SE-NW to E-W trending shears. Both the zonation and the offsets are subject of a focussed data integration study presented in Chapter 6.

4. The Arch Lake and Wylie Lake plutons show an increase in magnetic relief towards their margins that are involved in respectively the LLSZ and CLSZ. Based on field observations this increase in magnetic relief is interpreted to reflect an increase in the intensity of mylonitization with extensive redistribution of magnetic minerals along the foliation planes. This interpretation is consistent with the pre-to possibly synkinematic emplacement of the intrusions with respect to high grade shear zone deformation, as inferred on the bases of U-Pb zircon geochronology (McDonough *et al.*, 1995, Chapter 2).

5. The interpretation of the magnetic anomaly patterns provided indications for intrusive features that have not been recognized in field mapping. Circular and elliptical positive magnetic patterns with high internal relief occur at the boundary between the Arch Lake and the Southern Slave plutons. The patterns partly correspond with a separate phase of the Arch Lake suit, known as the La Butte granodiorite (Godfrey and Langenberg, 1986). The circular and elliptical anomaly patterns extend further east and west then the surface mapping of the La Butte phase and other circular anomalies further south extend below Paleozoic cover, possibly suggesting a distinct intrusive phase in the subsurface. A linear magnetic anomaly that transects the northern Slave pluton in an east-west orientation is interpreted as a dyke. This dyke corresponds on the surface to lineaments recognized in the Landsat TM image.

6. Two systems of northwest and northeast trending lineaments are evident on the magnetic, ERS-1 and Landsat TM data layers. These systems transect the internal fabric of the TBC, and offset lithological boundaries, which suggests that they formed relatively late in the deformation history. Another set, best seen on the TM data trends east and is particularly developed between the southern Slave and Arch Lake plutons. The kinematic significance of this lineament system remains to be field verified. The observation that this system transects all other systems, without apparent displacements suggests that these structures are related to one of the youngest events and may predominantly reflect mega-joints. Curvilinear elliptical lineament patterns in the ERS-1 and Landsat TM data are also shown on aerial photographs. These curvilinear patterns are broadly concordant to the margins of the Arch Lake and Slave plutonic suites and internal zonation within the Arch Lake granite.

PART II METHODOLOGICAL ASPECTS

4

DIGITAL FIELD DATA HANDLING: CARTOGRAPHIC ASPECTS AND APPLICATIONS*

ABSTRACT

The systematic digital management of geological field observations provides new perspectives for geological cartography and the interpretation of remotely sensed data. Digital field data handling techniques at some geological surveys has facilitated the efficient and seamless compilation, revision and publication of geological maps and the digital distribution of geoscience data sets. In addition, digital field database management has expanded the potential to represent site-specific geological information and incorporate this in the analyses of remotely sensed data. This chapter reviews the methodological aspects, discusses the implications for field mapping procedures and presents some of the less established but promising roles of field database management. Four application domains are discussed that have been implemented in this thesis. They include: (1) the automated representation of field observations in cartographic themes, (2) the use of field data to support image interpretation of remotely sensed data, (3) the automated projection of structural data for the compilation of cross-sections, (4) the compilation of map and profile representations of magnetic inversion models and structural data to aid the interpretation of aeromagnetic data. The methods enable geologists to incorporate on demand field-attributes in GIS analysis and potentially leads to new mapping and interpretation styles.

---

* Parts of this chapter are based on the papers:

Schetselaar, E.M., 1995, Computerized field data capture for geological data integration. Joint European Conference and Exhibition on Geographical Information Systems, The Hague, pp. 436-441.

Schetselaar, E.M., 1995, Computerized field data capture and GIS analysis for the generation of cross-sections in 3-D perspective views. Computer and Geosciences, v. 21, n. 5, pp. 687-701.

4.1 Introduction

In the last decade geological surveys have recognized the need to digitally encode primary field observations (Norwegian Geological Survey, 1992; Broome *et al.*, 1993; Ryburn and Blewett, 1993; Brodaric, 1996). This was because the computerized capture and management of field data appeared to yield large efficiency gains in cartographic production lines and geoscience data distribution. At the Geological Survey of Canada, for example, pioneer studies by small working groups indicated a number of advantages in applying these digital mapping methods, as it facilitated: (1) the compilation of field maps on a variety of geological themes, (2) the efficient generation, seamless compilation and maintenance of final cartographic products, (3) the systematic transfer of geological field observations to centrally managed geoscience databases and (4) distribution and publication of integrated geoscience data sets (Broome, 1997). In particular the last two uses have gained in importance as the management and analysis of geoscience data and the production of geological maps in cooperate mapping projects rely increasingly on exclusively digital procedures.

In addition to these efficiency gains, the digital management of field data, opened the possibility to incorporate geological field data in spatial analysis in a GIS environment. By defining spatial or non-spatial database searches, the user can interact with any field-collected geological attribute. Hence, the earth scientist is in a position to integrate the local most "factual" "least interpretative" observations with other spatial data sets. This may lead to integration strategies where the functionality of modern GIS is exploited to integrate authentic field observations in image enhancement, feature extraction and modeling (Schetselaar, 1995).

The evolution of second generation GIS software in the early nineties provided hybrid systems, supporting both vector and raster data structures that combine spatial analysis functions with image processing and cartographic capabilities (Batty, 1999). This extended functionality enabled geologists to display enhanced remotely sensed data or other image data on the background, while interactively overlaying and editing geologic map compilations. Another relevant development of GIS in the nineties has been the introduction of dynamically linked views, which enabled the user to view geological map objects in geographic space with their attributes simultaneously (Bonham-Carter, 1994).

The incorporation of primary field data in the integration and analysis of spatial data can be considered a substantial improvement in comparison to data integration studies where fully compiled geological maps have been employed.

This is because geological maps are generally less suitable for the integration tasks, because they are highly abstracted, generalized and subjectively compiled representations of reality. The lithological units of a compiled map, for example, are based on subjective decision criteria arbitrarily or purposefully aggregating lithological composition, stratigraphy with other field characteristics.

Contrary to conventional data archiving approaches digital field database management allows encoding primary geological field observations in numeric, text or descriptive form together with their map coordinates. Instead of representing only a few of the geological attributes on a map, all the data pertinent to a specific application can be selectively retrieved from the underlying database and compiled for map representation. Digital field database management has therefore not only revolutionized the efficiency of cartographic production, but also has expanded the potential for dynamic cartographic representation of site-specific geological knowledge and integrate this in the analysis of remotely sensed data. These capabilities provide field-based earth scientists with effective means to access all the available geological attributes that are considered relevant in supporting an interpretation or analytical task on demand in a GIS environment. This chapter explores the application domain of field data capture methodologies with respect to cartographic representation and spatial data integration that are relevant for the integrated analyses presented in this thesis. After a review of the organizational aspects of digital field data capture techniques in relation to geological mapping procedures, application examples are presented that exploit digital field database management for cartographic representation and the interpretation of remotely sensed data.

4.2 Geological mapping and field data capture methodology

Geological field mapping commonly proceeds along traverses that are usually oriented perpendicular to the strike of the prevailing geologic structures. Depending on the amount of bedrock exposure, mapping objectives and mapping scale, field observations are made at point localities positioned at more or less closely spaced regular intervals. The observations made at or in the immediate vicinity of a field station is identified by a code and plotted on a mapping base, such as a topographic map sheet or aerial photograph. Accurate ground positioning is of prime importance in field mapping, and is either based on relative or absolute positioning methods. Field station locations can be identified with respect to topographic features recognized in the surrounding landscape and plotted on the map base or by resection of three distant topographic features rayed in with a

compass. Absolute ground positioning by hand-held ground positioning systems (GPS) has increased in popularity. The planimetric accuracy ranges from about ten to a few hundreds of meters, and depends on whether one or two GPS receivers are used in differential mode. In addition to positioning field stations by GPS, the above mentioned conventional positioning methods should be applied. This is useful to improve on the accuracy of single hand-held GPS or evaluate the performance or identify possible sources of systematic errors of GPS.

Once the field station has been positioned and labeled, a multitude of outcrop observations can be attributed to it, including lithological descriptions, mineralogy, descriptions of texture and structure, structural orientation data, metamorphic mineral assemblages, mineralizations, motivation to collect samples etc. Transitions or sharp contacts may be visible in or between nearby outcrops, that may represent stratigraphic, tectonic or intrusive boundaries between lithological units, metamorphic isograds or transitions in the style and intensity of deformation. Because not all the geological features are visible in the outcrops at or in the near vicinity of the station, not all the different types of observations are recorded at each field station. Several types of observations, such as lithological descriptions that can not be plotted on the base map are written down in a notebook. Representative lithological and structural data should be plotted during progressing field mapping to maintain awareness of the overall geological pattern being assembled. Such working drafts are of fundamental importance to guide progressing mapping activity towards solving geological problems. This is crucial, for example, in classical field exercise areas where local determination of the asymmetry of folds or vergence-relationship between sedimentary bedding and axial planar cleavage provide the only clues to identify the hinge zones of macroscopic folds.

Additional observations that may be important to describe local aspects of the geology or further subdivide units, but for which the base map does not provide enough space, should also be recorded and sampled. A number of aspects on the nature of geological field mapping procedures can be distilled from the above summary that have direct implications for the way in which geological field data can be optimally encoded in digital format:

1. Geological field observations are inherently multiple-scale dependent and hierarchically related.

2. Not all the geological attributes of interest are observed at each field station.

3. Not all of the recorded geological observations, such as lithological descriptions are suitable for map representation.

4. Multiple observations of the same type, such as several attitudes of bedding in a fold, are linked to a single field station in the immediate neighbourhood of the observations.

Considering these four characteristics, a system that operates in a relational database environment appears to be the most appropriate (Brodaric, 1997). In this structure, the different themes, such as lithology, structure, geochemistry, are stored in separate tables linked to each other by a field common to all tables. Because of the explicit one-to-many relationships between each field station and the associated thematic attributes, the field station identification is the most appropriate database field to establish these links. Unlike spreadsheets, this data structure avoids redundancy in data entry and storage and supports complex querying mechanisms (Brodaric, 1997). Another important requirement of digital field mapping systems is that it should provide a dynamically linked interface between tabular and cartographic space to support interactive data entry, spatial querying, map edition and automated cartographic compilation. This last function is schematically illustrated in Figure 4.1. Relational database links between the map coordinates and structural measurements by the common station field and between the symbol field to the strike and dip fields makes it possible to selectively plot bedding and foliation data on a base map.

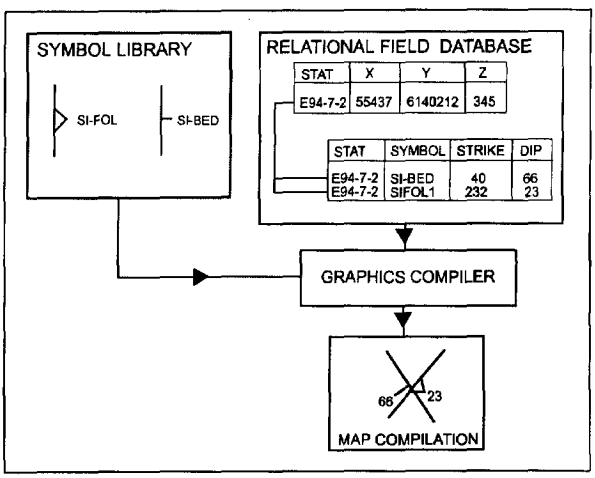

Figure 4.1 Automated map compilation of structural data from a relational field database. The database field STAT links the STRIKE, DIP and SYMBOL fields to the station field (E94-7-2) and map coordinates (X,Y). The SYMBOL field is linked to a symbol library representing structural elements. The STRIKE field defines the rotation of the symbol and the DIP field is plotted at the origin of the symbol.

Several geological surveys have developed tools dedicated to geological field data acquisition, data visualization and/or cartographic compilation (Brodaric and Fyon, 1989; Brodaric, 1997; Geological Survey of Norway, 1992; Ryburn and Blewett, 1993 among others). Although the niche of applying such tools is increasing narrowed by the expansion of the functionality of GIS tools, their user-interface is based on the organization of geological data collection and mapping. The advantage of these specific geological systems is that it insulates users from the complexities of data base design and facilitates the usage of consistent terminology (Brodaric, 1997).

A major limitation of using GIS as a field mapping system is that the primitives of the vector data structure (vertices, segments and polygons or cells) are inherently fixed to absolute map coordinates.

This inhibits, the flexibility required for field map compilation, where one wants to freely move and edit entities in 2-D map or 3-D space. In contrast, the functionality provided by computer aided design (CAD) systems, provide all the functionality needed for editing the position, scale and orientation of map entities. CAD and GIS functionality software developments are now rapidly converging and several desktop GIS's, have evolved sufficiently to perform much of these operations. The more open architecture of these systems, however, can be unpractical for those unfamiliar with GIS operations.

4.3 Implications of digital field data capture on field mapping routine

The implementation of the digital capture of field data does not necessarily result in field mapping routines that differ from conventional mapping procedures. Nevertheless, the flexibility and versatility in database design and the expanded functionality of cartographic representation tools may stimulate geologists to encode a greater proportion of their observations in a more systematic and quantitative manner (see for example sub-section 4.6.1).

Whether field observations are digitally encoded in the field, at base camp or in the office is largely dependent on the mapping objectives, skills of the mapping personal, available hardware and purpose of the mapping project. Pen-based palmtop computers connected to GPS receivers have been recently introduced in field mapping projects (Boyan Brodaric, pers. comm.). Simple pop-up menus provide checklists on the outcrop for data entry of descriptions and digital sketches providing a full substitute of the pencil and field notebook. The intellectual challenge of geological mapping, however, is obviously a world more then marking off checklists at each outcrop. Many field geologists are concerned

that an exaggerated push of this technology may impede on the creative and interpretative aspects of geological mapping (various pers. comms.). An important limitation, for example, is that the display capabilities of the currently available hand-held devices are not adequate to replace instant drafting of symbols and line work on hardcopy base maps. Such drafting routines, however, are extremely important to directly convey the interrelationships between the observations (e.g. Ramsay and Huber, 1987, Appendix F therein). The data collection of a mapping geologist proceeds along a mutable course on the bases of his or her 3-dimensional mental picture of the geological structure. The observations from the outcrops thus far visited are positioned and integrated in this picture to continuously update this preliminary model. One of the objectives of this mental exercise is to predict the locations that are most likely going to reveal interrelationships on which to build the geological understanding of the study area. This emphasizes the need for instantly drafting field observations on a mapping base. Full digital field mapping procedures seems attractive for those prepared to venture from the traditional interpretative drafting aspects of mapping. The display capabilities of the currently available hand-held devices, however, do not offer sufficient quality and durability to replace the hardcopy base maps.

4.4 A review of some field data management and mapping systems

This section reviews the functionality of some field mapping systems that have been developed by geological surveys. This review is not intended to give a complete system overview, but shows the typical range of capabilities of field data management systems that have been developed in the last decade. All of the described tools provide a framework for the entry and data base management of primary field observations. Some of them provide export to GIS or CAD systems for cartographic representation and spatial searches. The section includes a description of FIELDLOG. This system initially developed at the Ontario Geological Survey (Brodaric and Fyon, 1989) has been used for the digital management of geological field data in this thesis.

The Norwegian Geological Survey developed in the early nineties a field data entry tool GBAS based on dBASE^{TM} IV (NGU, 1992). This system provides a menu-driven user-interface designed for the entry of geological field data, in which pre-defined data base fields are used for storing: field station code and location, project data, lithological descriptions and structural orientation data. GBAS does not provide cartographic compilation capabilities and needs to be linked to a GIS using conventional data export and import capabilities.

REGMAP, developed at the Queensland department of mines, Australia (Lang *et al.*, 1990), provides a pre-defined data entry sheet on paper or notebook computer. The data entry sheet uses fixed fields for site description, lithology and structure and flexible data entry for any additional information recorded by the geologist. The entered data can be transferred to CAD systems for representation on maps and diagrams.

The Field data Management System (FMS v.2.1) is used by the New Jersey Geological Survey for managing structural geologic data (Pristas and Herman, 1997). The structural data are organized into ASCII files, through keyboard entry. Structural data can be sorted on location, stratigraphic unit and structural variables and can be plotted on map and profile views. FMS provides tools for automatically plotting structural data as symbols on maps or allows generating GIS themes in Arc/Info™.

The public domain software FIELDLOG, developed at the Geological Survey of Canada has been used (Brodaric and Fyon, 1989; Brodaric 1997; Brodaric and Harrap, 1999) for managing the field observations collected in the study area in northeastern Alberta.

The philosophy behind FIELDLOG is that it gives geologists full flexibility in database design, yet protects the users from its complexities. This is achieved by an underlying data model that abstracts geological mapping procedures (Brodaric, 1997). Instead of using standardized checklists for data entry, FIELDLOG (version 3.0) uses editable profiles from geological dictionaries. This allows for flexible mapping and project adaptable data entry, while sustaining the integrity of the used terminology (Brodaric, 1997). Dictionaries contain a catalogue of standardized terms or accepted abbreviations for lithological descriptions, mineralogy structure etc. FIELDLOG makes extensive use of profiles for data attribution and query functionality. A profile is a hierarchically arranged list of geological terms from the dictionary relevant for a specific mapping project. The use of profiles and dictionaries is intended to provide standardized terminology on the level of a mapping project while maintaining semantic consistency. For example an organization that maps in sedimentary and metamorphic terrain would define a dictionary of lithological descriptions containing terms for both sedimentary and metamorphic rock types: *shale, limestone, gneiss, schist.* The associated profile of the mapping project in metamorphic terrain would then only contain the terms: *gneiss* and *schist.*

The hierarchical arrangement of terms enhances the query capabilities, because each term encompasses a set of geologically relevant sub-terms. This avoids having to perform numerous specific queries to retrieve information, and instead

facilitates extraction of information based on its meaning. For example all planar structural observations could be retrieved at once, instead of having to retrieve separately each instance of a foliation, a bedding and an unconformity surface orientation.

The profiles can be interactively adapted to the needs of a specific mapping project and are therefore more flexible in comparison to the pre-defined data entry systems used in the Regmap and GBAS tools. FIELDLOG runs under AutoCAD^{TM} to support cartographic compilation, editing, drafting and representation. In addition, FIELDLOG supports cartographic map projections and geographic and metric coordinate systems to overcome the limitation of the linear surface representations of CAD systems. The forthcoming section describes the FIELDLOG data structure that was used for geological mapping and integrated analyses of field and remotely sensed data in this thesis.

4.5 Database structure for geological mapping of the Alberta Shield

The database structure and associated profiles designed for geological mapping in the Alberta Shield is shown in Figure 4.2. The database field *Number* is the general field station identifier and links the *outcrop* table containing fields for the station identification of the author, lithological descriptions, map coordinates, aerial photograph number, etc. with the *structure*, *photo* and *sample* tables. Profiles are attached to the *map unit*, *lithology*, *minerals*, *structure*, *sense* and *fabric* fields. The *struc*, *sense* and *fabric* profiles for the description and orientation of structural elements, shear sense indicators and fabric relationships respectively are in turn linked to symbol libraries, shown in respectively Figures 4.3(a), 4.4(b) and 4.5(a). These libraries contain the standard symbols of the Geological Survey of Canada and symbol libraries designed by the author for the cartographic representation of specific themes.

Each of the symbol fields can be linked with numeric fields, such as strike and dip to respectively rotate symbols in their proper orientation and to annotate the symbols with their associated dip readings. The table *sample* contains the fields to specify the rock samples taken for thin section analysis, lithogeochemistry and magnetic susceptibility measurements. The table *photo* specifies the film and frame number and descriptions of field photographs.

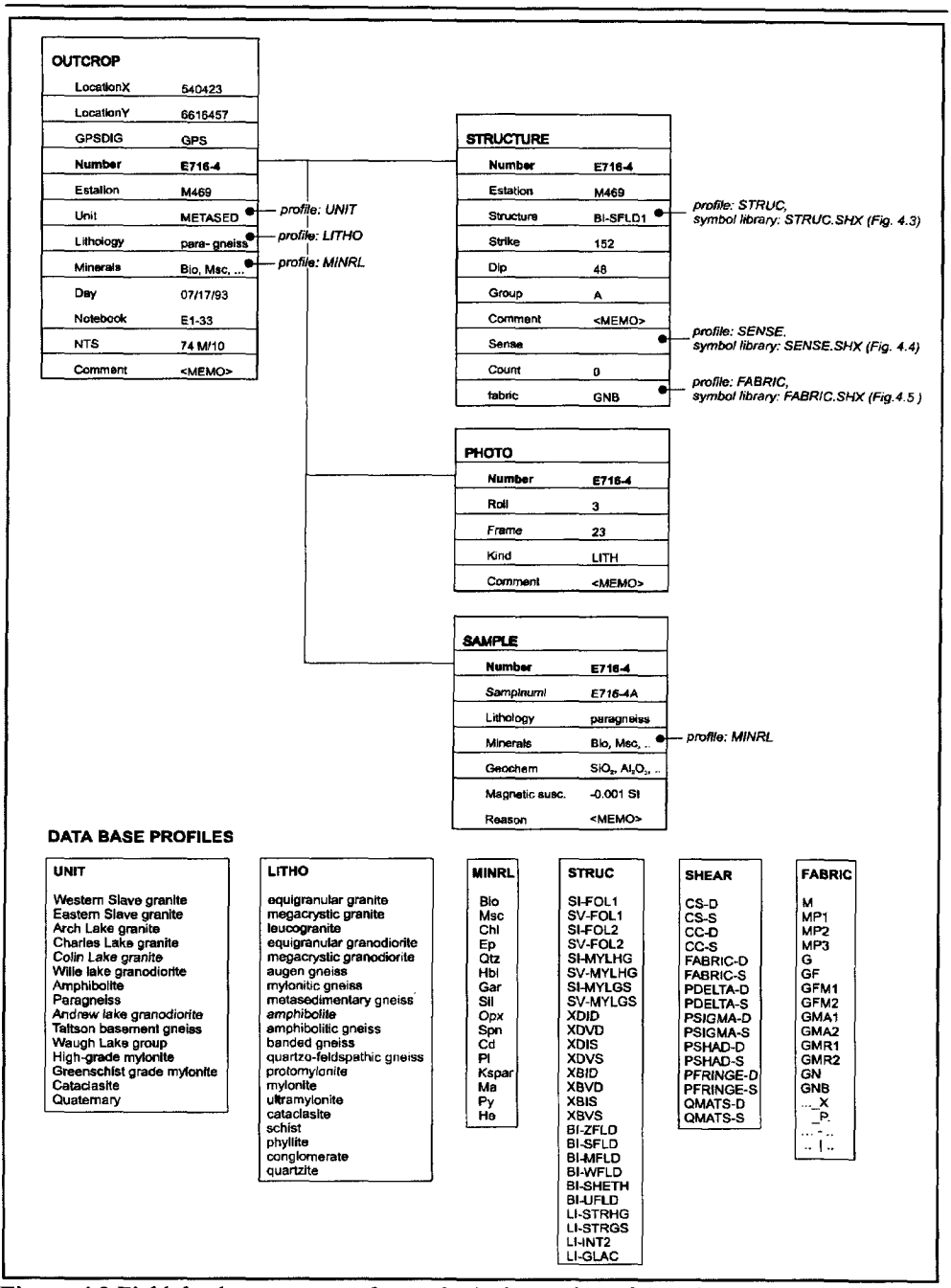

Figure 4.2 Field database structure for geological mapping of the Alberta Shield.

4.6 Applications facilitated by digital field data handling

The following sections present some application developments facilitated by the digital storage, management and automated map generation of field data. The methodologies have been partly applied in the forthcoming chapters for cartographic representation and the integrated interpretation of field and remotely sensed data.

4.6.1 Cartographic representation of geological field observations

Geological maps display a number of cartographic symbols to represent different point-located features, such as bedding and other planar or linear structural elements, sedimentary structures, metamorphic mineral assemblages, etc. Most of these symbols, such as the dip/strike symbol, are based on international standards or by the cartographic style of a particular geological survey. The symbols are generally simple aggregations of line elements or shapes, such that they can be easily drawn on the mapping base or transparent overlays.

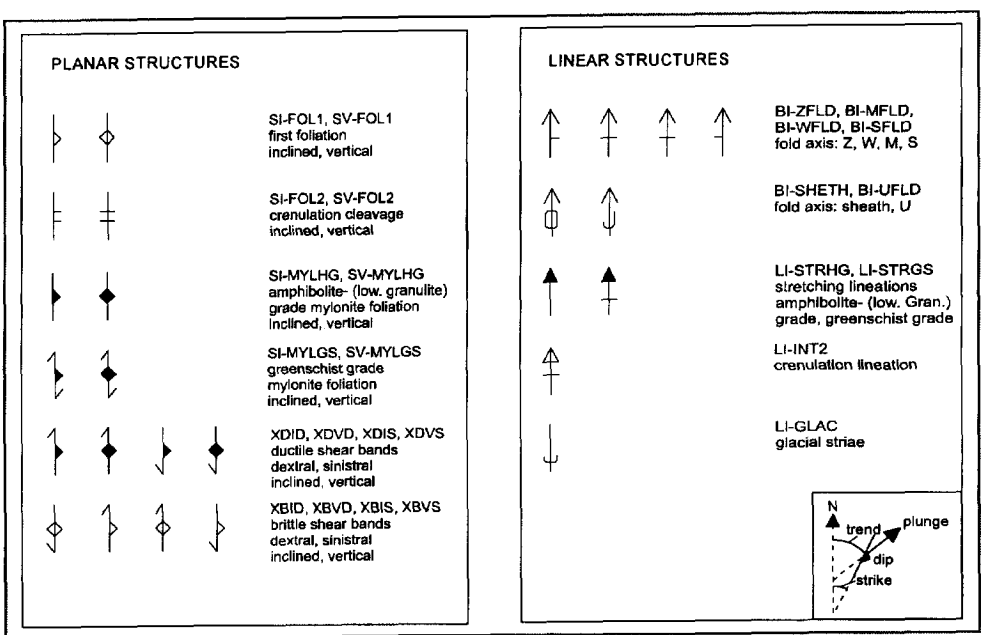

Figure 4.3-(A) Symbol library STRUC. SHX used for mapping structures of the NE-Alberta Shield adapted from GSC.SHX symbol library.

Figure 4.3 shows the symbol library that was used for structural geologic mapping in northeastern Alberta. The majority of these symbols are from the standard library of the Geological Survey of Canada. Some symbols were adapted or added for distinguishing the variety of fabrics that were found in shear zones. Symbols were added to represent brittle-ductile and ductile shear bands and their sense of movement. In addition, symbol sets were used to represent the metamorphic grade of mylonitic fabrics (Mike McDonough, pers. comm.).

Because in digital cartography, the reproducibility and the time needed for drafting symbols are not any longer constraining factors, the traditional style of geological cartography can be expanded to more informative, intuitive and realistic representations of observed geological phenomena. Exploiting digital cartographic capabilities may ultimately lead to the development of new cartographic styles and themes that allow geologists to represent the various aspects of their field observations in a more effective and complete manner.

Figure 4.4 shows, for example, a preliminary design of a symbol library by the author, for the cartographic representation of kinematic indicators. Kinematic indicators are structures observed on the scale of the outcrop or thin section from which geologists attempt to deduce the sense of movement in shear zones (Simpson and Schmid, 1983; Choukroune *et al.*, 1987; Ramsay and Huber, 1987; Hanmer and Passchier, 1991; Passchier and Trouw, 1996 among many others). The identification of shear sense from meso- and microscopic structures became increasingly popular among structural geologists in the eighties when the importance of shear zones in the kinematic analysis of orogenic belts became widely recognized (Hanmer and Passchier, 1991). Systematic and careful mapping of kinematic indicators in shear zones is essential to verify if the shear senses deduced from locally observed structures are regionally consistent (e.g. Hanmer and Passchier, 1991).

The symbols presented in Figure 4.4 represent some of the structures observed in outcrop or in thin section that are commonly used for determining shear sense. The longest dimension of a symbol is plotted parallel to the X-axes of the finite strain ellipsoid, under the assumption that the mineral or stretching lineation indicates the movement direction in a non-coaxial deformation regime. The symbols provide a view on the XZ plane of the finite strain ellipsoid. If the shear zone is vertical and strike-lineated the XZ plane is sub-parallel to the plane of map projection and the trend of the stretching lineation is approximately equal to the strike of the foliation.

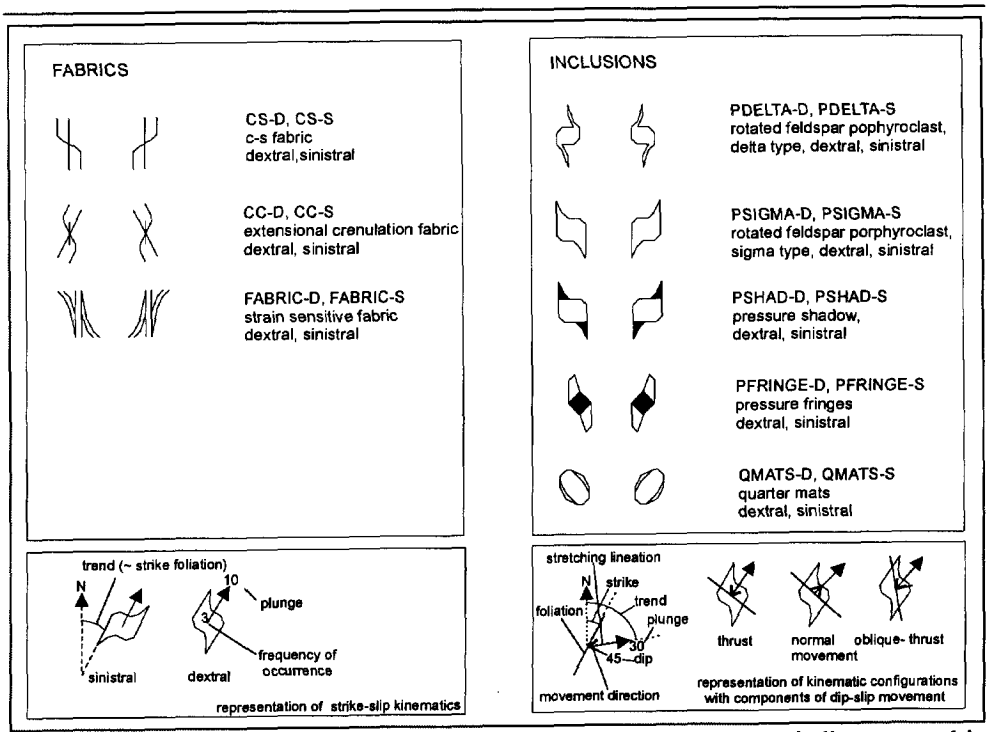

Figure 4.4 Symbol library SENSE.SHX for visualization of shear sense indicators used in the kinematic analysis of shear zones.

This situation is illustrated in the lower left inset of Figure 4.4. If mylonites in the shear zone are oblique- to dip lineated, the views on the XZ plane make an angle with the map plane. The symbols have to be plotted with the foliation elements and an indication of the movement direction in order to represent all possible kinematic configurations. The sense of movement of the hanging wall is inferred by viewing the symbol (with dextral asymmetry) from the direction that makes an angle of ninety degrees anti-clockwise with the movement direction. This configuration is illustrated in the lower right inset of Figure 4.4. A number can be plotted in the center of the symbol indicating how often the structure has been observed on a particular outcrop or thin section. This gives an indication of the significance of the kinematic interpretation at a particular location.

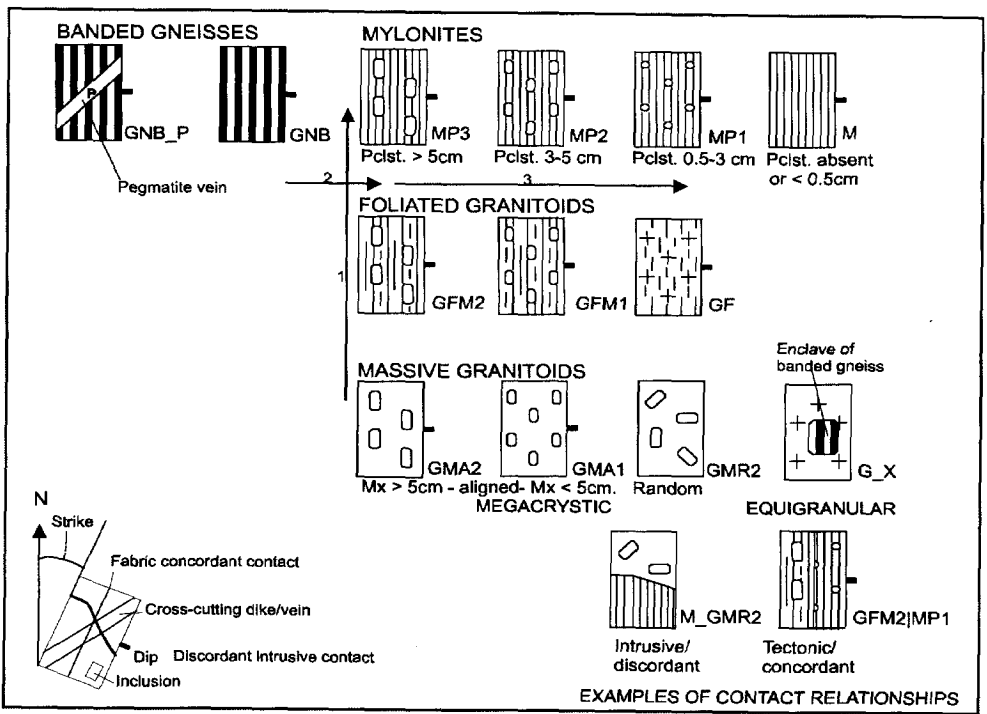

Figure 4.5 Symbol library of fabrics FABRIC.SHX representations for mapping contact relationships and strain gradients in granite-gneiss terrain (Pclst. = porphyroclast, Mx. = megacryst). The arrows indicate transitions of fabrics that possibly (dependent on the variations in fabrics of the protolith) represent strain gradients: (1) from massive granitoids, foliated granitoids to mylonites, (2) from banded gneisses to mylonites, (3) strain gradients within the mylonite series from proto- to ultramylonites.

The cartographic representation of the kinematic indicators combined with lineation and foliation data and text representations of metamorphic mineral assemblages may prove to be a valuable aid for unravelling the deformation histories of shear zones. Unlike the routinely used arrow symbols, the cartographic representation of kinematic indicators in combination with an understanding of the strain conditions under which they are formed, may provide additional insight that contribute to kinematic interpretations. Moreover the representation of the structures themselves allow others to make their own judgement on the reliability of kinematic interpretations, as its validity may depend on how frequent and what type of kinematic indicator is observed (Hanmer and Passchier, 1991).

By combining multiple database fields with automated symbol compilation, enhanced cartographic representations become possible. These representations can portray field knowledge in a more informative manner and communicate the essential elements to constrain interpretations. Figure 4.5 shows a preliminary design of a symbol library for representing fabrics and fabric interrelationships in mylonite, gneiss and foliated to massive granitoid units in the study area. The cartographic representations of these symbols may be considered useful in qualitatively inferring finite strain states and reconstructing relative age relationships between tectonic and intrusive events. A primitive rectangle oriented according to the strike of the foliation is filled with patterns to symbolize the nature, degree of layering and foliation, and spatio-chronological relationships between lithological components and fabrics. The symbol representations are considered particularly relevant for unravelling the geological history in deeply eroded gneiss terrain of the Precambrian Shield. This is because the locally observed intrusive and structural relationships in pavement outcrops often provide the only means to establish the order of geological events and to reconstruct the regional scale geological structure. The symbol library shown in Figure 4.5 shows a preliminary design for the granite-gneiss fabrics encountered in the study area. The map compilation of this symbol library was implemented experimentally and was not tested during field mapping. Detailed field notes and outcrop photographs, however, allowed encoding structural relationships between fabric elements.

The symbols display the intensity of the fabric by variable density of linear elements and widths in the foliated granitoids, gneisses and mylonites. If the protolith was relatively uniform and new growth along the porphyroclasts did not occur, their dimension may be used to qualitatively infer relative differences in finite strain states under ductile deformation conditions. Contact relationships between these foliated rocks and with intrusive rocks, such as granitoids, pegmatites and aplites provide insight on whether the contact is tectonic or solely intrusive. This kind of symbolization is also useful to represent relative age relationships between rock units. Since the fabric representations may reflect strain gradients within units or aggregations of a variety of rock types, they obviously do not have a one-to-one relationship with the lithological units of a geological map.

An example of this cartographic representation of fabrics combined with encoding of synkinematic mineral assemblages is shown in Figure 4.6. The arrows indicate the strain gradients that have been inferred from the fabric representations.

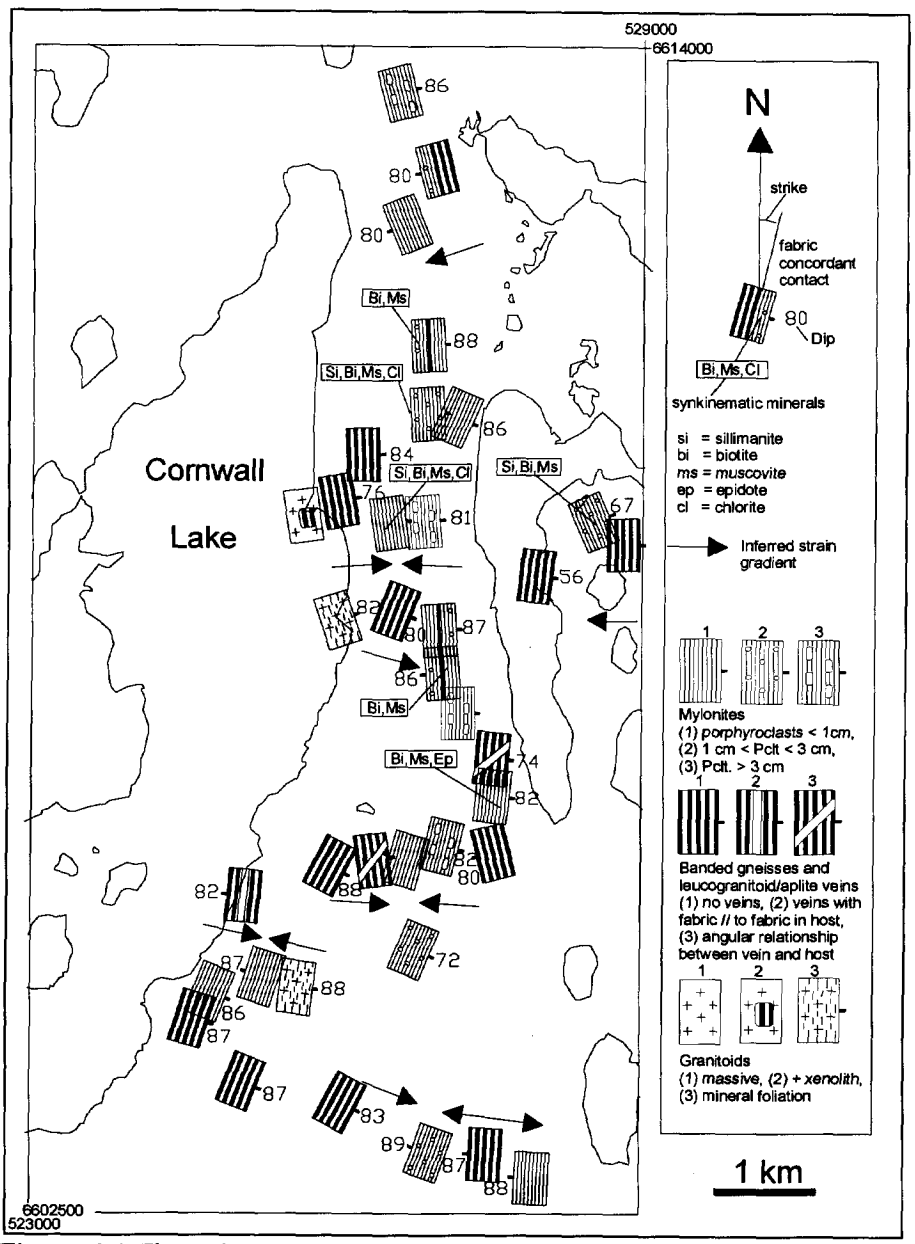

Figure 4.6 Thematic cartographic representations of fabrics and syn-kinematic mineral assemblages along segment of the Charles Lake shear zone.

A typical strain gradient within a single protolith could be represented by the sequence: banded gneiss, protomylonite with many large porphyroclasts, mylonite with small porphyroclasts, ultramylonite with a few small porphyroclasts. This representation form is clearly complementary to conventional field maps where the fabrics have been generalized and assigned to map units.

Contrary to conventional map compilations, the symbolization shows the locally observed fabrics and their relationships in their spatial context. This provides an additional aid to the syntheses of intrusive, metamorphic and tectonic events in a study area. Future developments of the cartographic representation of spatio-chronological fabric relationships would benefit from aggregated symbol compilation routines such that the various graphic elements of the symbol can be automatically sequenced, linking the relevant descriptive and numeric fields of the database.

4.6.2 Automated map compilation for structural interpretation

Commonly thousands of structural measurements are collected during the course of a geological mapping project. Once all these measurements have been digitized, they can be sorted on position, generation, lithological unit or orientation by using the querying functionality of the field mapping system. This can be done repeatedly until a satisfactory representation is achieved. Stereographic projections can be compiled from the map themes by interactively drawing polygon boundaries around structural domains. Figure 4.7 shows an example of such a compilation procedure for generating a map compilation of a shear zone segment. The query used in this example extracted only those stations where both the foliation and stretching lineation were measured:

> " SELECT LOCATION_X, LOCATION_Y FROM OUTCROP SELECT STRUCTURE, STRIKE, DIP FROM STRUCTURE WHERE STRUCTURE.GROUP = A "

The group label A encoded the situations where the orientation of both the mylonitic foliation and stretching lineation could be measured in an outcrop, permitting to extract the observations that are relevant for kinematic interpretation.

Although such querying mechanisms enable to build the map compilation systematically from the different structural themes, often in areas of dense field observation, unreadable map clutter results. Because it is difficult to generalize the observations afterwards, it is important to assess and encode the regional

significance of each measurement during data collection.

In low-grade metamorphic settings, it is usually possible to reconstruct from local observations the geometry of regional structures. The enveloping surface of a train of mesoscopic folds, for example, may serve at that location as a local estimate of the average attitude of the regional structure. In other settings where such hierarchical order in scale can not be easily predicted from field observations, such as in many high-grade gneiss belts, automated methods for generalizing structural data may be considered useful. An automated method for strike generalization, when a scale hierarchy has not been encoded is to calculate a local average from foliation data within the immediate neighbourhood of each other. The bi-directional average orientation of strikes is computed as (Fisher, 1993):

$$\Phi_{avg} = 0.5 \tan^{-1} \frac{\sum_{i=1}^{i=n} \sin(2\Phi_i)}{\sum_{i=1}^{i=n} \cos(2\Phi_i)} \qquad [4.1]$$

Where Φ_{avg} and Φ_i are respectively the average strike-angle and the strike-angle of the $i^{th.}$ observation. The spread of the directional data is inversely proportional to the resultant vector length R normalized for the number of measurements n and is defined as:

$$R = \frac{1}{n} \sqrt{\sum_{i=1}^{i=n} \sin^2(\Phi_i) + \sum_{i=1}^{i=n} \cos^2(\Phi_i)} \qquad [4.2]$$

R can be represented by varying the length of the average strike lines. For a group of n vectors with identical directions, R will equal n and a sample of perfectly opposing vectors would sum to zero (Fisher, 1993).

The strike-averaging method can be extended to three dimensions by averaging the three directional cosines derived from strike-dip measurements (Gaile and Burt, 1980; de Kemp, 1998). In order to obtain meaningful results, it is important to compute the average strike angles over structural domains, such that their outline enclose areas with a relative homogeneous variation in orientation without regionally significant structural discontinuities. Alternatively, to model and extract regional structure, the structural orientation data can be fitted to a trend surface (Agterberg, 1972).

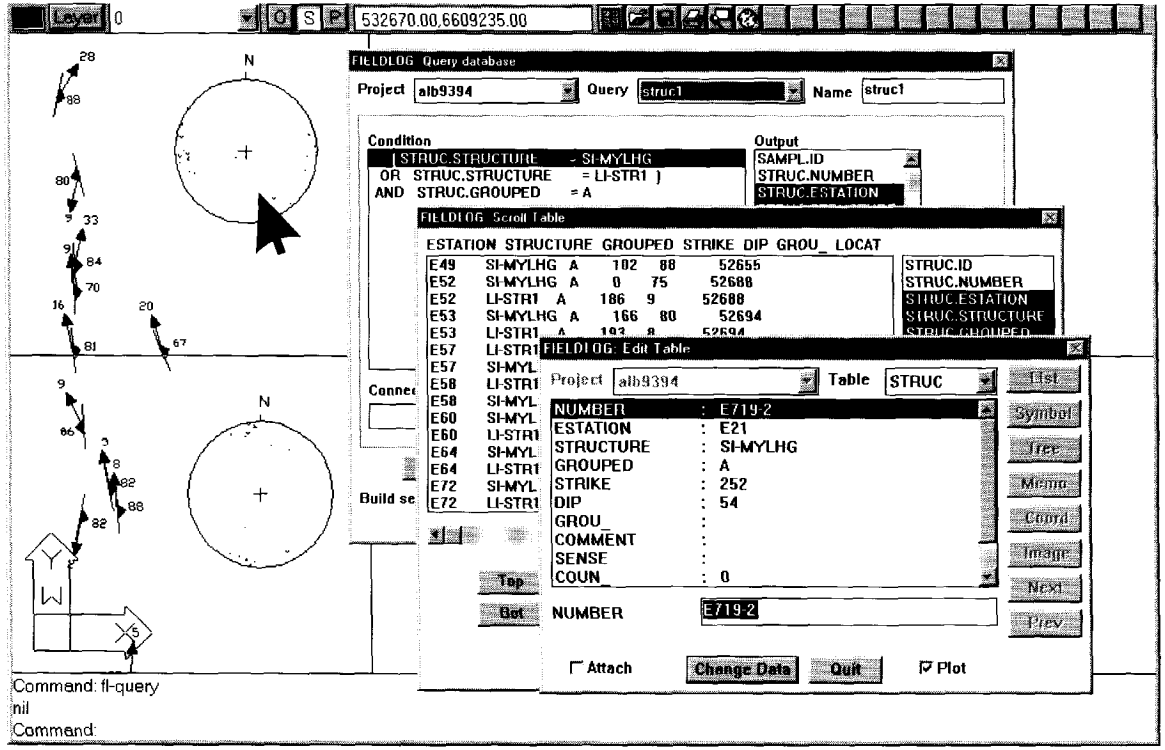

Figure 4.7 User interface of FIELDLOG for structural map compilation illustrating data retrieval, reporting, cartographic representation and editing functions within dynamically linked views.

The automated map compilation techniques are not only useful for structural interpretation in their own right, but they may also be exploited to support the image interpretation. Once the field observations are brought within a GIS environment and can be graphically represented, it gives the opportunity to develop interpretation themes where field- and enhanced remotely sensed data are visualized on demand. Exploiting spatial and non-spatial querying capabilities, the field data relevant to an interpretation task can be selectively retrieved and graphically represented as cartographic themes on scanned aerial photographs or enhanced satellite imagery. To assure that such procedures are meaningful the field data need to be generalized interactively or with the aid of the automated strike-averaging procedure.

Once an appropriate generalization has been achieved, the interactive representation of field data on a georeferenced image may be extremely useful to guide the image interpreter in attaching geological significance to image interpreted features. This is highly relevant in lineament interpretations where it often appears difficult to identify the structural origin of linear image features from the images alone. Interpreted lineaments could represent a variety of geological structures, such as lithological contacts, faults, mega-joints, foliation patterns and dykes. By comparing the spatial correspondence and orientation between image inferred linear features and field-observed structures, the interpreter can outline and classify the image-inferred features with a higher degree of confidence. The locally established relationships between lineament patterns and field observed structures could then be used as a keystone to extend the interpretation over a larger area. Such overlay techniques may from a technical viewpoint, appear trivial. The challenge, however, is to extract and represent those attributes that in combination with enhancement procedures, optimize the extraction of geologically meaningful information. Whether this can be applied successfully not only depends on the technical skills and familiarity with image enhancement methods, but also on an understanding of the geological processes that gave rise to a particular image pattern or anomaly. Such insight only comes with the experience of the interpreter and his or her familiarity with the geological and physiographic setting of the study area.

Figure 4.8 shows an example where the interpretation of a scanned orthophoto was supported by the representation of field data. Orientation measurements of glacial striations (azimuth), gneissic and mylonitic foliations (strike & dip) were extracted and cartographically represented to analyze the relationships between terrain morphology and geological structure using the following query:

```
" SELECT LOCATION_X, LOCATION_Y FROM OUTCROP
SELECT STRUCTURE, STRIKE, DIP FROM STRUCTURE
WHERE OUTCROP.LOCATION_X > 525000 AND
OUTCROP.LOCATION_X < 535000 AND
OUTCROP.LOCATION_Y > 6625000 AND
OUTCROP.LOCATION_Y < 6640000 AND
STRUCTURE.STRUC = S*-FOL1 OR
STRUCTURE.STRUC = S*-MYLHG OR
STRUCTURE.STRUC = LI-GLAC "
```

The wildcard character "*" enabled to extract both the inclined and vertical foliation data (i.e., SI-FOL1 and SV-FOL1). A structural map was compiled by linking the symbol library STRUC (Figure 4.3) to the STRUC database field. This automated compilation process is schematically illustrated in Figure 4.1. The map overlay was subsequently superimposed on the scanned orthophoto.

The field knowledge representation on the scanned aerial photo suggests that the north-south trending topographic highs outline the splays of a shear zone, in which mylonites were apparently more resistant to glacial scouring in comparison to gneisses. The mylonites of the Charles Lake shear zone stand out on the aerial photograph as smooth elongated topographic highs flanked on both sides by areas of lower elevation. ENE-SWS trending drumlins appear to be parallel to field measurements of glacial striations and confirm the SWS directed ice transport (Bednarski, 1997). The topographic highs associated with the mylonite zones do not show evident glacial scouring. The adjacent terrain underlain by gneisses, in contrast, shows drumlins that parallel the glacial striations. The structural control of topography shown by the combined visualization of image and field data enables the interpreter to differentiate and outline the mylonitic and gneissic foliation trends.

The structural interpretation of the aerial photograph without the representation of field data would obviously have been more ambiguous. In the northeastern quadrant, for example, it is difficult to differentiate between glacial lineaments and foliation trends solely based on photo interpretation. The representation of foliation and the glacial striation measurements, permit to gain confidence in assigning geological significance to the linear features on the image. Using the flexible retrieval and overlay GIS functions, the interpreter can selectively retrieve data from the field database or switch on and off symbol representations to emphasize a particular geological theme. The structural interpretation of the vertical magnetic data presented in Chapter 3 (Plate 3.1) is another example to illustrate the added value of this integrated interpretation methodology.

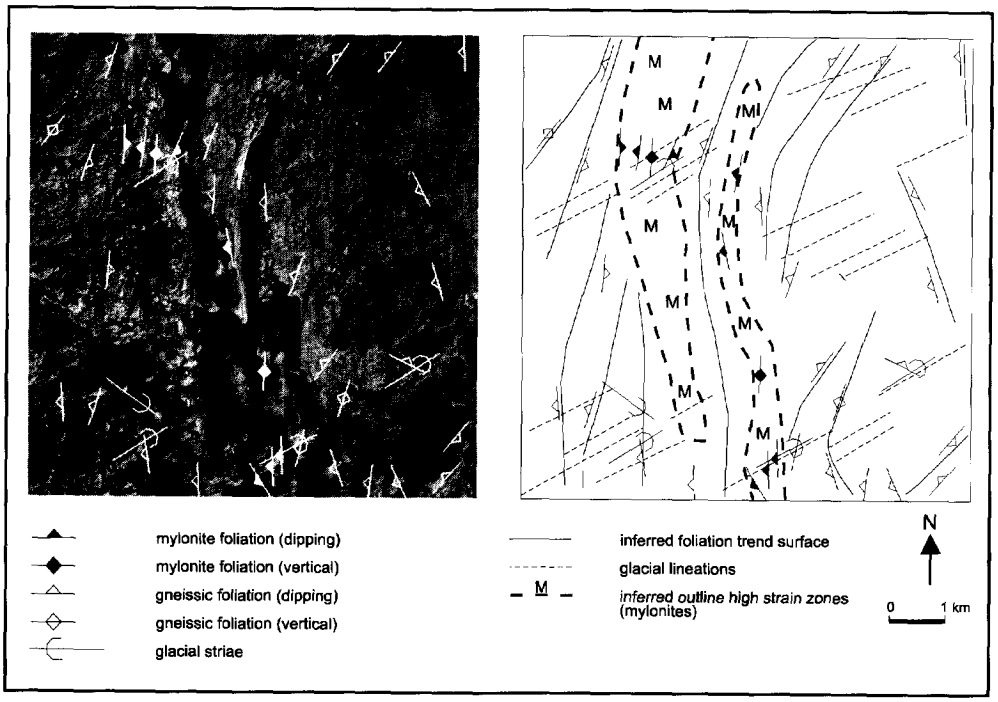

Figure 4.8 Cartographic representation of gneissic, mylonitic foliations and glacial striae referenced on scanned orthophoto. The mylonitic foliations coincide with prominent linear topographic highs on the aerial photograph. Glacial scours, prominently developed in domains of less-resistant gneiss adjacent to the topographic highs, correspond in orientation to glacial striations. The ground truth overlay shown in this example aids the interpretation of gneissic and mylonitic foliation trends.

4.6.3 Automated projection for generating cross-sections

Cross-sections are an essential part of a structural synthesis and may provide more insight in the geometry of fold and faults in comparison to maps. In this section a method is discussed that exploits the digital manipulation of structural

data and spatial analysis capabilities of GIS for representing cross-sections in 3-D perspective views.

In essence, cross-sections are interpretations of structures at depth extrapolated from data available at the surface. They may be constrained by data on the regional stratigraphy or lithology, by direct observations from drill holes or mines and by geophysical data.

Cross-sections are highly interpretative because they are based on the assumption that the structures at depth are simple projections of the structures observed at the surface (Twiss and Moores, 1992). The validity of this assumption depends on various factors, of which the most important to consider are: (1) the three-dimensional complexity of the geological structures, (2) the distance over which observations from the surface are projected at depth, and (3) the density of the field observations used in cross-section compilation.

Cross-sections can be expected to be a reasonable representation of structures at depth in settings where there is a dominant large scale folding geometry that is uniaxial (i.e. with a constant orientation of the fold axes). Classical manual drafting of structural cross-sections is a complex and labour-intensive task. For each structural element, corrections must be made for elevation, and additionally, true dips need to be converted to apparent dips. Once the optimal section line has been selected, the structural elements from nearby field stations must be projected to the section line. In general the following steps are involved in manual cross-section drafting (McClay, 1987):

1. A section line is drawn on the map more or less perpendicular to the structural grain of the area, and elevation points are plotted for the intersections of the section line with elevation contours.

2. Field stations are projected to the section line according to the fold axes. The intersection points are plotted on the proper elevation on the cross-section. This involves making an elevation correction when a down-plunge projection is used.

3. The apparent dip is calculated from the true dip, based on angles between the strike of the structural elements and the section line.

It is evident from the above description that the manual drafting of cross-sections is time-consuming and error-prone, particularly when many field stations need to be projected. For each cross-section to be re-drafted, for example by

changing the orientation of the section line or the class of structural elements to be projected, the same steps must be repeated. Therefore, manual cross-section drafting, before the section is constructed, requires careful planning of where to draw section lines, which field stations to project, and how to project them. Because redrafting can be time-consuming, in practice the drafting will be performed only once or twice. The automated projection method, however, allows the geologist to construct templates for cross-sections as many times as needed, and experiment with different projection parameters for alternative interpretations.

Automated compilation of cross-sections for 3-D visualization purposes differs fundamentally from methods developed for the representations of geologic bodies, which are routinely applied in the petroleum industry such as described by Marschallinger (1991). In the last, the representation of geologic bodies is achieved by interpolation routines using 3-D coordinates of geologic markers and subsurface information. The limitation of such modeling approaches is that they fail when geologic markers are absent or when there is insufficient topographic relief to constrain the attitude of geologic structures (especially when subsurface information is not available). Moreover those methods, because they rely heavily on statistical assumptions in order to carry out interpolation, are only reliable for modeling smooth surfaces, such as smooth antiforms, synforms or domal structures, unless the smaller wavelengths are adequately sampled. In order to depict the complex geometry of metamorphic areas, affected by folding on various orders of scale, alternatives should be considered in which structural orientation data collected in the field are exploited. Rather than attempting to capture the complex geometry of folds and faults by interpolation procedures from 3-D points or structural contours, 3-D projection of structural orientation data provide a simpler and more practical alternative in many geological settings. The automated projection method, discussed here, is fully integrated within the GIS domain. This gives the flexibility of using one system for the management, display, output and analysis of digitally stored geologic data on both map- and cross-section projection surfaces. Additional tools for stereographic projection and structural elements, also designed using standard GIS analysis functions, provide earth scientists with powerful and flexible modeling procedures in mapping and modeling geologic structures in 3-dimensions.

Methodology

Figure 4.9 shows schematically how cross-sections can be generated automatically using the spatial analysis functions of a GIS. By implementing

spreadsheet calculations on a 3-D point database, linked to 2-D spatial data structures, structural geologic data can be projected to user-defined projection planes. With additional coordinate transformations, the resulting cross-sections are stacked in 3-D perspective views. An automated routine was developed for projecting structural elements to vertical or inclined cross sections (Schetselaar, 1995). The method required the following functionalities:

1. Spreadsheet capabilities to enable computation of projection and transformation equations on point data (x,y,z) in 3-D.

2. Extensive spatial data conversion capabilities to enable conversions from and to different data structures, including raster to vector, vector to raster, vector to table and raster to table conversions. Essential conversions for automated projection are: (I) conversions from arcs/segments to point data to transfer 3-D line data to point data in table format; (ii) conversions from raster to point data to sample for location data (x, y) the corresponding elevation coordinates (z) from a raster DEM; (iii) conversions from point data to symbols to ensure graphical representation of topography and projected structural elements on a 2-dimensional inclined or vertical projection surface.

3. Screen digitizing capabilities, which allows the user to digitize on backdrop graphics. Instead of using hard copy geologic maps, section lines can be digitized directly on georeferenced digitized geologic maps displayed on the monitor. In addition, the structural interpretations are digitized on screen using the cross-section projection surfaces as backdrop graphics.

Topographic sections were generated to represent the projected geologic structures with reference to the earth surface. For the map coordinates of the section lines, elevation data (z) are read from the DEM, resulting in an array of 3-D coordinates (x, y, z) along the section line as shown in Figure 4.10. These coordinates are then converted to line segments.

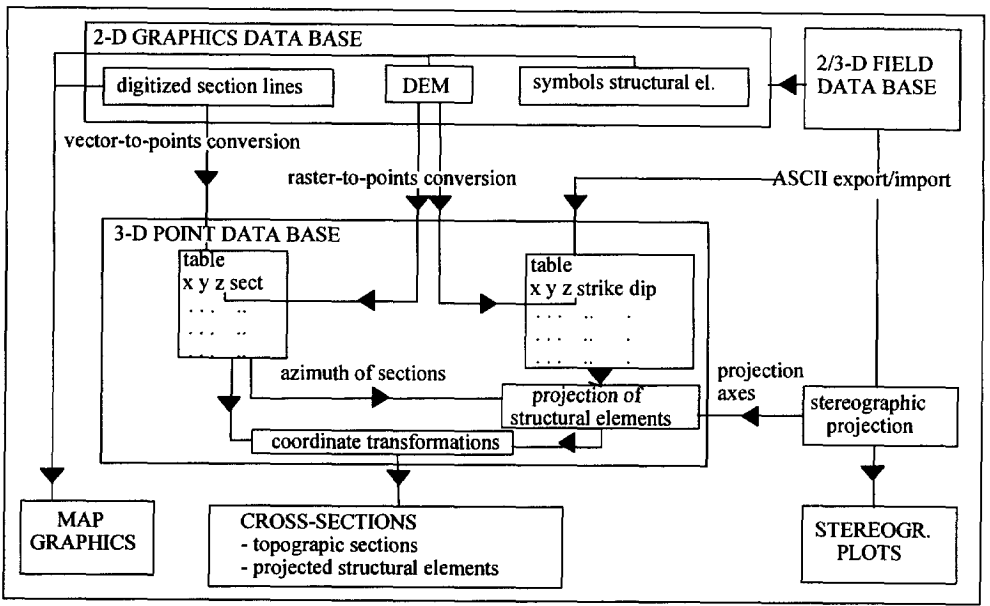

Figure 4.9 Flowchart illustrating methodology for generation of cross-sections in perspective views.

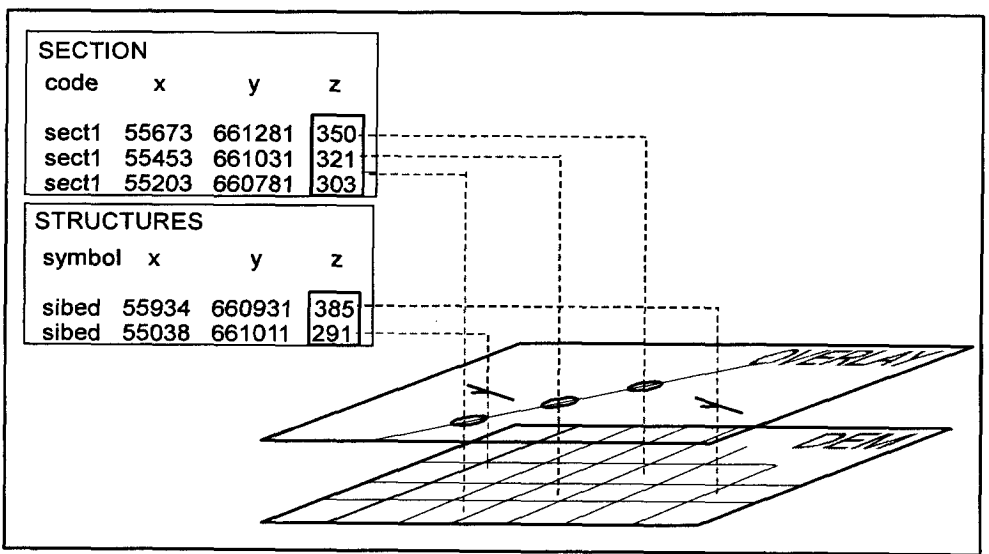

Figure 4.10 Raster-to-points conversion to sample digital elevation model to attribute elevation coordinates z to map coordinates (x, y).

The next step involves the automated projection of structural elements to a vertical or inclined plane intersecting the Earth's surface at the defined section line. Spreadsheet calculations are implemented on the 3-D point data set to:

1. compute intersection points (x_1,y_1) between projected stations and the section line:

$$x_1 = \frac{b_1 - b_0}{a_0 - a_1} \qquad y_1 = a_1 x_1 + b_1 \qquad [4.3]$$

where: a_0= slope section line in (x,y) plane
b_0= offset section line
a_1= slope projection axes in (x,y) plane
b_1= offset projection axes

2. compute horizontal distances (d) from the field stations (x_0,y_0) to the projected stations (x_1,y_1) on the section lines:

$$d = \sqrt{(x_1 - x_2)^2 + (y_1 - y_2)^2} \qquad [4.4]$$

3. compute elevation correction for down-plunge projection:

$$z_p = z_s \frac{\tan(\alpha)}{\cos(\beta)} d \qquad [4.5]$$

where: z_p = corrected elevation at projection
z_s = elevation at field station
d = horizontal distance between field station and projected station
α = plunge angle projection axis
β = inclination angle projection surface (β = 0 for vertical projections; β = α for inclined sections perpendicular to the fold axis)

4. compute apparent dips:

$$\text{apdip} = \tan^{-1}[\sin[\rho - 90]\tan^{-1}(a_0)]\tan(\phi) \qquad [4.6]$$

where: ρ = dip direction of structural element
ϕ = dip of structural element
a_0 = slope of section line in (x,y) plane

5. compute coordinates of perspective view (x_p,y_p):

$$x_p = d_x + \cos(\theta)\, d_s \qquad [4.7]$$

$$y_p = z_p \sin(\theta)\ d_s \qquad [4.8]$$

where: d_X = distance in x-direction along section line
d_S = distance between section lines (origin (d_X,d_S) = (0,0) is at left site of bottom section line)
θ = look direction for perspective view

First parallel section lines are digitized on a georeferenced raster image with an overlay of the structural orientation data displayed on the screen. Suitable backdrops may be rasterized geology maps, a relief-shaded digital elevation model, ortho-images or scanned topographic maps. To ensure maximum control and minimum projection distance the section lines should be drawn preferably through areas with high densities of structural orientation data. This may be accomplished by digitizing parallel segments offset perpendicular to their trends. The individual segments will be aggregated by the batch routine into one section.

After the section lines are digitized, a vector-to-points conversion is used to sample the section line with a user-specified sampling interval. This produces an ASCII table with x and y coordinate fields and attribute codes for each section line. The corresponding z coordinates are sampled from the DEM, as shown schematically in Figure 4.10. The 3-D coordinates are then converted into graphic elements to represent topographic sections. Based on the distance calculated between the section lines, a transformation of map coordinates into perspective view coordinates is defined. The same transformation is applied on the projected structural elements and the topography.

In order to project the structural orientation data, structural element type, dip direction and dip and location fields are imported into the 3-D point database. Z coordinates are sampled from the DEM and attributed to the field station locations (x,y) in the same way as described above. The orientation of the projection lines,

defined by average trend and plunge angles from stereo graphic analysis or defined for each element separately and the coordinates (x,y) of the intersections of the projection of each station with the section lines are calculated (equations 4.3 and 4.4). Elevation corrections are made when a down-plunge projection is used (equation 4.5). On the bases of the angle between the strike of each field station with respect to the section lines, true dips are converted to apparent dips (equation 4.6). The coordinates of the projected structural elements are converted to the perspective view coordinate system (equations 4.7 and 4.8), and plotted as dip lines on the previously compiled topographic sections using GIS annotation functions. Visually attractive and easily interpretable sections can be constructed by annotating structural elements of different type or generation in colour.

Screen digitizing functions facilitate the interpretation of the projected structural elements. Multiple cross-sections for different fold generation can be efficiently constructed by selectively retrieving different types of structural elements. Spatial and attribute queries are also useful in situations where the density of field observations results in clutter on the cross-sections. Zoom and selective display of the line work further contribute to flexible drafting and editing capabilities. The interpretation result can be stored as a digital raster file on disk or directly printed. Essential in the interpretation is that the operator recognizes the cleavage vergence relationships and takes into account the style of deformation as observed in the field. Obviously, the drafting of folded surfaces is an interpretative process requiring the expertise of the structural geologist, which will be difficult to substitute by automated methods.

Dynamically linked views of maps and stereographic projections, such as shown in Figure 4.12, provide additional views all contributing in facilitating structural interpretation.

An application example from the Rheinische Shiefergebirge, Germany

The methodology to generate cross-sections from automated projection of structural elements was applied on the Hercynian slate belt in the Rheinische Schiefergebirge, Germany. This was considered a more suitable area to illustrate the utility of the method, in comparison to the study area of the author. This is because, in contrast to the gneissic terrain, the slate-belt setting allowed reconstructing the regional fold structures from the attitude and cleavage vergence relationships of projected bedding and cleavage orientation data.

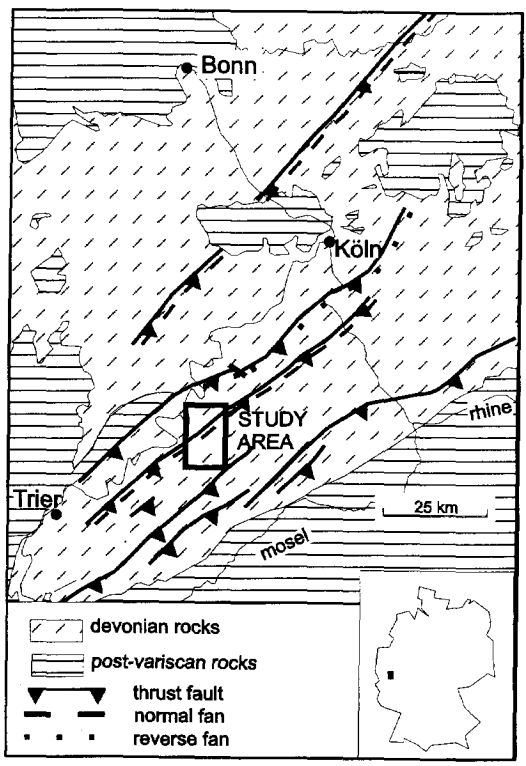

Figure 4.11 Generalized tectonic map of SW Rheinische Schiefergebirge after Bierman (1987) indicating location of major overthrust faults, cleavage fans and study area

A FIELDLOG database of structural orientation data collected by ITC* students participating in a field mapping exercise was maintained during three subsequent years. A general tectonic map of the region with the location of the study area is shown in Figure 4.12. The study area is located in a slate belt affected by two nearly coaxial folding deformation phases. Deformation of the Devonian slates took place during the Middle Carboniferous. The regional structure is characterized by northwest-directed tectonic transport. Major NW-directed overthrusts related to late stages of deformation are suggested by discontinuities in the stratigraphy and metamorphic grade, and contrast in pre-thrusting deformation. (Bierman, 1987). Two phases of deformation can be recognized in the field based on cleavage/cleavage (S1/S2) and bedding/cleavage (S0/S1) relationships. Cleavage vergence, easily recognized along most of the sections, allowed reconstructing the first- and second-generation fold structures. First generation folds are characterized by close to tight upright folds with half-wavelengths between 30 and 100 meters, and an associated axial planar domainal slaty cleavage (S1). Second generation folds are fewer than F1 folds and verge predominantly southeast. They are strongly asymmetric, and exhibit open to close interlimb angles, with steep overturned long limbs and shallowly NW-dipping

* ITC is an abbreviation for the International Institute for Aerospace Surveys and Earth Sciences, (the institute where the author is employed)

short limbs. The associated second -generation cleavage (S2), is a well-developed, spaced crenulation cleavage.

On a regional scale, the orientation of S0, S1 and S2 are affected by a regional fanning that has been explained by regional folding as a result of tectonic transport of the sedimentary cover over a ramp-flat basement geometry (Bierman, 1987).

Fieldwork along the sections was conducted by plotting field stations on 1:25,000 scale topographic maps and attributing field observations on lithology and structure in notebooks. Each day, these field observations were entered in a FIELDLOG database, designed for the field-mapping course. The coordinates of the field stations were digitized directly from the topographic map sheets, using a small portable digitizing tablet. Additional descriptions on the interpretation of the structures were stored in memo fields. Back in the office, a digital elevation model with a raster element size of 10 m was constructed from digitized contour lines by using a linear interpolation routine based on the Borgefors transform (Gorte and Koolhoven, 1990).

The digital elevation model provided elevation values to convert the 2-dimensional map coordinates to 3-dimensional coordinates (Figure 4.10). The raster cell size of 10 m was considered adequate, given that the accuracy of the positioning of field stations was approximately between 50 to 100 meters. Parallel sections were digitized using the DEM with an overlay of cartographic symbols representing the structural orientation data as a backdrop display. Database fields required for the projection routine ((x, y) coordinates, structural element type, dip direction, dip) were exported from the field database and imported into the attribute GIS database. The peak positions obtained from the stereographic projections were used to define an average projection trend and plunge. Because deformation is nearly coaxial and the structural trends are constant, no separate structural domains were defined.

In areas of more complex structure, variation of the projection axis can be incorporated by encoding structural domain polygons along the section lines or interpolating the trend and plunge of the field stations along a control line (deKemp, 1998). In using such projection methods, care must be taken that the projection lines of field stations at large distance to the section line do not cross-over before they reach the projection surface (deKemp, 1998).

All stations within a distance of 300 m from the section lines were used in the projection routine. Stations farther away were omitted by defining a query on the distance between field stations and the section line (calculated in equation 4.2).

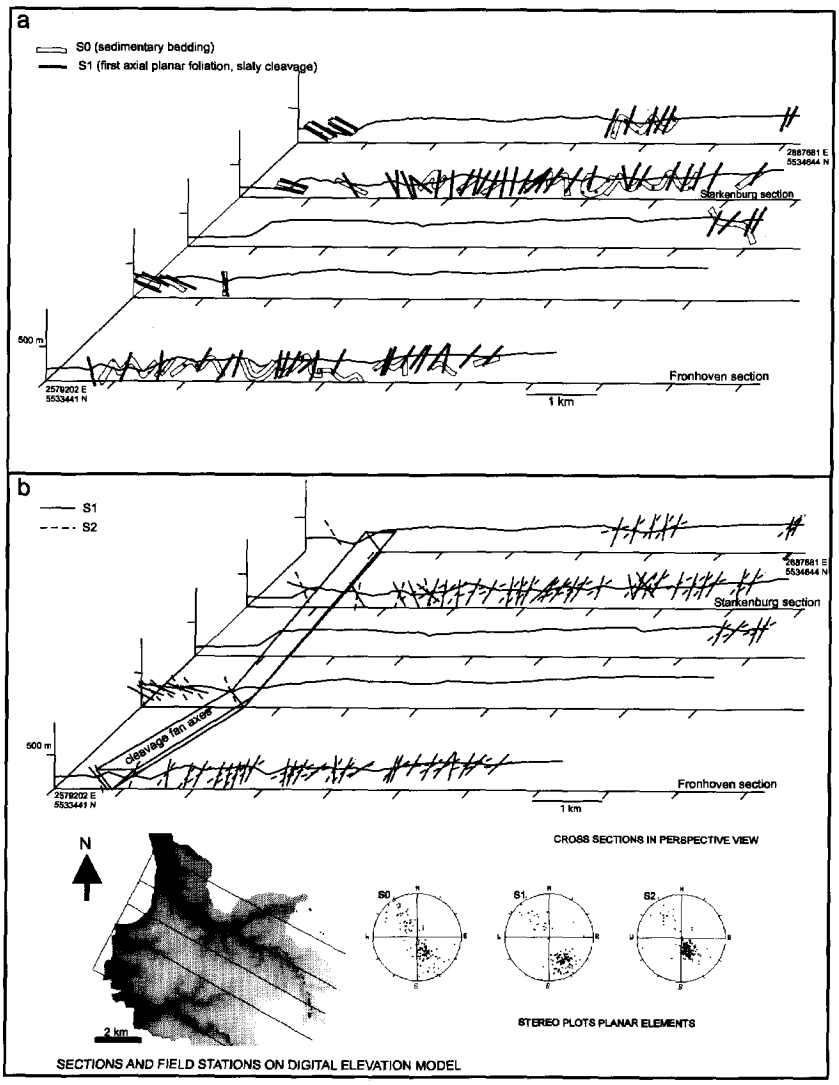

Figure 4.12 Cross sections in 3-D perspective views from the Rheinische Schiefergebirge, Germany; (a) reconstruction of first generation folds based on projection of bedding (S0) and first generation cleavage (S1); (b) projection of first and second generation cleavage. The continuation of the cleavage fan axis has been inferred between adjacent section lines. Insets show digital elevation model with overlay of field stations and section lines and equal area stereographic projections of the structural elements.

A constraint imposed upon retrieval extracted only those stations from the database were cleavage relationships could be measured (S0/S1 and S1/S2). This enhanced the interpret ability of the sections, providing cleavage vergence relationships for each projected field station.

Other constraints may be defined using the spatial and attribute query capabilities of the GIS, for example to extract specific structural relationships or data from specific lithologies.

Some annotated screen displays obtained from the automated projection procedure are shown in Figure 4.12. All structural elements were corrected to apparent dip and S0/S1, S1/S2 cleavage groups were represented separately to visualize cleavage vergence relationships.

Clutter was removed from the sections be selectively reducing the distance from where station were to be projected in areas with dense field observation. The interpretation (Figure 4.12(a)) was conducted by digitizing fold structures on the cross-sections. First generation folds were reconstructed based on S0/S1 cleavage vergence relationships. In addition the fold style, as observed in the field, was taken into consideration while drafting the interpretation.

The display of multiple stacked sections in a perspective view to some extent enabled to trace interpreted structures from one section line to another. For example, an important structural feature in the study area, is the normal cleavage fan, as shown in Figure 4.12(b) by the strong fanning of the S1/S2 cleavage relationships (Bierman, 1987). The position of its axis, separating south dipping from north dipping S2 elements, is represented by a wedge to constrain the shape and position of the axis of the cleavage fan. Although not fully constrained by all the section lines, the nonalignment of this axis either indicates strike-slip faulting at high angle or an en-echelon configuration of cleavage fans. No conclusions can be drawn on the exact reason for this nonalignment, as additional data from the poorly exposed areas between the Starkenburg and Fronhoven sections would be required. The example is here provided to illustrate the type of applications of modeling structures in perspective views. Applications in other geologic situations may be imagined, for example lithological markers and structural orientation data mapped at the surface could be projected on seismic sections at depth, providing a tool to correlate surface geology in seismic interpretation. After this intermezzo in the Rheinische Schiefergebirge of Germany, the author reverts to the application examples of the study area in northeastern Alberta to illustrate how similar automated projection methodologies can be exploited in the quantitative interpretation of aeromagnetic data.

4.6.4 Integrated visualization of magnetic inversion models and surface geological data.

The methodology to generate cross-sections by the automated projection of structural data, presented in the previous section can also be exploited for the integrated interpretation of subsurface models and depth-projected geological field data. The numerical interpretation of magnetic anomalies by inversion, for example, is a useful method to estimate width, depth, dip and susceptibility contrast with surrounding rock volumes of a causative magnetic body (Reeves, 1998). In inversion, the interpreter attempts to obtain a match between the observed magnetic field and calculated magnetic field over a magnetic source model of simple geometry, such as a dyke, rod or step. The best fit is obtained by an iterative procedure converging towards a best-fit solution such that the differences between the calculated and observed anomalies are minimized. Critical to the approach is to select isolated anomalies, which shapes are minimally influenced by neighbouring anomalies. Furthermore parameters, such as magnetic susceptibility contrast, base level and base slope obtained by the fit or constrained by the interpreter should be realistic (Gunn, 1997).

In settings where one expects a high degree of structural continuity between rock masses encountered on the surface with those at depth, one could jointly project the inversion models and the available structural data. This further contributes in assessing whether the results obtained from inversion modeling are geologically meaningful. Systematic encoding of the modeled parameters, such as the width, dip, strike, and depth of the source model should enable one to effectively integrate inversion models with geological observations projected on maps and cross-sections.

This idea was tested for a subset of the magnetic flight line data over the Taltson Basement Complex in the northeastern Alberta study area. About thirty anomalies were selected for inversion using MAGMOD3 Geosoft inversion program. A dyke with infinite strike and depth extent appeared to provide the best fits and seemed the most appropriate source geometry to model for the sub-vertical planar structure of the Taltson Basement Complex (see Section 2.3). The geometric and physical parameters of the best-fit solution were systematically entered in a separate table in FIELDLOG. The anomaly number and the position coordinates of the modeled anomalies were stored in the station table. The database field describing the type of model was linked to the structural symbol library. This provided the necessary relational database links for map plotting and automated projection.

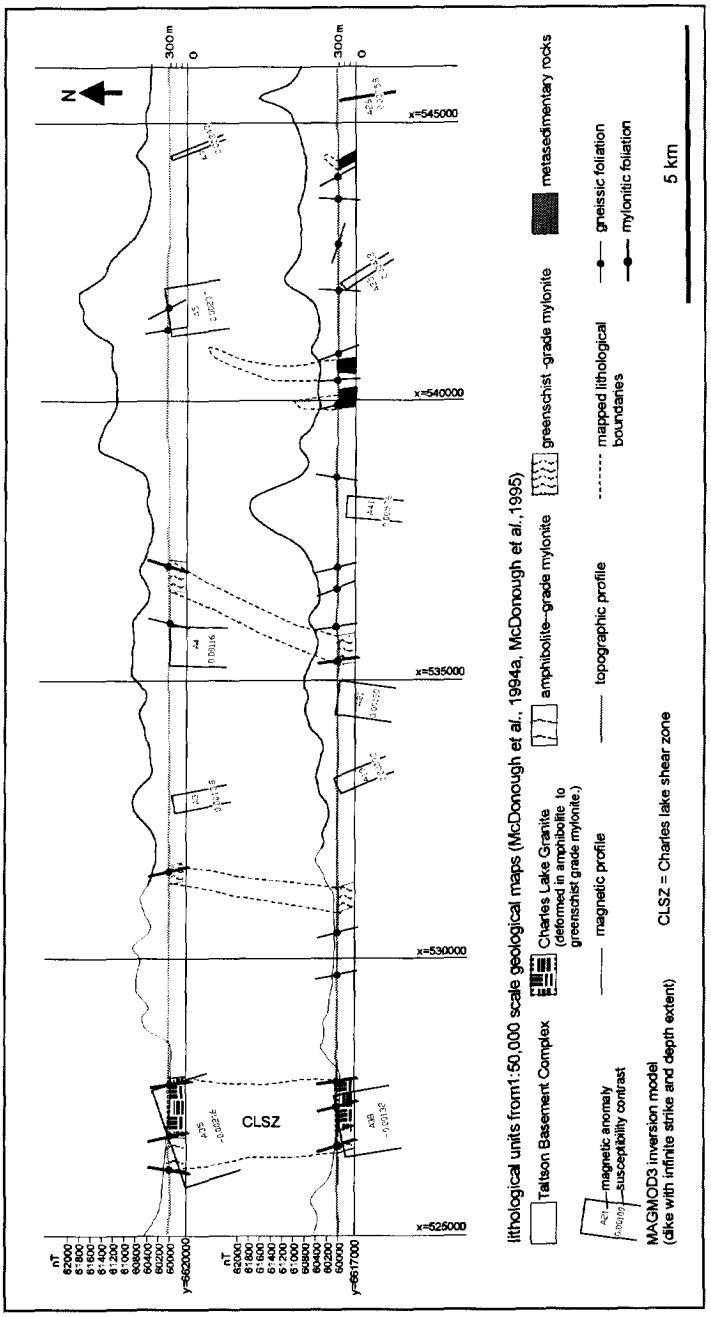

Figure 4.13 Vertical profiles and map representation of the Taltson Basement Complex showing projected magnetic inversion models and foliation data.

A combined representation of magnetic profiles, inversion models and foliation data is shown in Figure 4.13. The model and foliation elements were projected using the same procedures described in section 4.6.3. The mapped lithological boundaries were represented between the profiles and their dips were plotted in the profiles according to the orientation of nearby foliation elements. In general, the results show that the magnetic sources are at or near the surface and that, there is good agreement between the strike and dip of foliation elements and the dyke-models. Some additional deductions that can be made from the integrated representations shown in Figure 4.13 and local field knowledge are:

- Many of the anomalies do not relate to mapped lithological variations. Exceptions are the alignment of broad negative anomalies corresponding to the central splay of Charles Lake shear zone. Together with the field indications, discussed in chapter 3, for redistribution, recrystallization and oxidation of magnetite as a result of mylonitization, this suggests that many of the anomalies are structural in origin.

- Many of the dyke models extend to the surface while most of the remaining models have shallow depths of 50 meters. In combination with the similarity in dip and strike of the foliation data, this suggests that the anomalies relate to surface structure and that the high wave-number magnetic anomaly patterns can be used to interpret surface structures.

- In general, there is good agreement between the strike of the models and the general trend of the foliation data. The mapped lithological contacts are parallel to this trend and can be used as guides to trace anomalies from one flight line to the next (or vice versa).

Deductions such as the above illustrate how the combined map and profile visualizations highlight the similarities and discrepancies between the inversion models and surface geology, providing an aid in constraining geological interpretations.

4.7 Summary and concluding remarks

The applications presented in this chapter all benefit from digital field data management techniques. The examples illustrate how the systematic encoding, management and cartographic representation of primary field observations

enhances the capabilities of the geologist to interpret map-related and various types of remotely sensed data. Although they could have been carried out on an individual basis, all case studies would have been tedious digitizing and data conversion tasks too costly for the breadth of the individual applications.
To use digital field management techniques to its full potential it is essential to use a data structure designed on the basis of a data model for geological field data collection and mapping (Brodaric, 1997). Within this model, relational database linkages facilitate consistent data entry and spatial and non-spatial querying mechanisms for retrieving the subset from the field database that is relevant for an analytical task or interpretation. Such procedures have been extensively implemented for the interpretation work presented in this thesis, and include:

- Cartographic representation of structural and geomorphological themes to support interpretation of various enhanced remotely sensed data.

- Generate visualizations that combine magnetic inversion models, susceptibility measurements and surface geological data.

- Relate lithogeochemistry and mineralogical data from rock samples with airborne gamma-ray spectrometry data and derived products.

- Comparative analysis of the strike-lines of automatically extracted linear features from image data with foliation data.

- Compilation of training sets from bedrock units for automated classification of lithological units.

The above applications and case studies presented in this chapter provide only a few examples to demonstrate the utility of digital field data handling, of which the majority is relevant to the data integration work presented in this thesis. Many other and more advanced applications may be imagined. For example research has been conducted in modeling spatio-chronological relationships of geological entities for verifying the integrity of geological maps and legends (Ady, 1993) and for correctness and consistency control of geological data in general (Bonfatti and Monari, 1995). The implementation of such data modeling concepts would obviously benefit from the systematic field data encoding and management. The following observations are considered relevant for further application development:

1. GIS will be increasingly used during routine fieldwork practice in the near future. Tools for data entry, retrieval and cartographic representation in combination with image processing tools for enhancement are of prime importance in fieldwork situations. Currently, full-blown GIS may still be considered too complex and bulky in its data base structure to be used efficiently during fieldwork. Pen-based palm-top computers are useful for data entry on the outcrop, but at the time of writing display capabilities are currently inadequate to replace the hard copy base aerial photograph or topographic map.

2. Cartographic symbols can be used as an effective means to represent thematic field knowledge. Automated map compilation from user-designed symbol libraries widens the scope of geological cartography from the strike-dip symbol of conventional geological maps to cartographic visualizations that serve scientific interpretation of a wide range of field observed geologic phenomena and their interrelationships. The presented examples emphasize mapping applications in gneissic terrain and include cartographic representation of shear sense indicators, fabrics and local spatio-chronological fabric relationships. This kind of application development may also apply to other Earth science disciplines, such as sedimentology, where spatial interrelationships between local observations contribute to model macro-scale geological processes. The cartographic representation of the spatio-chronological relationships would highly benefit from the development of automated symbol compilation and aggregation functions.

3. The systematic and interactive visualization of field data in the structural interpretation of remotely sensed images is remarkably underdeveloped. The access and representation of structural field observations in the image processing and GIS environment enable geologists to use ground truth as guidelines and source of validation in image interpretation and pattern recognition analysis. The interpretation of structures recognized on their topographic expression in optical and radar remotely sensed data, for example, is facilitated by the cartographic representation of combined geomorphologic and structural themes. This application domain need to be further explored for other combinations of remotely sensed and field data.

4. Development of 3-D GIS applications would highly benefit from the digital capture, management and projection routines of original field measurements.

In polydeformed areas computer interpolation routines based on (x,y,z) coordinates only, are unsatisfactory to represent the geologic structure on various scales. This is because the complex structural geometry of folds and faults are normally highly undersampled and continuous lithological markers may often be lacking in such areas. Interactive analysis to include geological rationale in 3-D models, constrained by appropriate 3-D representations of structural relationships and style, and is therefore more likely a more successful alternative in 3-D structural geologic applications.

5

OPTIMING THE IHS COLOUR TRANSFORM FOR THE INTEGRATED VISUALIZATION OF MULTISOURCE REMOTELY SENSED DATA*

ABSTRACT

The integrated rendering of multisource remotely sensed data in composite images has become a popular technique to exploit complementary information in visual interpretation. A fundamental problem in its application is to implement the transformations from perceptual IHS to display-dependent RGB colour spaces in an unambiguous and optimal manner. This chapter addresses both aspects of this problem. First a processing strategy is presented that preserves the spectral balance of the multispectral image data and modulates the IHS coordinates uniformly. Contrary to conventional processing strategies, the H and S variations remain proportional to the relative spectral signatures of the input images taking the constraints of RGB space into account. Second the differences between the application of the spherical or cylindrical colour transformations in generating IHS composite images are investigated. High intensity ranges can be better enhanced in applying the cylindrical IHS transform. This may be exploited to emphasize textural and spatial details in the final result. The implications of both processing aspects are illustrated using IHS composite images generated by merging K, eTh and eU gamma-ray spectrometry grids with band 7 of Landsat Thematic Mapper. This data combination allows interpreting the geochemical information derived from the gamma-ray responses in the context of geological structures shown on the TM band. The processing methodologies, presented in this chapter have been applied for mapping structural patterns in one of the Taltson granitic suites and for the structural interpretation of the Charles Lake shear zone.

---

* This chapter is based on:

Schetselaar, E.M., 1998, Fusion by the IHS transform: should we use cylindrical or spherical coordinates? International Journal of Remote Sensing, v.19, n.14, pp. 759-765.

Schetselaar, E.M., 2000, On preserving spectral balance in image fusion and its advantages for geological image interpretation. Photogrammetric Engineering and Remote Sensing (submitted).

5.1 Introduction

The integrated visualization of multisource remotely sensed data in colour composite images has proven to be an effective visualization technique to exploit complimentary information in image interpretation (Haydn, 1982; Harris *et al.*, 1990; Chavez *et al.*, 1991 among others). These colour composites are generated by the application of an algebraic algorithm to the grid or pixel values of georeferenced image data. Such visualization methods, in the remote sensing community known as image fusion, are commonly applied for image sharpening, which aims at combining the resolving power of a high spatial resolution image with the spectral information of lower resolution multi-wavelength image channels (Carper *et al.*, 1990; Chavez *et al.*, 1991; Shettigara, 1992; Grasso, 1993; Vrabel, 1996 among others). In other applications, such as geology, composite images have been generated from data acquired by different types of sensors. In these applications space- and airborne measurements of different physical properties are jointly rendered to exploit complementary information in visual interpretation. Many data combinations have proven to be useful for geological mapping, including those of: multispectral image and imaging radar data (Harris *et al.*, 1990; Yésou *et al.*, 1993), gamma-ray spectrometry and imaging radar data (Harris *et al.*, 1990; Paradella *et al.*, 1997), gamma-ray spectrometry and Landsat TM data (Wilford *et al.*, 1997; Schetselaar, 1998), aeromagnetic and Landsat TM data (Reeves *et al.*, 1990), aeromagnetic and radar data (Harris *et al.*, 1990; Mussakowski *et al.*, 1991; Schetselaar and McDonough, 1996). The integrated visualization of complementary data sets proved particularly useful when different geological features (for example lithological composition and structure) have distinct textural or spectral image expressions. A key objective in the generation of composite images, therefore, is to preserve the spectral and textural integrity in each of the input images while highlighting the spatial relationships between them. Unlike mixing apples with oranges, however, it is important that the integrated enhancement of multisource remotely sensed data is driven by a clearly defined geological rationale. Insight in the potential of each data type in portraying geological features of a particular kind is necessary, in order to anticipate complementary information in the final result (Harris *et al.*, 1994).

Although many algorithms are applicable to integrate multisensor remotely sensed data (see Pohl and van Genderen, 1998 for a comprehensive review), not all techniques meet the requirement of mapping the image data on the perceptual attributes of human colour vision. If one, for example, uses registered images from different sensors to modulate the red, green and blue phosphors of the display

device directly, the colour variations of the composite image are not intuitively related to the input data. Techniques that do not suffer from this problem are those based on perceptual colour spaces, such as the IHS space. This is because each distinctly perceived colour parameter (intensity, hue, saturation) can be controlled and manipulated independently (Harris *et al.*, 1990). The IHS transformation, however, has often been uncritically applied using standard digital image processing functions as a "black box". As a result, factors that significantly control the quality of the results have not been considered. This may lead to a distorted, poorly optimized and even misleading representation of the image data in the final result.

In this chapter processing aspects of applying the IHS transform are considered with the aim to optimize this integration technique. First a method is presented aimed at preserving the spectral balance of three multispectral image channels in the IHS image composite. Distortion of the spectral balance are a frequently reported shortcoming of the IHS transformation technique (Chavez *et al.*, 1991; Harris *et al.*, 1994; Milligan and Gunn, 1997). This defect hampers the distinct perception of the image responses of the input data in the final result. Second the implications of using different IHS transformations on the image qualities are analyzed. Two IHS colour spaces have been frequently applied: one can be specified in cylindrical coordinates, while the second is given in spherical coordinates (Harris *et al.*, 1990). It will be shown that it is important to have insight in the differences between these two transformations in order to adapt the colour enhancement to the needs of a particular application. Image processing examples are presented to illustrate how both processing aspects influence the qualities of the IHS composite images. The presented methodologies were applied for geological interpretation of the composition and structure of the Arch Lake granite batholith (see Chapter 6) and the structural interpretation of the Charles Lake shear zone (see Chapter 7). A brief overview of colour coordinate systems and colour spaces is provided first to examine some of the requirements and limitations in applying the IHS transformation technique.

5.2 Tristimulus and chromaticity coordinates

Many systems have been designed to represent, quantify and measure human colour vision. The most widely accepted international standard, defined by the Commission Internationale d'Eclairage, is based on tristimulus colour theory (CIE, 1986). The main principle of this theory is that by matching three independent primaries any colour can be generated. On the basis of colour

matching experiments, the CIE has defined a set of non-physical imaginary primaries that allow any colour to be defined by a triplet of non-negative numbers. From these primaries two commonly used coordinates systems have been derived: (1) tristimulus coordinates and (2) chromaticity coordinates

1. Tristimulus coordinates

An arbitrary colour can be computed from the three tristimulus curves $x_{(\lambda)}$, $y_{(\lambda)}$, $z_{(\lambda)}$ (Figure 5.1) by integrating the relative spectral energy distribution of the light source $c_{(\lambda)}$ over the visible part of the electromagnetic spectrum:

$$X = \int_{380}^{780} c_{(\lambda)}\, x_{(\lambda)}\, d\lambda \qquad [5.1]$$

$$Y = \int_{380}^{780} c_{(\lambda)}\, y_{(\lambda)}\, d\lambda \qquad [5.2]$$

$$Z = \int_{380}^{780} c_{(\lambda)}\, z_{(\lambda)}\, d\lambda \qquad [5.3]$$

where λ is in nanometers, X,Y and Z are the tristimulus values proportional to radiance in W/sr.m^2, $c_{(\lambda)}$ is in W/sr.m^2.nm and $x_{(\lambda)}$, $y_{(\lambda)}$, $z_{(\lambda)}$ are the dimensionless tristimulus curves as defined by the CIE (1931). The $y_{(\lambda)}$ tristimulus function was conveniently defined to be the relative luminosity function so that in addition to the tristimulus value, the Y coordinate also gives the perceived brightness or relative luminance (Niblack, 1986).

Chromaticity coordinates

A standard way to define a colour independently from luminance is based on chromaticity coordinates, which can be derived by sum-normalization of the tristimulus coordinates:

$$x = \frac{X}{X + Y + Z} \qquad [5.4]$$

$$y = \frac{Y}{X + Y + Z} \qquad [5.5]$$

$$z = \frac{Z}{X + Y + Z} \qquad [5.6]$$

Because x, y and z sum to 1, one coordinate, z is defined as redundant. The chromaticity of a colour is therefore completely defined by the x and y coordinates and can be represented in the two-dimensional standard chromaticity diagram, shown in Figure 5.1(b). The chromaticity diagram is convenient in showing the range of colours or gamut that can be produced by mixing the three primaries of the display device (Agoston, 1979).

The colour mixtures produced on a television or computer monitor are commonly referred to as additive colours. Three adjacent phosphor dots, emitting light in the three primaries red, green and blue are juxtaposed at close distance, such that they are not separately resolved by the eye's retina but perceived as an area-averaged mixture.

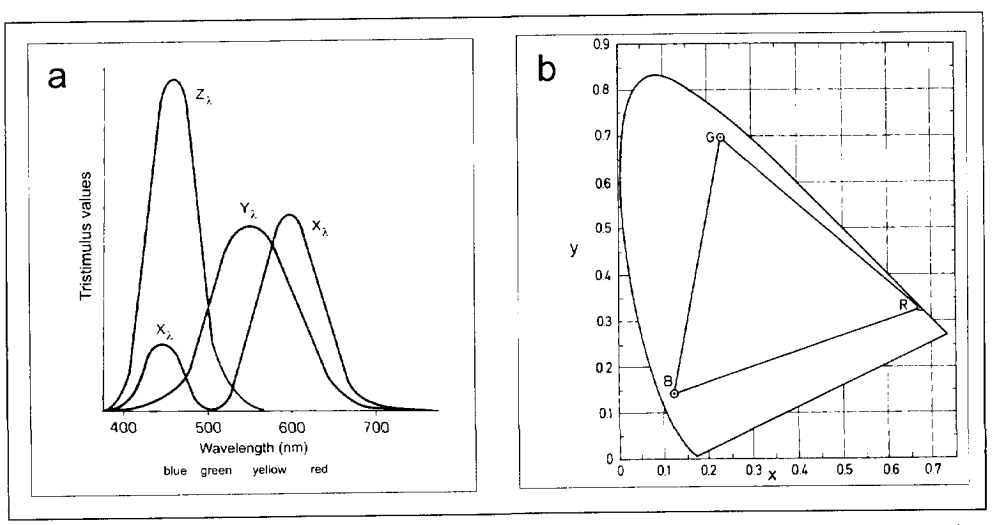

Figure 5.1 (a) Tristimulus curves for the CIE 1931 XYZ primaries (b) Chromaticity diagram and the typical range of colours (i.e., the gamut) available for the R = red, G = green and B = blue phosphors of a display device, after Agoston, (1979).

A typical example of the range of colours (e.g. gamut) that can be generated by the red, green and blue phosphors of a computer monitor is shown by the RGB triangle on Figure 5.1(b). This RGB triangle represents only a fraction of the total range of realizable colours. This is because a display device has a fixed set of primaries (red, green and blue) and uses only positive coefficients with a fixed maximum (Niblack, 1986).

5.3 RGB and IHS colour spaces

A colour space is a method by which one can specify, create and visualize colour. Several colour spaces have been designed to suit a specific application, display device or to enhance intuitive understanding of colour. One way of representing the range of colours displayable on a computer monitor is the RGB colour space (Figure 5.2). The three primaries red, green and blue are defined by the emission characteristics of the phosphors and form the axes of a tristimulus RGB space.

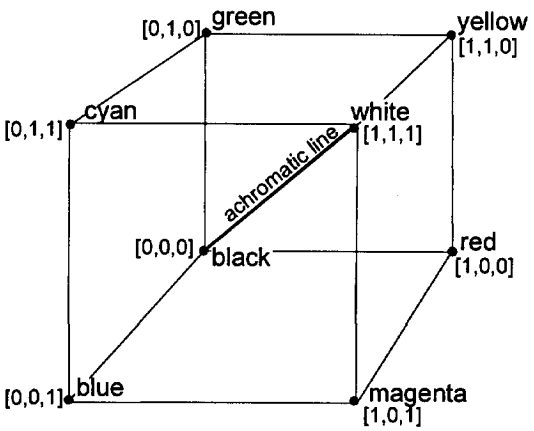

Figure 5.2 RGB colour cube

The values of the red, green and blue primaries are independently scaled to equal range of eight bits (e.g. 256 values) providing a total of 256^3 realizable colours, such that equal amounts in units red, green and blue are achromatic or gray scale colours ranging from black to white. A major drawback of the RGB colour space is that its properties do not relate intuitively to the attributes of human colour perception. If, for example, the saturation of a colour needs to be increased, the associated changes in rgb values are not intuitively straightforward. This limitation of the RGB space largely explains the popularity of perceptual colour spaces, such as the intensity, hue, saturation (IHS) space, where intensity (I) is a linear approximation of luminosity, hue (H) is defined as the predominant wavelength of a colour and saturation is defined as the purity or total amount of white light in a colour (Harris *et al.*, 1990).

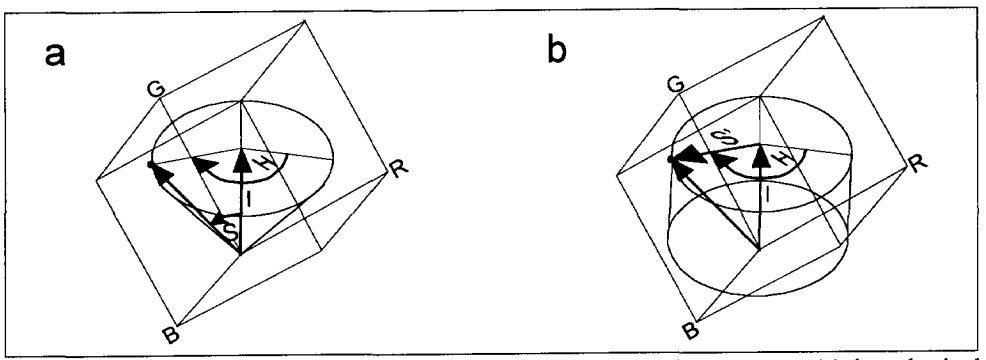

Figure 5.3 Geometrical representations of perceptual IHS colour spaces: (a) in spherical coordinates; (b) in cylindrical coordinates.

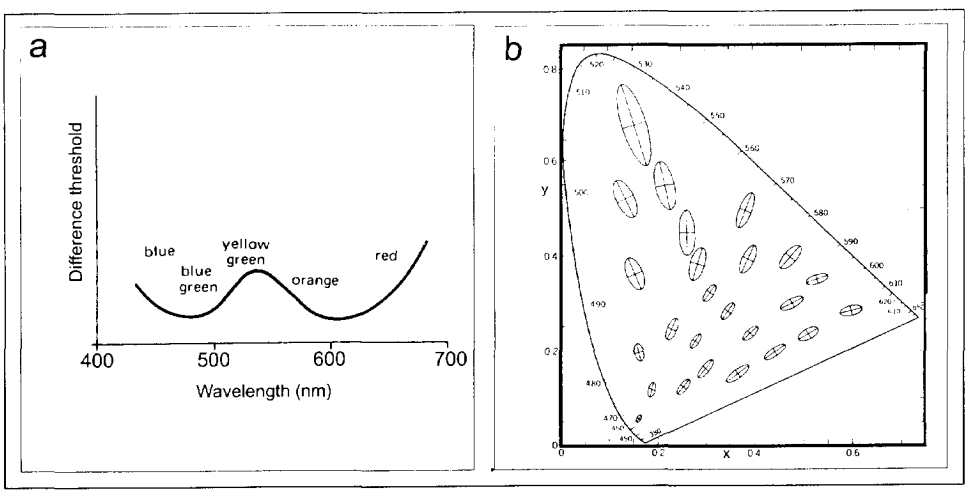

Figure 5.4 (a) Sensitivity of the human eye to chromaticity changes: (a) wavelength change necessary for a just noticeable difference (JND) in chromaticity as a function of wavelength; (b) Ellipses proportional to the change of a JND plotted on the chromaticity diagram after Wyszecki and Styles (1982).

Geometrically, the IHS colour space can be represented as a cone, parameterized in spherical coordinates (Figure 5.3(a)), where the vector length I along the achromatic line, defines intensity, the co-latitude S away from the achromatic line, defines saturation and the circumferential azimuth angle H, about the achromatic line defines hue (King *et al.*, 1984).

A commonly used alternative to this perceptual colour space is a cylindrical one (Figure 5.4 (b)). In this space the saturation coordinate is defined as the radial distance between a colour vector and the intensity axis. Although this radius does not correspond to one of the perceptual attributes of human colour vision, it is a convenient measure to define hue-invariant transformation by addition or subtraction of white light. Such a transformation has been compared with sun-illumination conditions of a natural scene, in which the saturation of the sunlit parts of the scene decreases such that they appear "washed out" (Milligan and Gunn, 1997).

In applying the IHS transform and interpreting the resulting composite images it is important to recognize that the IHS colour space provides only a crude approximation of a perceptual colour space. In a strictly uniform colour space the Euclidean distance between the colours approximates a perceptual difference between two colours (Niblack, 1986; Robertson and O'Callaghan, 1988). Because the sensitivity of the eye to chromaticity changes is dependent on wavelength (Figure 5.4(a)) equal numerical differences in hue and saturation in a geometrically defined colour space are only approximately equal to the perceived changes in hue and saturation. This non-uniform sensitivity of the eye is illustrated by the ellipses in the chromaticity diagram shown in Figure 5.4(b). The dimensions of the ellipses in Figure 5.4 are depicted in proportion to a just noticeable difference (JND, CIE, 1986). These are experimentally derived by measuring the sensitivity of the eye (averaged to a CIE standard observer) to changes in chromaticity (Niblack, 1986). This effect can also be appreciated by looking at the non-linear hue perception in the scale bars shown in Plates 7.1 and 7.2. Note for example the high variability in perceived hue differences per unit length in orange-red and low variability in the green segments of the scale bars.

Perceptually uniform colour spaces, such as the CIELUV space, (CIE, 1979) accommodate for these wavelength dependent differences (Robertson and O'Callaghan, 1988). A major disadvantage of a perceptually uniform colour space, however, is that they can not be universally applied. This is because the transformations from the coordinates of these colour spaces to the red, green and blue phosphors are dependent on the display device and therefore need to be obtained by calibration of the display device. When hard-copy colour images are the final interpretation product, additional calibrations are necessary to assure that the images are linearly mapped on the subtractive yellow, magenta, cyan (YMC) colour system of the printing device. Fortunately, for most image display applications the precise properties of the CIE colour spaces are not necessary, and hence not considered worth the effort (Niblack, 1986).

In the forthcoming sections, RGB and IHS spaces, their coordinates axes and the image channels that modulate these coordinates are capitalized (RGB, IHS). The notation of the vector defined by the digital numbers of three multispectral bands that refer to a single pixel or grid cell position is written as x_j for j = (1, 2, 3) or (x_1, x_2, x_3). The vector mapped in RGB space is annotated as (r, g, b).

5.4 Application of the IHS transform to the integration of multisource remotely sensed data

Although, as explained above, IHS space is in a strict sense not a uniform perceptual colour space, the relatively simple relations between IHS and RGB spaces, have made it a useful technique for integrating image data (Vrabel, 1996). Figure 5.5 shows a schematic diagram of the general processing method. First the image channels are mapped in IHS space, after which the composite image is accomplished by mapping the data in IHS space. The IHS channels are subsequently enhanced or replaced before they are transformed to RGB space for display. A number of integration methods to transform the image channels into the IHS coordinates exist. To meet the requirement of separate perception of the image channels, intensity and saturation are usually modulated individually. If multispectral data, such as gamma-ray spectrometry or multispectral data from optical sensors are involved, hue or hue and saturation in combination modulate the three multispectral channels, while intensity modulates a fourth image channel. This routine is known as intensity substitution (Shettigara, 1992) and involves the following processing steps: (1) transformation of three multispectral channels to IHS space, (2) substitution of the intensity by another image (i.e. the replacement image), (3) back-transformation of the H, S and replacement image to RGB space.

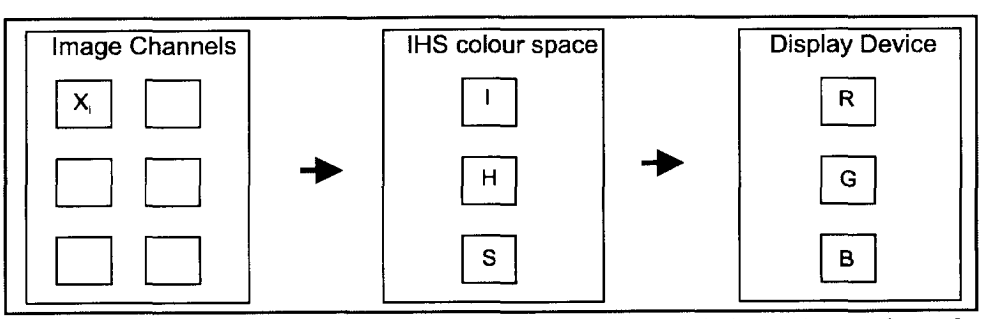

Figure 5.5 Schematic diagram illustrating the application of the IHS transform for generating integrated visualizations from multisource remotely sensed data.

This processing procedure can be expressed in a single transformation T that maps a 3-dimensional multispectral data vector (x_1, x_2, x_3) to a (r, g, b) vector in RGB space. In general form:

$$\begin{pmatrix} r \\ g \\ b \end{pmatrix} = T \begin{pmatrix} x_1 \\ x_2 \\ x_3 \end{pmatrix} \qquad [5.7]$$

T is a non-linear transformation that can be decomposed into a normalization for intensity three matrix transformations followed by a de-normalization with an intensity substitute i':

$$T = i'[A]^{-1}[E][A]i^{-1} \qquad [5.8]$$

$$i = \frac{1}{\sqrt{3}}(x_1 + x_2 + x_3) \qquad [5.9]$$

The matrix A defines a transformation that maps a multispectral data vector normalized for its intensity to the Cartesian IV_1V_2 equivalent of spherical IHS space (Shettigara, 1992; Figure 5.6):

$$[A] = \begin{bmatrix} \frac{2}{\sqrt{6}} & -\frac{1}{\sqrt{6}} & -\frac{1}{\sqrt{6}} \\ 0 & \frac{1}{\sqrt{2}} & -\frac{1}{\sqrt{2}} \\ \frac{1}{\sqrt{3}} & \frac{1}{\sqrt{3}} & \frac{1}{\sqrt{3}} \end{bmatrix} \qquad [5.10]$$

If A is applied without normalizing with i, (x_1, x_2, x_3) is mapped in cylindrical coordinates. Saturation and hue, as shown in Figure 5.5(b) are derived from v_1 and v_2 by:

$$s = \sqrt{v_1^{\,2} + v_2^{\,2}} \qquad [5.11]$$

$$h = \tan^{-1}\left(\frac{v_2}{v_1}\right) \qquad [5.12]$$

The matrix E in equation 5.8 is a diagonal scale matrix that defines a hue-invariant saturation enhancement:

$$[E] = \begin{bmatrix} e & 0 & 0 \\ 0 & e & 0 \\ 0 & 0 & 1 \end{bmatrix} \qquad [5.13]$$

Substitution of A, A^{-1} and E in equation 5.7 yields:

$$\begin{pmatrix} r \\ g \\ b \end{pmatrix} = \left(\frac{i'}{i}\right) \begin{bmatrix} \frac{1}{3}+\frac{2}{3}e & \frac{1}{3}-\frac{1}{3}e & \frac{1}{3}-\frac{1}{3}e \\ \frac{1}{3}-\frac{1}{3}e & \frac{1}{3}+\frac{2}{3}e & \frac{1}{3}-\frac{1}{3}e \\ \frac{1}{3}-\frac{1}{3}e & \frac{1}{3}-\frac{1}{3}e & \frac{1}{3}+\frac{2}{3}e \end{bmatrix} \begin{pmatrix} x_1 \\ x_2 \\ x_3 \end{pmatrix} \qquad [5.14]$$

Equation 5.14 directly maps a multispectral data vector (x_1, x_2, x_3) and the replacement intensity i′ to a (r, g, b) vector involving a user-defined saturation enhancement (e). This transformation provides a method for hue-invariant intensity substitution at reduced computational costs and provides a basis for optimizing the image enhancement with respect to the limiting properties of RGB space. Note that without saturation enhancement (e.g. e =1), the transformation matrix becomes the unity matrix, essentially demonstrating that intensity substitution by the IHS transform is identical to the Brovey or colour normalization CN transform. This is considered noteworthy, because the spherical IHS and Brovey transforms are repeatedly considered as distinct algorithms in comparative studies in the remote sensing literature.

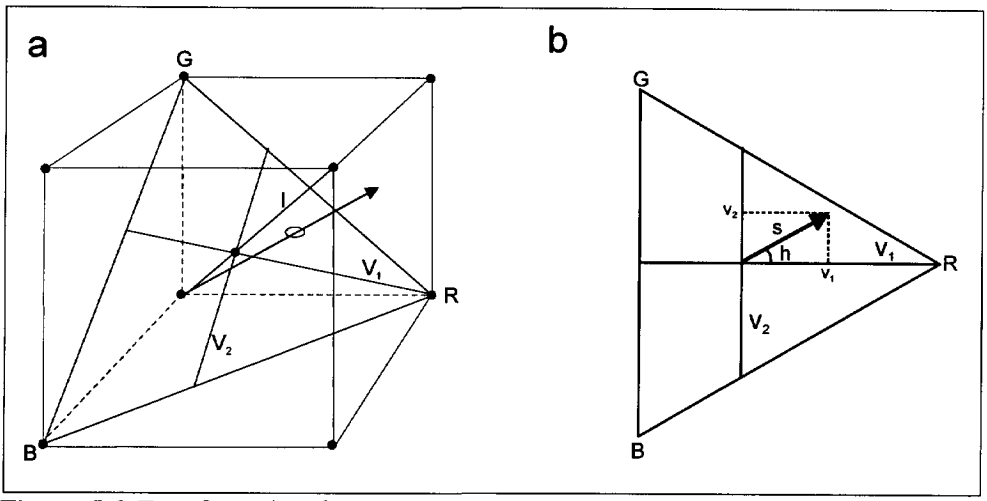

Figure 5.6 Transformation from RGB to IHS space; (a) transformation from r, g, b coordinates to Cartesian i, v_1,v_2 coordinates; (b) transformation from Cartesian v_1 and v_2 coordinates to polar s and h coordinates.

The IHS transformation can also be applied to integrate two or three images, each from a different sensor, such as combinations of optical, radar and geophysical images (Harris *et al.*, 1994; Paradella *et al.*, 1997). This is accomplished by first mapping two or three image channels in IHS space after which the H and S channels are transformed to RGB space, via:

$$v_1 = s\cos(h) \qquad [5.15]$$

$$v_2 = s\sin(h) \qquad [5.16]$$

The inverse matrix $[A]^{-1}$ is used to transform the image data set from V_1V_2I space to RGB space:

$$\begin{pmatrix} r \\ g \\ b \end{pmatrix} = \begin{pmatrix} \frac{2}{\sqrt{6}} & 0 & \frac{1}{\sqrt{3}} \\ -\frac{1}{\sqrt{6}} & \frac{1}{\sqrt{2}} & \frac{1}{\sqrt{3}} \\ -\frac{1}{\sqrt{6}} & -\frac{1}{\sqrt{2}} & \frac{1}{\sqrt{3}} \end{pmatrix} \begin{pmatrix} v_1 \\ v_2 \\ i \end{pmatrix} \qquad [5.17]$$

IHS composite images generated in this way are optimized for visual interpretation when the image of low spatial resolution or dominated by low spatial frequencies is mapped on hue and the image of high spatial resolution is mapped on intensity (Mussakowski *et al.*, 1992). This is because the spatial resolving power of the human eye for achromatic colours is about four times higher in comparison to the spatial resolving power for chromatic colours (Drury, 1993). The saturation channel can be used to modulate a third channel or can be set to a constant. Harris *et al.*, (1994) showed that the saturation level can be adapted to balance the hue and intensity contrasts. If the saturation level is low with respect to the maximum saturation possible, the data mapped on the intensity channel are enhanced at cost of chromatic contrast. If instead a high saturation value is used, the hue contrast is emphasized at cost of achromatic (i.e. intensity) contrast. Plates 7.1 and 7.2 provide typical examples of composite images generated by this technique.

Chromatic distortion and over-range pixels

The RGB channels obtained after applying equation 5.14 generally do not have numerical ranges for mapping the data directly to the [0-255] numerical range of the R, G and B primaries of a 24-bit display-device. Hence, the RGB image channels need to be scaled in order to optimize image display.

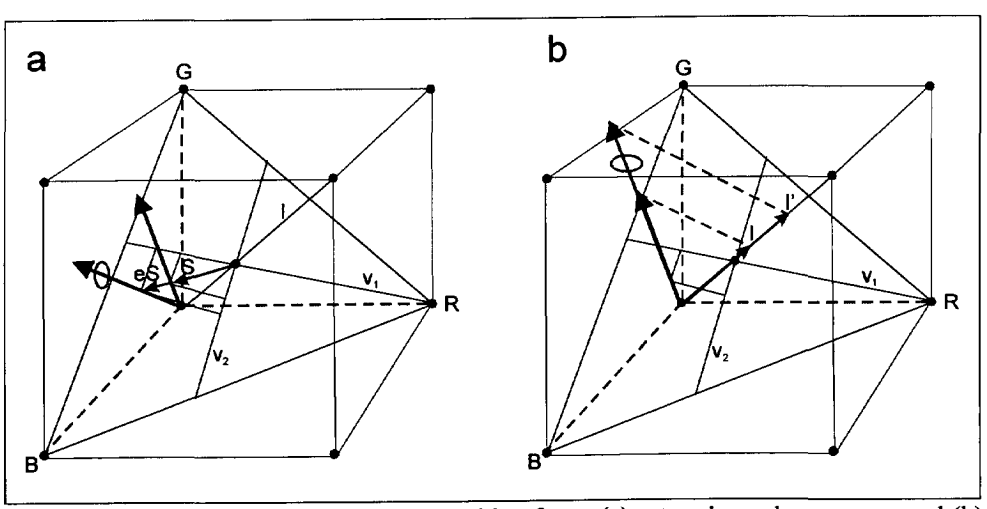

Figure 5.7 Over-range (r, g, b) vectors resulting from: (a) saturation enhancement, and (b) intensity substitution.

The byte range of 256 intensity levels for each of the RGB primaries of the display device is for convenience normalized to range from zero to one (0, 1/255, 2/255, ..., 255/255). Because the dynamic ranges of the in RGB space encoded image channels are generally not equal, the factors used to scale the image data along the axes of the three primaries are not necessarily constant. A major drawback of non-uniform scaling of merged image channels is that it results in chromatic (e.g. hue and saturation) distortion with respect to the spectral characteristics of the three multispectral channels. A better alternative that preserves the spectral balance with respect to these channels is to scale along intensity and saturation. However, in using this hue-invariant scaling, there is no a priori control on the proportion of (r, g, b) vectors that project within and outside the constraining faces of the RGB cube. These vectors will therefore be cut-off at the maximum range of the display, resulting in over-range pixels.

The two causes for over-range to occur are illustrated in Figure 5.7: A (r, g, b) vector, originally located within the ranges of the RGB cube, may project outside the RGB cube after applying saturation enhancement (Figure 5.7 (a)), or if the original intensity is replaced with an intensity of greater magnitude (Figure 5.7 (b)). Since in the conventional application of the IHS transformation there is no a priori control on the amount of pixels that exceed the limits of the RGB cube, both factors affect the perceived ranges in hue, saturation and intensity on the image display in an unpredictable manner. An ad-hoc solution is to adjust each of the RGB channels to the [0-1] range individually. As explained, above, however, independent scaling of the RGB channels results in chromatic distortions, degrading the perception of the relative spectral signatures of the multispectral data. Uniform scaling, preserves the spectral balance, but may result in poorly optimized displays with low chromatic and achromatic contrast. Clearly, there is a need for preserving spectral balance and being able to control saturation enhancement and the number of over-range pixels.

5.5 A hue-invariant transformation

A processing strategy is proposed such that the image data can be optimally mapped in RGB space without chromatic distortion. The advantages of this methodology are:

1. The image data are mapped independently on the attributes of the IHS colour space without chromatic distortion, providing a better intuitive visual perception of the imaged physical properties.

2. The input image channels are linearly mapped on the IHS colour coordinates. This implies that the increments of the multi-sensor data are in proportion to incremental changes in hue, saturation and intensity.

3. The amount and spatial distribution of over-range pixels are computed to optimize colour encoding of the display device. The saturation enhancement can be compromised against the percentage of over-range pixels.

Given a multispectral data vector x_j (j = 1,..,3) that does not extend along the intensity axis, and a replacement intensity image i', a limiting saturation enhancement factor e_{lim} can be computed for each pixel from 5.14, such that its corresponding (r, g, b) vector is just contained within the RGB cube:

$$\min(e_{jk}) = \min\left(\frac{i(c_{jk} - \frac{1}{\sqrt{3}}i')}{i'(x_j - \frac{1}{\sqrt{3}}i)}\right) \quad j=(1,2,3);\ k=(1,2) \qquad [5.18]$$

$$e_{jk} > 0, \quad i' > 0, \quad x_m - \frac{1}{\sqrt{3}}i \neq 0$$

where $c_{j,k}=1$ and $c_{j,k}=2$ are the limiting cube faces at respectively 0 and 1 positions along x_k.

The cumulative image histogram of all the minimum saturation factors (e.g. for each pixel) can be computed to select a saturation enhancement factor that compromises the saturation level of the display against the percentage of over-range pixels. For a particular minimum value of e, the spatial distribution of over range pixels can be mapped to verify if they are located within image patterns that are essential for the purpose of the interpretation. The saturation enhancement factor can then be adapted to assure that the loci of (r, g, b) vectors related to such image patterns remain within the RGB cube.

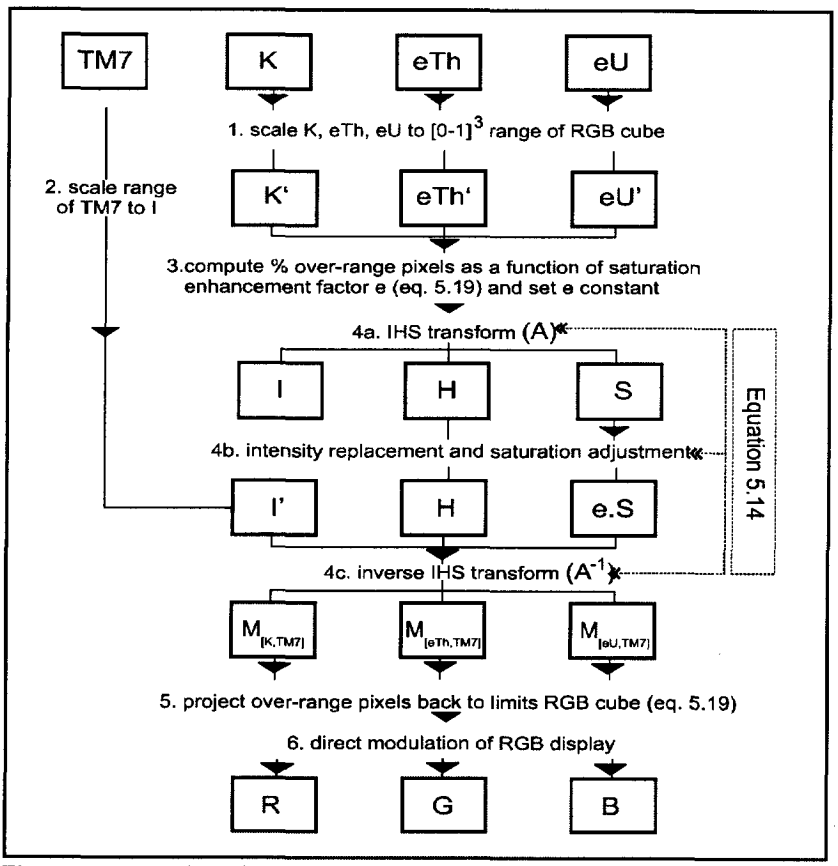

Figure 5.8 Hue-invariant method for intensity substitution with saturation enhancement control. The numbers in the diagram refer to the processing steps explained in the text.

Tracing back over-range pixels.

Any over-range pixel is cut-off at the maximum output range of the display device. The cut-off of over-range pixels leads to a chromatic distortion unless the (r, g, b) vector is achromatic (extending along the intensity axes) or one or more vector components equal to zero. A pastel yellow with rgb values (0.8,0.8,0.4), for example, is extended to rgb values (1.6,1.6,0.8) if the replacement intensity is twice the magnitude of the intensity. However, because of over-range of the r and g channels, on the display, the (r, g, b) vector will be cut-off at rgb values

(1,1,0.8). The magnitude of the blue component has increased with respect to the red and green components leading to a saturation distortion (from yellow to whitish yellow). The minimum saturation enhancement factor e_{lim} = 1/0.8. Multiplying the original (r, g, b) vector with the minimum saturation factor yields: (1,1,0.5). Note that although the back-traced vector is not in proportion to the replacement intensity, its extension along the original (r, g, b) vector indicates that its hue and saturation have been preserved. The back-traced (r', g', b') vector, after applying equation 5.14 and 5.18 can be simply computed for each (r, g, b) vector by:

$$\begin{pmatrix} r' \\ g' \\ b' \end{pmatrix} = \frac{1}{\max(r,g,b)} \begin{pmatrix} r \\ g \\ b \end{pmatrix} \quad \text{for any } e_{lim} \leq e_{cst} \qquad [5.19]$$

where e_{lim} and e_{cst} are respectively the limiting saturation enhancement factors computed for each individual pixel by equation 5.18 and the constant user-defined saturation enhancement factor applied to all pixels in equation 5.14.

Image processing example 1

A subset of northeastern Alberta data set acquired over the Arch Lake and Slave granites was used to compare the hue-invariant intensity substitution method with the conventional method in which the merged channels are scaled independently along the R, G, B primaries. The image channels and the results of the experiment are shown in Plate 5.1. The K, eTh and eU gamma-ray spectrometry channels were selected as the multispectral data set x_j. Landsat TM band 7, was used as replacement intensity i'. The gamma-ray spectrometry data were registered on Landsat TM band 7 on a 30-meter pixel (see chapter 3). This data combination was particularly useful for geological mapping, as it allowed interpreting the geochemical information of the K, eTh and eU gamma-ray spectrometry grids in the context of structural details expressed as linear features in TM band 7. This band, due to its low sensitivity to atmospheric noise, appeared superior for delineating geological structure.

This data set was also considered ideal for testing both methods, as the relatively homogeneous gamma-ray spectrometry responses over the plutons, yields homogeneous patterns on the original colour composite (Plate 5.1(B)) so that chromatic distortions in the results would become readily apparent. Moreover,

TM7 also showed low-spatial frequencies related to forest burns (high reflectance) versus non-burnt areas (low reflectance) which allowed to study interference with the multispectral responses of the gamma-ray data.

First a colour composite was generated from the gamma-ray spectrometry channels in which the K, eTh and eU channels were assigned to the R,G and B channels of the display (Plate 5.1(A)). A linear stretch was used to scale each channel to a [0-1] range. The linear stretch assured that the hue and saturation variations of the colour composite image could be visually matched to the hue and saturation variations of ternary legends (see for example Plate 3.3). The hue and saturation of the composite image therefore still reflect the relative radioelement concentrations. TM band 7 was also linearly scaled with a two-sided cut-off at 2,5 standard deviations to optimize contrast (step 2).

The percentage of over-range pixels was computed as a function of a variable saturation enhancement factor (step 3). The cumulative histogram of the saturation enhancement factors is shown in Figure 5.9. Two enhancement factors were selected: e = 1 and e =1.5 yielding respectively 2 and 5 % over-range. The scaled K, eTh and eU channels were transformed to IHS space, the intensity was substituted for the contrast enhanced TM7 and together with the H and S images transformed back to RGB space.

These three transformations were combined in a single transformation (equation 5.14) yielding three merged RGB image channels (step 4). The over-range pixels were projected back to the limiting faces of the RGB cube using equation 5.20 (step 5). The merged image channels $M_{[K,TM7]}$ $M_{[eTh,TM7]}$ $M_{[eU,TM7]}$ were directly displayed in RGB space and printed on a thermal laserjet printer (step 6).

Comparing Plates 5.1(A) and 5.1(C), reveals that the overall spectral balance between the colour composite and the IHS composite image has been preserved. This was expected considering that the method uniformly modulates S and H. Plate 5.1(D) shows the results of intensity substitution by the conventional method in which the merged image channels are scaled independently. This has resulted in a marked hue-shift towards green and magenta. The chromatic distortion resulted from the relative changes in the dynamic ranges from approximately (1:9:2) for the %K, ppm eTh and ppm eU channels to (1: 3:3) for the pixel values of the merged channels. As a consequence of the independent scaling applied to the merged channels in RGB space, the K and eU channels were scaled about 3 respectively 1.5 times less relative to the eTh channel in comparison to the scaling of the K, eTh and eU channels that was used to generate the ternary radioelement map shown in Plate 5.1(A).

Plate 5.1(E) shows the results of the hue-invariant transformation using a saturation enhancement factor of 1.5. This saturation enhancement leads to a better perception of hue contrast, at cost of perceived intensity contrast. Figure 5.9 shows a cumulative graph of over-range pixels as a function of the saturation enhancement factor e. Note that e needs to be about 0.4 to fit all the (r, g, b) vectors within the RGB cube. If e = 1 (i.e. no saturation enhancement), 2% of the pixels are over-range, corresponding to the image shown on Plate 5.1(C). For e = 1.5, corresponding to the image shown in Plate 5.1(E) about 5 % of the pixels are over-range (Plate 5.1(F)). Because these pixels have been projected back to the limiting faces of the RGB cube, their hue values have been preserved.

Many over-range pixels shown on Plate 5.1(F) are corresponding to lakes that do not degrade the interpretation of the land surface. The large patterns of over-range pixels in the upper left corner of Plate 5.1 (F), however, are related to bright pixels from land. The ranges in intensity and saturation of those pixels have been strongly reduced and are not any longer modulated in proportion to the dynamic ranges of the TM and radioelement grids. The hue variation of the saturation-enhanced image, however, has remained proportional to relative radioelement concentrations.

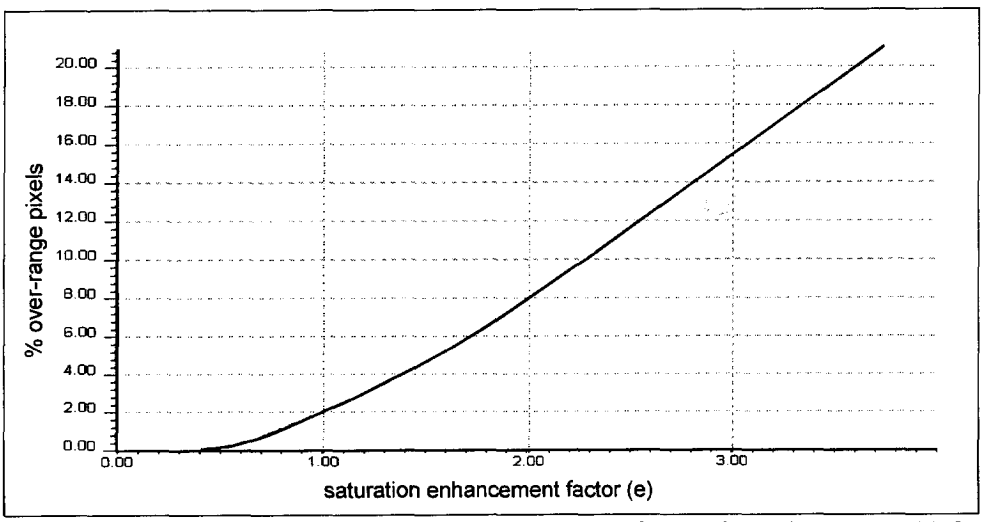

Figure 5.9 Percentage of over-range pixels as a function of saturation enhancement (e) for image integration example (1).

5.6 Implications of using the cylindrical or spherical IHS transform

While both the cylindrical and spherical IHS transforms have been commonly applied (Harris *et al.*, 1990), their effects on the resulting IHS composite images have not been considered. This section discusses the implications of the differences between both transforms with respect to image integration results. To gain geometrical insight in the properties of the cylindrical and spherical IHS transforms it is illustrative to consider the effects of using both transforms for intensity substitution on one (r, g, b) vector (Figure 5.10). The following differences become apparent when comparing the spherical (Figure 5.10(a)) and the cylindrical transforms (Figure 5.10(b)):

1. Both transforms are hue invariant but only the spherical transform is saturation invariant. If the saturation is kept constant varying intensity and hue defines a cone with I as the central axis. In the spherical transform the vector changes length parallel to itself such that the proportions between (r, g, b) values remain constant. A (r, g, b) vector subject to the cylindrical transform maintains equal distance to the intensity axis. This geometrically illustrates the addition or subtraction of white light, which alters the saturation level.

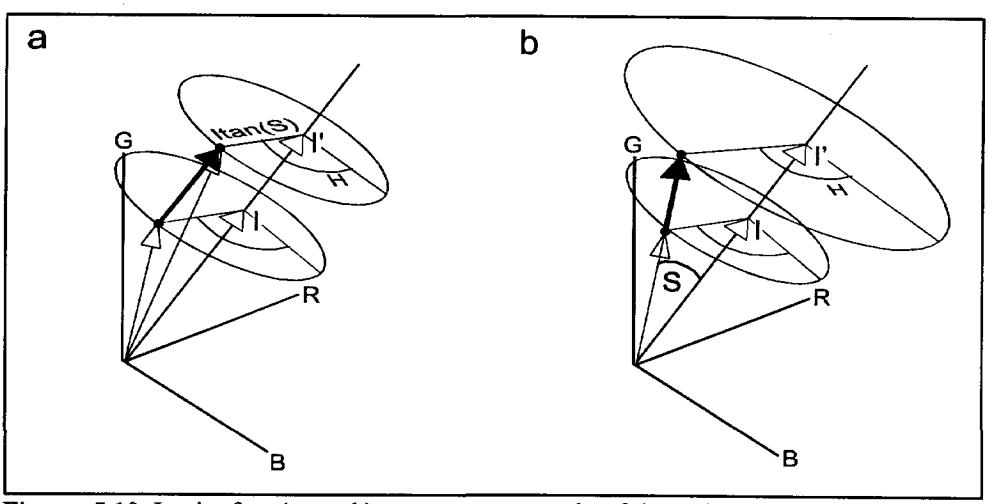

Figure 5.10 Loci of a (r, g, b) vector as a result of intensity substitution with: (a) cylindrical IHS transform and (b) spherical IHS transform.

2. In the cylindrical transform no convergence towards the origin occurs such that over-range may occur in two opposite intensity-parallel directions. In the spherical transform, (r, g, b) vectors decreasing in intensity all converge towards the origin. For large substituted intensity the (r, g, b) vectors diverge in dependence of the saturation and easily project outside the RGB cube.

Mapping the spatial distribution of over-range pixels

It was shown in section 5.4 that over-range constrains the enhancement of both the intensity substitute and the multispectral data in the final result. This section shows how the spatial distribution of over-range pixels for the spherical and cylindrical IHS transform can be computed. This allows assessing how both integration methods utilize the available ranges in intensity and saturation within the constraints of RGB space.

If no saturation enhancement is applied, the ratio i`/i and the distance of a (r, g, b) vector to the faces of the RGB cube controls if over-range occurs. For each multispectral data vector $x_j$, a maximum replacement intensity $i`_{lim}$ can be computed such that the locus of the resulting (r, g, b) vector remains within the RGB cube:

$$i_{lim} = \min\left(\frac{1}{x_j}\right) i \quad \text{for} \quad j=(1,2,3) \quad x_j > 0 \qquad [5.20]$$

Over-range pixels that project outside the RGB cube can then be mapped in a binary image B_{sph}:

$$B_{sph} = 1 \quad \text{for} \quad i'-i_{lim} > 0$$
$$B_{sph} = 0 \quad \text{for} \quad i'-i_{lim} \leq 0 \qquad [5.21]$$

The (r, g, b) vector resulting from applying the cylindrical transform on the multispectral data vector is defined as:

Contrary to the spherical transform, the resulting (r, g, b) vector may project through any of the six faces of the RGB cube. Therefore two limiting replacement intensities are defined to compute over-range pixels:

$$\begin{pmatrix} r \\ g \\ b \end{pmatrix} = \begin{pmatrix} x_1 \\ x_2 \\ x_3 \end{pmatrix} + \frac{1}{\sqrt{3}}(i'-i) \qquad [5.22]$$

$$i_{lim} = \sqrt{3}\min(c_k - x_j) + i \quad \text{for} \quad j=(1,2,3) \quad k=(1,2) \qquad [5.23]$$

where $c_{j,k=1}$ and $c_{j,k=2}$ are the limiting cube faces at respectively 0 or 1 position along x_j.

The binary image showing the over-range pixels is derived by:

$$\begin{aligned} B_{cyl} &= 1 \quad \text{for} \quad i'-i_{lim,k=2} > 0 \quad \vee \quad i'-i_{lim,k=1} < 0 \\ B_{cyl} &= 0 \quad \text{for} \quad i'-i_{lim,k=2} \leq 0 \quad \vee \quad i'-i_{lim,k=1} \geq 0 \end{aligned} \qquad [5.24]$$

The binary images B_{sph} and B_{cyl} computed by equations 5.21 and 5.24 display the amount and spatial distribution of over-range pixels for a given multispectral data set and replacement intensity. Such images can be used as criteria to choose between one of the two IHS transformations. If, for example a substantial higher percentage of over-range pixels with one of the methods is obtained, preference should be given to the other method.

Image processing example 2

The data combination, presented in the first image integration experiment, was used to evaluate the implications of employing the cylindrical or spherical IHS transforms. The intensity of the radioelement grids was again substituted for TM7 applying using both IHS transforms (Plate 5.2(A) and 5.2(B)). The same procedures were repeated but instead of completely substituting the intensity channel, the sum of Landsat TM 7 and the intensity channel was substituted (Plate 5.2(C) and Plate 5.2(D)) retaining some of the total radioelement response in the final result. Figure 5.11 shows binary images of the limiting intensities for the four intensity substitutions.

Comparing Plate 5.2(A) with Plate 5.2(B) and Figure 5.11(a) with 5.11(b) appears, as expected, to result in identical hue distributions but different saturation and intensity modulations. The colours on Plate 5.2(A) are more saturated in

comparison to the colours of Plate 5.2(B). This is clear in forest burn areas where on Plate 5.2(B) saturation has been reduced at cost of the high intensity values modulated by the Landsat TM7 image. The cylindrical transform resulted in the greatest number of over-range pixels which have either low or high replacement intensities as over-range occurs on opposite ends of the intensity axis. Over-range occurs over lakes for low intensities, whereas high intensity over-range pixels are related to forest burns. Over-range pixels related to low intensity values over lakes is however not aversely affecting the result as they are irrelevant for mapping the land surface. This exemplifies the need to map the origin and spatial distribution of over-range pixels. Over-range pixels with high intensity values, however, mostly occur on Plate 5.2(A) resulting for those pixels in a degraded hue and saturation contrast.

Comparing the images produced by the two methods confirms that the cylindrical transform yields a higher intensity contrast. This is particularly evident in the Slave pluton where far more structural details can be observed. These structural details, relating to fracture and fault patterns, are shown as bright pixels on the TM image.

The amount of over-range pixels can be effectively reduced by combining the TM image with the intensity of the gamma-ray spectrometry images, as shown by comparing Figures 5.11(a) and 5.11(b) with Figures 5.11(c) and 5.11(d). Because a component of the original intensity is retained in the replacement intensity, the low wave-number intensity contrast related to burnt versus non-burnt areas in the TM image, which initially obscured the continuity of the thorium rich core in the Arch Lake pluton (green and yellow hues), is better preserved. This goes obviously at cost of the rendition of detail from the higher spatial resolution of TM7. Comparing Plate 5.2(C) and Plate 5.2(D) shows that the IHS composite image generated by the cylindrical transform better enhances the structural details expressed on TM7.

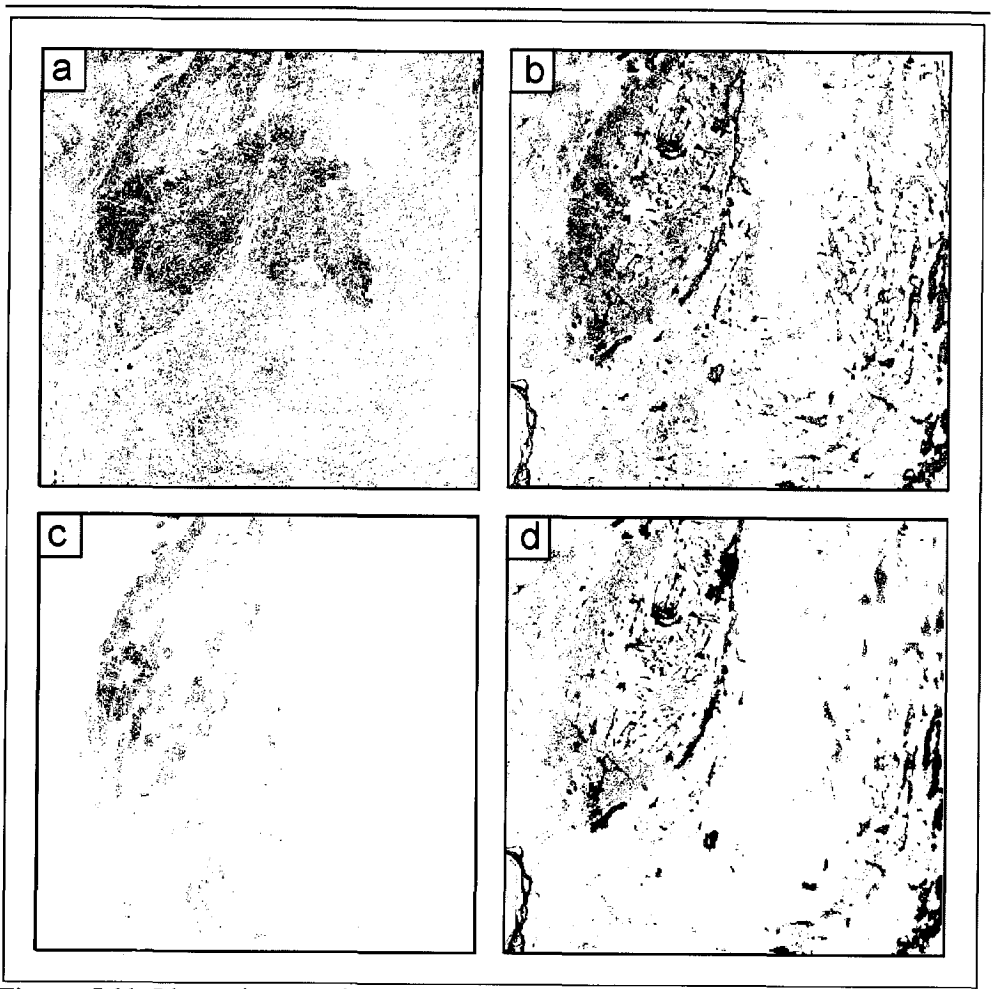

Figure 5.11 Binary images showing over-range pixels (black) obtained from image integration example (2) of which the results are shown in Plate 5.2; a) for Plate 5.2(A); b) for Plate 5.2(B); c) for Plate 5.2(C); and d) for Plate 5.2(D).

5.7 Summary and conclusions

Colour coding techniques are indispensable methods in the visualization of multisource remotely sensed data. It can currently be considered, however, to be the weakest link in the chain from data acquisition, corrections and calibration to interpretation. The criteria to use colour space transformations for integration and

display are often not clearly defined and based on arbitrary enhancement approaches leading to a poorly optimized and distorted visual representations. A method for intensity substitution has been presented, in which two imposed criteria assure that the perceived IHS attributes are proportional to the spectral characteristics of the image data:

1. To maximally spread the data within the RGB cube without inducing spectral distortion, the only enhancement permitted is independent linear scaling of intensity and saturation.

2. After enhancement of intensity and saturation, the data should be mapped in RGB space by applying the same linear scaling function to each channel.

If these two criteria are respected, the multispectral channels uniformly modulate the chromatic variation (i.e. hue and saturation variations), and can therefore be interpreted in proportion to relative units of measurement, whereas the intensity variations can be modulated in absolute units of measurement. In addition the method allows interpreting chromatic contrast of the IHS composite image with respect to a RGB colour composite of the three input multispectral channels, which facilitates visual interpretation.

Because, the scaling of the data is along the attributes of a perceptual space, careful control of over-range with respect to the display dependent RGB space (i.e. colour cube) is required. This problem has been tackled by computing the percentage and mapping the spatial distribution of over-range pixels as a function of saturation enhancement and tracing over-range pixels to the limits of the RGB space. A general guideline for a percentage of over-range pixels to obtain a composite image with a good colour spread and intensity contrast is difficult to define because it depends on the spatial distribution and if the over-range pixels are related to image patterns of interest. In practice is has been found that in an image with a good colour spread, 1-2% percent of the pixels are over-range (Robertson and O'Callaghan, 1988).

Many of the commonly applied enhancement procedures do not meet the conditions of undistorted and uniform modulation. For example, in histogram equalization the RGB channels are scaled in proportion to their frequency distribution and therefore do not uniformly relate to IHS coordinates. Also independent scaling of the RGB channels to optimally spread data within the RGB cube, leads to chromatic distortion. These enhancements are not recommended when increments in hue, saturation and intensity need to uniformly modulate

variations in the input data. A better alternative for preserving hue and intensity is saturation enhancement. Contrary to histogram equalization, saturation enhancement has the additional advantage of effective expanding highly correlated data in RGB space (Gillespie *et al.*, 1986).

A commonly implemented normalization to maximize the utilization of the volume constrained by the RGB cube is to normalize the saturation for the maximum realizable saturation for a particular hue. This normalization procedure maps vectors of constant saturation on a hexcone instead of on a cone. Such a procedure is not recommended when the IHS transform is used to integrate multi-source remotely sensed data, as the cyclic variation of saturation with hue, may lead to visible discontinuities in the final result.

If the perception of variations in hue and saturation need to be truly uniform (for example, when small colour differences around contrasting hues need to uniformly represent incremental variations in the input data) a uniform perceptual colour space that is independent on the display device should be employed. The transformations involved, however, are computationally demanding and not universally applicable, because careful measurement and calibration of the display device is required. This also implies that variations in RGB modulation of different display-devices are ignored in the application of the IHS transform so that the uniform modulation referred to in this chapter is with respect to RGB encoding and not to the colour perception of the observer.

Both the cylindrical and spherical IHS transforms are commonly employed for image fusion. The implications of using the cylindrical and spherical IHS transform have been considered. Both methods are hue-invariant provided that intensity and saturation are scaled independently. The cylindrical transform, at cost of chromatic contrast of high intensity pixels, provides better enhancement of the image that modulates intensity. This property can be exploited in situations where structural details shown on the high-resolution intensity substitute need to be optimally enhanced.

PART III INTEGRATION STUDIES

6

INTEGRATION OF MULTISOURCE REMOTELY SENSED DATA FOR MAPPING THE COMPOSITION AND STRUCTURE OF GRANITOIDS: THE ARCH LAKE GRANITE (1.94 GA.)*

ABSTRACT

Multisource remotely sensed data acquired over the Arch Lake granite display compositional and structural patterns not previously identified by geological field mapping. An integrated analysis of gamma-ray spectrometry, aeromagnetic, Landsat TM, geochemical and structural data was conducted to map and analyze these patterns and to obtain insight in their genetic significance. Image enhancement of the K, eTh and eU grids reveals that the Arch Lake granite is zoned in a complex manner with a Th-rich centre and Th-rich, locally U-rich outer margins. The Th-rich centre broadly corresponds to an increase in Zr and TiO_2 reflecting a mineralogical association between biotite, monazite, zircon and Fe-oxides. The negative trend of this Th-rich mineralogical association with SiO_2 wt% is not consistent with normally zoned plutons becoming increasingly felsic inwards. This association in combination with the spatially and spectrally distinct bimodal variation in K and eTh demonstrates that the Arch Lake granite is a composite intrusion. An IHS composite image of the K, eTh and eU grids and high-pass filtered Landsat TM7 with an overlay of mineral foliation data allowed interpreting the zonation with respect to internal structures. The radioelement domains are broadly parallel to the trend lines of a solid state mineral foliation outlining a synformal structure that was formed by solid state flow during and after emplacement. ESE-WNW to E-W striking offsets in the residual magnetic anomaly and the zonation patterns in dextral apparent sense correspond to lineaments on the residual aeromagnetic and TM7 images. Although the kinematic significance of these offsets need to be further field-verified, locally observed mylonite and cataclastic fabrics suggests that they are multistage shear zones active from medium-grade ductile to sub-greenschist grade brittle conditions.

---

* Parts of this chapter are based on the publication:

Schetselaar, E.M., 2000, Mapping the compositional and structural patterns of a granite batholith by integrating gamma-ray spectrometry, Landsat TM and geological data, The Arch Lake granite (1.94 Ga.). International Journal of Remote Sensing (submitted).

6.1 Introduction

Digital image enhancement and integration of multi-source remotely sensed data have shown to be a useful tool for reconnaissance geological mapping in several geologic and physiographic settings (Chavez and Bowell, 1988; Harris and Murray, 1990; Yésou *et al.*, 1993; Harris *et al.*, 1994; Paradella *et al.*, 1997; Nash *et al.*, 1996; Andersen and Nash, 1997; among others). The potential of systematically incorporating field data sets in such integrated analysis in focused geological studies, however, has been little exploited. Such analyses should ideally lead to a better recognition and classification of geological features and enhance insight in the underlying geological processes.

In this chapter an integrated analysis of remotely sensed and field data is presented that aims at the analysis of a zonation pattern within the southern sector of the Arch Lake granite intrusion. This zonation was previously identified in the interpretation of the ternary radioelement map generated from airborne gamma-ray spectrometry data (Plate 3.3, Figure 3.3). The ternary radioelement maps show that the Arch Lake granite is zoned in a complex manner. Th-rich domains are enclosed within a low Th K-rich domain, whereas the eastern and western margins of the batholith are in part Th-rich with local U anomalies (see Chapter 3). Airborne K, eTh and eU data within the mapped outline of the Arch Lake pluton were selectively enhanced and integrated with magnetic, Landsat TM, geochemical and structural data to increase insight in the origin of the zoning pattern and its modification by post- emplacement deformation. Because this internal zoning was not recognized in previous field mapping campaigns, the Arch Lake granite provided an interesting target for a focused remote sensing study.

Ternary radioelement maps of airborne gamma-ray spectrometry surveys acquired over exposed granitoid intrusions commonly show internal zoning in radioelements (Ford and O'Reilly, 1985; Broome *et al.*, 1987; Harris and Murray, 1990; Goossens, 1992; Dickson and Scott, 1997). These radioelement zonations have been interpreted to reflect magmatic differentiation, *sensu lato* (Charbonneau, 1991; Welman, 1998), fractionation in combination with segregation of intercumulus melt (Goossens, 1992), hydrothermal enrichment (Charbonneau, 1991) or a combination of the above processes. Understanding which processes gave rise to the radioelement zonation and associated mineralogical variations has implications in the search for mineralizations of U, Sn, W, Mo, Cu-Au and rare earth elements (Ford and O'Reilly, 1985; Goossens, 1992; Dickson and Scott, 1997).

Because the often subtle compositional variations within large intrusions are not easily resolved by traditional field mapping, remote sensing provides relevant tools for cost-effectively mapping granitoid batholiths (Wellman, 1998). The genetic origins of radioelement zoning patterns on gamma-ray spectrometry data, on the other hand, are difficult to interpret without supporting evidence from field data. Particularly geochemical analysis of samples along profiles normal to zoning patterns are essential, as they provide evidence for the causal compositional and petrogenetic trends (Stephens and Halliday, 1980; Atherton, 1981; Michael, 1984; Sawka *et al.*, 1990; Pitcher, 1993, among others).

The results of this integration study were not expected to provide such petrogenetic evidence. This was not a feasible task, considering that: (a) the available ground data were collected before these patterns were identified and (b) geochemical rock sampling and mapping campaigns within the Arch Lake granite were not within the scope of the project that supported the fieldwork of the author (Macqueen, 1997). Instead, the aim of this study was to investigate the potential of systematically integrating and analyzing multi-source remotely sensed data in mapping the internal compositional and structural patterns within the batholith and to verify the geological significance of the results on the basis of previously collected field data. Local field checks, however, were carried out to investigate some of the structural patterns obtained from the integrated enhancement of the gamma-ray spectrometry and Landsat TM data. A schematic flow chart of the implemented integration procedures is shown in Figure 6.1 where the numbered components are described in sequential order from Sections 6.4 to 6.9. These integration procedures are considered applicable to granite batholith mapping in general, provided that comparable data sets are available. In arid and semi-arid study areas with limited vegetation cover, additional contributions to mapping the composition of granitoid intrusions may be derived from multispectral image data acquired by satellites such as Landsat Thematic Mapper. Spectral analyses of Landsat TM data have proven to be applicable in mapping Fe-oxide and hydroxyl bearing minerals (Goetz and Rowan, 1981). The recently launched advanced spaceborne thermal emission and reflection radiometer ASTER provides increased potential for mapping compositional variations in granites. This system acquires multispectral data in the thermal range of the electromagnetic spectrum that covers diagnostic absorption features in the reflectance spectrum of silicate minerals (Abrams and Hook, 1995).

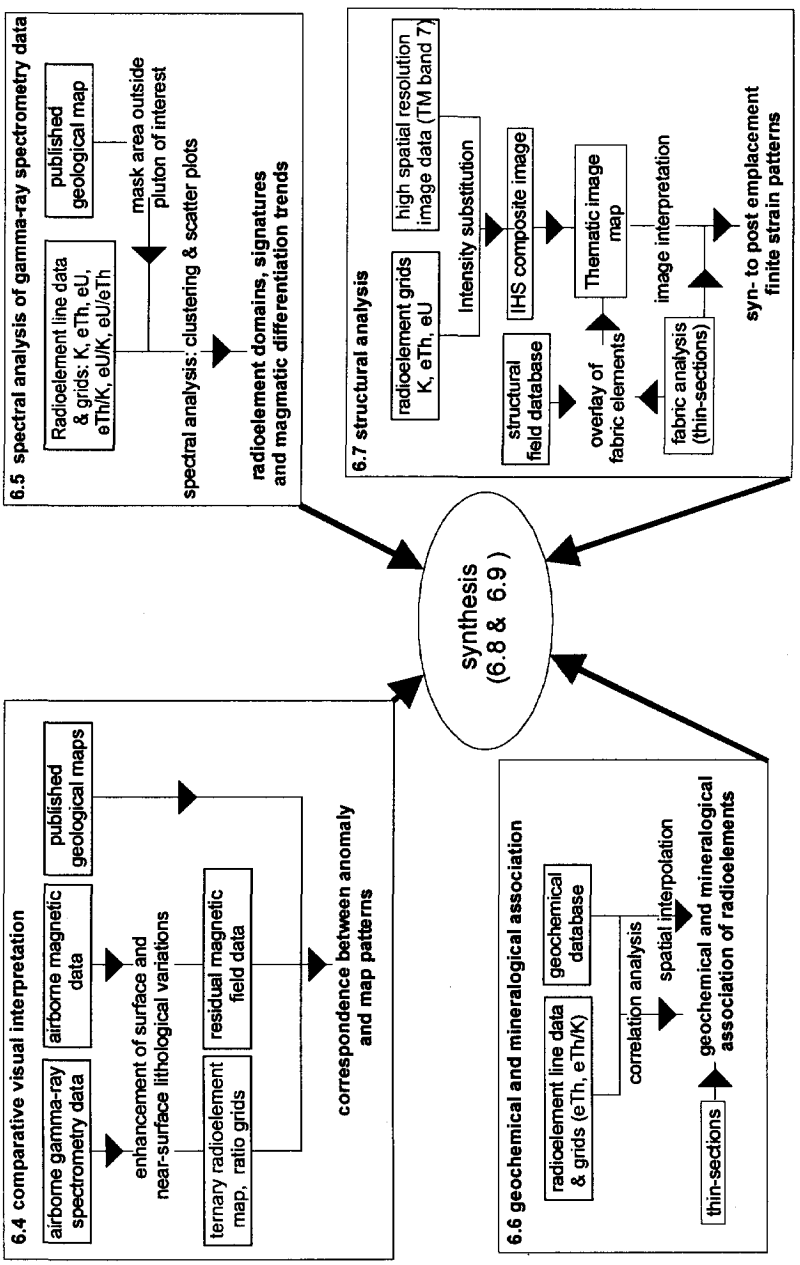

Figure 6.1 Integration strategy for the enhancement and interpretation of compositional and structural patterns in the Arch Lake granite

6.2 Geological observations

The magnetite bearing Arch Lake granite is one of the major S-type granites of the Taltson Magmatic Zone (TMZ) that extends as a 15 to 5 km wide and 100 km long northward tapering intrusive body, east of the petrographically similar but ilmenite-bearing Konth granite (Figure 6.2). The margins of the batholith are deformed in the Leland Lake (LLSZ) and Charles Lake (CLSZ) shear zones (McDonough *et al.*, 1995).

Further north, east of the Gagnon Lake shear zone (GLSZ) a mineralogically and texturally diverse assemblage of granites has been tentatively correlated with the Arch Lake granite on the basis of similar monazite ages and the presence of megacrystic phases (Berman and Bostock, 1997; Figure 6.2).

The Konth and Arch Lake granites are syeno- to monzogranites with up to 25 % 5 to 15 mm by 10 to 30 mm alkali feldspar megacrysts aligned in the foliation plane. Their peraluminous mineral content, however, differs due to the presence of spinel, cordierite, garnet and virtual absence of primary biotite in the Konth granite (Berman and Bostock, 1997) and the presence of primary biotite and accessory amounts of garnet in the Arch Lake granite (Godfrey and Langenberg, 1987; McDonough *et al.*, 1993). Both the Konth and Arch Lake batholiths contain irregular enclaves of Slave-like granite ranging from 200 meters to 5 km in length. Enclaves of paragneiss of variable dimensions are abundant in the Konth batholith whereas only a few small enclaves have been found in the Arch Lake granite (Figure 6.2; Godfrey and Langenberg, 1987; Berman and Bostock, 1997). Minor bodies of Arch Lake granite occur as elongate intrusive bodies along the periphery and within the Slave granite and as a few strongly foliated to mylonitized bodies, aligned along the foliation of the CLSZ.

On the basis of geothermobarometric calculations and the distribution of spinel and quartz in contact, Berman and Bostock (1997) concluded that the formation and emplacement of the Konth granite occurred at peak metamorphic conditions in the TMZ (920 – 1040° C and 6.9 + 0.9 kbar on the bases of garnet-orthopyroxene thermometry). Together with the virtual absence of primary biotite in the Konth granite and inclusion-free euhedral garnet in leucosome within paragneiss (Grover *et al.*, 1997), the ultra-high temperatures suggest that the S-type granites in the TMZ were produced by dehydration melting of pelitic rocks (Patiño-Douce and Johnston, 1991). Chacko (1997) came to similar conclusions on the basis of isotope studies of the Slave granite from the western edge of the exposed Alberta Shield.

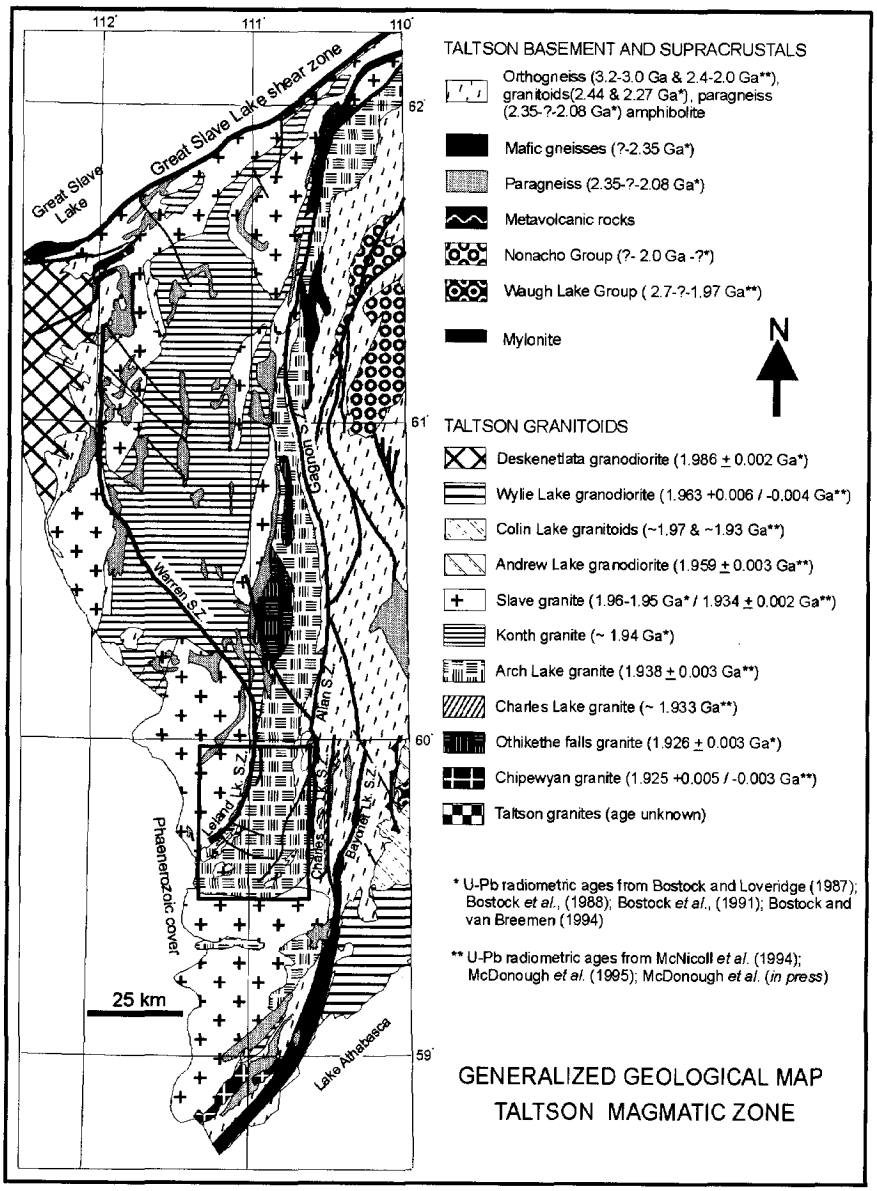

Figure 6.2 Generalized map compilation of the exposed Taltson Magmatic Zone after Berman and Bostock (1997) for the Northwest Territories and after McDonough *et al.* (1995) for Alberta. The box indicates the interpreted sector of the Arch Lake batholith.

One of the explanations for the high temperatures in the TMZ is the increased production of radiogenic heat due to the greater abundance of radiogenic isotopes in the Paleoproterozoic compared to the present-day crustal rocks. The inferred radiogenic origin for the high temperatures in the TMZ has also a local connotation, as one of the most prominent radioactivity anomalies of the Canadian Shield, exceeding 15 μR/h and Th exceeding 200 ppm (Charbonneau, 1991) is centered on the Konth granite. This anomaly shows a striking correspondence to the distribution of spinel and quartz in contact and modeled peak temperatures that exceed 900° C.

Because peraluminous granulite facies mineral assemblages are lacking in the Arch Lake granite, its formation and emplacement has previously been interpreted to have occurred at amphibolite facies metamorphic conditions (Nielsen *et al.*, 1981). Rare igneous orthopyroxene and quartz-spinel contact relations within the western margin of the batholith, the abundance of mesoperthite (Berman and Bostock, 1997) and the genetic association with the Konth granite, however, strongly suggest that the Arch Lake granite also formed at granulite-facies metamorphic conditions. One explanation of the overall lack of anhydrous granulite-facies minerals in the strongly deformed Arch Lake granite is that these minerals have been completely consumed by retrograde reactions in the period of protracted cooling and deformation (Plint and McDonough, 1995) that followed peak metamorphic conditions. The presence of primary biotite in the Slave and Arch Lake granites indicates nonetheless lower temperatures and/or increased H_2O activity during their formation and emplacement in comparison to the Konth granite (Berman and Bostock, 1997). A somewhat lower emplacement temperature of these granites is consistent with geothermobarometric calculations of paragneiss assemblages in the Slave granite (820-870° C, 6.3-6.5 kb from garnet-cordierite Fe-Mg exchange equilibria (Grover *et al.*, 1997). Whereas an increase in H_2O activity would offer an explanation for the above mentioned differences in Fe-oxide mineralogy between the Arch Lake and Konth granites (Charbonneau, 1991).

The southern sector of the Arch Lake batholith that is exposed in northeastern Alberta has been previously mapped on 1:31,680 scale along east-west traverses spaced at 1 to 2 kilometer intervals (Godfrey and Langenberg, 1987). A subordinate transitional phase (unit 162) to the common megacrystic phase (unit 161) was recognized in the field, containing fewer (5 percent) and smaller megacrysts (about 15 mm long) and somewhat less biotite (Godfrey and Langenberg, 1987). Due to the subtle transitional nature of this phase, it has been labeled but does no appear as distinct units on the map published by Godfrey and

Langenberg (1987). On the bases of the map distribution, this phase appears predominantly along the large enclaves of Slave granite.

The Slave and Arch Lake granites have been analyzed for major and trace elements as part of a petrological study of the Alberta Shield (Goff *et al.*,1986). Both the Slave and Arch Lake granites are calc-alkaline peraluminous suites with moderate K content. Their ACF and peraluminous indices classify both units as S-type granite. The distribution of the Na/K ratio, however, straddles the boundary between the I-type and S-type signatures (Goff *et al.*, 1986). Major and trace element trends, modeling of Ba, Rb and Sr, normative feldspar compositions as well as gneissic xenoliths, indicate that the Slave and Arch Lake granites were produced by partial melting of the gneissic rocks of the Taltson Basement Complex at granulite facies metamorphic conditions. R-mode factor analysis suggests that the Nb, Y and Zr compositions of the Slave and Arch Lake granites were directly inherited from the heterogeneity of the gneissic progenitor (Goff *et al.*, 1986). Recent isotope studies (Chacko and Creaser, 1995) and the widespread migmatization of the paragneiss enclaves with similar high temperature assemblages as found in the Slave and Konth granites, suggest that the paragneisses represent a significant portion of the parent materials (Grover *et al.*, 1997; Berman and Bostock, 1997).

6.3 Mineralogy and fabric

The following description of the mineralogical composition of the Arch Lake granite is based on 22 thin sections from samples collected in the southern sector of the batholith. The K-feldspar megacrysts as well as K-feldspar in the matrix are commonly submeso- to mesoperthitic or exhibits microcline crosshatch twinning. The matrix of relative weakly foliated samples consists of medium grained quartz and feldspar with irregular lobate grain boundaries. Primary biotite is commonly straw to olive green, and rarely brown in colour. The biotite is mostly anhedral, often chloritized and occurs as isolated interstitial grains, minor inclusions in K-feldspar megacrysts and in clusters together with medium grained quartz and feldspar. One chloritized biotite cluster contained poikiloblastic garnet with sillimanite inclusions, perhaps indicating that the clusters represent partially retrograded pelitic restite.

Monazite and zircon are preferentially associated or included in biotite but also occur in isolation from biotite. Inclusions of these minerals in biotite are surrounded by dark pleochroic halos (Figure 6.3(A)).

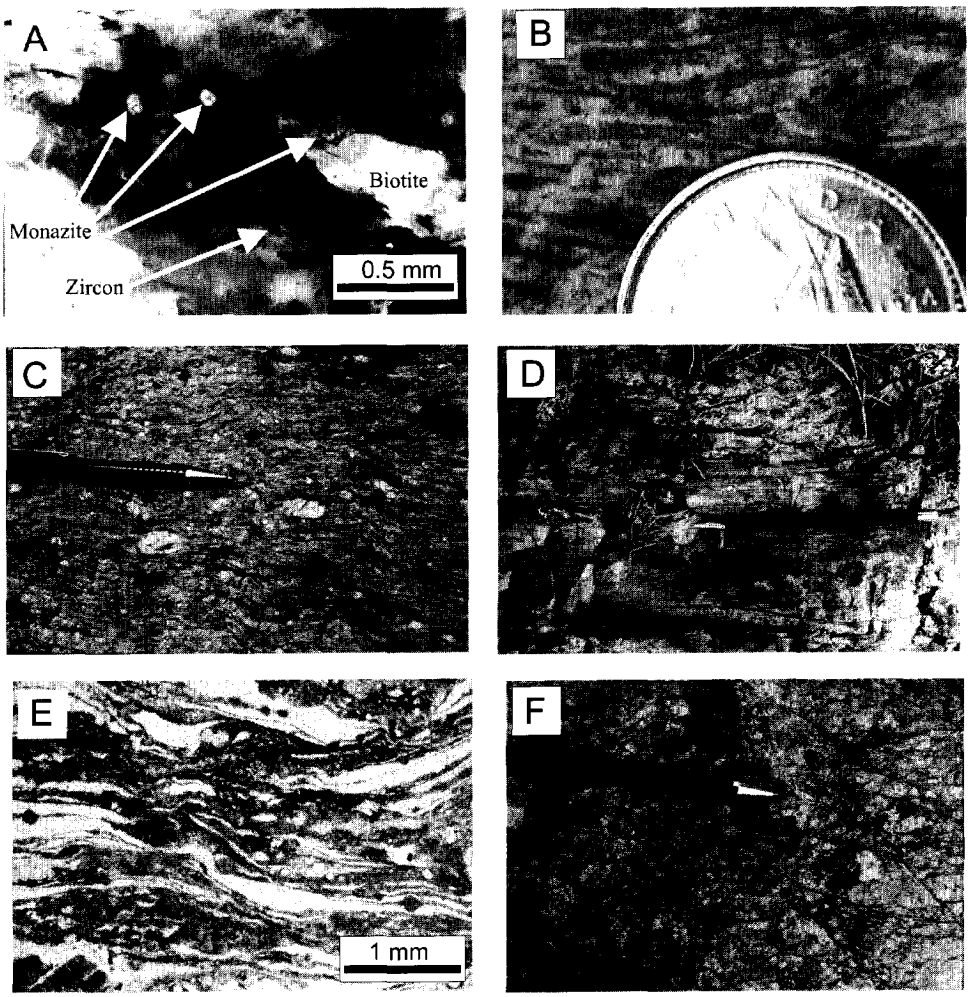

Figure 6.3 Thin section and outcrop photographs from the south-central sector of the Arch Lake batholith; (A) Monazite and zircon included in biotite with pleochroic halos indirectly indicating gamma radiation from the Th and/or U decay series; (B) Fabric of quartz and feldspar ribbons in local mylonite zone; (C, D) southward directed strain gradient from mylonite with bimodal size of K-feldspar porphyroclasts (C) to ultramylonite (D); (E) Microscopic photograph of mylonite with quartz ribbons (white) and layers of fine polycrystalline feldspar. Note shear band from upper left to lower right and antithetic book shelf gliding in K-feldspar porphyroclast at lower left suggesting dextral shear sense; (F) cataclastic deformation of mylonitic fabrics in E-W striking brittle fault zone.

These halos, formed by bombardment of the crystal lattice with alpha particles provide the direct evidence for gamma-radiation emitted from the radioactive decay of daughter isotopes of U and Th in their decay series. Opaque minerals, such as magnetite and hematite are also commonly associated with biotite and some biotite crystals contain abundant needle shaped crystals of rutile and sphene, suggesting that the biotite has been Ti-rich. Monazite is by far the most abundant accessory mineral. Crystals, up to 0.5 mm in dimension are commonly well rounded. Internally, these rounded monazite crystals show multiple euhedral zoning, which suggests that they are solid state residues. Zircon crystals are usually prismatic and one order of magnitude smaller in size. One sample contained accessory amounts of brown hornblende rimmed by biotite.

In outcrop, the Arch Lake granite appears to be variably strained. The solid state fabric ranges from weakly foliated megacrystic granite with weak elongation of quartz to penetrative S > L augengneiss and mylonitic fabrics with a general lack of mineral lineations (Langenberg and Ramsden, 1980). The high strain fabrics range in texture from augengneiss with porphyroclasts of alkali-feldspar wrapped by quartz ribbons to a strong penetrative fabric of quartz and feldspar ribbons with few K-feldspar porphyroclasts in local mylonite zones (Figure 6.3(B)). These fabrics are suggestive for deformation under medium to high-grade metamorphic conditions.

In thin section, the mylonitic foliation is defined by mica-rich bands of coarse biotite and muscovite grains parallel to ribbons of dynamically recrystallized quartz and feldspar. Myrmekite along foliation parallel crystal faces, core and mantle structures and flame perthite (Passchier and Trouw, 1996) in mylonitic fabrics suggest that the Arch Lake granite continued to be deformed in a ductile manner from medium to low metamorphic grades.

The range in metamorphic grades, inferred from these feldspar textures are consistent with upper greenschist facies to lower amphibolite facies mineral assemblages of coarse biotite and muscovite, epidote and quartz and the breakdown of K-feldspar to muscovite. The subvertical sheared margins of the Arch Lake intrusion consist predominantly of strike-lineated mylonites that pass directly into the enveloping country rocks (McDonough *et al.*, 1994a, 1994b, 1994c, 1994d). These fabrics are on the basis of their ribbons of K-feldspar (McDonough *et al.*, 1993) and their direct passage into enclaves of mylonitized pelitic rocks with granulite facies mineral assemblages were interpreted to have recrystallized at high grade metamorphic conditions (Grover *et al.*, 1997). Towards the internal sectors, the solid state foliation decreases in intensity and outlines a north plunging synformal structure decreasing in width towards north

(Langenberg and Ramsden, 1980). The outline of this synformal structure was identified in Chapter 3 as curvilinear trends in the interpretation of Landsat TM and ERS-1 images (Figures. 3.4, 3.5, 3.6, Plates 3.4 and 3. 5).

6.4 Interpretation of remotely sensed data.

The ternary radioelement, eTh/K radioelement ratio, residual magnetic anomaly and regional geological map patterns over the Arch Lake granite were compared by visual interpretation to study their mutual interrelationships with respect to the zonation pattern. The aeromagnetic data were included in this interpretation. Because magnetic minerals are sensitive to the petrogenetic affinity of the magma and the degree of differentiation conditions of emplacement, aeromagnetic data may show contrasting magnetization levels related to processes of magmatic differentiation (Clark, 1997). Charbonneau (1991) found that in ferromagnetic granites, like the Arch Lake granite, magnetite shows the general tendency to decrease with increasing acidity. The aeromagnetic data over the Arch Lake granite may therefore lend support to the interpretation of the gamma-ray spectrometry data.

Plate 6.1(A) shows a colour-shaded relief representation of the residual magnetic field. The residual magnetic field was computed by reduction to the pole, upward continuation to one kilometre, followed by subtraction of the pole-reduced field from the upward continued field by convolution filtering in the frequency domain (Telford *et al.*, 1990). This procedure removed the regional SSW-NNE directed regional trend evident on the total magnetic field representation (Plate 3.2) and was implemented to enhance the magnetic anomalies over the Arch Lake granite that are related to the relative shallow magnetic sources. The on average 875 meter upward continuation from the nominal flight height on 125 meter provided a balanced compromise between the enhancement of shallow magnetic sources and restricted amplification of noise.

Plate 6.1(B) shows the eTh/K ratio computed from the eTh and K grids. Ratioing of radioelement grids has been found to be a useful enhancement procedure as it tends to reduce the effects of environmental factors such as wetness and vegetation cover (Charbonneau, 1991) and because it enhances subtle variations in relative radioelement concentrations. The ratio was computed according to the method proposed by Grant (1998). This method exploits the poisson distribution model for gamma-ray measurements, which implies that the mean count rate is equal to the variance. By accumulating 500 counts (5% error) in the numerator and denominator from rings of grid cells around the cell for which

the ratio is computed a homogeneous noise level of 10 % is obtained for each grid cell (Grant, 1998).

A generalized geological map of the Arch Lake granite, based on the mapping by Godfrey and Langenberg, (1987) and McDonough *et al.* (1994(a); 1994(b); 1994(c); 1994(d)) is shown in Plate 6.1(C). This generalized map does not show the hundred meter scale alternations of units 160 and 161 (Godfrey and Langenberg, 1987) throughout the Arch Lake granite that reflect the above described subtle variations in the abundance and size of K-feldspar megacrysts. Nevertheless this map serves the purpose of illustrating the striking absence of internal compositional variations that correspond to the radioelement zonation pattern.

Plate 6.1(D) shows the ternary radioelement image of the Arch Lake granite with red modulating %K, green modulating ppm eTh and blue modulating ppm eU. The inward transition from reddish and brownish hues to yellow and green hues indicates that the zoning is mainly reflected in the thorium channel. The zonation in eTh is also reflected in the line data. The individual lines, however, show a more irregular response with respect to the gridded data, as the last have been smoothed in the gridding process (Charbonneau *et al.*, 1997).

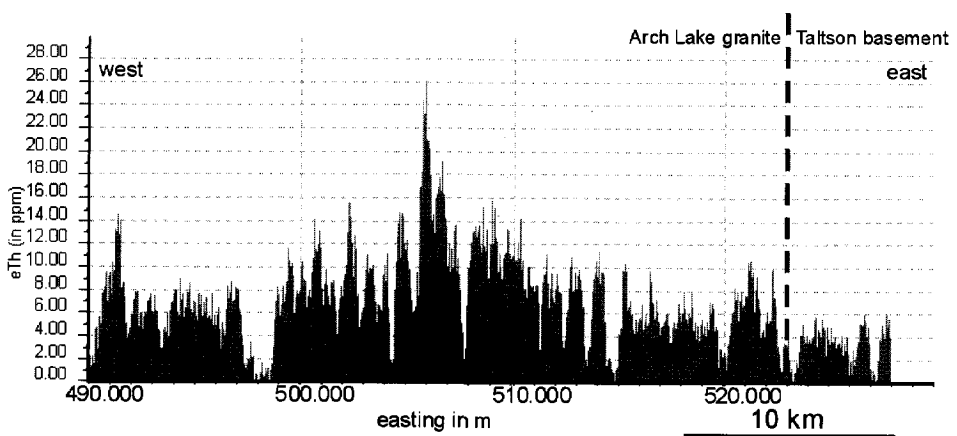

Figure 6.4 Airborne eTh line profile over Arch Lake granite (east-west flight direction).

Figure 6.4 shows a low-pass filtered flight line profile at approximately 6615000 northing. Note the sharp minima due to the low gamma-ray signatures over lakes. Airborne eTh concentrations within the central zone are on average between 8 to 14 ppm with a local spike of 26 ppm, whereas the estimated concentration of the Th-poor zones ranges between 4 to 8 ppm. The eTh/K zonation shows a greater continuity in the marginal zones in comparison to the ternary radioelement image, particularly along the eastern margin. This is because the effects related to a strong northward decrease in outcrop density and increase in vegetation cover in this area has been reduced on the eTh/K ratio grid (Schetselaar and Rencz, 1997). The enclaves of the Slave granites do generally not appear as distinct anomalies on the ternary radioelement image, but consistently correspond to Th-poor domains in the Arch Lake batholith.

The relative low U content of these domains in comparison to the Slave granites west of the intrusion is reflected in a difference in colour on Plate 6.1(D) between red-brown and magenta hues. The residual magnetic image exhibits a central high, with a larger width in comparison to the eTh/K and eTh highs on respectively Plate 6.1(B) and 6.1(D). The paired magnetic low and high (B and C on Plate 6.1(B)) on the eastern margin broadly coincide with respectively the thorium rich and thorium depleted zones of the ternary radioelement image (Plate 6.1(D)). These anomalies are separated from the central zone by a linear magnetic low (B on Plate 6.1 (A)). This lineament corresponds on Plate 6.1(C) to the Arch Lake fault zone, a predominantly brittle shear zone that splays from the principle displacement zone of Charles Lake shear zone (CLSZ) (McDonough *et al.*, 1994(a); 1994(b)).

The outlines of the thorium rich zones on the residual magnetic field data reveals large mismatches between their outline and inconsistent interrelationships. The internal magnetic highs (C on Plate 6.1(A)) correspond to both low and high eTh concentrations and the magnetic high west of the fault zone D on Plate 6.1(A) extends about five kilometre further west in comparison to the thorium rich central zone on Plate 6.1(D). The reasons for the poor correlation remains, without constraints on the magnetic mineralogy and subsurface configuration of magnetic sources poorly understood. The correspondence between shear zones and linear negative residual magnetic field anomalies, however, suggests that the strong deformation of the Arch Lake granite may have obscured magmatically induced magnetic susceptibility contrasts. The linear magnetic lows (B on Plate 6.1(A)) may reflect the destruction and oxidation of magnetite to hematite (Sprenke, 1986). Contrary to the poor correspondence between the radioelement and magnetic anomaly patterns, both anomaly patterns show a striking coincidence

between two conspicuous SE to E striking offsets (E on Plate 6.1(A)) that display dextral apparent displacement. These offsets in combination with their correspondence to negative linear magnetic anomalies strongly suggest localized faulting. Further south at Cockscomb Lake an E-W trending mylonite zone dipping about forty to sixty degrees north appears on the published maps of Godfrey and Langenberg (1987; Plate 6.1(A)). Inferences on the metamorphic grade and kinematics of this 250 meters wide and 6 km long zone were, however, not reported.

6.5 Spectral analysis of gamma-ray spectrometry data

The interpretation of ternary radioelement and ratio images presented above, permitted to outline the main radiometric domains. Although such procedures are useful in outlining the overall radiometric signatures (Broome *et al.*, 1987), subtle relationships and spectral trends between the K, eTh and eU airborne radioelement concentrations may be overlooked. Additional insight in the spectral relationships between the K, eTh and eU airborne concentrations is obtained by analyzing their interrelationships in K- eTh- eU space (Kuosmanen, 1994; Wellman, 1998). Plate 6.2(A) shows the scatter plots of eTh plotted against K, eU against K and eU against eTh. In order to represent the main trends of such large data sets (n = 150462) the scatter plots are mapped in pseudo colour such that with increasing density hue ranges from magenta, blue, green, yellow and red.

Generally, the higher densities from blue to red show elongated clusters due to the inherently strong correlation between K, eTh and eU in granitoids (Dickson and Scott, 1997; Wellman, 1998).

An interesting feature is the subordinate steeper linear cluster added on to the main linear distribution in the eTh-K scatter plot. This cluster plot in K-eTh space shows that what could have been interpreted on the basis of the ratio grid alone as a continuous trend from low eTh/K to high eTh/K values, represents in reality two spectrally and spatially distinct trends.

To test this interpretation it was verified if both trends would re-appear in flight line data of the Th-poor and Th-rich domains. Figure 6.5(a) shows the eTh-K scatter plot for all the flight line samples within the Arch lake granite (n = 14780), whereas Figure 6.5(b) and Figure 6.5 (c) show scatter plots from respectively the Th-rich central and circumventing Th-poor domains as outlined on Plate 6.1(A).

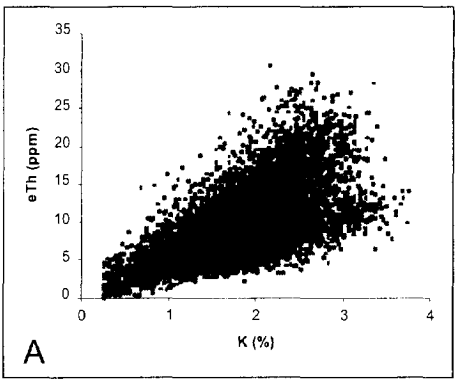

Figure 6.5 eTh-K scatter plots of airborne gamma-ray spectrometry data over Arch Lake granite. (A) flight-line data within total area; (B) flight line data within Th-rich central zone (outline is shown in Plate 6.1(A); (C) flight line data within Th-poor zones (enclaves of Slave granite shown in Plate 6.1(C) are excluded)

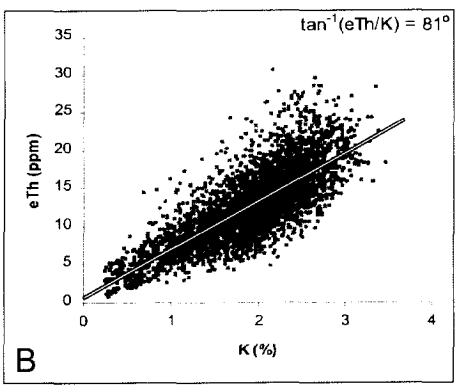

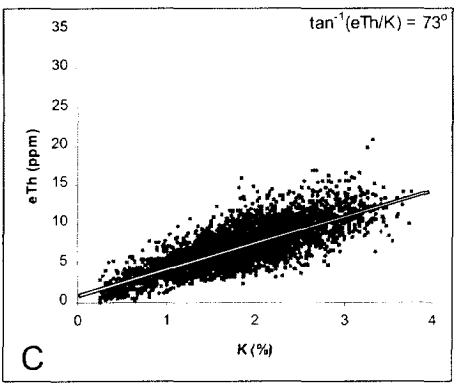

The scatter plot of the flight line samples resembles the scatter plots obtained from the K and eTh grids, illustrating the preservation of the overall spectral qualities in the gridded data. Comparing the scatter plots of flight line data within and outside the Th-rich domains confirms the presence of two distinct trends in eTh-K space similar to the linear trends within the eTh-K space of the gridded data. The estimated slopes of these trends yield $\tan^{-1}$(eTh/K) values of 74 and 81 degrees, both falling in the range of eTh/K values in the thorium poor respectively thorium rich zones on Plate 6.1(B). To analyze the transition between these trends in a spatial sense, the eTh/K ratio was plotted against distance from the central axis of the western part of the central Th-rich domain that is not transected by shear zones using a distance calculation function (Aronoff, 1991). The resulting equal distance contours are shown in Figure 6.6 (A) and a graph on which the eTh/K ratio of the line data is plotted against distance is shown in Figure 6.6 (B). A step-like increase of the eTh/K ratio is apparent between 3 to 4 km from the central axis, which divides the profile in two approximately horizontal trends.

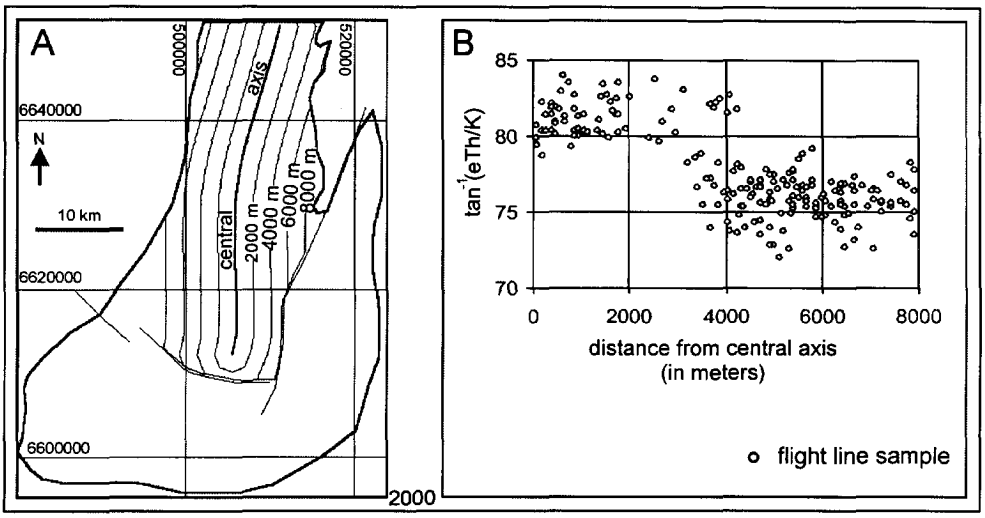

Figure 6.6 (a) Equal distance contours from central axis in meters; (b) Plot of eTh/K ratio versus distance from central axis of the Arch Lake batholith. Note the distinct break at distances between 3-4 km.

This supports the interpretation that the Th-poor and Th-rich domains reflect spectrally distinct trends. The positive sign of these trends is consistent with those interpreted to reflect magmatic differentiation (Dickson and Scott, 1997; Wellman, 1998).

Cluster analysis was implemented to subdivide the data set on its overall spectral signature in a relatively automated and objective manner using the K, eTh, eU, eTh/K, eU/K and eU/eTh grids. All radioelement and ratio grids were standardized to zero mean and equal variance to avoid dominance of the large concentration range of the eTh grid over the smaller numerical ranges of the other grids. The ISODATA unsupervised clustering algorithm (Tou and Gonzalez, 1974) was used with eight initial clusters aligned on the diagonal axes in six-dimensional space. The convergence threshold was set to 97 % so that the iterative cluster allocation continued until 3 % of the grid cells changed allocation from one iteration to the next. Subsidiary clusters with similar radioelement signatures were merged resulting in a final map of four clusters with distinct radioelement signatures. The hue assigned to the clusters correspond to the mean K- eTh- eU signature of the ternary radioelement image shown in Plate 6.1(D), facilitating comparison with Plate 6.1(A). A plot of the vector means of these clusters is shown in Plate 6.2 (B). Note that the cluster analysis supports the visual

interpretation of Plate 6.1(D) in the sense of identifying the distinct Th-rich central and the linear domains with local U anomalies on the margin.

The central domain (clusters +K+eTh and +K++eTh++eU on Plate 6.2(B)) has also elevated K concentrations, a feature that is not so evident on Plate 6.1(D). The cluster analysis identified U-rich sub-domains in both the Th-poor and Th-rich domains. The first domain shows a radioelement signature that is similar to the Slave granites which perhaps indicates assimilation of Slave material or magma mixing between Slave-like and Arch Lake magmatic pluses. This speculation is consistent with the transitional radioelement signature between the Arch Lake and Slave granites as shown on Plate 6.1(D) and a certain degree of correspondence between these clusters and the enclaves of Slave granite, shown on Plate 6.1(C).

6.6 Geochemical and mineralogical associations

In an attempt to assess the regional significance of the association between U- and Th-bearing accessory minerals, biotite and Fe-bearing oxides observed in thin section, the interrelationships between major and trace elements from the geochemical data set and airborne eTh were analyzed. This analysis was based on a subset of 59 samples from geochemical data collected by the Alberta Geological Survey (Goff *et al.*, 1986).

The low density and small volumes of rock samples in comparison to the airborne measurements constrained the assessment to be qualitative only. The analysis of this data set is also limited in comparison to geochemical surveys that include analysis of the majority of trace elements. The trace element used as indicators for Th- and U- bearing minerals, for example, was restricted to Zr, as an indicator for Zircon. Analyses of Ce and La as indicators for monazite, were not available. Textural evidence from thin sections previously described, however, indicates that monazite and zircon are closely associated and preferentially included in biotite. The scatter plots, shown in Figure 6.7, of Zr against TiO_2 (Figure 6.7(a)), TiO_2 against Fe_2O_3 (Figure 6.7(b)), Zr against biotite (Figure 6.7(c)), TiO_2 against biotite (Figure 6.7(d)) are consistent with the above described microscopic observations and suggest that zircon (together with monazite) is associated with biotite and Ti-bearing iron oxides. This mineralogical association and the negative trend of this association with SiO_2 (Figure 6.7(e)) is a common theme of peraluminous granites (Chatterjee and Muecke, 1982; Ford and O'Reilly, 1985; Maurice and Charbonneau, 1987; Charbonneau, 1991; Goossens, 1992), and also holds for the Konth- and Slave granites (Charbonneau, 1991; Charbonneau *et al.*, 1997).

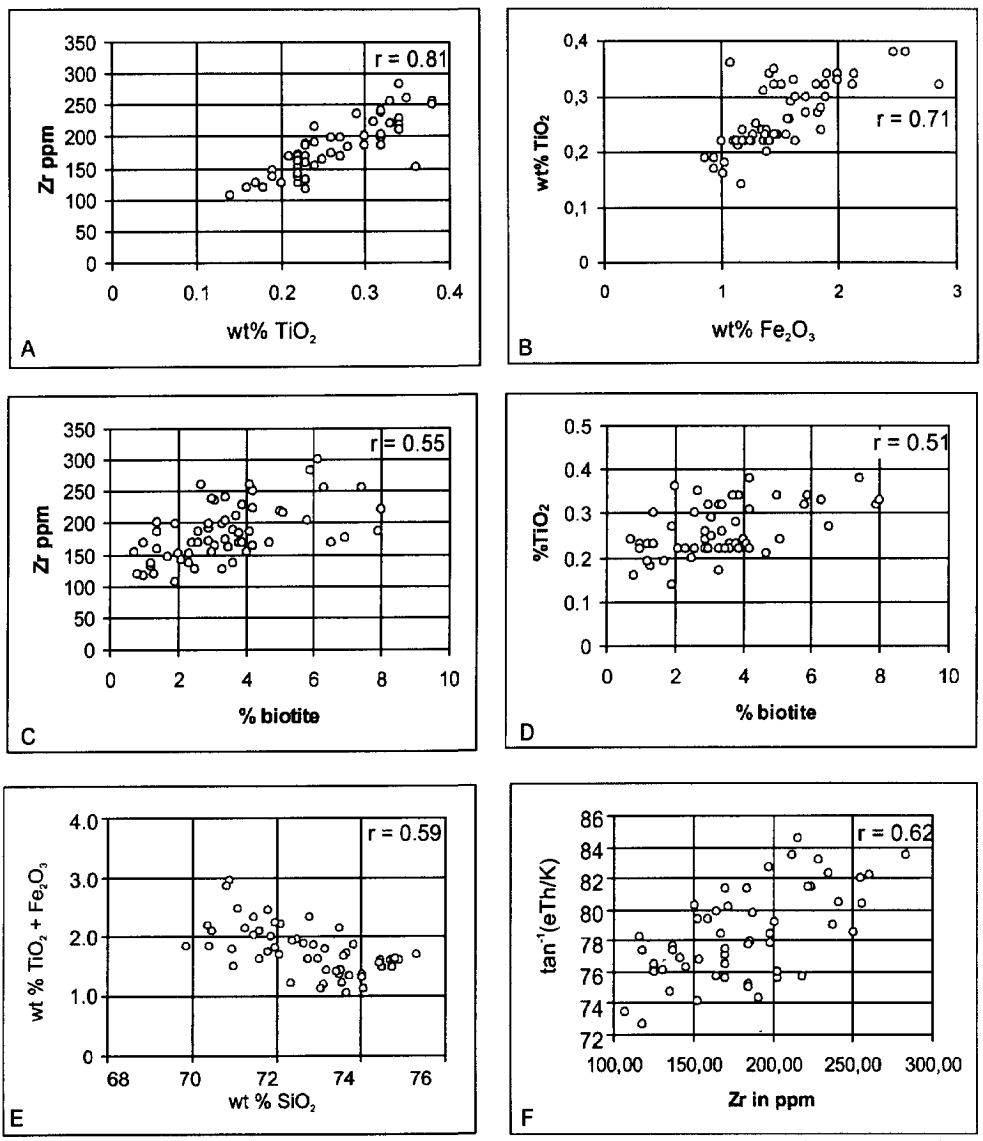

Figure 6.7 Scatter plots of whole rock geochemistry from Arch Lake granite (59 samples), modal % biotite (from point counts of thin sections) and $\tan^{-1}$ (eTh/K) grid values. (A) Zr (ppm) against wt% TiO_2;(B) wt% TiO_2 against wt% Fe_2O_3 (C) Zr against modal % biotite; (D) wt% TiO_2 against modal biotite % (E) wt% TiO_2 + Fe_2O_3against SiO_2; (F) $\tan^{-1}$ (eTh/K) values from airborne gamma-ray spectrometry grid against Zr.

The scatter plot of airborne $\tan^{-1}$(eTh/K) versus Zr (Figs. 6.8(f)) was generated by sampling the ratio grid at the rock sample positions. The ratio was used instead of the eTh grid to reduce attenuation effects. The relationship is still expected to be ambiguous, in the first place by the extreme dissimilarity in sampled volume. Nevertheless the eTh/K ratio shows a moderately correlated positive trend with Zr. These relationships, as well as the mineralogical association between zircon monazite and biotite that the eTh variations predominantly reflect the amount of Th concentrated in monazite, zircon and sphene, and indirectly reflect the variations in modal percentages of biotite and Ti-bearing Fe-oxides.

The weight percentages of TiO_2, Zr, biotite, SiO_2 and the Rb/Sr ratio were spatially interpolated to compare regional whole-rock geochemistry patterns with the airborne radioelement patterns. Although no clear overall trends between Rb-Sr and Ba-Sr which fit simple crystal fractionating models were found (Goff *et al.*, 1986), the Rb/Sr ratio was next to wt% SiO_2 considered as a magmatic differentiation index. Initially an attempt was made to use ordinary kriging for interpolation, but the semivariograms, appeared to be swamped by high nugget effects and alternating low and high semivariances at short lag ranges. Because no reasonably fits could be obtained from these semivariograms, an inverse distance moving average interpolation was used instead. A slowly decaying weight function was selected using an exponent of 0.01. In combination with a large search distance of 15 km this interpolation emphasized the broad spatial trends at cost of the local variations.

Plate 6.3 shows the interpolated patterns of TiO_2, Zr, SiO_2, Rb/Sr, % biotite and the eTh grid. With the notion that the interpolated patterns can only be globally interpreted, the TiO_2, Zr and to some extent % biotite patterns are broadly similar and show higher concentrations in the central Th-rich zone. The Rb/Sr and SiO_2 patterns resemble each other to some extent but are markedly different from Zr and TiO_2. Both patterns show north-south directed gradients across the Th-rich centre roughly perpendicular to the east-west directed trends in TiO_2 and Zr interpolation patterns. Although the SiO_2 and Rb/Sr patterns do not reflect the Th-rich central zone, the highest Rb/Sr domains enclose the highest U and Th values (cluster +K++eTh++eU, on Plate 6.2(B)). The high eU and SiO_2 content of these zones are consistent with the positive trend of U with SiO_2 for evolved stages of magmatic differentiation (SiO_2 > 70 wt%) (Dickson and Scott, 1997; Bea, 1999). The U-enriched gneisses of the Taltson Basement Complex at the eastern margin of the Arch Lake batholith (Plate 3.3, and Figure 3.3) may indicate that this stage was associated with hydrothermal enrichment of country rocks.

6.7 Integration of Landsat TM 7 and K, eTh, eU grids for structural analysis

The geometry of the radioelement zonation was analyzed with respect to the internal structure of the Arch Lake granite by integrating the K, eTh and eU grids with Landsat TM7 and structural data in an IHS composite image (Shettigara, 1992; Harris *et al.*, 1994; Wilford *et al.*, 1997). The integration of the radioelement grids with images of higher spatial resolution, adds spatial detail and provides a sharpened rendition of the otherwise fuzzy ternary image map (Wilford *et al.*, 1997). Because the concentric foliation and fault patterns are well shown on the TM image, the combined visualization allows interpreting the geochemical information provided by the K, eTh and eU grids in a structural context.

Landsat TM band 7 was selected from the six 30 meter resolution bands of Landsat Thematic Mapper, because this band is the least affected by atmospheric noise and provided maximal enhancement of topographic features reflecting foliation and faults. This facilitated the lithogeochemical information derived from the gamma-ray spectrometry channels to be interpreted with respect to the internal structure of the Arch Lake intrusion. Assuming that radioelement zonation primarily reflect mineralogical variations genetically related the formation of the Arch Lake granite, the radioelement patterns provide useful strain markers for interpreting structures that formed after and possibly during emplacement.

As demonstrated in Chapter 5 the unwary application of IHS colour-coding techniques may lead to colourful, but uninterpretable images. It is critical to being able to control the processing, in such a way that the individual data sources complement one another optimally in the final result while spectral distortions are minimized (Schetselaar, 1998). For this application the image integration aimed at optimally enhancing the structural information of the Landsat TM data in the IHS composite image, provided that the radioelement zonation reflected in the K, eTh and eU grids could still be recognized.

The processing method used to generate the IHS composite image is shown in Figure 6.8. Landsat TM band 7 was pre-processed by Fourier analysis using a circular high pass filter in the frequency domain with a cut-off wavelength of 900 meters. This filter enhanced the continuity of the curvilinear trends, as it eliminated most of the longer wavelength contrasts, such as contrasting vegetation patterns related to forest burns (Plate 3.4). The IHS composite image of TM band 7 and K, eTh, eU grids is shown in Plate 6.4 with an overlay of planar and linear structural features.

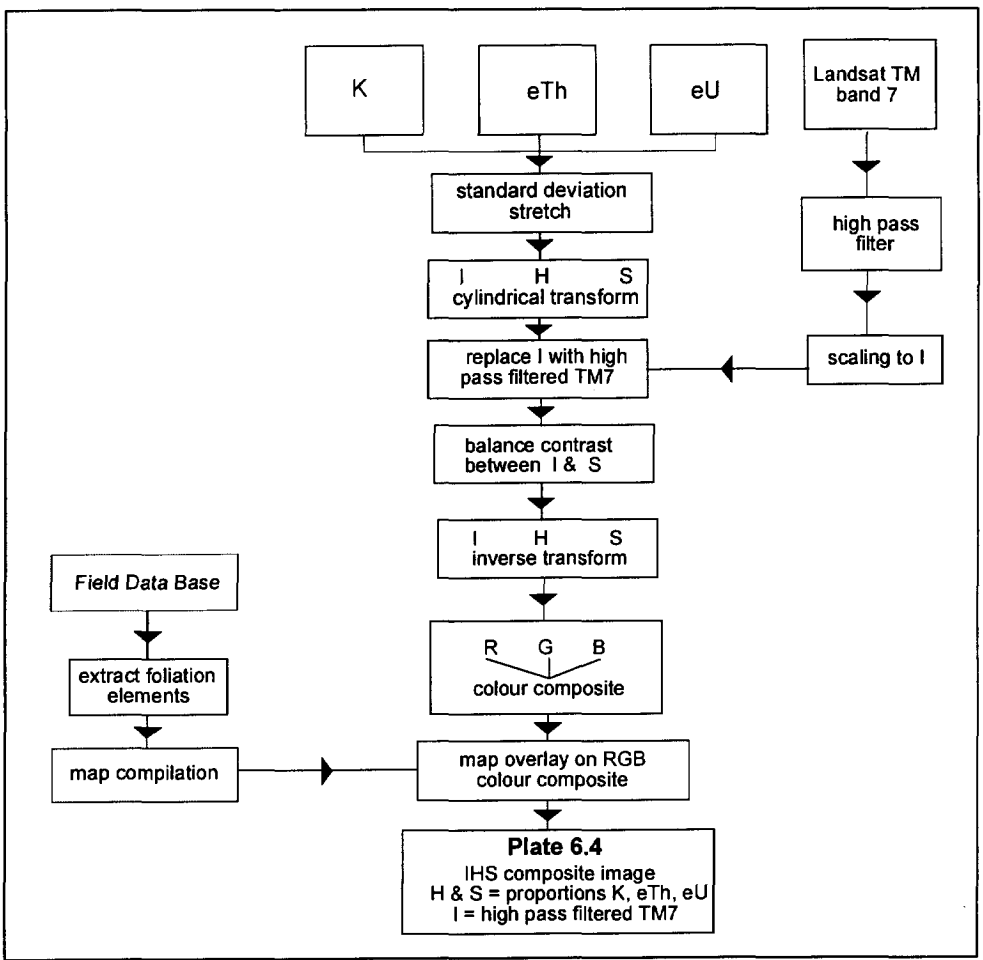

Figure 6.8 Processing procedure for generating IHS composite image from Landsat TM7, K, eTh, and eU grids with structural overlay of mineral foliation data (Plate 6.4).
In order to enhance the subtle intensity contrasts associated with foliation patterns, the cylindrical IHS transform was applied at cost of hue and saturation contrast (see Chapter 5).

The symbols outlined in black represent foliation measurements including those collected by Godfrey and Langenberg (1987). The dip amount is classified using different symbols in three classes from 0-30, 31-60 and 61 to 90 degrees. Although the intensity and nature of the mineral foliation was not recoverable, its

representation is considered useful to show the general foliation trends within the pluton and to verify the correlation with the enhanced curvilinear trends in the TM data. A compilation of an image interpretation of Plate 6.4 and mylonites zones mapped by Godfrey and Langenberg (1987), and McDonough *et al.*, (1994(b); 1994(d)) is shown in Figure 6.9.

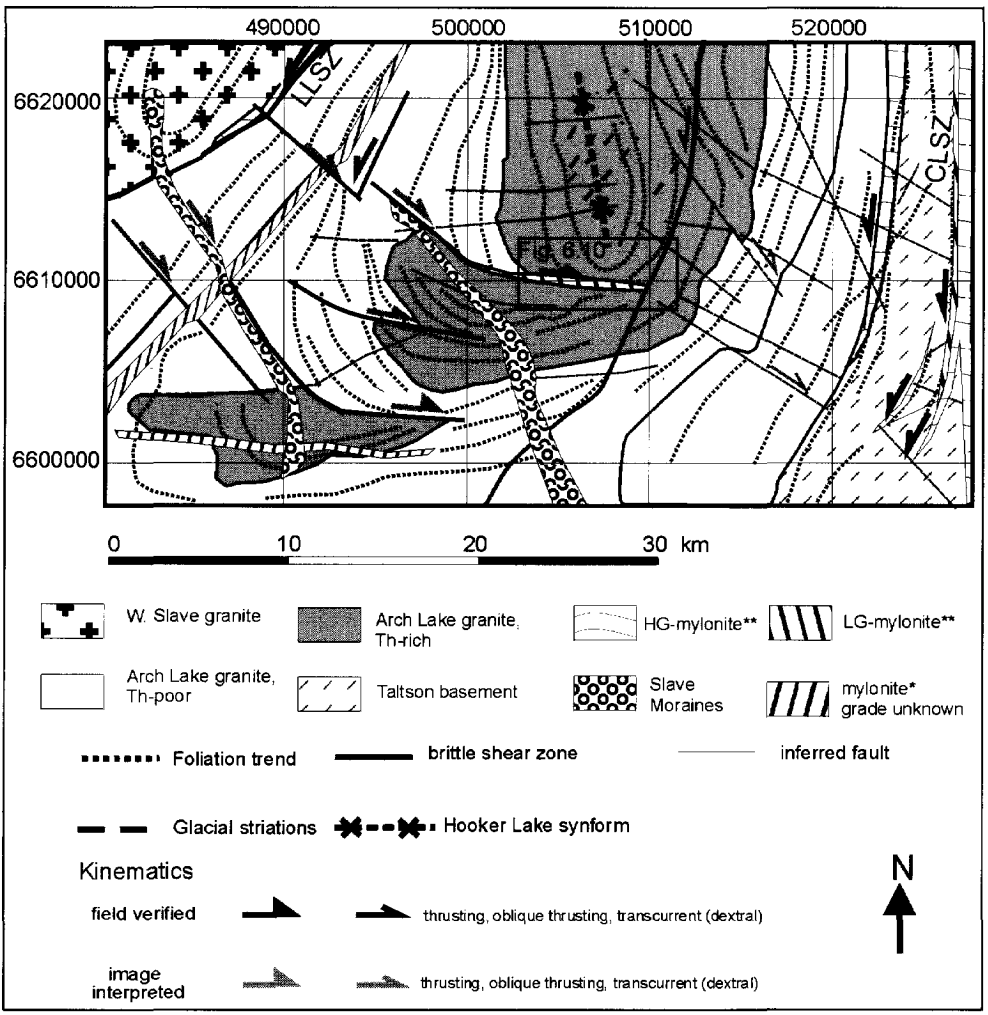

Figure 6.9 Interpretation of IHS composite image of K, eTh, eU grids and Landsat TM 7 (Plate 6.4) combined with map compilation of shear zones (*after Godfrey and Langenberg, 1987, ** after McDonough *et al.*, 1994a and 1994b).

On the basis of the curvilinear patterns around the Th-rich centre and the structural elements the north plunging synform could be outlined. This synform was formerly identified and mapped by aerial photograph interpretation and foliation strike-lines and tentatively associated with doming of the Slave pluton (Langenberg and Ramsden, 1980). The radioelement zonation appears to be approximately parallel to the curvilinear solid state foliation trajectories for most of its inferred strike length, although local angular relationships between E-W striking foliation elements and N-S trending radioelement domain boundaries can be seen in the lower left quadrant (Plate 6.4). The overall concordant geometry between the radioelement zonation, internal solid state foliation trajectories and the sheared pluton margins suggest that the mineral foliation formed after and possibly during emplacement. The space required for the emplacement of the southern Arch Lake granite could, on the basis of this overall concordant relationship and the steeply inclined and intensifying fabric towards the margins, have been partly accommodated by mechanisms of forceful emplacement, such as diapirism and ballooning (Hutton, 1996). In general, however, patterns with similar overall concordant geometry in plutons may have other equally permissive explanations (Patterson and Fowler, 1993) and may also be explained entirely by post-emplacement deformation. The short time interval between the crystallization age of the Arch Lake granite (1.938 $\pm$ 0.003 Ga.) and the minimum age of high grade mylonitization, constrained by the 1.934 + 0.002 Ga. U-Pb zircon crystallization age of a Slave-like granite dike intruding the mylonitized western margin of the Arch Lake intrusion (McDonough *et al.*, 1995), however, constrains emplacement to be approximately synkinematic with respect to high-grade mylonitization of the pluton margins.

The integrated visualization shown in Plate 6.4 also yields insight in the post-emplacement deformation of the Arch Lake granite. The apparent offsets in the radioelement zoning, the coinciding lineament on the IHS composite and linear negative residual magnetic anomaly and the abrupt change in foliation strike-direction across the offsets (Plate 6.1(A)) all suggest these offsets to be due to localized shear and/or faulting. The apparent dextral sense of movement of the thorium rich central zone is corroborated by similar sense of movement of the magnetic anomaly pattern along the lineaments shown on Plate 6.1(B). This fault system appears to have accommodated the strain that resulted in the arched outline of the southern extension of the batholith pluton by displacements in a dextral (apparent) sense. At the margin with the Slave granite in the west, the same system also displaces the magnetic anomalies associated with the LLSZ, in dextral apparent sense.

The apparent displacement of the thorium central high along the lineament varies from about 8 km at its western margin towards practically nil at its eastern margin bounded by the NNE-SSW-trending brittle shear zone. This gradient in apparent displacement is associated with a northward decrease of the total width of the Arch Lake intrusion. Assuming that the Th-rich lobes were spatially continuous before post emplacement deformation, strike-slip movement can not explain the isolated southerly Th-rich lobe in map view but would require components of thrusting. Given the overall lack of kinematic field data within the Arch Lake granite, this interpretation needs further verification.

Two NW to NNW trending bands of reddish hues and smooth image texture can be traced over the synformal foliation patterns. These features correspond to the northerly extension of the Slave Moraine and mark the western edge of the former Laurentide Ice Sheet. The Slave Moraine, consist of stratified sands and gravels interbedded with thick lenses of diamict, deposited during the Late Winconsin phase of glaciation at approximately 10 Ka (Bednarski, 1997). These Quaternary features are easier to identify from the combination of the red hues of the K-rich sediments and their smooth image texture on TM7 in the composite image in comparison to their separate rendition (see Plates 3.3 and 3.4).

Local field checks were conducted to verify the nature and continuity of the inferred shear zone. Another E-W striking mylonite zone was mapped by Godfrey and Langenberg (1987) (Plate 6.1(C)). The width of this mylonite zone ranges between 300 and 600 meters and the total strike length sums to of about 8 kilometers. The kinematics and metamorphic grade of this mylonite zone was unfortunately not reported.

The structural field observations collected during the ground verification campaign are presented in Figure 6.10. Although the degree of exposure along the lakeshore did not permit to fully confirm the continuity of this zone on the ground, it is on the basis of the linear negative magnetic expression (E on Plate 6.1(A)) and TM lineaments interpreted as a continuous tectonic feature. In three places a southward strain gradient could be traced across the E-W trending lineament over a distance of about 200 meters.

Towards the south a weakly developed foliation defined by elongated quartz and the preferred orientation of biotite dipping between 30 and 40 degrees north passes into augengneiss and quartz-feldspar ribbon mylonites (Figure 6.3(B)) with bimodal porphyroclast sizes (Figure 6.3 (C)). These mylonites and protomylonites dip moderately north concordant to the mineral foliation that outlines the Hooker-Lake synform.

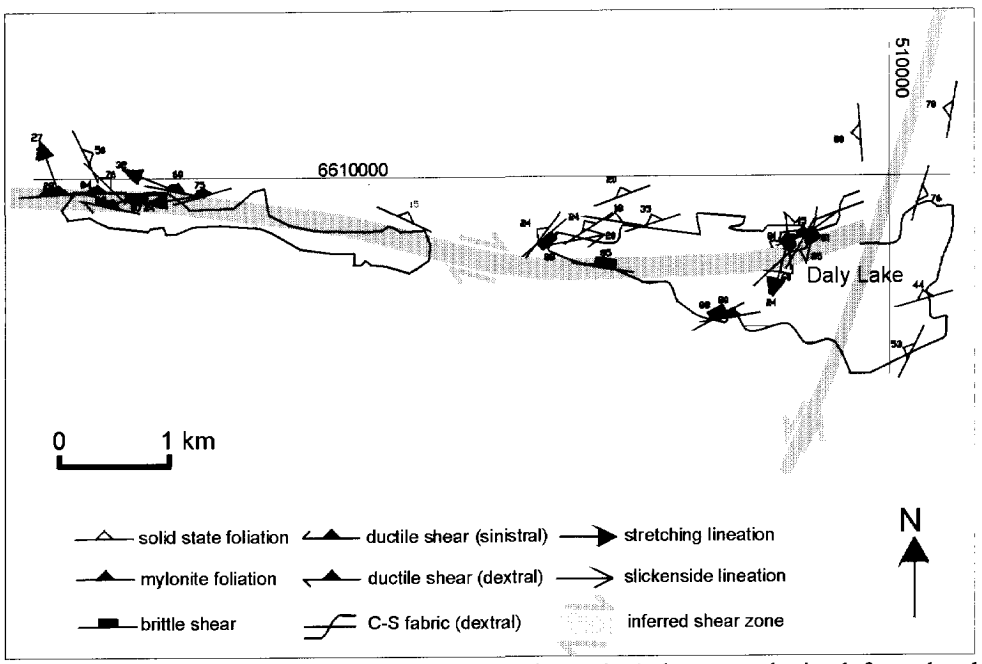

Figure 6.10 Structural map compilation from the Daly Lake area obtained from local ground verification of the offsets in the radioelement zonation (Plate 6.1(D) and Plate 6.4). See Figure 6.9 for location.

These mylonitic fabrics possibly represent a local strain intensification of the deformation phase in which the synformal structure was formed. At Daly Lake this fabric is overprinted by NNE trending sinistral shears and locally folded in steeply north plunging crenulations. A sub-vertical zone of upper greenschist facies ultramylonite with an estimated minimum width of 25 meters bound the mylonite zone to the south. Outcrops of highly fractured mylonite are found south of the strike-extension of this ultramylonite at the western tip of Daly Lake. The fractures in these outcrops strike predominantly east and display subhorizontal slickensides. The mylonites along the lineament show evidence of dynamic grain size reduction of feldspars and quartz and strong development of quartz ribbons.

The ultramylonite contains abundant epidote and muscovite and shows evidence for reaction assisted deformation (Dixon and Williams, 1983) by the breakdown of K-feldspar to muscovite and sericite. Both high angle and low-angle bookshelf gliding of elongated K-feldspar porphyroclasts is common. Quartz ribbons are spectacularly developed and locally display dextral extensional shear

band cleavage (Figure 6.3(D)). Thin-sections from the brittle deformation zone show discrete fractures that crosscut and displace quartz ribbons and feldspar crystals indicating reworking of ductile fabrics under brittle deformation conditions. Unfortunately stretching lineations and shear sense indicators were rarely found. Two measurements indicate NW-SE and WNW-ESE oblique movement with a large transcurrent component along foliation planes dipping steeply towards the north, while one dip-lineated mylonite indicated normal or thrust fault movement along a moderately inclined foliation plane. Two lineations at an outcrop at the western margin indicated a transcurrent movement direction. At two locations, subvertical shear band cleavage (Figure 6.3(E)) and C-S fabrics indicated dextral shear sense (Figure 6.10).

6.8 Discussion

Th-rich phases in the Konth and Slave S-type granites were interpreted on the bases of the spatial association of biotite monazite and zircon, reflected in a positive correlation with TiO_2, Fe_2O_3, MgO, trace elements and negative correlation with SiO_2 as magmatically less evolved (Charbonneau, 1991; Charbonneau *et al.*, 1997).

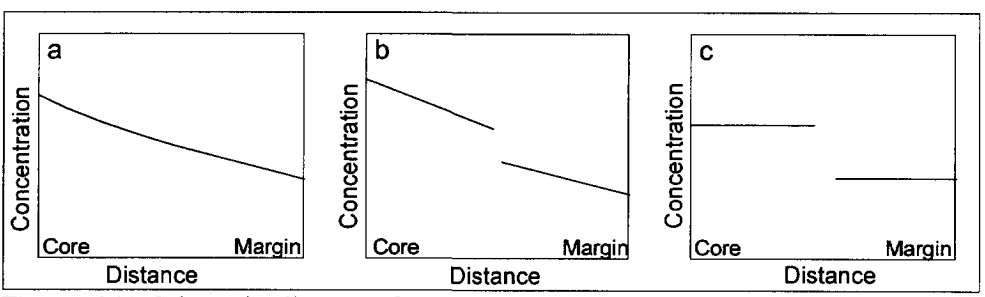

Figure 6.11 Schematic diagrams for compositional trends within zoned plutons after Pitcher (1993). (a) continuous, likely to have established in situ; (b) stepped discontinuities produced by periodic upwelling of differentiating core magma; (c) totally discontinuous as a result of multipulse infills.

The analyses presented above suggest that similar relationships hold for the Arch Lake granite. Furthermore, the comparative analysis of the spatial patterns from gamma-ray spectrometry data and lithogeochemical data, supported by local mineralogical observations, provides insight in the regional compositional variations. This integrated approach provides ground to speculate on the origin of

the radioelement patterns with respect to general explanations for compositionally zoned granitoid intrusions.

In a review on their genetic significance, Pitcher (1993) argues that zoned plutons originate from a combination of processes, including 1: fractional crystallization by sidewall accretion, 2: recharges by mafic magma, 3: magma mixing and multipulse injection of melts either fractionated elsewhere or derived by successive remeltings. Zoning is especially evident in I-type plutons where silica content and mafic index increases, respectively decreases inward from the margin usually from quartz diorite, granodiorite to granite. Laboratory gamma-ray spectrometry measurements suggest that such plutons can be expected to show an increase in K, U and Th from the pluton margin (Dickson and Scott, 1997). Schematic models for compositional trends of zoned granitoid intrusions that distinguish between in situ periodic upwelling and multipulse infills are shown in Figure 6.11.

Normally zoned granitoid plutons, in which in fractional crystallization is the dominant process, as shown in Figure 6.11(a) are expected to show a gradual inward increase in SiO_2. Pitcher (1993) argues on the basis of a worldwide survey that plutons with compositional trends such as depicted in Figure 6.10(a), are relatively rare in nature.

The inward increase of eTh, Zr and TiO_2, reflecting the association between radioactive accessories with biotite and Fe-oxides and the negative correlation of this association with SiO_2 appears to be at odds with normal zoning patterns. Because the map patterns of SiO_2, poorly reflect the TiO_2, Zr and eTh patterns and no clear fractionation trends have been found (Goff *et al.*, 1986) fractionation by itself could not have been the predominant factor in causing the zoning patterns within the Arch Lake granite. Because the two spatially distinct radioelement domains with spectrally distinct trends of eTh with K are not consistent with any of the models based on a single magmatic pulse, a scenario of multipulse injection is here favoured, even though the boundaries between these intrusive phases are apparently cryptic in exposure. These observations are in favour of the models shown in Figures 6.11(b) and 6.11(c). The positive trends between Th and U within the Th-rich domain, resulting in the identification of a U-rich and Th-rich domain in the cluster analysis, is consistent with trends resulting from late states of magmatic differentiation. They may represent compositional trends within the individual magmatic pulses, comparable to those shown in Figure 6.11(b).

If the subtle mineralogical variations associated with the radioelement zoning was not identified by detailed mapping (Godfrey and Langenberg, 1987), it is doubtful whether the contacts between the different phases can be recognized

anywhere in the field. Table 6.1 shows the modal analysis of the Arch Lake granite samples grouped for the Th-poor and Th-rich clusters shown in Plate 6.2 (B). The modal analysis obtained from the NE-Alberta data petrology data set (Goff *et al.*, 1986) was based on a minimum of 1000 counted points.

ClustersPlate 6.2(B))	Qtz	Plg	Kfp	Bio	Msc	Chl	Ep	Ass.	Tot	Zr	n
1: -K-eTh-eU & -eTh	27.3	27.7	39.6	2.91	0.87	0.89	0.62	0.32	100	164	35
2: +K+eTh+eU & K++eTh++eU	26.6	27.9	38.8	4.00	1.21	0.91	0.53	0.47	100	211	18
Two-sided t-test, 2 % sigf. Level $+: x_1 = x_2$, $-: x_1 \neq x_2$	-	-	-	+	-	-	-	-	-	+	-

Table 6.1 Mineralogy in % from point counting (Zr (in ppm) from chemical analysis) of Th-rich and Th poor clusters in Arch Lake granite. Data from Alberta Geological Survey Qtz = quartz, Plg = plagioclase, Kfp = K-feldspar, Bio = biotite, Msc =muscovite, Chl = chlorite, Ep = epidote, Ass.= accessory minerals, Tot = total.

Six samples were excluded from the data set because these samples were from the masked pixels of the cluster map. Zr from the chemical analysis was included to trace the mineralogical association between zircon and biotite. A two-sided student-t test at a significance level of 2% was implemented to test for significant differences between the mean model compositions between the two domains. The mineral compositions in Table 6.1 show that differences in modal percentages over the Th-rich and Th-poor domains are not significant with the exception of biotite and Zr content, again suggesting the association between biotite and radioactive accessory minerals. The subtle variations in biotite, ranging from about 3 to 4 % would be very difficult to recognize in outcrop but could raise the gamma-ray response from Th and/or U within the associated accessory minerals significantly. Moreover, considering that the boundaries between the radioelement domains are predominantly subparallel to a penetrative solid state foliation, the deformation of the Arch Lake granite may have obscured any contact relationship in outcrop beyond field recognition.

The spatial association between monazite and zircon with biotite is a common theme of peraluminous granites (Ford and O'Reilly, 1985; Charbonneau, 1991; Legault and Charbonneau, 1993; Charbonneau *et al.*, 1997). Zircon and monazite possibly acted as preferential nucleation sites for the crystallization of biotite or were shielded from solution in clots of restite material. Berman and Bostock (1997) explained the higher percentages of primary biotite in the Slave and Arch

Lake granites in comparison to the Konth granite as due to increased activity of H_2O or a decrease in temperature in their formation and emplacement. Similar more subtle variations may have caused the variations in biotite within successive stages of melt generation and emplacement that formed the Arch Lake intrusion. The close spatial association between radioactive accessory minerals and biotite, may have been enhanced by the generation of melt in biotite dehydration reactions. Monazite and zircon may have gone in solution in quartzofeldspathic components, whereas they remained relatively inert if they were shielded by biotite. This may have lead to a preferential concentration of accessory minerals in biotite rich phases preserved in situ or mobilized in restite at decreasing temperature or increasing H_2O activity. This interpretation has general implications for the interpretation of gamma-ray spectrometry surveys over granitoid intrusions. Zoning in the radioelements may not only reflect magmatic fractionation, but may also reflect compositional variations in melt due to changes in the compositions of parent materials or metamorphic conditions during melt formation and emplacement. The associated subtle mineralogical variations may be related to the intensity of migmatization and the composition of the parent materials, possibly controlling the amount and composition of in situ or mobilized restite. To test such hypothesis and to fully unravel the petrogenetic significance of the chemical and mineralogical differences between the intrusive phases of the Arch Lake granite requires detailed geochemical work. That the variations in biotite and accessory mineral content may directly reflect the compositional variation of the progenitor has been previously suggested on the bases of geochemical modeling results (Goff *et al.*, 1986). The multiple internal euhedral zoning within rounded crystals of monazite, indicate that Th- and U-bearing mineral fractions have been assimilated as solid residues.

With the available data and current level of observation, the degree to which late- to post-magmatic hydrothermal processes and weathering have affected the distribution of radioelements is difficult to assess. Particularly U is known to mobilize due to hydrothermal processes or to become depleted by weathering (Dickson and Scott, 1997). The first of the two processes may explain, as inferred above, the U anomalies along the periphery of the Arch Lake granite and the internal U anomalies associated with the NNE trending brittle shear zone. Th is, however, immobile relatively to U and the eTh anomaly patterns do not appear to be associated with the internal shear zones rich in Th-bearing secondary minerals, such as sphene and epidote. Even when some of the Th is mobilized in secondary alteration products, these generally remain in spatial association with primary minerals. It was shown in Section 6.6 that there is broad correspondence between

regional concentric patterns of eTh and interpolated patterns of TiO_2 and Zr. Textural evidence indicate that zircon, monazite and sphene occur in spatial association to biotite of which monazite is the predominant and most Th-rich phase. These observations suggest that the eTh anomaly patterns reflect Th fixed to the early stage products of magmatic crystallization.

The effect of post-emplacement strain on the radioelement concentrations remains another poorly known factor. Gamma-ray laboratory spectral measurements have shown that the radioelement concentrations of gneisses derived from granites were not significantly altered (Dickson and Scott, 1997). Radon risk assessment studies in the Appalachian region of the Eastern United States, however, have shown that U (and the daughter isotope radon) may be enriched in shear zones due to the introduction of U-bearing fluids and volume loss associated with grain-size reduction of U-bearing accessory minerals (Gundersen, 1991). The mylonitization at lower temperature ($T < 500^oC$) may have enriched K as a result of the breakdown of K-feldspar to muscovite in reaction-assisted deformation (Dixon and Williams, 1983; Hippertt, 1998). Considering, however, the overall lack of a consistent relationship between the Th dominated radioelement zoning and the distribution of shear zones and the relative immobility of Th, with respect to U (Gundersen, 1991), these effects are considered to be subordinate in comparison to primary compositional variations. It can, however, not be excluded that some of the internal U anomalies near the internal shear zones and anomalies at the eastern margin of the batholith may be associated with hydrothermal enrichment induced by mylonitization.

The overall concordance between concentric foliation and radioelement zonation pattern in combination with geochronological evidence suggest that the internal foliation patterns were initially formed in response of strain induced by emplacement, although more evidence is required to confirm this geometrical interpretation. Transcurrent flow along the LLSZ and CLSZ also may have facilitated emplacement by creating space and most likely controlled the overall sheet like geometry further north and the high aspect ratio of the Arch Lake batholith.

Lineaments on Landsat TM and magnetic data correspond to offsets of the magnetic anomaly, radioelement patterns, and displace the high grade LLSZ in an apparent dextral sense. In the absence of detailed field observations any explanation on the regional kinematic significance of these zones remains highly speculative. Kinematic field observations, from the mylonite zone at Daly Lake, are scarce but suggest dextral movement at upper greenschist metamorphic conditions. Considering the northward decrease in total width of the Arch Lake

batholith, one interpretation for the westward gradient in apparent offset is that the E-W trending shear zones accommodated strain incompatibilities between domains of variable shortening, somewhat analogous to differential shortening in thrust belts along tear faults. Down-dip lineated mylonites in the margins of the LLSZ and CLSZ, the north trending macroscopic folds inferred from foliation trajectories (McDonough *et al.*, 1994(a) and 1994(b)) and rare N-trending open mesoscopic folds within and along the margins of the Arch Lake batholith (Chapter 2), suggest that part of this shortening may have been accommodated under ductile deformation conditions. The way in which the strain was partitioned over ductile respectively brittle deformation regimes, however, remains unanswered.

6.9 Summary and conclusions

Gamma-ray spectrometry data acquired over the exposed Arch Lake granite in Alberta show a conspicuous and complex radioelement zoning, in particular eTh, that reflect mineralogical variations in the batholith that have not been recognized in field mapping and geochemical sampling campaigns. The integrated analysis of gamma-ray spectrometry, aeromagnetic Landsat TM, geochemical provides a tool to map the regional extend of the compositional and structural patterns within the batholith in Alberta and provides in combination with previously collected geochemical and structural data insight in the most probable processes of origin. Because the subtle differences in mineralogy in association to the radioelement zoning may be difficult to detect in the field, enhancement and spectral analysis of gamma-ray spectrometry data is valuable in supplementing traditional field methods in mapping compositional variations in granite intrusions. In addition, irrespective of the pretogenetic interpretation of radioelement zoning patterns, the integrated enhancement of gamma-ray spectrometry data with optical image data and structural field observations provide strain markers that yield insight in the post-emplacement deformation history of syn- to prekinematic batholiths. The main findings obtained from the analyses of the Arch Lake granite are summarized in the following:

1. A ternary radioelement image of the Arch Lake batholith in Alberta shows a central high with eTh concentrations that exceed 12 ppm circumvented by a Th-low. The outer margins also show high Th concentrations with local U anomalies exceeding 5 ppm.

2. Spectral analysis of gamma-ray spectrometry data by unsupervised classification and analysis of scatter diagrams detected subtle trends that were overlooked in interpreting ternary images of the K, eTh and eU grids. Two spectrally distinct trends evident in K-eTh space of flight line data correspond to the eTh-rich central and circumventing Th-poor domains of the zoning pattern. Cluster analysis further subdivided these domains into U-poor and U-rich sub-domains. The U-rich clusters in the Th-rich domains are on the bases of their correspondence to the highest Rb/Sr ratio and high SiO_2 content and U anomalies in the enveloping country rocks interpreted as the most evolved intrusive phase. This stage may have resulted in hydrothermal U-enrichment of the country rock.

3. Thin section studies indicate the coexistence of the thorium bearing minerals monazite and zircon that together with hematite and magnetite occur in spatial association to biotite. The high correlation of Zr with TiO_2 and TiO_2 with Fe_2O_3 and moderate correlation of biotite with Zr, biotite with eTh, Zr with eTh and Zr with eTh/K are interpreted to partly reflect this mineralogical association. The correspondence analysis between interpolation patterns of SiO_2, TiO_2, Zr and the Rb/Sr ratio with the gamma-ray spectrometry data is important to verify the association between the geochemical patterns and the airborne radioelement concentrations in a spatial sense. Such analysis is restricted here to a global comparison, because of the low sample density of the geochemical data over the pluton and the high nugget effects in the semivariograms of the major and trace elements. Considering these limitations, the central eTh and eTh/K anomalies appear to broadly correspond to spatially interpolated patterns of TiO_2 and Zr, whereas the spatial pattern of SiO_2 and Rb/Sr poorly reflect the overall zoning.

4. On the basis of the spatial and spectral analysis of the gamma-ray spectrometry, the Arch Lake intrusion is shown to be composite. The presence of spectrally and spatially distinct radioelement signatures within the Arch Lake granite, the step-like inward increase in the eTh/K ratio and the moderate negative correlation between the thorium rich mineralogical association and SiO_2 are not consistent with normal zoning resulting from fractionation within a single magmatic pulse. Considering, in addition the shear-zone related setting, a scenario of multipulse emplacement offers a favourable explanation for these observations. Detailed geochemical work from sample profiles normal to the zoning pattern is essential to test this interpretation and to

further unravel the petrogenetic significance of the Th-rich mineralogical association.

5. The spatial association between radioactive minerals and biotite, reported in this study and other studies of peraluminous S-type granitoid intrusions has implications of the interpretation of gamma-ray spectrometry data over granitoid intrusions. The zoning in airborne K, U and Th, may not only be due to magmatic fractionation, as generally inferred in the literature, but may also reflect the amount and composition of restite and/or variable metamorphic conditions at successive stages of melt generation and emplacement.

6. IHS composite images by combining the K, eTh and eU grids with an enhanced Landsat TM image provides combined visualization of lithogeochemical and structural information, with minimal loss of the relative spectral and spatial integrity of the data (Chapter 5, this thesis). Application of the cylindrical IHS transform allowed enhancing subtle curvilinear patterns in Landsat TM data in intensity contrast at cost of chromatic contrast of the K, eTh and eU grids. In combination with an overlay of mineral foliation data, this image allowed to study the relationships between the compositional patterns and internal structure of the batholith.

7. The combined visualization of radioelement domains and foliation trends, suggest a complex post-emplacement deformation history with interference of NNE and SE to E striking shear zones. There is an overall concordant relationship between the internal radioelement zoning, the internal foliation trajectories and the sheared margins of the batholith. U-Pb zircon ages constrain the emplacement of the Arch Lake granite to be approximately synkinematic with respect to mylonitization of its margins. The overall internal concentric patterns of the solid state foliation parallel to the sheared margins suggests that the Arch Lake suit was emplaced forcefully by mechanisms such as ballooning or diapirism.

8. East-west trending offsets of the zoning pattern correspond to Landsat TM and magnetic lineaments and previously mapped mylonite zones. Local field checks along these lineaments confirm their structural significance. East-west trending high-grade mylonitic gneisses along one of these lineaments are reworked to ultramylonite and cataclasite at and below greenschist facies metamorphic conditions, suggesting a locally complex deformation history

after emplacement. The kinematic significance of the east-west trending shear zones is at present poorly constrained and further field verification of the lineaments and previously mapped internal mylonite zones is required. Scarce kinematic data, however, suggest a dextral sense of shear along greenschist grade mylonite and ultramylonite zones, consistent with dextral apparent offsets of the Th-rich central zone and the arched outline of the southern sector of the batholith.

7

INTEGRATION OF ERS-1, AEROMAGNETIC AND FIELD DATA FOR MAPPING SHEAR ZONES, CHARLES LAKE SHEAR ZONE*

ABSTRACT

In this chapter a strategy for mapping shear zones by the integrated interpretation of synthetic aperture imaging radar, airborne magnetic and structural fabrics is presented. An important component of this integration strategy is focussed on establishing the genetic relationships between the aeromagnetic data, imaging radar data and structural fabrics using available field observations and magnetic susceptibility data. Ground validation of inferred structural features from the ERS-1 scene shows that mylonite zones are preserved as linear topographic highs shown as bright zones on this SAR image, whereas linear anomalies on vertical derivative magnetic data predominantly reflect pre-existing structural trends along the shear zone. The mapped surface trace of the CLSZ corresponds to a central total field magnetic low that best fits a vertical to steeply east dipping dike assumed to be inductively magnetized in a reverse direction. This magnetic body, extending downwards from the near subsurface, reflects a zone of magnetite oxidation genetically associated with mylonitization under retrograde metamorphic conditions. The complementary image expressions provide a synergistic view of regional shear zone geometry that has been exploited for structural interpretation. The integration methodology offers a reconnaissance tool to predict and map shear zone geometry in unevenly exposed terrain and poorly mapped areas.

---

* Part of this chapter is based on the publication:

Schetselaar, E.M. and McDonough, M.R.M., 1996, Shear zone mapping using ERS-1 SAR images of the Paleoproterozoic Taltson magmatic zone, Canadian Shield, northeastern Alberta. ITC Journal 1996-2, pp.166-175.

7.1 Introduction

The mapping and kinematic analysis of ductile shear zones is important to gain insight in the anatomy of the exhumed roots of orogenic belts and the associated processes of crustal deformation (Hoffman, 1989; Tapponier *et al.*, 1990; Hanmer *et al.*, 1992; among others). Although in many areas ductile shear zones have been mapped along strike in painstaking detail, many are poorly mapped, unevenly exposed or disappear underneath sedimentary cover. Even in well but discontinuous exposed terrain, the geometric map compilation of a shear zone from field observations is not always straightforward, bearing in mind that a belt of anastomosing sub-parallel splays may be mapped in many different ways from the same set of field observations.

Because remote sensing provides synoptic views over large regions of the surface or subsurface, several types of remotely sensed data have been used as a tool to trace shear zones in areas of sparsely or unevenly distributed field observation. Sultan *et al.* (1988) delineated structural features of the Nadj shear system for 1200 kilometers after restoring displacements associated with the Red Sea rifting on mosaics of Landsat TM scenes acquired over the Arabic-Nubian Shield in Egypt and Saudi Arabia. Yésou and Rolet (1990) mapped the structural trends associated with the Amorican shear zone by a lineament interpretation of multispectral SPOT scenes. Harris (1991) enhanced aeromagnetic, airborne radar and Landsat TM data for compiling a tectonic map of the Cobequid-Chedabucto fault systems and the Lundy shear zone in eastern Nova Scotia. Corsini *et al.* (1991) mapped a ductile strike-slip duplex structure that links the Patos and Pernambuco shear zones in the Proterozoic basement of northeastern Brazil using a mosaic of Landsat TM scenes and structural field observations. Broome and Henderson (1992) analyzed the geometry and kinematics of the Wager Bay shear zone in the Northwest Territories, Canada from aeromagnetic data and structural field observations. Although most image interpretations of these studies were substantiated by field observations, relatively little attention has been directed towards establishing the relationships between aeromagnetic anomalies, image lineaments and field data in more detail. A better understanding of the image expression of shear zones should lead to more effective enhancement procedures and should ultimately increase the geological significance and validity of structural interpretations of shear zones on the basis of remotely sensed data.

The purpose of this chapter is to outline the relationships of linear trends on ERS-1 and aeromagnetic data to the structural fabrics of the Charles Lake shear

zone (CLSZ). The CLSZ is part of a system of north-south trending ductile transcurrent shear zones that is exposed for about 300 km from Lake Athabasca to Great Slave Lake in the Northwest Territories (Figure 7.1). The CLSZ forms an anastomosing system of splays of mylonite formed at variable metamorphic grade with local preservation of high-grade kinematic indicators that are consistently sinistral over a strike length of more than 100 km (McDonough *et al.*, 1995). A detailed review of the structural fabrics of the CLSZ and its kinematic interpretation (McDonough *et al.*, 1995 and unpublished data) has been provided in Chapter 2. Aeromagnetic and ERS-1 data show an excellent expression of this shear zone. The individual (Figures 3.3 and 3.5) and combined interpretation (Plate 3.6) of the remotely sensed data set, presented in Chapter 3, revealed that there is a close agreement between linear high wave-number anomalies on total field magnetic data and lineament patterns on the ERS-1 scene. A high degree of correlation between the azimuths of these linear trends and the strike orientation of planar structures measured in the Taltson basement indicate that these structural trends reflect gneissic and mylonitic foliation.

To assure that the enhancement and integration of ERS-1 and aeromagnetic data is meaningful with respect to regionally interpreting shear zone geometry, it is important to confirm that these structural trends either represent pre-existing or tectonically induced planar fabrics in relation to the deformation history of the shear zone. Therefore, prior to the integrated enhancement and interpretation of the data set, ground validation procedures were conducted to verify if the structural trends shown on the magnetic and ERS-1 data are related to gneissic and mylonitic fabrics. These validation procedures included: (1) a detailed ground validation of inferred structural features from the ERS-1 scene, (2) a comparative analysis between magnetic susceptibility measurements, magnetic profile maps, 2-D inversion models and structural fabrics across a segment of the CLSZ and (3) a comparison of lineaments automatically extracted from gridded total field magnetic data and the ERS-1 scene with strike-lines of gneissic and mylonitic foliations. Because linear trends shown on remotely sensed data may represent a variety of geological or other natural or man-made features (Drury, 1992), the validations are essential to attach geological meaning to structural interpretations. Linear features inferred in the image interpretations presented in Chapter 3, for instance, not only reflect foliation trends, but also represent brittle faults, fractures, dikes, glacial striations, moraines or lithological contacts. The general processing strategy implemented for the interpretation of the CLSZ presented in Figure 7.2, shows how structural and magnetic susceptibility measurements supported the ground validation and integrated interpretation of the remotely sensed data set.

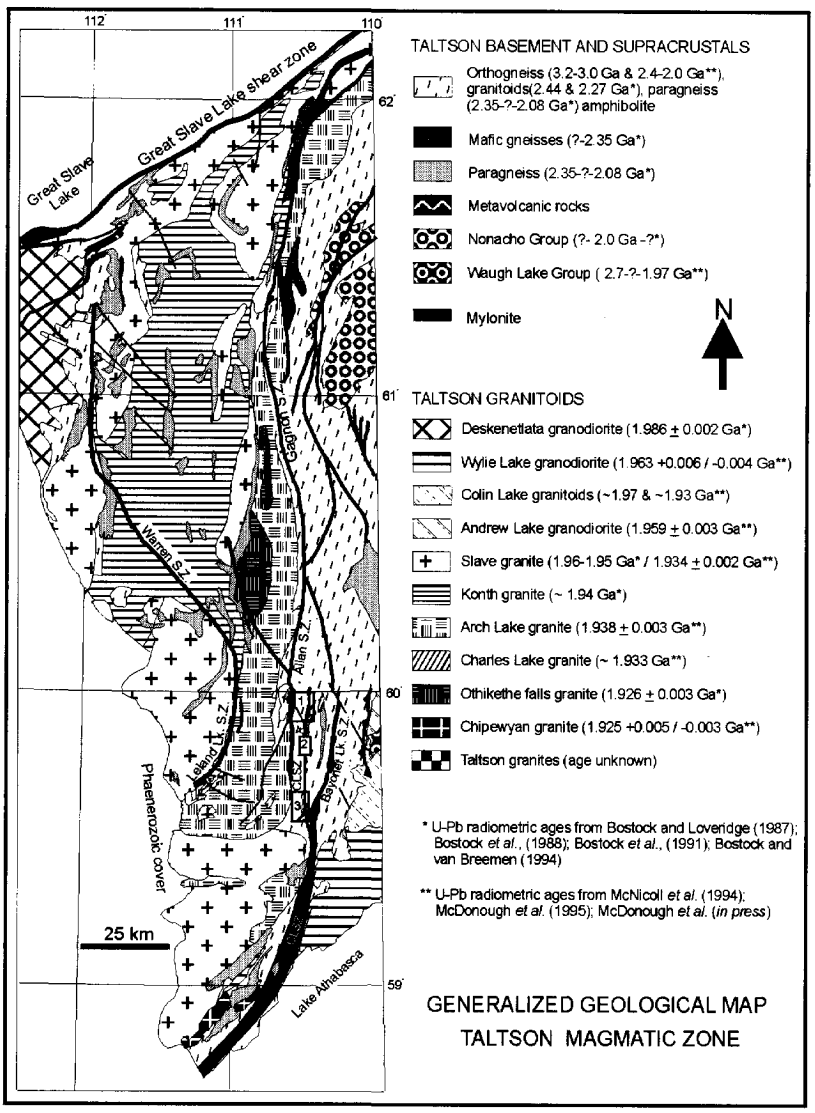

Figure 7.1 Generalized geological map of the Taltson magmatic zone after McDonough *et al.*, 1995 and Berman and Bostock, 1997. The large box indicates the area covered by the ERS-1 and aeromagnetic data set (Plate 7.1). Small boxes indicate validation areas: (1) control area for comparative orientation analysis (section 7.4, Fig. 7.11), (2) area for ground validation of aeromagnetic data (Fig.7.8), (3) area to illustrate interpretation details of IHS composite image (Plate 7.2) and geometrical features of the CLSZ (Fig. 7.15).

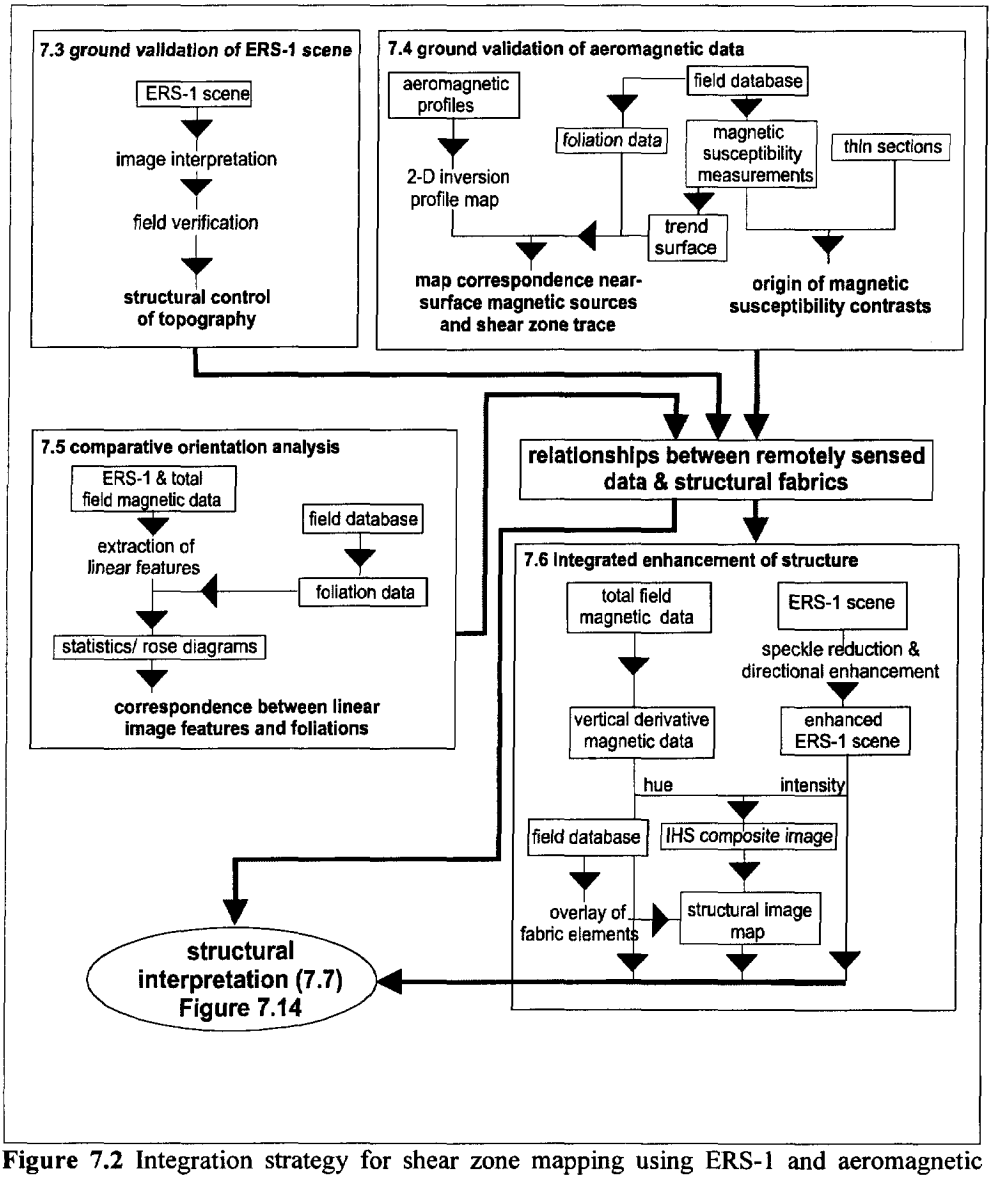

Figure 7.2 Integration strategy for shear zone mapping using ERS-1 and aeromagnetic data, magnetic susceptibility measurements and structural orientation data. The numbers of the boxes refer to the sections in the text.

7.2 Field description of the Charles Lake shear zone

The field descriptions presented in this section extend on the review of the CLSZ presented in Chapter 2. The CLSZ constitutes a braided system of anastomosing sub-vertical 0.5 to 1 km wide splays predominantly consisting of strike-lineated mylonite. The CLSZ passes into the strike-lineated Allen (ASZ) and Gagnon (GSZ) shear zones in the Northwest Territories together forming a crustal-scale transcurrent shear zone along the western margin of the Rae craton (Figure 7.1). Towards the north a dextral splay of the shear zone belt curves towards ENE direction into the lower amphibolite-grade mylonites of the Great Slave Lake shear zone (Hanmer *et al.*, 1992). The ductilely and cataclastically deformed parent materials mainly comprise orthogneiss of the TBC, Charles Lake granite, and granitoids in the margins of the Arch Lake and Wylie Lake intrusions. Paragneiss enclaves are rarely involved in the CLSZ, providing only local evidence to determine the metamorphic grade of mylonitization. The sparseness of indicative minerals and the continuous shear zone activity during slow protracted cooling to greenschist grade metamorphic conditions (Plint and McDonough, 1995) undoubtedly accounted to the conflicting interpretations in the literature of the metamorphic grade at which mylonitization commenced. Nielsen *et al.* (1981) interpreted the mylonites to have formed at greenschist-grade metamorphic conditions, on the basis of the widespread distribution of chlorite within the mylonite zones. Bostock *et al.*, (1984) and Hanmer *et al.*, (1992) interpreted the Allen and Gagnon Lake shear zones on the basis of their continuity with mylonites of similar grade in the GSLSZ and their mineral assemblage to have formed from lower amphibolite to greenschist grade metamorphic conditions. (McDonough *et al.*, 1995; Grover *et al.*, 1997) inferred granulite facies conditions during the initiation of mylonitization on the basis of straight striped fabrics composed of alternating layers of recrystallized feldspar and quartz ribbons and synkinematic granulite facies assemblages in protomylonitic paragneiss.

These protomylonitic fabrics, however, are not only found in the mylonite zones of the CLSZ, but occur throughout the gneisses in the Taltson basement. The field observations of the TBC gneisses described above indicate that mild mylonitization at granulite grade, accompanied folding and migmatization throughout the TBC. These fabrics, that were approximately formed at peak metamorphic conditions (Berman and Bostock, 1997; Grover *et al.*, 1997), may alternatively be considered as pre-kinematic with respect to the initial strain localization event that gave rise to the CLSZ.

Thin sections of paragneiss enclaves from the CLSZ, without evidence for retrogression at lower amphibolite to greenschist grade conditions, contain synkinematic sillimanite and muscovite growing parallel to alternating polycrystalline ribbons of recrystallized feldspar and quartz and sillimanite wrapping K-feldspar porphyroclasts. Garnet is abundant whereas cordierite and spinel are absent. K-feldspar porphyroclasts show undulous extinction, subgrain boundaries and myrmekite along their foliation parallel faces, suggesting medium- to high-grade deformation conditions (Passchier and Trouw, 1996). The metamorphic grade of this fabric is inferred to be retrograde with respect to the granulite facies assemblages of K-feldspar, sillimanite, garnet, cordierite and spinel. Although the extent to which these observations are regionally representative is not fully known, they locally indicate that the strain localization that gave rise to the CLSZ initiated at higher amphibolite grade metamorphic conditions. The widespread occurrence of epidote and synkinematic hornblende in mylonitized orthogneiss without signs of further retrogression suggests that these high-grade mylonites were extensively reworked into lower amphibolite grade mylonites. Mylonitized orthogneiss with strong shape-preferred orientation of quartz and flame perthite in K-feldspar porphyroclasts contain synkinematic blue-green amphibole locally wrapping the K-feldspar porphyroclasts. Kinematic indicators, such as shear lenses, sigma and delta type porphyroclasts, shape preferrred orientation of quartz and shear bands in amphibolite rafts consistently indicate a sinistral sense of movement (McDonough *et al.*, 1995).

Upper greenschist- to lower amphibolite grade strike-lineated mylonites with mineral assemblages of quartz, green biotite, muscovite and epidote preferentially reworked Charles Lake granite into subvertical sheets of coarse porphyroclastic mylonite and locally along their contact with TBC gneiss into 10 meter wide zones of ultramylonite. Rounded K-feldspar porphyroclasts display typical core-mantle structures in thin section, consistent with low to medium-grade metamorphic conditions. Shear lenses, sigma-type porphyroclasts and C-S fabrics are consistently sinistral. Biotite and muscovite in these medium-grade shear zones are in turn retrograded to chlorite in low-grade shear zones (unpubl. obs.). Kinematic indicators comprise delta-type porphyroclasts, asymmetric pressure shadows of quartz around K-feldspar porphyroclasts, quarter mats of muscovite, C-S fabrics all consistently displaying a sinistral sense of shear (unpubl. obs.).

A major splay of the Charles Lake shear zone, the Bayonet Lake shear zone (BLSZ, Figure 2.3), forms a 1 to 3 km wide belt of sinistral and dextral high-grade strike-lineated mylonites (McDonough *et al.*, 1995). These high-grade mylonites

are locally reworked into discrete strike-lineated greenschist grade mylonites (McDonough *et al.*, 1995).

Domains of dip-lineated to oblique-lineated steeply dipping high-grade mylonites and mylonitic gneiss locally flank the strike-lineated domains of CLSZ and BLSZ. West of Lake Athabasca the main foliation swings about ten degrees eastward, passes into a 10 kilometer wide heterogeneous oblique- to dip-lineated wedge shaped domain of mylonitic gneisses and mylonites, maintaining steep dips, predominantly towards ESE (McDonough *et al.*, 1995, Plate 7.1(B)). Kinematic data in this oblique- to dip-lineated domains are scarce but both northwest and southeast directed tectonic transport directions have been inferred from oblique subgrain fabrics in quartz (McDonough *et al.*, 1995).

Both the dip-slip and strike-slip movement predate intrusion of the Chipewyan granites at 1.925 + 0.005/-0.003 Ga. and postdate intrusion of the Wylie granodiorite at 1.963 +0.006/-0.004 Ga. permitting these movements to be synchronous in a transpressional setting (McDonough *et al.*, *in press*). Further north the evidence for extensive retrograde reworking of high-grade fabrics to strike-lineated lower amphibolite to upper greenschist grade mylonite, however, strongly suggest that the CLSZ is multistage, in which events of strike-slip movement outlasted dip-slip movement.

7.3 The application of SAR images in mapping geological structure

Synthetic aperture imaging radar data (SAR), such as acquired by ERS-1, have been widely utilized for geological mapping in various physiographic settings (Elachi *et al.* 1982). Imaging radar has proven particularly useful in areas with dense forest cover similar to those in northeastern Alberta where optical sensors (e.g. Landsat TM) are of restricted use, because the spectral response of vegetation communities predominate the tonal and textural qualities of the image (Drury, 1992).

The SAR image response is controlled primarily by the physical properties of the imaged surface. In decreasing order of importance these are: surface attitude, surface roughness, and dielectric constant (Elachi *et al.*, 1982). Surfaces normal to the radar incidence yield a large amount of backscatter directed towards the receiver, and consequently produce bright image tones. Smooth, sloping surfaces with normals parallel to incident radiation tend to act as mirrors, yielding a very high response. Subtle variations in surface slope in areas of low relief are accentuated by radar imagery, especially for large incidence angles (Blom, 1988). Topographic features may be of smaller dimension than a single pixel (Blom *et al.*,

1984; Drury, 1992). For example, slope facets of 2 meter in width with favourable orientation were detected on SEASAT images with a pixel size of 25 m (Blom *et al.*, 1984).

The physiography of the Canadian Shield is particularly well suited for the use of SAR images for geologic interpretations (Lowman, 1995). Numerous studies from different parts of the Canadian Shield have demonstrated the utility of airborne and satellite SAR for geological mapping (Singhroy *et al.*, 1993; Schetselaar, 1994). The prevailing subdued relief of the Canadian Shield minimizes geometric distortions such as layover and foreshortening. As shown in Chapter 3, this allows to geometrically correct SAR images with reasonable accuracy without having to apply costly and computation-intensive topographic corrections (Lowman, 1995). Differential erosion by glaciation has in many areas etched out structure and lithology to a remarkable extent and the forest cover south of the tree-line forms a relative uniform reflector enhancing differences in backscatter due to variation in local incidence angle by topography (Lowman, 1995). The geological setting of the study area is a favourable one for the structural interpretation of shear zones from ERS-1 data. This is because of their general N-S strike and good topographic expression, such that the landforms are oriented perpendicular to radar energy that is incident from the east.

7.4 Ground validation of structural features inferred from ERS-1 data

In Chapter 3 a general interpretation was presented with outlines of the main structural features. In this section the results of ground verification of image inferred features associated with the CLSZ and other structural features are presented. These features, labeled A through H, are indicated on the geometrically registered ERS-1 scene (Figure 7.3). The interpretation of a photo-reproduction of this image during field mapping in 1993 and 1994 resulted in the identification of previously unmapped shear zone splays (Schetselaar and McDonough, 1996).

Despite locally dense vegetation cover, topographic highs of variable scale are effectively imaged in this glaciated terrain. Ductile shear zone splays are expressed as elongate N-S trending linear topographic highs with smooth outcrop surfaces parallel to the structural strike and gentle to moderately slope angles between ten to thirty degrees. A typical example of a smooth gently dipping outcrop surface of quartzo-feldspathic banded high-grade mylonite is shown in Figure 7.4. Because of the 23^{o} depression angle of the ERS-1 antenna, incidence angles from the east facing slopes are large, yielding large amounts of backscatter.

Figure 7.3 Geometrically corrected ERS-1 scene. Labels A through H refer to the inferred and ground-verified structural features discussed in the text.

The gently sloping to horizontal outcrop surfaces in the centre of the topographic highs, show dark image tones, which suggest radar smooth outcrop surfaces. The west facing backslopes are partly or completely in shadow and yield the darkest image tones. The net result is bright N-S trending lineaments bounded on the west by broader zones of darker image tones.

The Leland Lake shear zone (LLSZ) is underlain in large part by less resistant pelitic gneisses, and is therefore confined to a topographic low between the more resistant Slave and Arch Lake plutons. Within this low a few linear topographic highs suggest structural control by the LLSZ. The bright and most continuous response from LLSZ (A on Figure 7.3) coincides with the topographic front formed by the eastern edge of the Slave pluton, which effectively forms the western margin of the shear zone. This suggests that the topographic expression of shear zones is negative when they bound the margins of massive granitoid plutons. In contrast to the LLSZ, the CLSZ exhibits an anastomosing pattern of medium- to high-grade shear zone splays of mylonitized orthogneisses that form structurally controlled topographic highs with 10 to 80 m of relief and smooth outcrop morphology, yielding bright linear zones (B on Fig. 7.3) on the image. Subtle bends in the topographic highs (C on Fig. 7.3) are consistent with the bending of mylonite foliation trends within shear zone splays, indicating strong structural control of topography. A left-hand deflection of SAR lineaments trends towards the center of the CLSZ. It yields a composite sinistral fabric on the image that corroborates abundant sinistral kinematic information observed in outcrop and thin section (sigma-type porphyroclasts, shear bands, mafic pull-aparts, asymmetric pressure shadows and C/S fabrics). West of Cornwall Lake, a bright SAR lineation (D on Fig 7.3) coincides with mylonites on the western margin of the shear zone, and is in part attributable to the morphological expression of the eastern margin of the Arch Lake pluton.

The Shield in northeastern Alberta has been extensively scoured during Wisconsin glaciation. Drumlins and glacial striations indicate a predominant SW-ice transport direction (Bednarski, 1997). The strength of the bedrock against shear stress imposed by debris at the base of the ice cap is largely controlled by the internal strength of the intact rock, spacing of joints and fractures and dip of the fractures with respect to terrain slope (Selby, 1982). The uniform ice movement direction in combination with the uniform strike in the Taltson basement resulted in a strong structural control of the topographic relief. Interpretation of aerial photographs supported by map representation of glacial striations, mylonitic and gneissic foliation measurements, suggest that the mylonites are more resistant to glacial erosion in comparison to their protoliths.

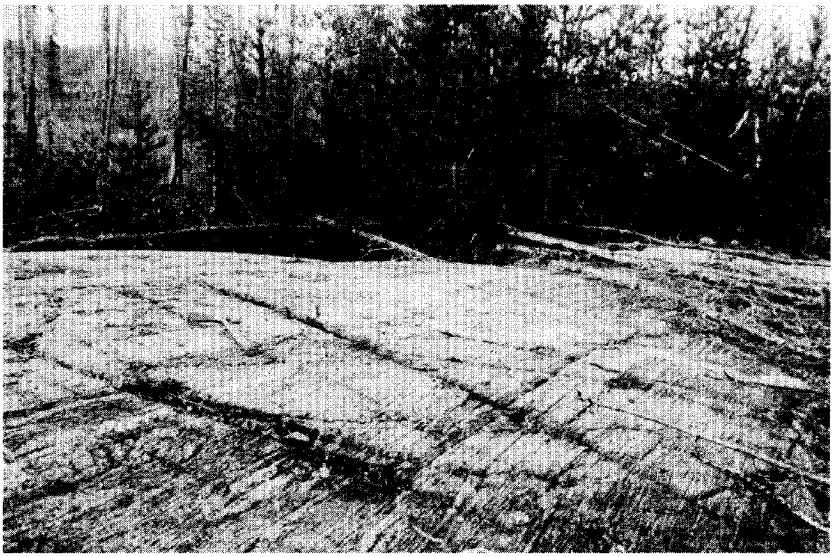

Figure 7.4 Photograph of banded mylonite, (looking north). Note the elongated outcrop morphology sub-parallel to the strike of the foliation and facing the ERS-1 look direction.

Figure 7.5 Landscape photograph of structurally controlled topographic low (looking NE). Such valleys are related to brittle fault zones that are shown as lineaments (H) on Figure 7.3.

Drumlins are preferentially developed in areas of low elevation underlain by gneisses of the Taltson basement. These areas flank the elongated topographic highs underlain by mylonite without evident glacial scours and drumlins (see Chapter 4, Figure 4.8). Three features of mylonites likely contributed to their high resistance to glacial erosion and preferred strike-parallel moulding, resulting in the generation of smooth elongated topographic highs:

1. Low joint density and preferred fracturing subparallel to mylonitic foliation that favoured abrasion and plucking perpendicular to the mylonitic foliations;

2. Dynamic recrystallization of quartzo-feldspathic hornblende bearing orthogneiss with low mica content resulted in grain size reduced and cohesive fabrics enhancing the resistance to abrasion, and;

3. Silicification by retrograde fluidization in the shear zone further enhanced resistance to abrasion.

Gneisses of distinctly different erosion potential are juxtaposed along steeply west dipping basement-cover contacts. Topographic lows appear to be underlain by pelitic gneisses bounded by thin zones of resistant mylonites at the basement contact. These interfaces may have acted as corner reflectors producing markedly bright zones (E on Fig 7.3) on the image.

Numerous thin bright zones (F on Fig 7.3) in the Taltson basement gneisses and paragneiss cover can be discerned east of the CLSZ. In the Potts Lake area, these coincide with previously unmapped greenschist grade shear zones that are associated with sulphide mineralization in pelitic gneisses. Several of these splays, not previously mapped, were identified in the ground verification campaign (Schetselaar and McDonough, 1996).

Some of the ground verified lineaments do not correspond to shear zones. For instance, the bright zone south of Potts Lake (G on Fig 7.3) is associated with pelitic gneisses that were crenulated and silicified at greenschist-grade metamorphic conditions into zones that parallel the axial planar crenulation cleavage, but do not occupy a shear zone. In addition, some shear zones are not obvious on the SAR image. The Bayonet Lake shear zone (Figure 7.1) has minimal topographic expression within a larger topographic high formed by ductilely deformed mylonitic basement gneisses. It therefore lacks the morphological expression necessary for generation of a SAR response.

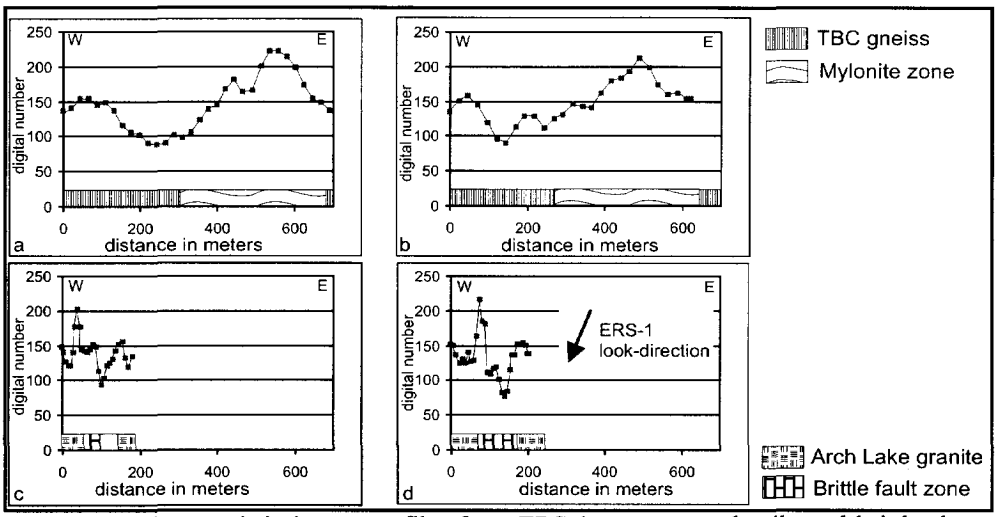

Figure 7.6 Characteristic image profiles from ERS-1 scene over ductile and brittle shear zones.

North-south brittle structures locally are parallel to the ductile shear zone splays upon which they are superposed. These features and other brittle fault zones, in contrast to ductile shear zones, are expressed as sharp lineaments (H on Fig 7.3) confined to topographic lows that are occupied by muskeg, swamps, or lakes. A landscape photograph of a structurally controlled topographic low over a brittle fault zone is shown in Figure 7.5. Cataclasites forming cliffs on their margins confirm that the lineaments pertain to zones of brittle deformation. Glacial scouring by plucking may be enhanced in such zones by high fracture densities and possibly by pre-glacial weathering. Image profiles over topographic highs and lows associated with respectively mylonite and brittle fault zones are shown in Figure 7.6. The marked differences in width and asymmetry between the profiles over ductile and brittle deformation zones illustrate their distinct image expressions.

7.5 Ground validation of aeromagnetic data

Watanabe (1965) analyzed the magnetic mineralogy and measured magnetic susceptibility of mylonites with respect to their parent materials in the Taltson basement. Laboratory and fieldwork revealed that the lower magnetic susceptibility of the mylonites with respect to their protoliths (Figure 3.2) resulted

from the oxidation of magnetite to hematite during mylonitization. In an attempt to reconcile these observations with recent field and aeromagnetic data, magnetic susceptibility measurements and total field magnetic profiles across a segment of the CLSZ were analyzed. The magnetic susceptibility measurements of powdered samples were obtained from the Alberta Geological Survey (Sprenke *et al.*, 1986)

The validation area was chosen across a segment of the CLSZ where the density of magnetic susceptibility measurements was the highest, yet limiting the assessment to thirteen samples (see Figure 7.1 for the location of this area). A second order trend surface was fitted through these thirteen magnetic susceptibility measurements and integrated with total magnetic field profiles. Magnetic profiles were selected for quantitative modeling using MAGMOD, an iterative non-linear inversion routine to compute the parameters of an inductively magnetized body of simple geometry (Geosoft, 1994). Four magnetic profiles over the CLSZ, with limited interference from secondary or adjacent magnetic bodies were considered suitable for inversion. In all four cases the best fits were obtained by using a tabular dike model with infinite depth and strike extent. The dike models and their associated depth, dip, width and susceptibility contrast parameters are shown in Figure 7.7.

Figure 7.8 shows the geological map compilation of the validation area (generalized after McDonough *et al.*, 1994). The protoliths of the medium-grade (amphibolite to upper greenschist-grade) mylonites in the central splay comprise the megacrystic Charles Lake granite and biotite-hornblende gneisses of the Taltson basement complex. The modeled magnetic bodies, shown in plan view in bold, are plotted to scale and annotated with the depth and susceptibility contrast parameters obtained from the best fits. Total field magnetic profiles were superposed as well as the magnetic susceptibility values and the derived second order trend surface.

The results obtained from magnetic inversion appeared to give geologically meaningful results when compared with the attitude of the foliation data. The locations of the dike models broadly correspond to the eastern margin of the mapped surface trace. The western margin is, however, not exposed but could, considering the width of the magnetic bodies, extend one kilometer further west underneath Charles Lake.

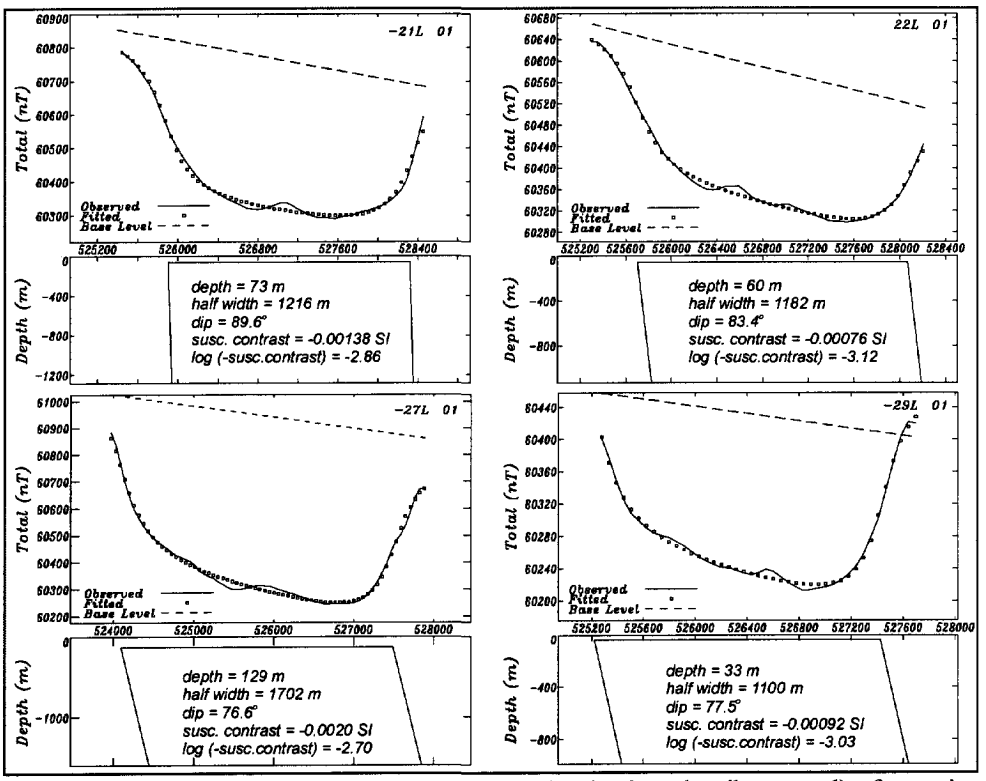

Figure 7.7 2-D dike inversion models (with infinite depth and strike extend) of negative magnetic anomalies over the central segment of the CLSZ (see Figure 7.8 for location).

Towards the south the magnetic low on the profiles bifurcates into two anomalies separated by a subsidiary positive anomaly. This pattern is broadly reflected in a widening and divergence of shear zone splays on the geological map and the magnetic susceptibility contour lines. The correspondence between the mapped surface trace of the CLSZ and the linear magnetic low suggests that this anomaly is genetically related to shear zone deformation (Figure 3.3).

The depths obtained from the vertical to steeply dipping dike models range approximately from 30 to 130 meters. The question why the models do not extend entirely to the surface can not be unequivocally resolved. It may be related to surface weathering that resulted in the alteration of magnetite and/or from the effects of topography, lakes and overburden. Similar depth ranges were previously obtained for the inversion of negative anomalies of the CLSZ further south and linear anomalies in the Taltson basement further east (Figure 4.12).

Also the magnetic susceptibility contrasts obtained from the inversions proved to be realistic, as the susceptibility contrasts obtained from the best fits are in the same order of magnitude as the gradient in magnetic susceptibility over the CLSZ.

The mylonitic foliations are predominantly located within the magnetic low. On the basis of striped fabrics consisting of alternating layers of recrystallized quartz and feldspar some of these fabrics were inferred to have formed under high-grade metamorphic conditions (McDonough *et al.*, 1995). In using such field criteria in inferring the metamorphic grade of the mylonites, the effects of alterations by retrogression are not considered. Alternatively, on the basis of their textural appearance in the field, some of these mylonitic fabrics could have been erroneously interpreted to be of high-grade origin due to the virtual absence of diagnostic peraluminous minerals. The metamorphic grade during mylonitization could have been high enough for the crystal-plastic deformation of feldspar into ribbons (T >500° C, Passchier and Trouw, 1996) but may have been low enough to alter magnetite. Thin sections of lower amphibolite facies mylonites with epidote and synkinematic hornblende, show extensive evidence for the breakdown of magnetite and ilmenite. Magnetite and ilmenite grains with coronas of sphene are enclosed in synkinematic hornblende. Magnetite is also commonly altered to hematite (Figure 7.9(B)). The lack of retrogression of hornblende in these samples suggests that the breakdown of magnetite and ilmenite initiated at or above lower amphibolite facies conditions. This interpretation is consistent with observations of Skilbrei *et al.* (1991) who found similar textural evidence for extensive breakdown of magnetite in granulite-grade gneisses retrograded in the amphibolite facies. It is not clear to what extend the alteration of magnetite to hematite resulted from the mylonitization or if it is purely the result of exogeneous alteration related to the infiltration of water in later formed brittle faults.

A comparison of the variations of the total field within the magnetic low (Plate 3.2) with the generalized geological map (Figure 2.3) and the magnetic susceptibility measurements (Figure 3.2) shows that magnetic susceptibility contrasts between the parent materials has also played a role. The lowest total field levels (~< -150 nT) within this negative anomaly (Plate 3.2) correspond to bodies of Charles Lake granite and paragneiss enclaves. These units have relatively low magnetic susceptibilities in comparison to the Taltson basement gneiss (Figure 3.2). This suggests that the magnetic low results from the combined effects of deformation and retrograde metamorphism superposed on susceptibility variations of the protoliths.

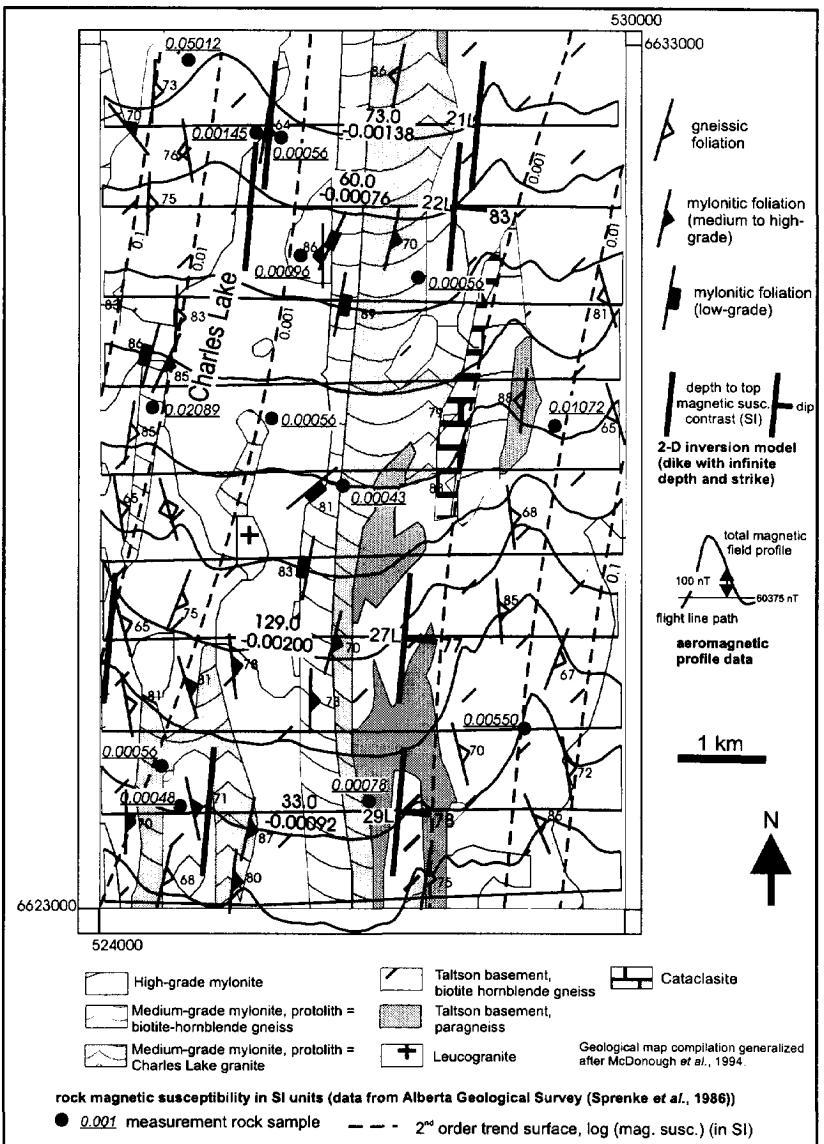

Figure 7.8 Map compilation of magnetic susceptibility measurement of 13 rock samples, aeromagnetic profiles, modeled magnetic sources (dike models), structural fabrics and geological units over segment of the CLSZ. Note the good correspondence between the location and direction of the trend surface, the central negative magnetic anomalies and the mylonitic foliation trends.

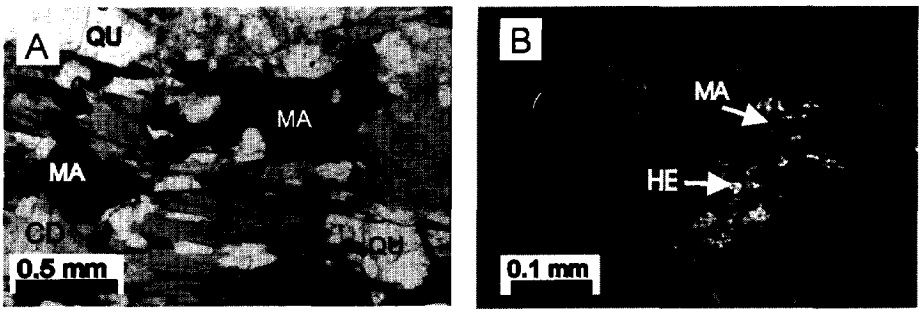

Figure 7.9 Microphotographs of magnetite bearing gneiss and mylonite. (A) Lobate elongated grain of magnetite in high-grade paragneiss (transmitted light); Magnetite altered to hematite in lower amphibolite-grade epidote and hornblende bearing mylonite, (reflected light view of the mylonitic fabric shown in transmitted light in Figure 2.5 (C));. CD = cordierite; BI = biotite; QU = quartz; MA = magnetite; HE = hematite.

The magnetic anomalies over the Taltson basement, east of the CLSZ, do not correspond to distinct lithological units, and may be associated with subtle compositional- or strain-induced variations in the growth, recrystallization and redistribution of magnetite along the foliation during regional high-grade metamorphism (Sprenke *et al.*, 1986). The metamorphic growth of magnetite during high-grade metamorphic conditions is consistent with PT peak metamorphic conditions over the Taltson basement (Grover *et al.*, 1997, see Chapter 2) and shown in thin sections where elongated magnetite with lobate grain boundaries constitute high-grade mineral assemblages in paragneiss (Figure 7.9 (A)).

7.6 Comparative analysis of magnetic and ERS-1 lineaments and foliation strike lines

Automated linear feature extraction was implemented on the ERS-1 and total field magnetic data in a control area in order to assess the correlation between the orientation ERS-1 and magnetic lineaments and structural fabrics measured with a geological compass as objective as possible. The control area is located in the extreme north of the study area (Figure 7.1) where it was envisaged that the expression of structure in the shear zone and the adjacent domains of lower finite strain permitted to extract sufficient lineaments in both data sets for comparing their orientation.

The automated extraction of lineaments from image data is based on techniques to detect strings of pixels with significantly different intensity. These techniques have received wide attention in the field of pattern recognition where they are known as edge detection algorithms (Budkewitsch *et al.*, 1994). A technique, universally applicable to geometric image analysis including edge detection, is offered by mathematical morphology.

Mathematical morphology, established in the sixties on the basis of set theory, offers an universal approach to geometrical image analysis and image algebra (Serra, 1982) and has been commonly applied for geological applications (Fabbri, 1984; Serra, 1982; Martel *et al.*, 1989). In practice the geometric aspects of an image are analyzed by morphologic filter operations (Serra, 1982). An elementary geometric figure, the structuring element is swept over every pixel of the image. At each pixel position the structuring element is compared with the underlying portion of the image with the same size as the structural element. Openings and closing was applied on the grey-scale images (8 bit images with 0-255 pixel value range) to extract local minima and maxima. The maximum operator (i.e., a dilation) assigns the local maximum value (the maximum value in the neighbourhood defined by the structuring element) of the image to the central pixel of the structuring element, whereas the minimum operator (i.e., an erosion) assigns the local minimum value to the central pixel position. By combining minimum and maximum operators the local extremes can be extracted from an image. An erosion followed by a dilation, is called opening and extracts local maxima from the image. A dilation followed by an erosion, is called closing, and extracts the local minima. To illustrate these concepts, an example of one-dimensional analysis along an image profile of a 40 X 40 ERS-1 image sample is shown in Figure 7.10. Figure 7.10(a) shows the profile of the unprocessed image. Figure 7.10(b) shows the result of applying an erosion to the image profile, using a symmetrical structuring element of 5 pixels with the origin of the element positioned at the central pixel. This operation reduces the peaks and enlarges the valleys. The erosion is followed by a dilation, which reduces the remaining valleys and enlarges the remaining peaks. The combined operation, i.e. an opening, results in the removal of local maxima with widths smaller then that of the structuring element. In order to extract these local maxima the function obtained by opening, shown in Figure 7.10(c), is subtracted from the original profile in Figure 7.10(d). A threshold is defined when the grey-scale image is converted to a binary image, extracting peaks of a user-defined amplitude (Figure 7.10(e)). This in combination with an opening or closing is known as the top-hat transform (Serra, 1982). Figure 7.10(f) shows the 40 X 40 image sample of the Lee filtered ERS-1 data.

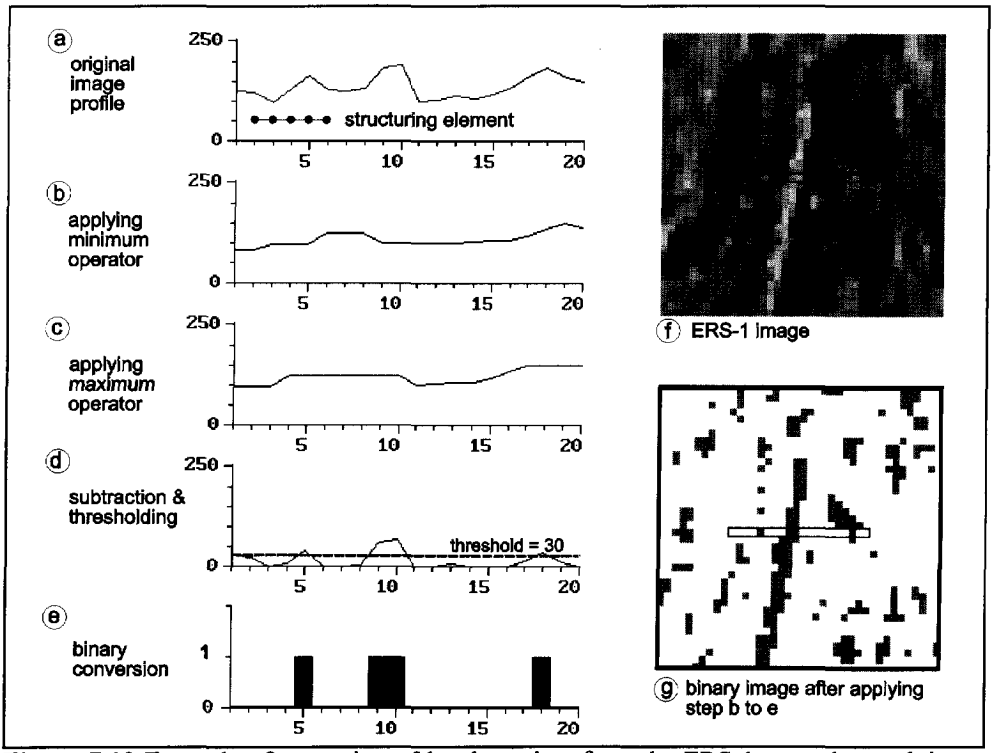

Figure 7.10 Example of extraction of local maxima from the ERS-1 scene by applying a top-hat transform with a two-dimensional structuring element (see the text for an explanation of the automated extraction).

The rectangular box in the centre of this image shows the pixels samples used in the one-dimensional analysis. Figure 7.10(g) shows the binary image resulting from opening and defining a threshold at DN 30. This image may be further improved by further processing using various types of binary filters.

The analysis of the ERS-1 image was focused on the extraction of local maxima by opening only. Closing on the dark linear features was omitted because this would result in the extraction of small lakes of which the shape is not structurally controlled. The total field magnetic data were first reduced to the pole to centre the anomalies above their source. Both local minima and maxima were extracted, because both appear to reflect the predominant structural trends. The widths of the edges to be extracted was constrained by a disk shaped structuring element with a diameter of approximately 7 pixels (diameter ranges between 7.6

and 7.0 due to the square image format). After setting thresholds on the grey-scale images that separated spurious pixels from linear patterns the images were converted to binary format for further processing. The threshold for the ERS-1 image was set at DN 30. For the magnetic data thresholds were not defined, as the initial extraction of extremes provided continuous linear features with low amounts of additive noise. A binary filter was applied to eliminate individual pixels. As a result small pixel clusters were removed after several iterations, while continuous shapes were preserved. A skeletonizing algorithm was applied to thin the linear objects (Gorte, 1994).

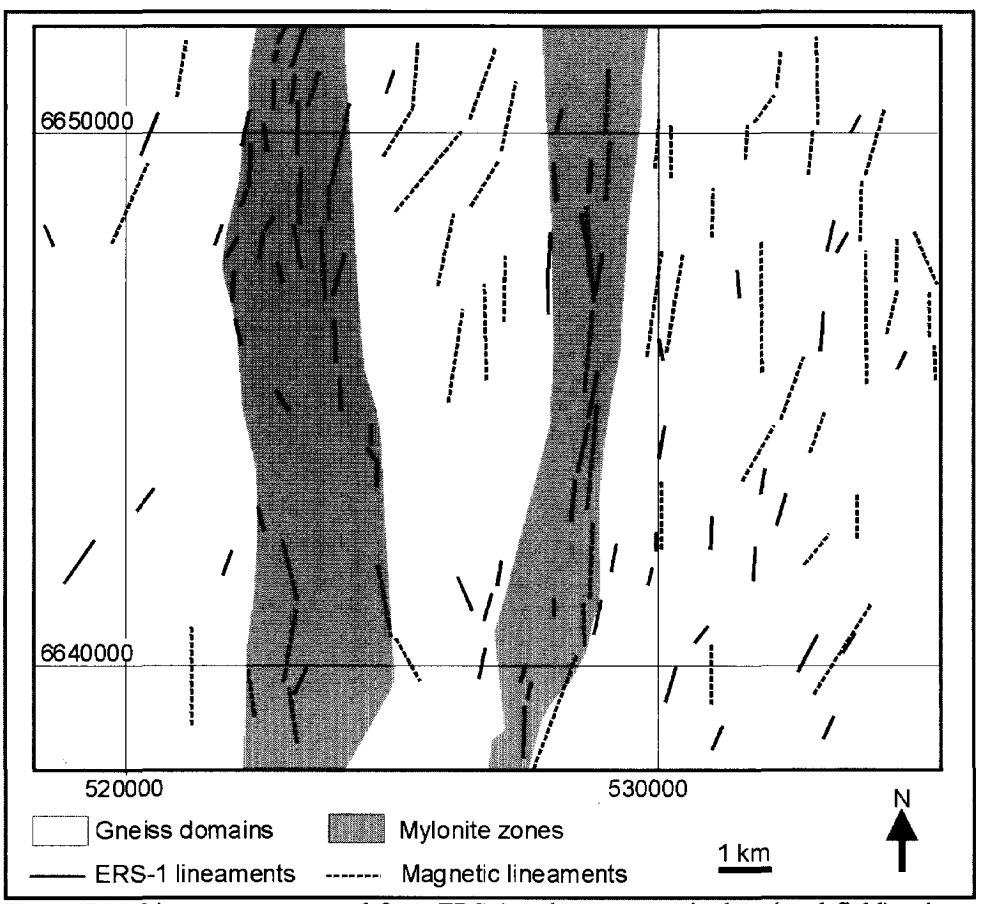

Figure 7.11 Lineaments extracted from ERS-1 and aeromagnetic data (total field) using a disk shaped structuring element with a diameter of 7 pixels.

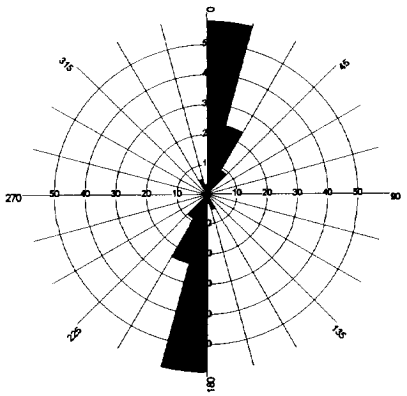

ERS-1 lineaments in gneiss domains (n = 34)

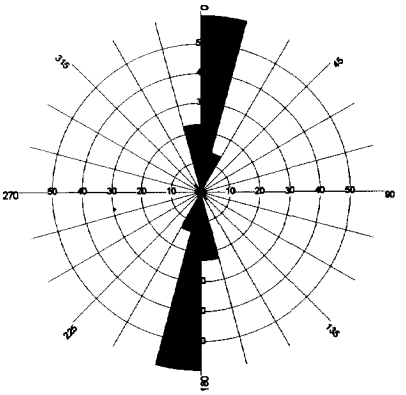

ERS-1 lineaments in mylonite zones (n= 38)

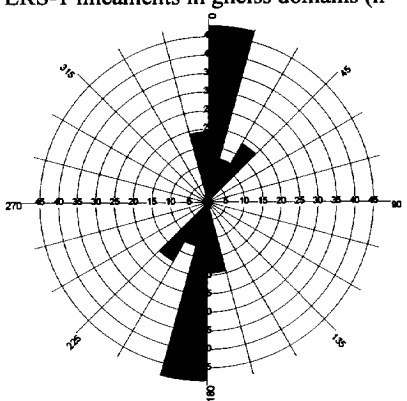

magnetic lineaments in gneiss domains (n = 41)

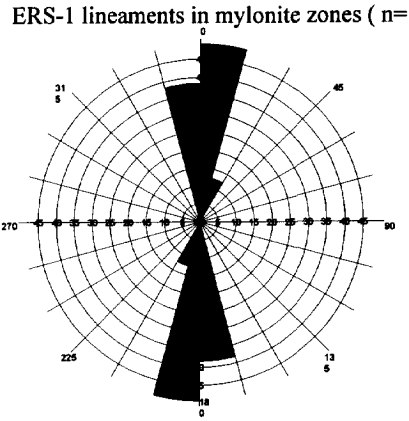

magnetic lineaments in mylonite zones (n=19)

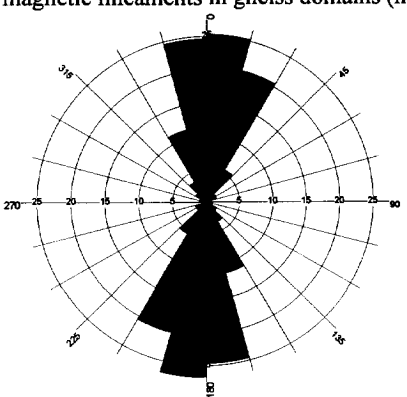

gneissic foliation strike lines (n=484)

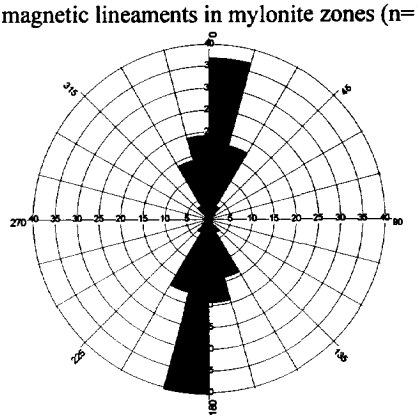

mylonitic foliation strike lines (n=57)

Figure 7.12 Rose diagrams of lineaments and foliation data.

Figure 7.11 and Figure 7.12 show respectively a map of the extracted magnetic and ERS-1 lineaments and the rose diagrams of the azimuths of the extracted lineaments and strike angles of the mylonitic and gneissic foliations in the two domains. Note the strong correlation in orientation between the strike lines and their close correspondence with the strike-angles of the foliation data. The similarity in the dominant directions between the mylonite zones and the gneissic domains reflects the low angular to concordant relationships between the structural trends in the gneissic domains and mylonite zones.

The rose diagrams of the magnetic and foliation strike lines in the gneiss domain show a secondary NNE trend. This secondary trend is also shown in Figure 7.11 and represents strike directions of pre-existing foliation in low-strain domains between and east of the shear zone splays.

7.7 Image enhancement and interpretation methodology

The analyses presented above confirm the existence of a strong association between surface lineaments, linear magnetic anomalies and structural fabrics within and along the CLSZ. The expression of the regional foliation in the ERS-1 image is primarily controlled by the scouring of glaciers that preferentially etched out the shear zone splays in the topographic surface. The new growth and redistribution of magnetite by deformation under high-grade metamorphic conditions produced linear negative and positive anomalies, outlining the pre-existing gneissic fabrics preserved in the domains of relative low strain between shear zone splays. Alteration of magnetite to hematite during retrogression destroyed this high-grade magnetic fabrics producing broad magnetic lows with lack of internal magnetic relief (Sprenke *et al.*, 1986). Because these structural expressions are complementary in outlining pre-existing and shear zone induced fabrics, an integrated interpretation approach has been implemented. Aeromagnetic and imaging radar, however, acquire measurements of the subsurface and surface respectively. Corresponding linear magnetic trends and ERS-1 lineaments are therefore not necessarily associated with the same structural feature. The integrated interpretation is thus limited to identifying coherent structural patterns and interrelationships in the data rather than analyzing linear features on an individual basis.

The enhancement and interpretation methodology is schematically illustrated in Figure 7.2. The first vertical derivative was computed from the total magnetic field to enhance high wave-number anomalies associated with shallow magnetic sources mainly reflecting the regional foliation pattern in the TBC. The first

vertical magnetic derivative data (Figure 3.2) was relief shaded using an illumination azimuth of 270 degrees and an elevation angle of 20 degrees above the horizon (not shown).

A 7 x 7 Frost filter (Frost *et al.*, 1982) was applied on the ERS-1 sub-scene for reduction of speckle. This filter, as well as other adaptive speckle reduction filters, weights smoothing against preservation of edges based on the local contrast in the filtered neighbourhood (7 X 7) of the pixel. Such a filter reduces speckle in homogeneous areas while preserving texture and other high frequency information in heterogeneous areas. Tests of the performance of different speckle reduction filters have shown that the Frost filter is particularly good in preserving linear edges in SAR images (Shi and Fung, 1994). The dynamic contrast of the filtered image was improved by masking radar rough water surfaces from the data set. A threshold on the co-registered TM 7 image of DN 10 effectively masked most of the water. Thereafter the image was filtered with a simple 3 X 3 linear filter for enhancement of north south oriented lineaments related to topographic highs using the following 3 X 3 kernel:

```
-1  0  1
-2  4  2
-1  0  1      gain: 1/12   offset: 0
```

The value of 4 at the central pixel position added back one third of the original image and preserved the image expression of the topographic highs (dark image tone of the western backslopes and bright image tone of the eastern foreslopes). Linear contrast enhanced intermediate and final results of these processing steps and the originals of two image samples are shown in Figure 7.13. Note that the expression of topographic highs is retained after speckle reduction (Figure 7.13 (b) & (f)) and that image contrast is enhanced after masking water surfaces with rough radar signature (Figure 7.13 (c) & (g)). The enhanced total field-, first vertical derivative magnetic and ERS-1 images were first interpreted individually. Profile and colour- shaded relief representation of the total field were used in combination with the inversion models to outline the central magnetic low over the shear zone. The first vertical derivative magnetic data permitted to outline structural trends in the high-grade gneiss domains along the shear zone, whereas the enhanced ERS-1 scene was optimal in outlining structural trends within the shear zone.

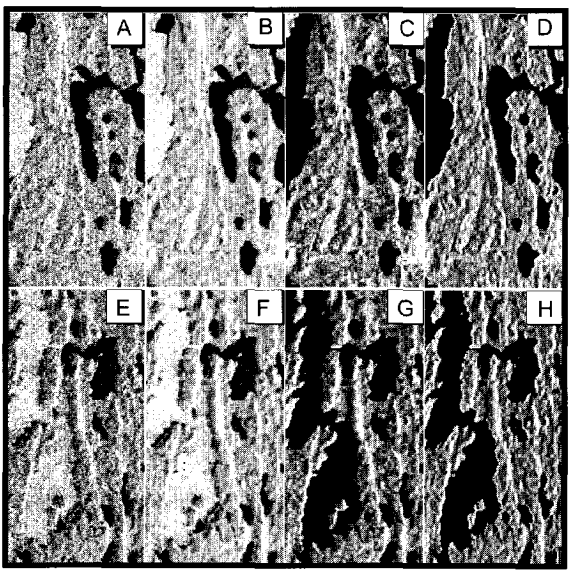

Figure 7.13 Image samples from the ERS-1 scene to illustrate the effects of enhancements; (A,E) unprocessed, (B,F) after speckle reduction (Frost filter), (C,G) linear stretch after masking radar-rough water surfaces; (D,H) directional enhancement of N-S lineaments using 3/3 sobel filter.

In order to assess the spatial interrelationships between the structural expressions and verify the continuity of structural trends from one interpretation to the other, the processed ERS-1 sub-scene was integrated with vertical derivative magnetic data to be visualized in a IHS composite image.

The cylindrical IHS transform was used for optimal enhancement of the ERS-1 sub-scene. The vertical derivative magnetic data were assigned to hue by rescaling the 4 byte range to a range of 0 - 360 degrees. The filtered SAR image was assigned to intensity and scaled to a range of 0-1, whereas saturation was held constant at 40 % of the maximum saturation. This saturation level was considered optimal in maintaining maximum intensity contrast with preservation of hue contrast. To retain the image signatures of the vertical derivative magnetic data over water, the water masked pixels of the processed ERS-1 image were set equal to an intensity of 0.7. A map compilation of mylonitic and gneissic foliations was overlaid on the IHS composite image to support the structural interpretation of the image patterns.

Plates 7.1(A) and 7.1(B) show respectively the IHS composite image and a map compilation of an area of approximately 30 x 110 km extending from the west shore of Lake Athabasca to the border with the Northwest Territories with the main inferred structural trends. Note that the southern portion of the image extends beyond the southern limit of the ERS-1 scene and only displays the vertical derivative magnetic. Because a constant intensity level was assigned to the water

masked pixels, the magnetic anomalies can be easily traced over lakes without interference of the geological insignificant response from water. The masking procedure, however, introduced small patches of dark pixels inherited from TM band 7. These patches represent pixels over water from the Landsat TM image with digital numbers exceeding the threshold used for masking water pixels. Plate 7.2 shows an enlarged part of Plate 7.1 to illustrate examples of image patterns where the integrated visualization of the enhanced magnetic and ERS-1 leads to a complementary expression that facilitates structural interpretation. The following examples, indicated with the same numbers on Plate 7.2, were identified:

1. Lineaments on the ERS-1 image complements the magnetic data by providing structural detail in areas with absence of internal magnetic relief, such as the principle splay of the CLSZ.

2. On the other hand, where regional foliation is not expressed due to sedimentary cover or water, only the magnetic data contribute in the expression of structure.

3. In areas of complex magnetic response the magnetic data leads to an undersampled representation, typically leading to bull-eye shaped anomaly patterns between the flight lines. Provided that there is good correspondence between parallel structural trends in both data sets, the spatially continuous acquisition and relative high spatial resolution of the ERS-1 data, assists in tracing the most likely alignment of such ambiguous anomaly patterns.

4. Due to the relative high spatial resolution and continuous acquisition, sharp lineaments can be seen in the intensity contrast from the ERS-1 data that are not apparent in the hue contrast of the vertical derivative magnetic data. Some of these lineaments offset or abut the magnetic anomalies providing interpretation guidelines for tracing the continuation, deflection or truncation of structures.

The lithological units on Plate 7.1 were recompiled from the generalized geological map of the area (McDonough *et al.*, 1996) whereas the foliation trajectories are based on the interpretation of Plate 7.1(A). The regional compilation of the foliation data was derived from structural field observations of McDonough *et al.* (1995) and supplemented by data sets from Godfrey (1980) that provide a denser distribution of foliation data in the granitoids. Stereographic

projections show the distribution of foliation and lineation data of two structural domains outlined by dashed lines.

7.8 Structural interpretation

A detailed interpretation of the structural features of the CLSZ is shown in Figure 7.14. The CLSZ, on total field magnetic data identified as a prominent linear magnetic low, is also reflected in the vertical derivative magnetic data as a linear and prominent anomaly with low internal relief. Linear positive and negative anomalies, that flank this high strain zone, show generally good correspondence with the strike of mylonitic and gneissic foliations. A left-handed deflection in the foliation trajectories occurs along the central splay of the CLSZ (box A on Figure 7.14). These deflections may be explained by bending-in sense of older or contemporaneous planar fabrics as the zone of higher strain is approached. Such deflections are commonly used as a shear sense criterion (Henderson and Broome, 1990; Ramsay, 1980; White *et al.*, 1986) and such a criterion has been inferred from bending on linear trends along shear zones on magnetic anomaly maps in other areas (Henderson and Broome, 1990). Shear sense indications inferred on the basis of remotely sensed data should obviously be treated with caution and always require field verification. It should be confirmed that the line defined by the intersection of the deflected planar markers and the shear zone is normal to the image plane and that the movement direction lies within the image plane (e.g. the image plane is about parallel to the XZ plane of the finite strain ellipsoid; Passchier and Williams, 1996). Moreover, without field data it is difficult to rule-out alternative kinematic explanations for deflecting structural trends, such as local perturbations of the flow field or previous folding events that are unrelated to the strain history of the shear zone.

Figure 7.15 shows a detailed structural map compilation over part of the deflection pattern west of the CLSZ with outlines of the structural interpretation (annotated by broken lines). Kinematic indicators within the medium-grade mylonites that are indicated with symbols on this map consistently show sinistral sense of shear (Figure 7.16). The map compilation shows that some of the deflecting trends outline a subsidiary splay of the shear zone. This splay represents a concordant dike-like body of Charles Lake granite mylonitized at lower-amphibolite to upper greenschist grade conditions.

Narrow ten-meter wide zones of ultramylonite form the contacts between TBC gneiss and Charles Lake granite sheet-like body suggesting that this contact is a rheological interface that controlled strain localization. This splay dies out further

south in a domain of Taltson basement gneiss, in an area where in the field no strain gradients were apparent. Both mylonite foliations and stretching lineations bend from an orientation parallel to CLSZ towards a NNE strike direction. These observations suggest that the deflected trends can not be considered as passive markers but partly outline a local subsidiary synthetic splay that parallels curved panels of high-grade gneiss. The parallel relationship between the pre-existing high-grade gneiss and lower-grade mylonites and ultramylonites along this splay may be explained by local transposition along planar surfaces bounding panels with contrasting rheology. Such interfaces may have controlled strain localization that formed the secondary splay under retrograde metamorphic conditions. In a hypothetical model for such strain localization, shown in Figure 7.17, it is envisaged that the Charles Lake granite intruded the shear zone after cooling below granulite grade metamorphic conditions (McDonough *et al*, in press) but prior to strain localization in the lower amphibolite to upper greenschist facies (Figure 7.17 (A)). During cooling from high-grade to medium-grade metamorphic conditions, the intrusive contacts between the Charles Lake granite and the TBC, acted as rheological interfaces in localizing strain (Figure 7.17 (B)).

In the extreme north a mega-scale lens of gneiss, between bifurcating splays (B on Figure 7.14) shows structural NE striking trends. These trends parallel steep (70-80°) NW-dipping foliations that strike about fourty degree clockwise with respect to the mylonitic foliation in the shear zone. A sigmoidal pattern with a similar angular relationship occurs between two mylonite splays further south (C on Figure 7.14) and is also reflected in the strike orientations of the foliation measurements north of Cornwall Lake (Figure 7.15). Geometrically these structural trends outline patterns with monoclinic symmetry that seem analogous to outcrop-scale C/S fabrics (Berthe *et al.*, 1979). In this analogy the gneissic foliation within this wedge would correspond to S planes, while the two bounding shear zones splays would represent C planes. Yésou and Rolet (1989) inferred kilometric scale C/S fabrics from enhanced SPOT images of the Amorican Shear Zone, Brittany, France, from the type locality of their outcrop-scale analogues described by Berthé *et al.* (1979). The scale-invariant geometry of C/S like fabrics ranging from the thin section to continental scale has been recently addressed by Hippertt (1999). If these patterns would truly represent the mega-scale analogue of a C/S fabric it should be confirmed, however, that the S and C planes formed approximately synchronously. Such a synchronous relationship can not be confirmed in the study area, as the C planes correspond to domains of localized strain that experienced extensive retrograde reworking, whereas the S planes represent pre-existing high-grade gneiss fabrics.

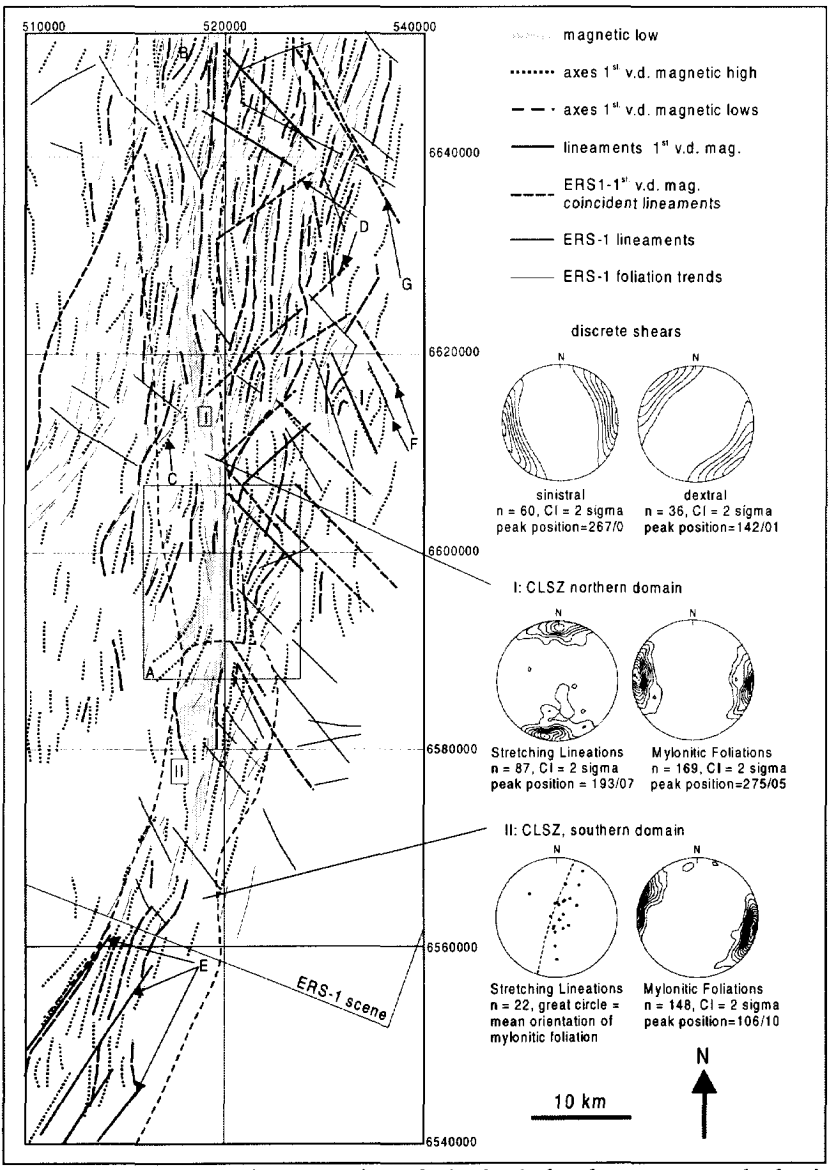

Figure 7.14 Structural interpretation of Charles Lake shear zone on the basis of ERS-1 and aeromagnetic data. Labels A through G indicate inferred structural features discussed in the text.

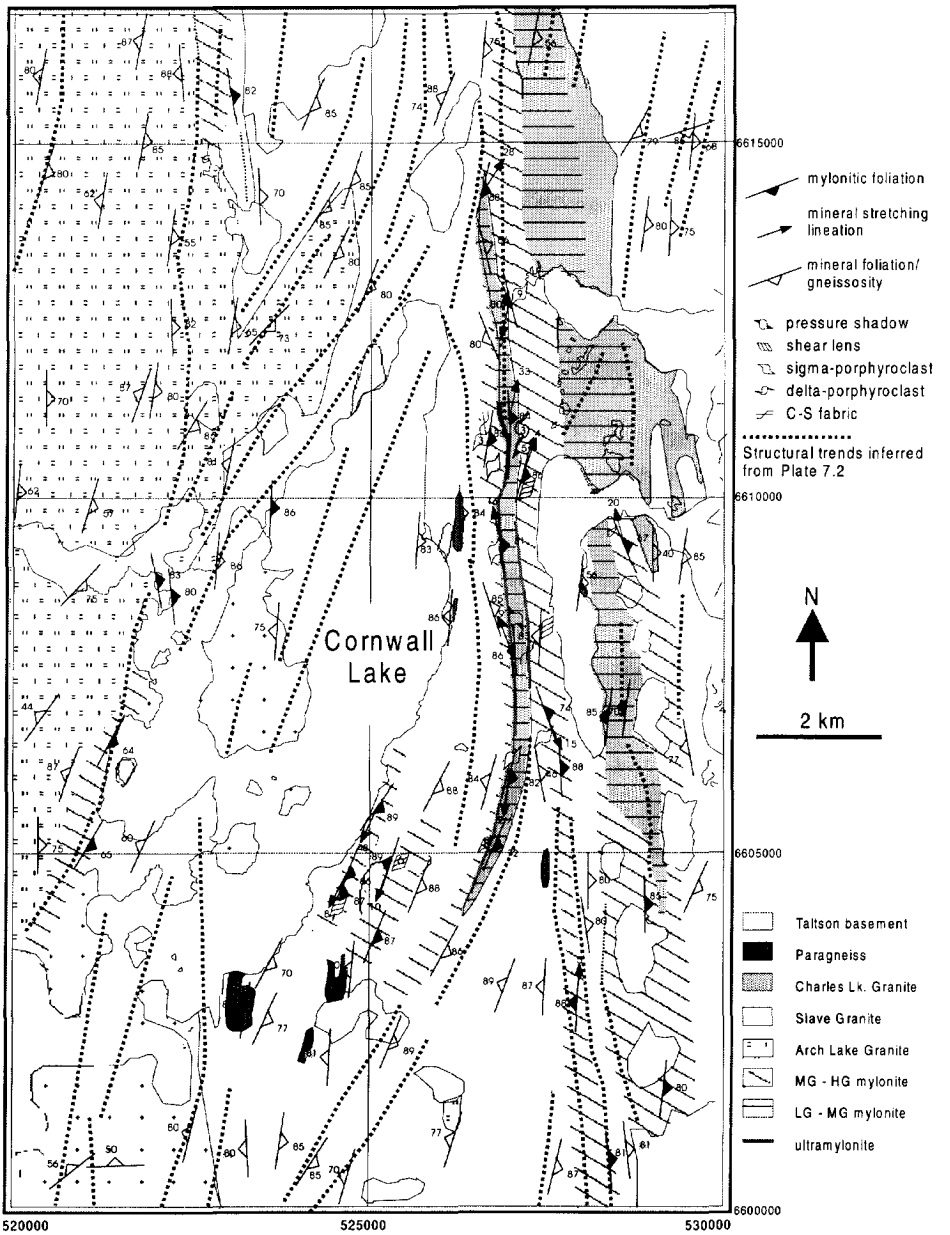

Figure 7.15 Map compilation of the CLSZ from structural fabrics, shear sense indicators and interpreted structural trends in the Cornwall Lake area.

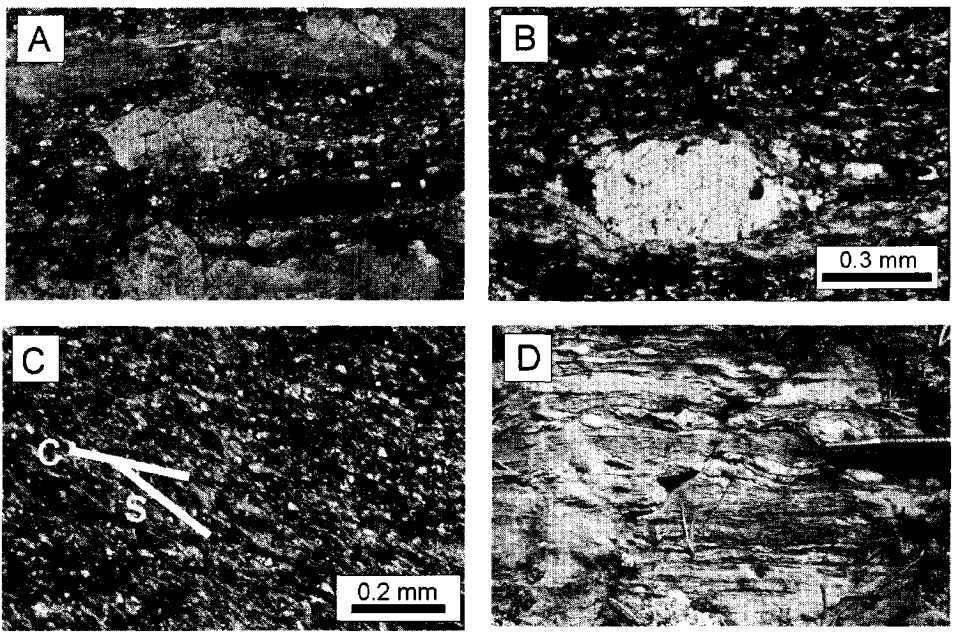

Figure 7.16 Outcrop and microscopic kinematic indicators in medium-grade mylonites in the Cornwall Lake area. In (A-C) protolith is Charles Lake granite in D the protolith is biotite-hornblende gneiss; (A) Sigma-type winged K-feldspar porphyroclast transected by anthithetic slip surface in heteroclastic protomylonite; (B) Pressure shadows of quartz at K-feldspar porphyroclast (crossed polars); (C) C/S fabrics in crossed polarized light; (D) Foliation fish and sigma-type feldspar porphyroclasts.

Figure 7.17 Hypothetical model for the formation of a secondary shear zone splay. The dike-like intrusion of the Charles Lake granite that predated mylonitization at greenschist metamorphic grade (A) gave rise to a rheological interface (possibly because the solidified granite was still hot) that became a secondary zone of synthetic shear during mylonitization at greenschist metamorphic grade as the contact rotated towards a parallel orientation with the walls of the shear zone (B).

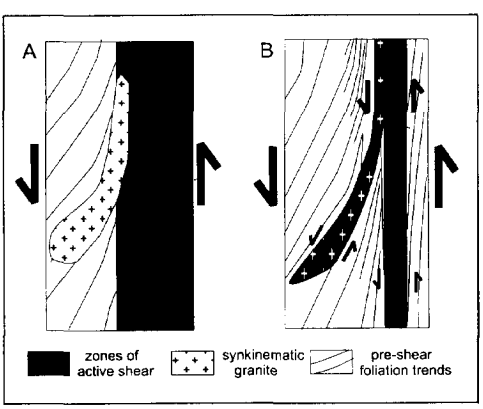

There is also no field evidence for mega-scale duplex-like structures within these domains. Alternative outcrop-scale analogues such as shear lenses (Ghosh and Sengupta, 1987), or abrupt strain transitions along anastomosing splays (Bell and Hammond, 1984) may provide better outcrop-scale explanations for these mega-scale asymmetric patterns.

East of CLSZ the magnetic anomalies are truncated by a system of NE-striking lineaments (D on Fig. 7.14). The magnetic anomalies and some of the foliation data show a weak deflection towards these lineaments (Plate 7.1(B)).

The southernmost lineament of this system corresponds to a lower greenschist grade shear zone with dextral C/S fabrics that displaces the eastern splay of CLSZ in dextral sense (McDonough *et al.*, 1995). Another NE-striking lineament system is evident within domain II (E on Fig. 7.14). Both systems correspond in orientation to outcrop-scale discrete extensional shears that form with similar sinistral shear striking NNW a conjugate set of lower greenschist grade shears (See stereographic projections in the inset of Figure 14). This conjugate system accommodated bulk SSW-NNE extension, in which the synthetic sinistral system, in analogy to extensional shear bands (Platt and Vissers, 1980), strikes about five to ten degrees west from the N-trending mylonitic foliation in the CLSZ. Another set of NW-striking lineaments (F on Fig. 7.14) corresponds to a brittle fault system, One of these lineament (G on Fig. 7.14) corresponds to a brittle fault zone with an apparent sinistral displacement of about 4 km (McDonough, 1997). This fault system is regionally extensive throughout the western Canadian Shield and related to the emplacement of the McKenzie dike swarm (Lowman, 1994).

7.9 Summary and conclusions

Shear zones, forming linear topographic highs are expressed as bright zones on SAR imagery and linear anomalies on vertical derivative magnetic data such that they, in combination with structural field data, provide a complementary image of the regional geological structure. The fist vertical derivative of the magnetic data predominantly show structural trends that outline pre-existing high-grade planar fabrics, whereas the ERS-1 data preferentially show structural trends outlining mylonitic fabrics within the higher strain zones. Hence, IHS composite images of ERS-1 and vertical derivative magnetic data with overlay of foliation and lineation data provide a synergistic view of the shear zone. Provided that the relationships between the aeromagnetic data, ERS-1 and structural fabrics can be locally established, the integration methodology presented in this chapter offers a reconnaissance tool to predict shear zone geometry and map shear zones in

unevenly exposed terrain, underneath overburden and in poorly mapped areas. Features of the shear zone, identified in this integrated image analysis, include: the regional trends of pre-existing and shear zone-related planar fabrics, bifurcating and subsidiary splays and the outlines of the zone of high strain accumulation formed by intense mylonitization during retrograde metamorphism. The following summarizes the main conclusions of applying the integration methodology on the well-exposed Charles Lake shear zone:

1. The location of pluton margins with respect to shear zones and the high resistance glacial erosion of quartzo-feldspathic mylonites versus adjacent gneisses are the most important factors controlling the topographic expression, and therefore the SAR response of shear zones in the Taltson magmatic zone. The topographic highs show a marked contrast with the topographic lows associated with zones of brittle deformation, suggesting that the SAR image data acquired over glaciated terrain may provide unique opportunities to distinguish between brittle and ductile structures.

2. The surface trace of the CLSZ corresponds to a prominent magnetic low superimposed on the magnetic susceptibility contrasts between protoliths that can be fitted to a vertical to steeply east dipping dike model extending downwards from the near-subsurface. The range in magnetic susceptibility contrast obtained from the magnetic inversion is in agreement with susceptibility measurements of rocks sampled at the surface. The magnetic low outlines a zone of retrograde mylonitization regionally reflecting the breakdown of magnetite and ilmenite in the lower amphibolite and greenschist facies. Because the magnetic relief within this zone is subdued, the ERS-1 complements the lack of internal structural expression in the high strain zone in the IHS composite image.

3. The combined representation of SAR image data and first vertical derivative magnetic data on IHS composite images provides complementary information that serves as a tool to interpret the regional-scale geometry of shear zones by the interpolation of mylonite fabrics between field stations. The radar/magnetic IHS composite image proved to be particularly useful in identifying local truncations, deflections and displacements of structural magnetic anomaly trends along sharp lineaments in the intensity modulated radar image seen through the magnetic data modulated in rainbow spectrum. The integration of magnetic and radar data has previously been successfully

applied in mapping regional structures (Harris, 1991; Mussakowski *et al.*, 1991). To attach geological meaning to the interpretation of such merged image composites, it is essential to verify that the linear features in both the magnetic and ERS-1 data are related to the trends of the same structural fabrics.

4. Structural trends of planar fabrics in domains of relative low strain show a systematic angular relationship with respect to the structural trends and planar fabrics in the high-strain zones. These low strain domains occur as lenses between individual splays of the CLSZ and the Taltson basement east of the CLSZ, display more easterly strike angles with respect to the north trending foliation trajectories in the shear zone and locally appear to deflect towards individual splays of the shear zone. Detailed field mapping is required to verify whether these mega-scale patterns are genetically associated with shear zone kinematics or whether they are the preserved manifestations of earlier deformation events.

5. The left-hand deflection of SAR lineaments and magnetic anomalies across the CLSZ is confirmed to reflect a similar deflection in mylonitic foliation data. The asymmetry of this deflection is consistent with sinistral sense of shear deduced from abundant kinematic indicators from field and thin section observations. The extent to which previous deformation events or local perturbations of the flow controlled this geometry, however, is not clear. Local subsidiary synthetic secondary shear zones splay-off from the central higher strain domain in parallel orientation to the high-grade gneiss fabrics indicating local strain partitioning along pre-existing planar fabrics.

6. A lineament system was identified that probably corresponds to a system of NE striking shears. One of these lineaments corresponds to a lower-greenschist grade dextral shear of confined width. The shears were recognized on the vertical derivative magnetic/ERS-1 IHS composite image by the deflection of linear anomalies along lineaments in the ERS-1 data. The orientation and apparent deflection of these lineaments in combination with observations of local but similar shears in the field suggest that they are the regional scale expression of the dextral set of a conjugate system of greenschist-grade ductile shears. Synthetic sinistral shears strike, on average, eight degrees west, whereas antithetic dextral shears strike on average fifty-three degrees east to the mylonitic foliation. The dextral set is preferentially

developed in the CLSZ. This conjugate system formed relatively late in the deformation history accommodating bulk SSW-NNE directed extension. NW trending lineaments correspond to a system of brittle faults that is extensive throughout the Slave and Churchill provinces and parallels the McKenzie dyke swarm.

8

INTEGRATION OF LANDSAT TM, GAMMA-RAY, MAGNETIC AND FIELD DATA TO DISCRIMINATE LITHOLOGICAL UNITS IN VEGETATED GRANITE-GNEISS TERRAIN*

ABSTRACT

Image classification of geological units in vegetated granite gneiss terrain from multispectral data is hampered by vegetation cover and limited spectral contrast of its lithological variations. In this chapter an alternative methodology is presented employing airborne gamma-ray spectrometry and magnetic data. The methodology includes the selection of combinations of data channels and their transformations to enhance the discriminative power of the lithology classification. An analysis of the training set compiled from 2795 field stations, showed that the K, eTh and eU gamma-ray spectrometry and total and residual magnetic field channels provided an overall classification success rate of 65 percent for a total of ten lithological units. Parametric classifications based on this training set yielded 67 percent coincidence with the geological map, whereas a neural network classifier provided only 23 percent coincidence. Exploiting the spatial autocorrelation of the geophysical signatures by adding averaged filtered channels slightly improved the coincidence percentage to 70 percent and enhanced the continuity of linear enclaves within larger lithological units. The contribution of magnetic data to the classification depends on to what extent the anomaly spectrum and its processed derivatives reflect surface geology. It was found that both the short and long wavelengths in the spectrum contributed to the classification performance. This is explained by the geological structure of the area where both broad and narrow units extend downward sub-vertically. A comparison of the results with regional geological map patterns identified targets for map refinement and exploration.

---

* This chapter is based on the publication:

Schetselaar, E.M., Chung, C.F., Kim, K.E., 2000, Integration of Landsat TM, Gamma-ray, magnetic and field data to discriminate lithological units in vegetated granite-gneiss terrain. Remote Sensing of the Environment, v. 71, pp. 89-105.

8.1 Introduction

Image classification techniques for lithological mapping have been successfully applied using multispectral optical remote sensing data in arid and semi-arid areas. The application of multispectral data has obviously been less successful for mapping lithology in vegetated terrain where the bedrock is partly or completely hidden by forest canopy or extensively covered with moss and lichens (Satterwhite *et al.*, 1985; An *et al.*, 1995). In such areas, lithological units can only be inferred indirectly if there is an association between the vegetation and the underlying bedrock substrate (Harrington *et al.*, 1991; Belanger, 1991). Irrespective of vegetation cover, additional limitations apply to granite gneiss areas where the prevalent granitoid and gneissic units have similar mineralogies with relatively small variations in quartz, plagioclase, alkali-feldspar, mica, amphiboles, pyroxenes and accessory minerals. Spectra of these rock types show only subtle differences in the position and depth of visible and short wavelength infrared absorption features that may not be resolved by sensors with broad bands, such as Landsat TM (Mather *et al.*, 1998). New sensors, such as the advanced spaceborne thermal emission and reflection radiometer (ASTER) acquiring six channels in the thermal infrared, enhances the capabilities of discriminating lithology, as it enables to detect diagnostic features in the spectra of silicate minerals (Michael J. Abrams, pers. comm., 1999).

Alternative data for mapping granite-gneiss terrain are provided by airborne gamma-ray spectrometry and magnetic data indirectly reflecting radioactive and magnetic accessory mineralogy of the bedrock. Gamma-ray spectrometry data provide estimations of the concentrations of potassium (K), uranium (eU) and thorium (eTh) in materials at the Earth surface. It has been shown that ternary colour images of the K, eTh and eU channels reflect many of the lithological variations in granite-gneiss terrain (Broome, 1990; Charbonneau, 1991; Jaques *et al.*, 1997). Although gamma radiation emitted from bedrock is not masked to the same extent as electromagnetic radiation of the optical and infrared wavelengths, gamma radiation is attenuated by overburden, wetness and vegetation (Grasty *et al.*, 1984). Magnetic data are not attenuated by surface cover but because a potential field is measured, the anomaly spectrum reflects magnetic sources from near surface to depths of 10 km or more.

Dependent on the geological setting, magnetic data may poorly reflect surface geology. Additional complexities arise from the orientation of the induced magnetic field, which may yield anomaly patterns that are asymmetric in shape and have peaks that are offset with respect to the sources. These properties restrain

the registration of individual magnetic anomalies with their associated features on geological maps. Patterns of magnetic anomalies, however, may closely match the outlines of bedrock units if rock units with strong magnetic susceptibility contrasts extend from the surface downward with a sub-vertical to vertical orientation. A vertical inclination can be simulated by reduction to the pole to center the anomalies above their source. Other processing routines (downward continuation and vertical derivatives) are useful to emphasize the effects of near-surface magnetic sources (Telford, 1990).

8.2 Objectives

In this chapter an approach is presented for mapping lithological units in vegetated granite gneiss terrain by integrating gamma-ray spectrometry, magnetic and field data. The objectives are:

- To evaluate the contribution of the geophysical variables and their derivatives in the classification performance of bedrock units, particularly with respect to magnetic data.

- To compare the performance of various classification algorithms in a training area where control from field observations and detailed geological maps was available.

- To analyze the classification results of the total study area in a reconnaissance context by interpreting the differences between the classified- and regional geological map patterns.

In the context of the last objective, the classification is not considered here as a technique aimed at replacing traditional geological mapping. Instead it is conceived as a reconnaissance mapping and interpretation technique to assist the geologist in fieldwork planning, map compilation and the identification of areas for map refinement and exploration. It can also be considered as an automated and more objective approach in comparison to the attempt presented in Chapter 3 to combine the visual interpretations of the data in a single map compilation.

Airborne- and ground radioelement concentrations correlate well for the major granitoid plutonic suits, although airborne concentrations are generally lower because of the attenuation effects of overburden, wetness and vegetation (Charbonneau *et al.*, 1997). Thin sections of the granitoid units show that the

accessory minerals monazite, uraninite and zircon primarily control thorium and uranium concentrations. Because potassium anomalies over bedrock are not related to mineralization, potassium in outcrop areas also most likely reflect primary compositional variations (Charbonneau *et al.*, 1997). Some potassium anomalies, however, relate to glacial sediments rich in potassium feldspar.

Linear regression analysis between multispectral TM- and gamma-ray signatures have shown that the eU channel is less attenuated by vegetation and overburden in comparison to the eTh and K channels (Lavreau and Fernandez-Alonso, 1991; Schetselaar and Rencz, 1997). This lower attenuation of the eU channel is probably due to the inhibition of radon gas in water saturated soil, a daughter isotope formed in the decay series of uranium (Grasty *et al.*, 1984). The correlation coefficients between outcrop abundance and gamma-ray signatures are moderate, ranging from 0.3 to 0.5, and the relationships spatially vary with changes in multispectral signatures of the ground cover over the study area due to forest burns (Schetselaar and Rencz, 1997). Therefore no systematic correction for differential attenuation could be applied for the entire study region.

Usually the number of lithological units involved in classification experiments range from four to eight, suggesting that application areas are chosen that are geologically simple (An *et al.*, 1995) or contain assemblages composed of a mixture of rock types (Mather *et al.*, 1998). In this study, the latter type of simplification was applied by the recompilation of the eighteen lithological units shown on six 1:50,000 geological maps to a total of ten units. For example, enclaves of amphibolite and small leucogranite with maximum dimensions of one to a few hundreds of meters locally occur within the Taltson basement complex. These units were masked, because their longest dimensions, broadly perpendicular to the geophysical flight lines, are an order of magnitude smaller than the 1-km flight line spacing. Therefore these small units are not adequately represented in the training set.

Mylonites and cataclasites, associated with shear zones were masked as well. Due to the intense deformation within shear zones, the mineralogy and fabric of the original rocks are altered so that the lithologies within shear zones do not represent their unaltered equivalents. Descriptions of the lithological units can be found in Chapter 2. Table 8.1 summarizes the field characteristics of the eighteen map units and provides the rationale used for map generalization. The remote sensed data used in the classification experiments are shown in Figure 8.1.

ROCK UNIT	LITHOLOGIC DESCRIPTION	D	RE-COMPILATION
1. Leucogranite	Weakly to non-foliated white to pink muscovite-bearing pegmatitic granite		Masked because surface area is small with respect to flight-line spacing
2. Colin Lake Granodior.	megacrystic diorite, granodiorite and muscovite-bearing granites	1	
3. Charles Lake Granite	Foliated megacrystic granite with large equant K-feldspar megacrysts	2	
FAULT ROCKS 4. High-grade mylonite 5. Low-grade mylonite 6. Cataclasite	Well banded quartzo-feldspathic mylonite, protomylonite and ultramylonite with amphibolite pull aparts Amphibolite to greenschist-grade layered locally biotite- rich mylonite to protomylonites with abundant feldspar pophyroclasts Highly fractured granite and gneiss with random fabric		Masked because these rocks are derived from a number of different protoliths (units 3,4,5,6 and 10). Geophysical signatures are a function of both the deformation processes and the original unit
7. Wylie Lake Granite	Biotite-hornblende granodiorite with K-feldspar megacrysts	3	
8. Western Slave Granite	Massive to moderately foliated medium to coarse grained white to pink equigranular quartz monzonite, monzogranite and granite	4	
9. Arch Lake Granite	Massive to well foliated gneissic, locally mylonitic syenogranite with equant 1 x 3 cm K-feldspar megacrysts	5	
TALTSON BSMT 10. Metasedimentary rocks	Banded pelitic, locally migmatitic grey to green gneiss with coridierite, biotite, garnet and sillimanite	6	
11. Andrew Lake Granodiorite	Megacrystic biotite hornblende granodiorite to diorite	7	
12. Eastern Slave Granite	Equigranular granite with small K-feldspar meggacrysts	8	
13. Syenogranite gneiss 14.Hornblende granite gneiss 15. Layered gneiss	Well banded biotite, K-feldspar rich syeno granite gneiss Well banded, locally mylonitc hornblende granite gneiss Well banded mylonitic biotite-hornblende granite to granodiorite gneiss	10	Grouped in one assemblage because mineralogical compositions are highly variable within units and overlap among units. Field criteria for distinction between units can not always be applied
16. Amphibolite	Well foliated biotite amphibolite		Masked because surface area is small with respect to flight-line spacing
17.Waugh Lake Group	Low-grade chlorite biotite phyllites, schists, quartzites,pebble conglomerates of quartz pebbles in a greywacke matrix	9	
18. Quaternary Cover	Glacioflivial sediments and till		Masked because units do not apply to the bedrock from which they are derived.

Table 8.1 Description of lithological units after McDonough *et al.* (1995)

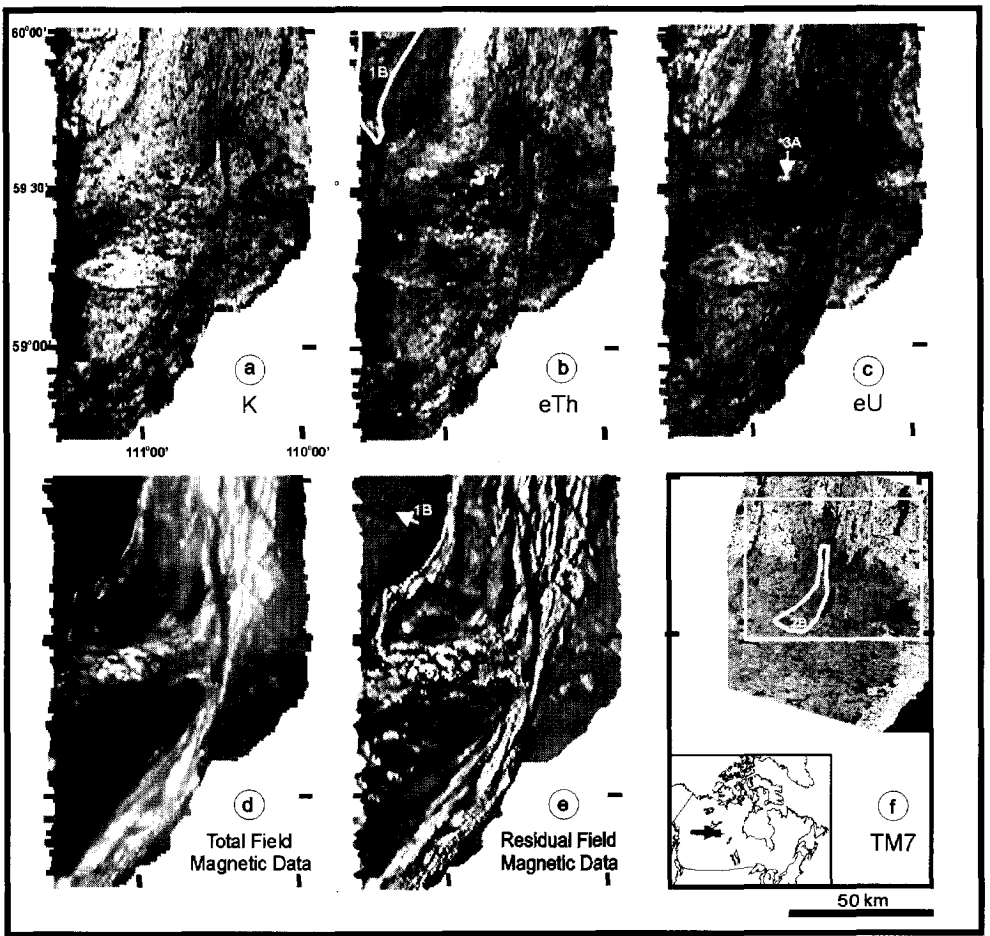

Figure 8.1 Remote sensing data used in the classification experiments: (a) potassium channel; (b) equivalent thorium channel; (c) equivalent uranium channel; (d) total magnetic field (reduced to the pole); (e) residual field magnetic data; (f) Landsat TM band 7; Box on (f) shows the location of the training area. Labeled polygon and arrows correspond to geological features discussed in the text.

The total field magnetic data were reduced to the pole and further processed to generate a grid of the residual magnetic field, on which the effects of deeper sources are subdued in favor of the shallow sources (Telford, 1990). The to the pole-reduced magnetic field was continued upward to 1000 meter by filtering in the wave-number domain. This procedure provided an adequate enhancement of

the narrow anomalies related to the units of restricted width, such as the Charles Lake granite and the metasedimentary rocks. This increased the discrimination potential of lithological variations within the basement complex.

The visual interpretation of the remotely sensed data presented in Chapter 3 revealed that the geophysical data reflect to a considerable extent the surface lithological units. The exact relationships between the lithological units and the geophysical data are unknown. For example, geophysical measurements on rock samples show that the variability of magnetic susceptibility contrast within units is in the same order of magnitude as the variability between units (Sprenke *et al.*, 1986). The magnetic susceptibility contrasts within units may depend on many factors, including the variations of the primary magnetic mineral content and its alteration due to metamorphic, tectonic, metasomatic processes and weathering (Clark, 1997). Radioelement concentrations, although less affected by metamorphism, also show high variability for any given rock type, such that global classifications on the basis radioelement concentrations are not possible (Dickson and Scott, 1997). The relationships between the remotely sensed data and the lithological units are further complicated by the dipolar nature of the magnetic field, distribution of magnetic sources at depth and attenuation respectively masking effects of vegetation and overburden on the gamma-ray and Landsat TM data. Because it is in practice not possible to jointly model all these processes, at least not on the scales applicable to regional geological mapping projects, the problem has been tackled by empirically establishing functional relationships between the lithological units and the remotely sensed data.

8.3 Classification algorithms

The image classification aims at the optimal prediction as to which class a pixel belongs based on measurements represented on that pixel. Let $x(p) = (x_1, \ldots, x_m)$ be an observation at a pixel p of an m-dimensional random feature vector $X = (X_1,\ldots,X_m)$ representing an m-dimensional multivariate image data set. In classification an optimal decision rule is formulated for allocating the pixel p to the j^{th} class C_j (j=1,...,n) (e.g. a lithological unit). The posterior probability for pixel p to belong to class C_j given the observation x(p) can be defined by:

$$P(x(p) \in C_j) = \frac{\pi_j f_j(x)}{\sum_{j=1}^{n} \pi_j f_j(x)} \qquad [8.1]$$

where π_j (j =1,...,n) are the mixing proportions of the n classes that sum to unity and which can be interpreted as the prior probabilities that an entity belongs to class C_j (j=1,...,n) and f_j is the probability density function for class C_j. The pixel p is allocated to the class C_j with the highest posterior probability. A posterior probability threshold is defined below which no decision is made that p belongs to a class; p is then assigned the label "unclassified". The prior probabilities can be set equal or can be estimated from the training set as being proportional to the number of samples per class.

If the probability density functions of the classes are known, the solution of equation 8.1 is straightforward. In practice, however, the probability density functions are estimated from training samples taken from the class density distributions. The available classification algorithms differ in the way the probability density functions f_j are modeled and estimated from the training data. In this study the maximum likelihood, predictive and artificial neural network classifiers were used.

Parametric classifiers: (a) maximum likelihood and (b) predictive methods

Parametric classification methods estimate the probability density functions of the classes from the training data under the assumption that they are multivariate normal distributed. In the maximum likelihood method the sample class means and covariance matrices are considered valid estimates of the mean and covariance matrices of the classes. This is known as the "plug-in rule" (McLachlan, 1992). In the predictive approach, the predictive probability distribution functions, known as the multivariate Student t-distribution functions (Press, 1972; McLachlan, 1992) are computed, one for each class. The fundamental difference from the maximum likelihood method is that the uncertainty to what extent the sample statistics are good estimates of the class statistics is taken into account. For large sample sizes, the student t-distribution approaches the normal distribution, so that the differences between the two approaches are small. For small sample sizes, however, the predictive approach has proven to give superior results as it tends to moderate the exaggerated view of the class posterior probabilities obtained by the "plug-in rule" (e.g. Aitchison *et al.*, 1977; McLachlan, 1992).

(c) artificial neural network classifier

Classification algorithms based on artificial neural networks have gained considerable popularity in the last few years (Paola and Schowengerdt, 1995).

Contrary to parametric algorithms, they do not require the assumption of multivariate normal distributed data. A three-layer feed-forward network was used in this study consisting of a layer of input nodes, a layer of hidden nodes and a layer of output nodes. Each node of the input layer is connected to the nodes of the hidden layer, which are connected to the nodes of the output layer. Before the training samples are fed into the network, random weights are assigned to all the connections between the nodes of the three layers. Let $S_p = (x_1,...x_m, c)$ denote a training sample from class C_j at pixel p. The measurements $(x_1,....., x_m)$ of S_p are presented to the m input nodes and values T_k are assigned to the k output nodes. One of these T_k values is set close to one, representing the class C_j whereas the remaining T_k values are set to zero. The measurements are multiplied by the weights assigned to the connections between the input and hidden nodes while fed forward. The values arriving at the hidden nodes are summed and subject to a continuous differentiable (sigmoid) activation function to constrain the output to a range between zero and one. Next the activations are sent from the hidden nodes to the output nodes and are multiplied by the weights connecting the nodes between the hidden and the output layers. The values are summed at each output node and again are subjected to the activation function, yielding O_k activations at the output nodes. An error function E is defined as the sum of the differences between the activations O_k and the desired values T_k at the output nodes:

$$E = \frac{1}{2}\sum_{k=1}^{k}(T_k - O_k)^2 \qquad [8.2]$$

The goal of training is to update the weights so that this error is minimized. Using the back propagation algorithm (Rummelhart and Williams, 1986) the change in the weights W_{kj} between the output and the hidden layers is defined by:

$$\Delta W_{kj} = -\eta \frac{\partial E}{\partial W_{kj}} \qquad [8.3]$$

Where the indices k and j refer to the k'th and j'th node of respectively the output and hidden layers and η is a constant known as the learning rate. The error is then back propagated to update the weights W_{ij} between the input and hidden layers. The next sample is fed into the network and the same procedure is repeated. This approach is termed 'data adapted training' because the weights are updated for

each training sample. In 'block adapted training' the weights are updated after a complete set of training samples of a class has been transferred through the network. This approach was applied to compensate for the large dissimilarities in sample size which in data adapted training would result in insignificantly small weight adaptations for the classes with few samples.

Spatial considerations

Although image classification is applied in a spatial context, the technique by itself is non-spatial. In other words we could sample pixels in any order from the image, classify them irrespective of their neighbours and to where these pixels are located in image space. Several methods exist to include spatial information in the estimation process (Atkinson and Curran, 1994).

We followed the approach of Switzer (1980) which is simple to apply for any classification algorithm by augmenting each data channel with an average filtered channel considering a neighbourhood of eight adjacent pixels. This method exploits the spatial autocorrelation between pixels within each of the image variables assuming that the alternation of lithological units occurs on a larger scale than that of a single pixel.

The effects of Switzer's method can be intuitively understood by appreciating that the probability of a pixel belonging to a particular class increases when the average of the neighbourhood pixels approaches the mean of that class in addition to the probability that the central pixel belongs to that class. The weight of the contextual classification is adjusted according to the correlation between the averaged and original multi-channel data. The lower this correlation, the greater the influence of the average filtered channels. In the extreme that there is no correlation between training pixels and their neighborhoods, the average filtered and original channels receive equal weights in the classification. On the other hand when the homogeneity is larger than the local neighborhood, the correlation is unity and adding the average filtered channels has no effect.

8.4 Classification strategy

The classification strategy used for predicting the ten lithological units consists of five processing steps and is schematically shown in Figure 8.2. The analysis first focuses on a training area where field observations and geological maps are used to compile the training set. In the second step, the discriminative power of different combinations of image variables is evaluated; and in the third step, the

extent to which the classification algorithms reproduce the geological map is assessed. Once the image variables with the highest discrimination power and the best performing classification algorithms is found, in the fourth step the classification is applied to the entire study area. In the last step, the discrepancies between the classified patterns and regional map compilation are interpreted to identify targets for further field study.

Step 1: Compilation of the training set

The training set for the classification experiments was initially based on 3753 records exported from the Fieldlog database (Brodaric, 1997, Chapter 4 of this thesis), containing the map coordinates and the names of the eighteen map units. These units were generalized into ten units using the criteria listed in Table 1. Field stations located within a distance of 200 meters from the lakes were removed from the training set to eliminate mixed land and water pixels with a strong attenuation in gamma-ray response. The final training set consisted of 2795 training samples, each having values of the seven TM channels, the K, eTh and eU gamma-ray spectrometry channels, and the total and the residual magnetic fields.

Step 2: Image variable selection by exploratory analysis

In order to find the set of image variables with the highest classification potential, classification success rates for Landsat TM, gamma-ray, magnetic data and combinations of these data types were computed from the training pixels. The classification success rate is defined as the proportion of correctly allocated training samples against miss-allocated training samples. Figure 8.3 shows a summary of this analysis in a bar diagram. The success rates should be interpreted in a relative sense, because the training set should not be used for both defining the classification rules and estimating its performance. Therefore, a cross-validation experiment was conducted in which ten percent of the training data was predicted ten times by the classification rules computed from the remaining training samples. The average classification accuracy of these ten experiments was similar to the success rates computed from the entire training set. This suggests that the success rates could also be interpreted in absolute sense.

The overall success rates in Figure 8.3 show that the Landsat TM channels provided the lowest, whereas the magnetic data provided the highest discriminative power. The success rates significantly increased by using combinations of different data types.

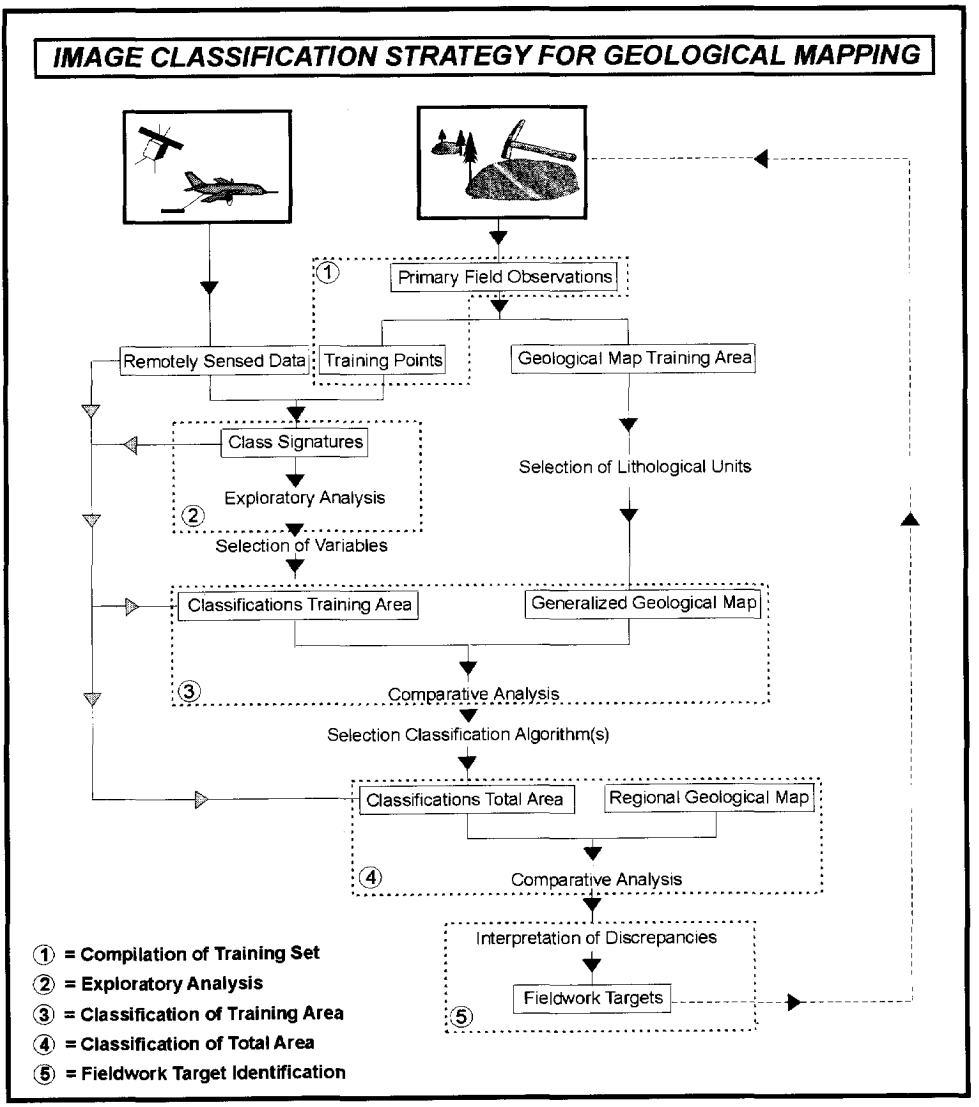

Figure 8.2 Schematic flowchart showing strategy for image classification of lithological units in a field mapping context. The numbers refer to the processing steps described in the text.

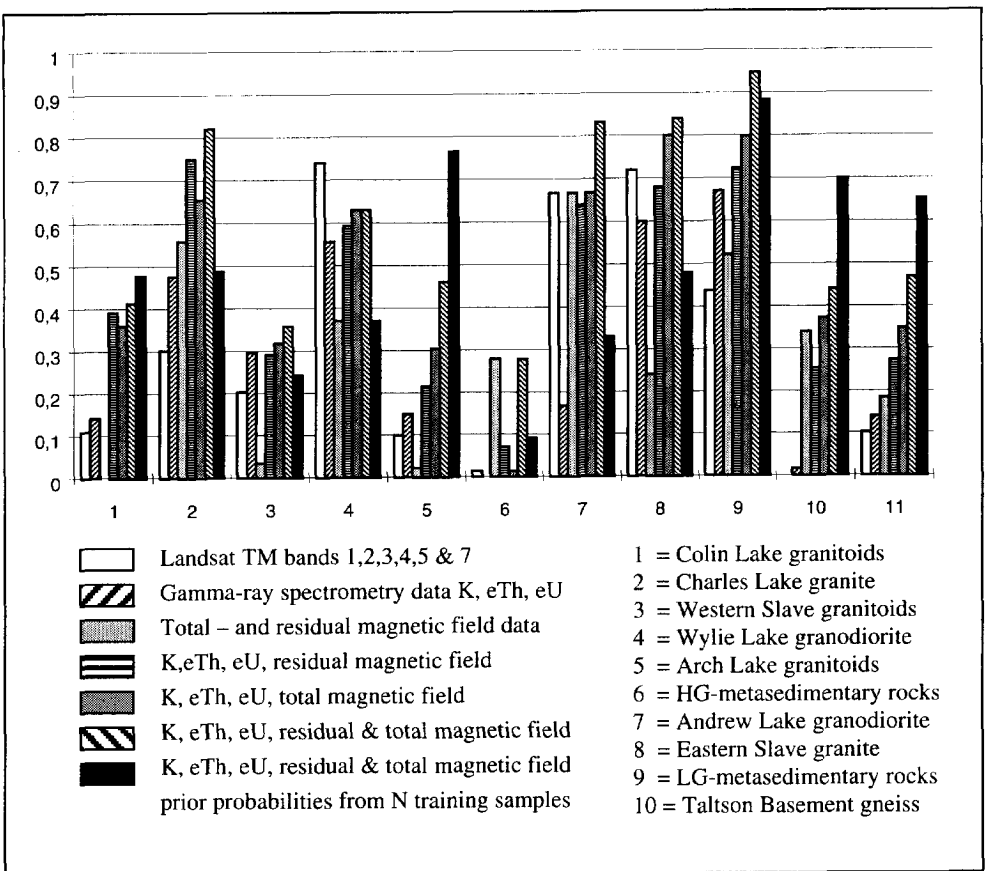

Figure 8.3 Bar chart showing the classification success rates for different data combinations

The overall success rates increased with 23 % and 14 % by respectively adding the residual and total field magnetic data to the gamma-ray spectrometry channels. The first increase is the result of a better discrimination of lithological units 2 and 3 that occur as linear enclaves within the Taltson basement complex.

The total magnetic field provided slightly better discriminative power for most of the granitoid plutons (units 3, 4, 5, 7 and 8), the low-grade metasedimentary rocks (unit 9) and the Taltson basement gneisses (unit 10). This suggests that the contributions are complementary and by adding both image variables together, the overall success rate was raised 34 % , yielding a maximum of 47%.

The overall success rate further increased to 66 % when the class sample sizes were used to estimate the class prior probabilities. The combination of the TM bands and the gamma-ray spectrometry channels yielded lower percentages and using all twelve channels together did not increase the overall success rate. Also transformations, such as ratios of the gamma-ray spectrometry data and variance filters for the textural characterization of the magnetic data did not improve the overall success rate.

Step 3: Classification of the training area

The selection of suitable algorithms to classify the total study area was based on the percentages of coincidence between the geological map compilation and classified patterns. Figure 8.4(a) shows the results for the three algorithms based on equal prior probabilities and Figure 8.4(b) shows the coincidence percentages for the parametric algorithms in which priors were computed from the class sample sizes. The classified map patterns produced by the three algorithms are shown in Plate 8.1.

Figure 8.4 shows about equal performances for the majority of the classes from the predictive and maximum likelihood algorithms, significantly higher with respect to the performance of the neural network classifier.

The neural net classifier showed low coincidence percentages for the classes with large sample numbers (units 5 and 10) explaining the low overall coincidence percentage of 23 percent. Many pixels were miss-allocated to unit 6 (metasedimentary rocks) at cost of unit 10 (Taltson Basement gneisses). On the other hand, the neural network classifier performed better for some of the smaller units such as the Andrew Lake granitoids (unit 7) and Waugh Lake Group (unit 9).

An additional neural net classification was carried out in which a training set consisting of units 1, 2, 5, 6, 9 and 10 with equal sample sizes of 40 samples per class was used. Results showed that the success rates dramatically increased from about 30 to 90 percent, mainly by an increase in success rates of the large classes (5 and 10). The overall coincidence percentages between the classified- and compiled map pattern remained similar suggesting that the error obtained by block adapted learning is poorly representative for the classes with large sample sizes.

As expected from the theoretical consideration above, the predictive classifier shows somewhat higher coincidence percentages for the classes with small sample numbers, such as class 7 and 8. Because these classes have small sample sizes, this difference is not reflected in the overall coincidence percentages, which explains why the classified patterns on Plate 8.1 are almost identical.

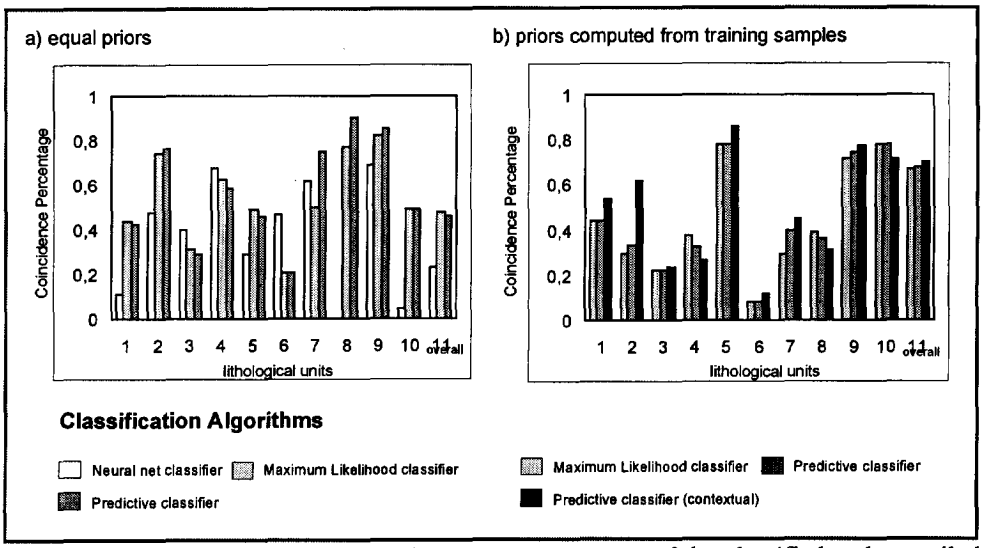

Figure 8.4 Bar charts showing the coincidence percentages of the classified and compiled geological map patterns for maximum likelihood, predictive and neural network classification methods (a) for equal prior probabilities, (b) prior probabilities computed from the class sample sizes.

When the priors were computed from the training set, a maximum coincidence of 67 %, close to the success rate, was obtained for the predictive method. The overall coincidence percentage further increased to 70 % when the image variables were augmented with their averaged filtered derivatives, according to the approach of Switzer (1980).

Step 4: Classification of the total area

Based on the results obtained for the training area, the maximum likelihood and predictive algorithms were selected for the classification of the total area. In this reconnaissance context priors were set equal so as to provide an unbiased view of the classification performance. The priors computed from the training set were not considered valid, because the number of samples per geological unit in the training area are not representative for the general geologic pattern of the total study area. This is evident, when the geological map compilations on Plate 8.1 and Plate 8.2 are compared. Plate 8.2(b) and 8.2(c) respectively show the classifications for the maximum-likelihood and the predictive methods. The parametric classifications again both yield comparable patterns. The maximum likelihood classifier provides

the best overall representation of the generalized geological map pattern shown in Plate 8.2(a). The smaller classes, such as class 8 and 9 are better represented on the predictive classification. This result is however obtained at cost of large misclassified patterns of class 7 that appear within class 3.

Contrary to the classified pattern on the training area, the enclaves of Slave granitoids (class 3) within the Arch Lake granitoids (class 5) appear on both classified patterns. This is most likely due to the under representation of this class in the training area, which result in lower posterior probabilities, as the priors probabilities were computed from the sample size. Both methods failed in recognizing the large enclaves of metasedimentary rocks in the south of the study area.

Step 5: Comparative analysis and fieldwork target identification

The coincidence percentages between the classifications and the geological map of the training area and the similarities between the patterns of the classifications of the total area and the generalized geological map suggest that the parametric classifiers provide a reasonable lithological characterization of the study area. The technique is evidently not capable of replacing field mapping, as many discrepancies between the map and classification patterns exist, irrespective of the applied classification algorithm. Three factors may explain such discrepancies:

- The geophysical data do not provide sufficient discrimination potential to classify lithological variations that were recognized by the geologist as distinct units in the field.

- Noise factors, such as vegetation and Quaternary cover result in variations in the gamma-ray responses that are not related to bedrock geology.

- Generalizations in the geological map compilation omitted geologically significant lithological variations and anomalies expressed in the geophysical signatures.

The last factor is of particular interest for geological mapping and exploration. By identifying geologically significant signatures that were not identified or omitted in field mapping, targets for map updating and exploration may be identified. This factor also implies that the coincidence percentages can not be

interpreted in terms of classification accuracy. Only a cross-validation on the bases of field stations, as performed in step 2, will provide some indication of the classification performance. The following paragraphs provide examples of each of the above listed discrepancies and are numbered according to the above factors. The patterns related to these discrepancies are outlined on Plate 8.2 and labeled accordingly.

1A. Poor discrimination potential of high-grade metasedimentary rocks

An illustrative example of the first type of discrepancy applies to the high-grade metasedimentary rocks (unit 6) that occur as enclaves within the Taltson basement complex (unit 10). All classifications provided low coincidence patterns (< 20%) for this class although some occurrences in the north of the study area appear on the classified patterns. A diagnostic criterion to recognize this unit in the field is its characteristic metamorphic mineral assemblage consisting of garnet, sillimanite and cordierite. This mineral assemblage is not associated with the radioactive mineralogy, mainly comprising monazite, zircon and uraninite, and explains why the metasedimentary rocks have no diagnostic gamma-ray signatures to differentiate them from the enveloping orthogneisses. Nevertheless the metasedimentary rocks appear to have lower magnetic susceptibilities (Sprenke *et al.*, 1986) which entirely explains the discriminative power of the magnetic data as shown on Figure 8.3. There is however confusion with unit 10 due to similarities in magnetic response between metasedimentary rocks and shear zones within the Taltson Basement Complex. Shear zones also show lower magnetic susceptibilities as a result of the oxidation of magnetite to hematite during deformation at greenschist grade (Sprenke *et al.*, 1986). The large enclaves of metasedimentary rocks in the southwestern part of the area have been misclassified as Arch Lake and Colin Lake granitoids (unit 4 and 1 respectively). Apparently there is variability in the composition of the metasedimentary rocks, such that the smaller enclaves in the training area are not representative for the larger enclaves in the southwest.

1B. Confusion between granitoid units and zonations within granitoids

Large discrepant patterns are related to some of the granitoid plutons. The Wylie Lake suit (unit 4) has been classified as the Colin Lake, Arch Lake and Western Slave granitoids (units 1, 3 and 5). A change in style of deformation, from an east-west to a north-south foliation was chosen as a criterion for distinguishing

between the Colin Lake and Wylie Lake granitoids (Goff *et al.*, 1986) rather then compositional criteria. This directional criterion is not considered by the classification algorithms and explains the confusion between the two units in the classification. Other patterns of confusion between granitoid units occur on the predictive classification between the Western Slave and Andrew Lake granitoids (units 3 and 7). The discrepancies yield spatially continuous patterns, which may have geological significance. For example both on the magnetic and gamma-ray spectrometry data the most westerly pattern can be recognized as a distinct unit bounded on the east by an elliptical unit that is outlined by curvi-linear magnetic anomalies (1B on Figures 8.1b and 8.1e.) The fact that this feature is recognized on multiple types of geophysical data suggests its geological significance. It is however unlikely that granitoid units from plutons spaced 80 kilometers apart with differences in crystallization ages of about 35 million years (McDonough *et al.*, 1995(b)) are intermixed without evidence for intrusive cross-cutting relationships. Based on such geological considerations this discrepancy is preferably interpreted as a separate magmatic phase within the Western Slave granite that has similar geophysical properties as the Andrew Lake granodiorite.

2A. Effects of Quaternary cover units

Patterns related to Quaternary cover are seen in the eastern part of the study area directly north of Colin Lake (2A on Plate 8.2(c)). Quaternary deposits, consisting of glacio-fluvial sediments (Bednarski, 1997) were masked on the geological map of the training area. These sediments are potassium rich as shown on the potassium channel. These deposits are systematically misclassified as the Arch Lake Granite (unit 5) which is also relatively rich in potassium.

2B. Effects of vegetation cover

Misclassifications due to vegetation attenuation effects are seen at the eastern margin of the Arch Lake granite where the southern part of the margin shows a transition to Arch Lake granite to Charles Lake granodiorite (unit 2), a unit occurring as dikes within the Taltson basement (unit 10). This transition trends perpendicular to the geological structure and corresponds to a variation in the density of the vegetation cover that is visible as a grey tone variation on Thematic Mapper band 7 (2B on Figure 8.1(f)) and the gamma-ray spectrometry channels (Figs. 1a, 1b, 1c and 1f). The lower responses in all three channels in the densely vegetated area probably caused the misclassification, but differential attenuation of

the eU with respect to the eTh and K channels may also play a role. Attenuation effects are partly compensated by the classification algorithms as they tend to separate classes on the uncorrelated part of the class signatures. Attenuation effects do, however, interfere with lithology related variations in the total radioelement concentration. Nevertheless the total concentration apparently contributed to the lithological discrimination, as its removal by employing only ratio images in step 2, yielded lower classification success rates.
The attenuation effect of vegetation cover was confirmed by a calibration procedure of the gamma-ray responses for an area of 30 x 30 km including polygon 2B (Figure 8.1). The vegetation and outcrop abundance could be reasonably modeled in this area, such that after calibrating the gamma-ray data for outcrop abundance an improved representation of the geological units was obtained (Schetselaar and Rencz, 1997).

3A. Uranium anomalies

Circular and linear patterns within the Arch Lake granite have been systematically classified as the uranium rich Colin Lake and Wylie Lake granitoids by all the classification algorithms. On the gamma-ray spectrometry data these areas coincide with uranium anomalies. Similar uranium anomalies were identified along the margin of the Konth pluton, which constitutes the northern extension of the Arch Lake granite (Charbonneau, 1991). The small circular anomaly (3A on Plate 8.2(c)) yielded a higher uranium response in a field gamma-ray spectrometry survey (Brian Charbonneau, pers. comm. 1994).

3B. Distinct magmatic phase within the Arch Lake granitoids

A large area between the Western Slave and Arch Lake granitoids is classified as the Taltson basement. This area corresponds to elliptical magnetic anomalies with high internal relief, abundant Quaternary cover and few bedrock exposures. It is classified as class 10 due to its high total and residual magnetic response. The circular anomaly pattern is however contrasting to the linear anomaly pattern in the Taltson basement and therefore makes such an origin unlikely. On contoured magnetic maps, the circular anomaly was interpreted as a partly buried intrusive phase slightly more basic in composition then the Arch Lake Pluton (Sprenke *et al.*, 1986).

8.5 Discussion

The neural net classifier was less successful in predicting the compiled geological maps, particularly for the classes with large sample sizes. This is an unusual result because neural network classifiers usually show better performance in comparison to parametric algorithms (Paola and Schowengerdt, 1995). The extreme dissimilarity in sample sizes (between 18 and 1235) is probably an important factor to explain the relative poor performance of the neural net. In data-adapted learning the weight adaptations of the small classes are swamped by the large ones. In block adapted learning all the classes are weighed, irrespective of their sample size, such that the misclassifications between class 6 and 10 results in large amounts of misclassified pixels. In addition, the error function does not appear to be representative for classes with complex distribution functions, such as class 5. These are preliminary explanations and more research in the learning process of the individual classes would be required to corroborate this inference.
A weakness of parametric methods, commonly cited in the remote-sensing literature, is that the assumption of normal distribution is usually not valid. This weakness is not so severe as it may seem, because it suffices to model the relative differences between the probability distribution functions of the classes rather than modeling their absolute values (McLachlan, 1992). Moreover the modeling of these differences is only critical in those data intervals where the probability density functions overlap (Ripley, 1996). For this particular classification problem where a training set with an extreme dissimilarity in class sample size was used, the classification problem appears to be better resolved by using parametric classification algorithms.

Total- and residual aeromagnetic data provide complementary contributions to the lithological characterization of the study area by raising the correctly allocated pixels of the training set from 41 % for using the gamma-ray spectrometry data alone to 67 % for all five variables. The increase in classification performance results in a better characterization of the internal lithological variations in the basement complex consisting of granitoid gneisses (class 10), high-grade metasedimentary rocks (class 7) and megacrystic granitoid sheets (class 3). The residual magnetic field particularly contributes in the classification of rock units that form linear enclaves within this basement complex, that are not easily resolved on the total magnetic field, and is further enhanced by including contextual information from neighboring pixels in the classification. On the other hand the total field magnetic data enhances the classification of the large granitoid plutons and the low-grade metasedimentary rocks of the Waugh Lake basin.

From the theoretical point of view, the decay-laws of potential fields with source-distance, prohibit the use of magnetic and gravity data in a pixel-by-pixel classification process. For magnetic data additional complexities arise from the dipolar nature of the inducing field and its complex geographic variation in orientation. In practice, however, there may be situations where the magnetic anomalies closely outline their near-surface magnetic sources with limited interference from sources with larger distances from the plane of observation. The extent to which the shape of the anomalies is diagnostic in a pixel-by-pixel classification is mainly dependent on the direction of induced magnetization and the three-dimensional distribution of magnetic susceptibility contrasts at various distances from the plane of observation. The most favorable settings are those that approach a model where lithological units are bounded by vertical contacts in combination with a steep to vertically inclined inducing field. The significant contribution of total- and residual field magnetic data in the bedrock characterization in the results is explained by such a setting. Both the large granitoid units and units of restricted width in the basement complex are bounded by sub-vertical structures with considerable depth extension. The magnetic susceptibility contrasts between the large units are emphasized in the low spatial frequencies of the anomaly spectrum whereas structural discontinuities within these units, clearly visible as linear anomalies in the residual magnetic signatures (see Figure 8.1(d)) are only weakly reflected. Conversely the complementary contribution of the residual magnetic data is largely reflected in the higher performance for rock units of restricted width, such as units 2 and 6 that occur as linear enclaves within the basement complex The implication for including potential field data in bedrock classification is that understanding to what extent the anomaly spectrum reflects surface geology is of fundamental importance. Such insight can be obtained by a qualitative comparative analysis of total field image maps and derivatives with generalized geological map patterns, and evaluating the changes in the classification success rates when the magnetic data are included.

Derived products, such as pole-reduced, residual and vertical derivative fields are useful to enhance near-surface magnetic sources, but their limitations depend on the quality of the data and additional factors such as magnetic inclination. More research is needed to test the applicability of other enhancement procedures, such as analytic signal, pseudo gravity anomaly mapping, susceptibility mapping and textural characterizations. In all circumstances, however, one should be aware that magnetic signatures from sources at depth, which are not representative for the bedrock encountered at the surface, can appear in the classified map pattern. It is interesting to compare the classification results with the integrated visual

interpretation shown in Plate 3.6, although a comparison is hampered by the subjectivity of the visual interpretation conducted by one individual familiar with the geological map pattern. Comparing the overall map patterns the human interpreter appears to emphasize the general patterns, using contextual information in outlining the major units and ignoring what he or she considers as noise. In the classification approach, on the other hand, units are identified on the basis of subtle or complex multivariate signatures. Internal variations of units within and east of the Taltson basement have been identified that do not appear in the integrated visual interpretation.

A disadvantage of the supervised classification approach is that only those units that have been identified by the geologist in the field will appear on the classification result. The internal zonation in the Arch Lake granite discussed in Chapter 6, for example, is obvious on the ternary radioelement map (see Plate 3.3) and is also automatically detected by the unsupervised classification approach (see Plate 6.2), but does not appear on the supervised classification results (see Plate 8.2). This is likely to result from the parametric classification approaches that model the class signatures with smooth functions (e.g. Gaussian distributions), ignoring their potential complexity. This effect is further enhanced for large class training sets, if the number of samples is used for weighing the classification functions by prior probability estimates. This problem justifies the development of stratified approaches combining supervised and unsupervised (e.g. clustering) algorithms. One could for example first use a supervised approach to map the major assemblages in an area and subject the signatures of each assemblage to a clustering to map the internal variations that may not have been identified in the field.

8.6 Summary and conclusions

The classification experiments presented in this chapter show that a complex geological pattern in a training area consisting of ten lithological units coincides for 70 % with classifications based on airborne geophysical data, about equal to the classification success rates computed from the training set. Testing various combinations of image channels revealed that two wavelength representations of the magnetic field in combination provided the highest discriminative power, whereas, six Landsat TM channels provided the lowest discriminative power. The maximum likelihood and predictive classifiers show comparable performance significantly higher then the neural net classification. The predictive classification, however, shows less bias towards large class sample sizes in comparison to the

maximum likelihood classification. This is because the predictive method averages over the uncertainty in the estimation of the class distribution functions, whereas the maximum likelihood classifier uses the sample statistics regardless the sample size of the classes.

The maximum likelihood classification shows better overall resemblance with the generalized geology as both representations are biased towards the large units. On the other hand, miss-classified patterns obtained with the predictive method suggest the occurrence of spatially continuous internal zoning of granitoid units that are probably geologically significant but not represented on the geological maps.

The classification approach has been fully integrated in geological mapping in which the field stations were used to compile a training set. Contrary to the random selection of training samples from geological maps, it assures that training samples from the subjectively compiled units are excluded from the training set. In a comparative analysis between compiled and classified map patterns, discrepancies between the map and classified patterns were identified. Some of these discrepancies correspond to those identified by visual interpretation in Chapter 3 and provide interesting targets for further geological assessment, map refinement and exploration.

9

CONCLUSIONS, OUTLOOK AND RECOMMENDATIONS

In this thesis integration methodologies for the interpretation of multisource remotely sensed- and field data were developed. The effectiveness of these methodologies was evaluated through interpreting lithostructural patterns in a granite-gneiss terrain of the Canadian Shield. The challenge was to develop integration methodologies that incorporated primary field data in the analysis and then to extract meaningful geological information. What follows summarizes the main contributions of this research.

1. Integration methodologies were developed that exploit complementary information derived from multisource remotely sensed- and geological field data in geological syntheses. The following points highlight the results in applying the integration methodologies to the southern Taltson magmatic zone:

- Both the integrated visual interpretation and the automated pattern recognition have proven to be effective in outlining discrepancies with recently published geological maps. Even in repeatedly and extensively surveyed areas, such as the Shield of northeastern Alberta, both automated and qualitative interpretation of multisource remotely sensed data have provided results that went unnoticed before. An internal zonation in radioelements in one of the major Taltson batholiths was identified and subject to a focussed integration study (see below). Other discrepancies such as a dike-like anomaly, structural trends across the boundaries between granitoid plutons and potassium and uranium anomalies still await field verification. From this point of view the presented methodologies are clearly cost-effective in refining geological mapping and identifying targets for further field study and exploration.

- The spatial and spectral analysis of gamma-ray spectrometry flight-line data and grids allowed to identify compositional variations of the Arch Lake granite that were not previously resolved by field mapping and a regional litho-geochemical survey. The relationships between the gamma-ray responses, the modal mineralogical composition, the rock geochemistry and the relationships between radioactive accessory and rock-forming minerals were locally established to interpret the genetic origin of the zonation.

Bimodal trends in K-eTh space that are spatially delimited by a step-like break of the eTh/K ratio. In combination with interpolated geochemical data and mineralogical observations this strongly suggest that the Arch Lake granite is a composite intrusion formed by the emplacement of distinct magmatic pulses. The compositional differences between distinct compositional radioelement trends reflect subtle but significant variations of monazite and zircon.

- The integration of gamma-ray spectrometry data, a high-pass filtered Landsat TM7 and mineral foliation data in composite image maps appeared effective to interpret the compositional zonation with respect to the internal structure of the southern Arch Lake batholith. The compositional zonation shows an overall concordant relationship with the curvilinear trend lines of a solid state mineral foliation outlining a synformal structure that parallels the sheared margins of the pluton. U-Pb zircon ages constrain the emplacement of the Arch Lake granite to be approximately synkinematic with respect to mylonitization of its margins suggesting that the Arch Lake granite emplaced during regional non-coaxial deformation.

- The results indicate that the IHS integration technique is also applicable in analyzing post-emplacement deformation of the interiors of large pre- and synkinematic batholiths. E-W trending offsets of the compositional zonation, along lineaments on magnetic and Landsat TM images, correspond in location and orientation to ductile and brittle shears that have accommodated displacements with a significant dextral strike-slip component.

- Integrated enhancement and representation of structural fabrics, imaging radar (ERS-1) and magnetic data appeared effective in outlining structural trends within and along the Charles Lake shear zone, a principle transcurrent structure of the Taltson magmatic zone. Field verification and comparative analysis of the strikes of foliation data and automatically extracted lineaments confirms that the linear features in the ERS-1 and aeromagnetic data correspond to the trends of gneissic and mylonitic foliation.

- Integrated cartographic representation of 2-D magnetic inversion models, magnetic susceptibility measurements and structural fabrics in combination with microscopic observations permitted to establish the relationships between the shear zone and its magnetic expression. Because the magnetization levels are subdued within the high strain zone, imaging radar data complements the

lack of internal structural expression in the magnetic data. This complementary expression was exploited in the structural interpretation of vertical derivative magnetic/ERS-1 composite images.

- Integrated enhancement and representation of directionally enhanced imaging radar vertical derivative magnetic data and structural fabrics provides a regional view of the shear zone. This integration method proved effective for interpreting regional structural trends with subtle strike variations and regional geometric elements, such as bifurcating and secondary splays. A prominent left-handed deflection, of pre-existing foliation trends, is consistent with sinistral kinematic indicators observed in outcrop. A NE-trending lineament system was identified on the basis of apparent deflections of magnetic anomalies along lineaments on an ERS-1 scene. This system corresponds in orientation with the dextral set of outcrop-scale conjugate shears and to a dextral greenschist grade shear zone. This system formed relatively late in the deformation history and most likely accommodated NNE-SSW bulk extension.

Although the above conclusions demonstrate that the integration methodologies contribute to building geological insight, a major limitation identified is that their contribution to structural interpretation is largely confined to obtaining regional geometrical insight. Although the methods allow outlining structural styles and trends in areas of sparsely and unevenly distributed field data, the inferred structural geometries permit alternative kinematic interpretations to be equally valid. Field verification remains essential to establish the 3-D kinematic framework of the imaged geological structures and to confirm any tectonic hypothesis.

2. It has been demonstrated in this thesis how relational database management of geological field observations can be exploited in supporting the analysis of remotely sensed data. Querying strategies and cartographic representation of geological themes provide an effective means to support image interpretation and validate results obtained from automated feature extraction and computer modeling. New areas of development in the direction of field knowledge representation were identified all aimed at the dynamic access, interaction and visualization of ground truth in a digital image analysis and GIS environment. Such dynamic querying and map representation functions were extensively exploited in this thesis to support interpretation work and analyze the

relationships between image signatures and ground observations. All these tasks could not have been realized without systematic storage, database management and cartographic representation of the available geological field observations.

3. Image processing techniques for generating IHS composite images from multisource remotely sensed data were refined to improve the potential of this technique for enhancement of geologically significant image patterns. A hue-invariant image integration was developed that maintains the spectral balance of the multispectral data set. This technique uniformly maps the image data on distinct perceptual colour attributes in an optimal manner and allows interpreting the multispectral data in relative units of the pixel values of the input images, and the intensity substitute in absolute pixel values. The method provides control on the amount of over-range and in optimizing a balanced perception of the input data.

4. Image classification patterns from gamma-ray spectrometry and magnetic data coincided for about 70% to the units of geological map compilations of the northeastern Alberta Shield. Tests of various combinations of image channels revealed that total and residual wavelength representations of the magnetic field provided the highest discriminative power, whereas the six thirty meter resolution Landsat TM bands provided the lowest discriminative power. The classification experiments were implemented in the context of a geological mapping project using the authentic field stations for the compilation of a training set. Dependent on the geological and geographical setting the methodology is considered a useful reconnaissance mapping and interpretation technique in support of field mapping and exploration projects.

Outlook and recommendations for future research

With the growing amount and accessibility to geological field data, geological remote sensing can be expected to evolve from a pure reconnaissance tool to an interpolation tool by incorporating available ground data in qualitative and quantitative interpretation methods. Systematic interpretation of multisource remotely sensed data sets with respect to geological maps and geological field observations may expose inconsistencies with the latest published geological maps or yield new previously unrecognized geological features even in long extensively

surveyed areas. In this context, the main advantage of the digital integration methods presented in this thesis is that they provide cost-effective approaches to refine geological understanding and map re-evaluation. To optimally exploit this potential requires not only systematic approaches where field mapping is directed towards obtaining ground truth and insight in the geological features of interest, but also surveying methodologies that specifically aim at establishing the interrelationships between the remotely sensed physical measurements and field observed geological features. Some of these methods, such as laboratory and field techniques to measure density, magnetic susceptibility, gamma-ray responses and optical spectra have been well established. Others are less commonly applied or underdeveloped, such as:

1. Surveying methodologies for description of landforms directed to establish the relationships between structural control of relief and remotely sensed data acquiring image from the Earth's surface;

2. Thin section studies directed towards identifying and quantifying the gamma-ray response of radioactive and magnetic mineralogy;

3. Comparative analysis of orientations from image extracted linear features and foliation data;

4. Comparative analysis of gamma-ray responses with geochemical data sets.

The purpose in each of these study topics is to use locally established interrelationships between geological phenomena, quantitative measurements or qualitative observations as keystones in the geological interpretation of large regions. Although previously conducted field surveys, such as geochemical surveys and petrophysical measurements of rock samples may not always be ideally suited for this purpose, they are invaluable to locally validate and reinforce interpretations where no investments for new surveys are made. These knowledge-driven methods, contrary to the commonly implemented image enhancement cookbook recipes, provide a sound basis for enhancement and interpretation. As in any mapping effort, however, the degree to which the locally observed relationships can be extended towards larger regions must be critically and repeatedly re-evaluated during progressing investigations.

Dynamic access to field knowledge by exploiting spatial querying and analytical GIS functionality to support qualitative and quantitative interpretation is

a key factor in making remote sensing operational for geologists. Although within the geological remote sensing community, image analysis and interpretation work without incorporating field data is still common place, earth scientists outside this community will be increasingly justified to question why the available field data were ignored to support and validate the analysis. At present such analysis, at least applied in a systematic manner, is extremely rare.

On the other hand any regional field mapping effort should be under increasing attack, at least for its cost-effectiveness if the available remotely sensed data sets and methodologies to exploit these data for geological reconnaissance are completely ignored. Contrary to previously published map compilations, remote sensing provides hard and relatively objective data with dense or continuous coverage over extensive regions. It then provides an alternative and more objective basis against which the validity of evolving geological models and views can be tested. Two fundamental problems that apply to the geological interpretation of multisource remotely sensed data sets, beyond the scope of the geologically-oriented studies presented in this thesis, require further research:

1. More systematic approaches are needed to assess the spatial relationships between geological field observations and remotely sensed data. Obviously in the field local details are identified that can not be resolved on remotely sensed data. On the other hand, particularly in remotely sensed data acquired over poorly exposed terrain, features may be identified that can not be resolved by studying outcrops. Because field observations are of a higher order of scale, spatial resolution and for the majority of a descriptive nature, the solution to this problem is not straightforward, and somewhat comparable to the well-known generalization problems in cartography. As previously mentioned systematic field data collection in which it is attempted to systematically record, classify and model the regional significance of each observation may offer part of the solution.

2. More research efforts are required that aim at deriving geological information from the different physical properties measured by remote sensing devices. For regional mapping, this is in practice still confined to visualization and empirical analyses that combine the knowledge and interpretation skills of the expert with image enhancement and pattern recognition techniques. An important reason for the lack of process-based approaches is that multisource remote sensing data sets often contain measurements of unrelated physical properties (e.g. the backscatter measured in synthetic aperture radar versus the

total magnetic field measured with a magnetometer). An inversion model that jointly relates unrelated physical responses has, as far as the author is aware, not been attempted. So far joint-inversion is limited to physically related data such as gravity and magnetic or gravity and seismic data. In addition, to test the applicability of joint-inversion methodologies requires well-known training areas, with substantial surface and subsurface control, in a relatively simple geological setting. A mined ore body with substantial control in 3-D would provide a good test site.

SUMMARY

With the growing availability of spatial data obtained from a multitude of remote sensing platforms and field techniques, the demand to analyse such multivariate data in an integrated manner to support geological mapping increases. This is particularly relevant in densely vegetated or poorly exposed settings, where the application of the individual surveying techniques is usually limited.

It has been previously shown that multisource remotely sensed data contribute in a complementary fashion to geological mapping. Their application is however usually limited to regional reconnaissance mapping. An important limitation of these applications is that the patterns extracted from remotely sensed data can not be unequivocally related to the geological features they reflect. A lineament outlined on a satellite image, for instance, can be related to several geological features, such as a lithological boundary, a fracture or a fold axis. With the exception of the inaccessible poorly mapped or covered areas, remote sensing studies appear to have contributed little to geological insight. One of the apparent reasons for these limitations is that the available geological knowledge has not been integrated effectively in the interpretation process.

This thesis presents digital integration methods for geological interpretation of multisource remotely sensed data sets supported by full access and interaction with geological field data. The integration methods were applied on a densely forested test area in the Canadian Shield of northeastern Alberta constituting the exposed part of the Paleoproterozoic Taltson magmatic zone. Several remotely sensed data became available in this area under the auspices of the Canada-Alberta agreement of mineral development. Participation in the fieldwork component of this project allowed validating the interpretation of the remotely sensed data on the ground. Airborne magnetic and gamma-ray spectrometry data, spaceborne Landsat TM and ERS-1 image data were in combination with geological field observations stored and geometrically registered in a geographic information system (GIS). This data structure facilitated integrated analyses and representations that allowed developing several "themes" for enhancement and interpretation strongly rooted on geological reasoning. This thesis addresses both the methodological aspect as well as the applications of geological data integration, presented in three parts: 1: reconnaissance studies on the geology of the study area in relation to the remotely sensed data, 2: methodological aspects of geological data integration and 3: geological applications supported by spatial data integration.

I. Reconnaissance

Geological knowledge obtained from the literature and fieldwork is the first condition to place the results of the integration studies in the context of recent geological insight of the study area. Chapter 2 provides a geological review of the Taltson magmatic zone. The Taltson magmatic zone is on the basis of recent geochronological work and regional syntheses considered as a Paleoproterozoic Andean magmatic arc modified by continental collision between the Archean Churchill province and Paleoproterozoic Buffalo Head terrane. Vertical shear zones, active during and after the emplacement of the Taltson plutonic suites accommodated southward escape of crustal fragments under a sinistral transpressional regime.

The geological interpretation of the multisource remotely sensed data set with outlines of inferred lithotectonic assemblages and structures are presented in Chapter 3. This reconnaissance study allowed assessing the overall geological information content of the data set. The interpretations suggest that the airborne magnetic and gamma-ray spectrometry data have the highest potential for lithological mapping. The Taltson plutonic granitic and granodioritic suits can be outlined on differences in relative abundance of potassium, thorium and uranium airborne concentrations, whereas the older gneisses of the Taltson basement can be differentiated on prominent linear magnetic anomaly patterns. The ERS-1 and Landsat TM images hardly show any of the lithological variations, but clearly reflect foliation patterns within the Taltson gneisses and granitoid plutons. The systematic comparison between the image-inferred and mapped geological patterns, led to the identification of several discrepancies. Circular positive magnetic anomalies and a linear anomaly suggest the presence of postkinematic intrusions in the subsurface, whereas a linear positive magnetic anomaly is interpreted as a dyke. The gamma-ray spectrometry data show several internal zonations within the Taltson granitoids that were not previously recognized by field mapping. The most prominent radioelement zonation is the subject of focussed enhancement and interpretation in Chapter 6.

II. Methodological Aspects

The systematic encoding and database management of geological field data is a key-factor to apply remote sensing in the operational context of a geological mapping project. In the more conventional digital approaches, the boundaries of published maps are digitized, leading to static, generalized and subjective

representations of the geology. In more advanced spatial databases, query mechanisms and cartographic representation of geological field data can be incorporated to warrant on demand dynamic utilization of all the geological attributes conceived useful in the interpretation process. The organizational and methodological aspects of such new field-knowledge driven digital interpretation approaches are presented in Chapter 4. Several application domains for handling field data in a digital environment are identified and illustrated by case study examples.

In the last decade the integrated visualization of multisource remotely sensed data in composite images has proven to be an effective method for exploiting complementary geological information derived from the image data of different sensors. Chapter 5 presents an improvement to the existing methodologies. This method uniformly addresses the chromatic perceptual colour attributes hue and saturation in rendering multisource remotely sensed data, preserving spectral balance. It includes optimization with respect to saturation enhancement and eliminates the hue-distortion of over-range pixels. The chromatic colour variations in the composite image are uniformly addressed in proportion to the relative numerical variations in the input data. This enhances the interpretation potential of this visualization technique.

III. Integration studies

The mapping of granite batholiths by traditional methods is due to their large dimensions and homogeneous composition time-consuming and difficult. Previous studies have shown that remote sensing techniques may contribute. Gamma-ray spectrometry data, in particular, allow mapping subtle compositional variations in granites that are not easily resolved by traditional mapping methods. In Chapter 6 a methodology is presented for mapping the internal composition and structure of one of the Taltson batholiths. Compositional and structural patterns of the southern part of the Arch Lake batholith were interpreted on the basis of gamma-ray spectrometry, aeromagnetic, Landsat TM images and available field data. The integrated approach not only aims at mapping the internal compositional variations from the gamma-ray spectrometry data, but also exploits previously collected lithogeochemical data, to locally establish the mineralogical association of the radioelements. The integration of remotely sensed and field data provided ground for speculating on the magmatic evolution and on the deformation of the batholith during its emplacement and subsequent cooling. This study learnt that subtle trends in the airborne estimates of radioelement concentrations can be identified in

multivariate space that are not revealed in ternary radioelement maps of the K, eTh and eU grids. The image representations in geographic space must be linked to multivariate space to unravel compositional trends between the radioelements. Furthermore ratio grids are useful in the identification of subtle trends, as they reduce the effects of attenuation by soil moisture and vegetation. It was shown that the eTh zonation was reflected in a dual trend in K-eTh space that appeared as a distinct break on a graph in which the eTh/K ratio of flight line samples was plotted against the distance from the central axis of the batholith. In combination with mineralogical observations and interpolated lithogeochemical patterns this suggests that the Arch Lake granite is a composite intrusion formed from distinct magmatic pulses. The refinement of IHS integration techniques developed in Part II was implemented to integrate edge-enhanced Landsat TM image and the K, eU and eTh grids and foliation data. The resulting composite images combined the structural information from the Landsat TM image with the geochemical information from the gamma-ray spectrometry data. This visualization was effective in portraying the spatial relationships between the compositional and structural patterns in the Arch Lake batholith.

Because remote sensing provides synoptic views over large regions, the mapping of the regional geometry of shear zones is another potentially useful application. Linear features extracted from ERS-1 radar data, first vertical derivative magnetic data and structural orientation data of the Charles Lake shear zone show a strong degree of correlation and therefore provided a favourable data set for interpreting shear zone geometry. To assure that the integrated enhancement was meaningful for regionally interpreting shear zone geometry, the relationships between image patterns of the imaging radar, magnetic anomalies and structural fabrics were investigated. The image radar data appears to preferentially reflect the internal structure of the shear zone, whereas the pre-existing fabrics along the shear zone are shown on the magnetic data. The negative magnetic anomaly over the Charles Lake shear zone is related to the alteration of magnetite to hematite in high-grade gneisses that were mylonitized during cooling in the amphibolite and greenschist facies. The integrated enhancement and interpretation of this data set allowed outlining pre-existing as well as shear zone induced fabric elements.

A third application in Chapter 8 integrates the remotely sensed data with field data to classify lithological units of the Taltson magmatic zone. Classification techniques from multispectral data is severely hampered by vegetation cover and limited spectral contrasts of its lithological variations. In this thesis a classification method was developed for identifying lithological units from airborne gamma-ray

spectrometry and magnetic data. The automated classification approach has been integrated in a geological mapping context where training samples were derived from field stations. The methodology assists geologists in fieldwork planning and map compilation providing an assessment of to what extent the geophysical data reflect surface geological maps. Similar to the integrated visual interpretation, discrepancies with the compiled geological map can be identified, providing targets for further geological assessments and interpretations. The classification and other methods treated in this thesis are considered particularly relevant to support geological mapping and exploration.

SAMENVATTING

Met de toenemende beschikbaarheid van ruimtelijke gegevens opgenomen door remote sensing en veldtechnieken is er een groeiende vraag naar geintegreerde interpretatie en analysemethoden ter ondersteuning van geologische kaarteringen. Dit is vooral van belang in dicht beboste of slecht ontsloten gebieden, waar de toepasbaarheid van de afzonderlijke kaarteringstechnieken gelimiteerd is.

Eerdere studies hebben aangetoond, dat verschillende typen remote sensing gegevens complementair bijdragen aan geologische kaartering. De bestaande toepassingen zijn echter veelal gelimiteerd tot regionale studies zodat het vaak onmogelijk blijkt de ruimtelijke patronen eenduidig geologisch te verklaren. Een lineament op een satellietbeeld, bijvoorbeeld, kan een manifestatie zijn van een breuk, een lithologisch contact of een veelvoud van landschapselementen die geen direkte geologische oorsprong hebben. Met uitzondering van ontoegankelijke en slecht ontsloten gebieden waar onvoldoende geologische grondgegevens beschikbaar zijn, wordt de bijdrage van remote sensing door geologen daarom vaak als teleurstellend ervaren.

Een belangrijke oorzaak van dergelijke teleurstellingen is dat de beschikbare geologische veldgegevens vaak niet op een effectieve manier in het digitale interpretatieproces geintegreerd worden. Het op een interactieve manier betrekken van de beschikbare veldgegevens in de digitale analyse en interpretatie van remote sensing gegevens is echter een voorwaarde voor een meer effectieve toepassing van remote sensing in geologische kaartering.

Deze dissertatie behandelt geïntegreerde methoden voor de geologische interpretatie van multivariate remote sensing gegevens ondersteund door interactieve representatie en analyse van geologische veldgegevens. De integratiemethoden zijn toegepast op een dicht bebost Precambisch kristallijn massief (de Taltson magmatische zone) in het noordoosten van de provincie Alberta, Canada. Verscheidene remote sensing gegevens van dit gebied kwamen beschikbaar onder auspiciën van de Canada-Alberta overeenkomst voor delfstofexploratie. Tevens ondersteunde dit project geologische kaartering, radiometrische datering en geothermobarometrische studies. Participatie in de veldkaartering van dit project maakte het mogelijk de interpretatie van de remote sensing gegevens met veldgegevens te valideren. ERS-1 en Landsat Thematic Mapper satellietbeelden, metingen van het magneetveld en gammastraling vanuit de lucht werden in combinatie met geologische veldgegevens in een geografisch informatie systeem (GIS) opgeslagen en geometrisch geregistreerd. Dit verschafte de basis voor de ontwikkeling van geïntegreerde analyse- en

representatiemethoden gericht op thematische geologische interpretatie. Zowel methodologische aspecten als geologische toepassingen zijn onderzocht, die in deze thesis in drie delen aan de orde komen: 1. verkennende interpretaties, 2. methodologische aspecten van de integratie en 3: geologische toepassingen.

I. Verkennende interpretaties

Geologische kennis verkregen uit de literatuur en veldwerk is een allereerste vereiste om de geïntegreerde analysen van remote sensing gegevens in de context van recente geologische inzichten van het studiegebied te plaatsen. Hoofdstuk twee beschrijft de lithologische opbouw en structuur van het studiegebied in Alberta dat de zuidelijke Taltson magmatische zone beslaat. De Taltson magmatische zone wordt op basis van regionale synthese en recente radiometrische dateringen beschouwd als een Paleoproterozoische continentale magmatische boog van het Andiene type, gedeformeerd door continentale collisie als gevolg van de convergentie tussen het Archaische Churchill Kraton en het Paleoproterozoiche Buffalo Head terrein. Vertikale ductile schuifzones, actief tijdens en na de intrusie van de Taltson plutonen en batholieten, begrensden in zuidelijke richting bewegende fragmenten aardkorst onder een sinistraal transpressief regiem.

Een verkennende kwalitatieve interpretatie van de dataset met betrekking tot gepubliceerde geologische kaarten geeft een idee in welke mate de remote sensing gegevens de algehele geologische patronen van het studiegebied weergeven.
Uit deze interpretaties blijkt dat van alle data typen de "airborne" magnetische en radiometrische gegevens de lithologische eenheden het beste weergeven. De Taltson granitische en granodioritische intrusieven worden weerspiegeld in verschillen in de relatieve K, Th en U abundanties, terwijl de oudere gneizen van het Taltson basement het best kunnen worden onderscheiden op interne lineaire magnetische anomaliepatronen. De lithologische informatie die afgeleid kon worden uit de interpretaties van ERS-1 en Landsat TM beelden bleek nihil te zijn, maar wel worden de foliatie-trends binnen de Taltson gneizen en graniet intrusies weerspiegeld. De systematische vergelijking tussen de interpretaties en gekaarteerde patronen leidde tot de identifikatie van verscheidene discrepanties. Interne magnetische anomalieën wijzen op het voorkomen van postkinematische intrusieve lichamen in de ondergrond en een gangvormige intrusie. De radiometrische gegevens laten interne variaties in de verschillende granietlichamen zien die voorheen onbekend waren. In Hoofdstuk 6 wordt het meest prominente zonatiepatroon onderzocht middels verdere beeldverwerking en

de geïntegreerde interpretatie van radiometrische, magnetische, Landsat TM, lithogeochemische en structurele veldgegevens.

II. Methodologische Aspecten

Een systematisch beheer van geologische veldgegevens is van cruciaal belang om de toepasbaarheid van remote sensing voor geologische veldkaarteringen te vergroten.
Hoofdstuk vier behandelt de methodologische aspecten van de opslag en het beheer van geologische veldgegevens in een relationele database structuur. Verschillende voorbeelden illustreren hoe de interactieve en thematische kartografische representatie van primaire veldobservaties de interpretatie van de remote sensing gegevens kunnen ondersteunen.

De gecombineerde visualisatie van verschillende typen remote sensing gegevens is in de laatste jaren een bruikbare techniek gebleken voor exploratie en geologische kaarteringen. Hoofdstuk 5 behandelt een verbeterde methode voor de toepassing van deze beeldintegratie techniek. Deze methode behoudt de relatieve spektrale waarden van de invoergegevens in het uiteindelijke resultaat. Dit garandeert dat de chromatische kleurwaarden in proportie tot de relatieve numerieke waarden van de invoergegevens kunnen worden geinterpreteerd. Toegepast op radiometrische gegevens betekent dit dat de kleurverschillen in het composiete beeld gerelateerd blijven aan relatieve abundanties van kalium, uranium en thorium. Tevens worden de implicaties van het gebruik van verschillende transformaties in deze methode belicht die bijdragen tot de optimale toepassing van beeldintegratietechnieken.

III. Integratie studies

De kaartering van granitische intrusieven met traditionele veldmethoden is vanwege hun grote afmetingen en subtiele verschillen in samenstelling moeilijk en arbeids-intensief. Hoofdstuk zes behandelt een methode voor de kaartering en interpretatie van de interne samenstelling en structuren van intrusieve granietlichamen op basis van radiometrische, magnetische airborne geofysische metingen, Landsat TM beelden, en geochemische, mineralogische en structurele gegevens. De geïntegreerde beeldverwerking en analysen geven naast de identificatie en kaartering van zonatiepatronen inzicht in de relatie tussen de regionale verdelingen van de radioelementen en de magmatische evolutie van het granietlichaam. Analyse van radiometrische gegevens laat een regionaal complexe

zonatie in thorium zien die onopgemerkt is gebleven in eerdere geologische veldkaartering en geochemische analyse van gesteentemonsters. De Th-zonatie is geassocieerd met bimodale trends in K-eTh plots die suggereren dat de Arch Lake graniet is opgebouwd uit meerdere magmatische pulsen. Op basis van visualisatie van radiometrische gegevens in ternaire komposiet beelden kunnen deze trends makkelijk over het hoofd worden gezien. Voor een volledige interpretatie is het van belang de radiometrische gegevens in de K-eTh-eU multivariate ruimte te analyseren. De gecombineerde visualisatie van de radiometrische K, eTh en eU kanalen, Landsat TM7 en foliatiemetingen brengt de relatie tussen de samenstelling en interne structuur van het granietlichaam in beeld. Dit geeft inzicht in de intrusieve en post-intrusieve deformatiegeschiedenis van het granietlichaam.

Aangezien remote sensing gegevens een synoptisch overzicht van grote gebieden geven, is de regionale kaartering van geologische structuren een andere nuttige toepassing. Hoofdstuk zeven behandelt een methode voor de kaartering en geometrische interpretatie van ductiele schuifzones. Lineaire structuren in ERS-1 beelden en de eerste verticale afgeleide van magnetische gegevens blijken sterk gecorreleerd te zijn met regionale foliatiepatronen in de gneizen en mylonieten van het Taltson basement en vormen tesamen een bruikbare dataset voor het interpreteren van de geometrische elementen van de schuifzone. Om een integratiemethodiek te ontwikkelen die betekenisvol is met betrekking tot de structuur van de schuifzone, zijn de relaties tussen de beeldpatronen, de topografische en magnetische respons en de foliatie in en buiten de schuifzone onderzocht. Het blijkt dat de beeldvormende radargegevens vooral de interne regionale structuur van de schuifzone laten zien, terwijl de magnetische gegevens de foliatiepatronen buiten de schuifzone weerspiegelen. Een verminderde magnetische expressie van de interne structuur van de schuifzone is geassocieerd met negatieve magnetische anomalie. Deze anomalie wordt veroorzaakt door omzettingen van magnetiet in gneissen die zijn gemylonitiseerd gedurende retrograde afkoeling in de amfiboliet en groenschist facies.

Een derde toepassing in Hoofdstuk 8 behandelt de integratie van de remote sensing gegevens en veldgegevens voor de automatische classificatie van lithologische eenheden in de Taltson magmatische zone. Deze methode is een minder subjectief alternatief voor het extraheren van lithologische eenheden in vergelijking tot visuele interpretatie (Hoofdstuk 3). De implementatie van deze classificatie experimenten zijn gebaseerd op een training set van geologische veldgegevens, radiometrische, magnetische en Landsat TM beeld variabelen. De voorspellende waarde van verschillende datacombinaties en algoritmen wordt

getest in een calibratiegebied en vervolgens toegepast op het hele studiegebied. De verkregen classificatiepatronen zijn geinterpreteerd met betrekking tot gepubliceerde geologische kaarten. Een vergelijking van de gepubliceerde geologische kaarten en classificatiepatronen bevestigen de discrepanties die in de eerdere interpretaties waren geïdentificeerd en leidde tevens tot nieuwe geologische kaartering en exploratie doelen. Deze classificatie en de andere behandelde methoden in deze dissertatie worden beschouwd als bruikbare toepassingen ter ondersteuning van geologische kaartering en exploratie.

REFERENCES

Abrams, M. and Hook, J.S., 1995, Simulated ASTER data for geological studies. IEEE Transactions on Geoscience and Remote Sensing, v. 33, n. 3, pp. 692-699.

Ady, B.E., 1993, Towards a theory of spatio-chronological relations for geoscience, unpublished M.Sc thesis, 75 pp. Department of geology, University of Toronto.

Agoston, G.A., 1979, Color theory and its application in art and design. Springer Series in optical sciences, Springer-Verlag, Berlin Heidelberg, 137 pp.

Agterberg, F.P., 1974, Developments in Geomathematics; mathematical background and geoscience applications. Elsevier Scientific Publishing Company, Amsterdam, The Netherlands, 596 pp.

Aitchinson, J., Habbema, J.D.F., and Kay, J.W., 1977, A critical comparison of two methods of statistical discrimination. Applied Statistics, v. 26, pp. 15-25.

An, P., Chung, C.F., and Rencz, A.N., 1995, Digital lithology mapping from airborne geophysical and remote sensing data in the Melville Peninsula, northern Canada using a neural network approach. Remote Sensing of the Environment, v. 53, pp. 76-84.

Andersen, H. and Nash, C.R. 1997, Integrated lithostructural mapping of the Rössing Area, Namibia using high resolution aeromagnetic, radiometric, Landsat data and aerial photographs. Exploration Geophysics v. 28, pp. 185-191.

Aronoff, S., 1991, Geographic Information Systems, A management perspective, WDL Publications, Ottawa, Canada, 294 pp.

Aspler, L.B. and Donaldson, J.A., 1985, The Nonacho basin (Early Proterozoic), Northwest Territories, Canada; sedimentation and deformation in a strike-slip setting, *in* Biddle, K.T., and Christie-Blick, N. (eds.). Strike-slip deformation, basin development and sedimentation: Society of Economic Paleontologists and Mineralogists, Special Publication 37, pp. 193-209.

Atherton, M.P., 1981, Horizontal and vertical zoning in the Peruvian Coastal Batholith. Journal of the Geological Society of London v. 138, pp. 143-149.

Atkinson, P.M., and Curran, P.J., 1994, The effect of the support on the precision of cokriging from remotely sensed data *in* IAMG '94, International Association for Mathematical Geology, proceedings of annual conference, Mont Tremblant, Quebec, Canada, pp. 9-14.

Baadsgaard, H. and Godfrey, J.D., 1972, Geochronology of the Canadian Shield in northeastern Alberta II. Charles-Andrew-Colin Lake area. Canadian Journal of Earth Sciences, v. 9, pp. 863-881.

Batty, M., 1999, New Technology and GIS *in* Longley, P., Goodchild, F., Maguire, D.J. and Rhind, D.W. (eds.) Geographical Information Systems, v. 1, John Wiley and Sons, New York, 580 pp.

Bea, F., 1999, Uranium: element and geochemistry *in* Encyclopedya of Geochemistry, Marshall, C.P. and Fairbridge, R.W. (eds.), Kluwer Academic Publishers, London, 712 pp.

References

Bednarski, J.M., 1997, Quaternary Geology along the Shield margin, northeastern Alberta *in* Macqueen (ed.) Exploring for minerals in Alberta: Geological Survey of Canada Geoscience contributions, Canada-Alberta agreement on mineral development. Geological Survey of Canada Bulletin 500, pp. 81-106.

Belanger, J.R. 1991, Remote Sensing of geochemical anomalies related to ultrabasic rocks and Gold and Uranium mineralization. Canadian Journal of Remote Sensing v. 17, n. 2, pp. 112-121.

Bell, T.H. and Hammond, R.L., 1984, On the internal geometry of mylonite zones. Jounal of Geology, v. 92, pp. 667-686.

Bennett, M.R. and Doyle, P., 1997, Environmental Geology, Geology and the Human Environment, John Wiley & Sons, New York, 501 pp.

Berman, R.G. and Bostock, H. H., 1997, Metamorphism in the northern Taltson magmatic zone, Northwest Territories. The Canadian Mineralogist, v. 35, pp. 1069-1091.

Bérthe, D., Choukroune, P., Jegouzo, P., 1979, Orthogneiss, mylonite and non-coaxial deformation of granites: the example from the South Amorican Shear Zone. Journal of Structural Geology, v. 1, pp. 31-42.

Bierman, C., 1987, Basement topography and thrust fault ramping, a model to explain cleavage fans in the Mosel area, Rheinische Schiefergebirge. Geologie en Mijnbouw, v. 66 pp. 333-341.

Blom, R.G., Crippen, R.E., Elachi, C., 1984, Detection of subsurface features in Seasat radar images of Means Valley, Mojave Desert, California. Geology 12, pp. 346-349.

Blom, R.G., 1988, Effects of variation in look angle and wavelength in radar images for geologic applications: implications for SIR-C and Magellan. Proceedings IEEE international geoscience and remote sensing symposium, Edinburg, U.K., v. 2, pp. 731-739.

Bonfatti, F. and Monari, P.D., 1995, Conceptual modelling as a means for organizing geological information *in* Proceedings Joint European Conference and Exhibition on Geographical Information, March 26-31, The Hague, pp. 442-447.

Bonham-Carter, G.F., 1994, Geographic Information Systems for Geoscientists. Pergamon, 398 pp.

Bostock, H.H., 1988, Geology of the north half of the Taltson Lake map area, District of Mackenzie *in* Current Research, Part C, Geological Survey of Canada, Paper 88-1C, pp. 189-198.

Bostock, H.H., van Breemen, O. and Loveridge, W.D., 1987, Proterozoic geochronology in the Taltson magmatic zone, N.W.T., *in* Radiogenic Age and Isotopic Studies: report 1. Geological Survey of Canada, Paper 87-2, pp. 73-80.

Bostock, H.H., 1991, Further geochronology of plutonic rocks in the northern Taltson magmatic zone, District of Mackenzie, N.W.T., *in* Radiogenic Age and Isotopic Studies: Report Paper 90-2, pp. 67-78.

Bostock, H.H. and van Breemen, O., 1994, Ages of detrital and metamorphic zircons from a pre-Taltson magmatic zone basin at the western margin of Rae Province. Canadian Journal of Earth Sciences, v. 31, pp. 1353-1364.

Brodaric, B. and Fyon, J.A., 1989, OGS Fieldlog: a microcomputer–based methodology to store, process and display map-related data. Ontario Geological Survey, Open File report 5709, 73 pp.

Brodaric, B., 1997, Geological field data capture and manipulation using Fieldlog v.3.0 Digital mapping techniques 97, Proceedings of a workshop on digital mapping techniques: methods for geologic map data capture, management and publication. U.S. Geological Survey Open-File report 97-269, pp. 77-82.

Brodaric, B. and Harrap R., 1999, GSC Fieldlog v 3.0 Users Guide and Manual. Geological Survey of Canada, Ottawa, 120 pp.

Broome, H.J., Carson, J.M., Grant, J.A., Ford, K.L., 1987, A modified ternary radioelement mapping technique and its application to the south coast of Newfoundland. Geological Survey of Canada, Paper 87-14, pp. 31-45.

Broome, H.J., 1990, Generation and interpretation of geophysical images with examples from the Rae Province, northwestern Canada shield. Geophysics, v. 55, n. 8, pp. 977-997.

Broome, J., Brodaric, B., Viljoen, D., Baril, D., 1993, The NATMAP digital geoscience database management system. Computer and Geosciences, v. 19, n. 10, pp. 1501-1516.

Broome, J., 1997, Evolution of geological mapping methodology at GSC-Ottawa *in* A.G. Gubbins (ed.), Proceedings of Exploration 97, pp. 169-174.

Carper, W.J., Lillesand, T.M., Kiefer, R.W., 1990, The use of intensity-hue-saturation transformations for merging SPOT Panchromatic and Multispectral Data. Photogrammetric Engineering & Remote Sensing, v. 56, n. 4, pp. 459-467.

Chacko, T. and Creaser, R.A., 1995, Hercynite-bearing granites and associated metasedimentary enclaves from the Taltson magmatic zone, Alberta, Canada: a natural example of high-temperature pelite melting *in* The origin of granites and related rocks (M. Brown and P. M. and Piccoli, eds.). U.S. Geological Survey, Circular. 1129, pp. 161-162.

Chacko, T, 1997, Ultra-high temperature metamorphism at Pelican Rapids, Taltson Magmatic Zone, NE Alberta: Possible implications for Early Proterozoic collisional orogens. Geological and Mineralogical Association of Canada, program abstracts, 22, A24.

Chavez, P.S., Bowell, J., 1988, The comparison of the spectral information content of Landsat Thematic Mapper and SPOT for three different sites in the Phoenix, Arizona Region. Photogrammetric Engineering and Remote Sensing, v. 57, n. 3, pp. 1699-1708.

Charbonneau, B.W., Geophysical signature, 1991, Geochemical evolution and radioactive mineralogy of the Fort Smith radioactive belt, Northwest Territories, Canada. *in* Primary Radioactive Minerals (The textural patterns of radioactive mineral paragenetic associations). Theophrastus Publications, Athens, Greece, pp. 21-48.

Charbonneau, B.W., Holman, P.B., Hetu, R.J., 1994, Airborne geophysical survey, Northeast Alberta, open file 2807. Geological Survey of Canada, Ottawa.

References

Charbonneau, B.W., Holman, P.B., Hetu, R.J., 1997, Airborne gamma spectrometer-magnetic-VLF survey of northeastern Alberta *in* R.W. Macqueen (ed.) Exploring for minerals in Alberta: Geological Survey of Canada Geoscience contributions, Canada-Alberta agreement on mineral development (1992-1995). Geological Survey of Canada, Ottawa, pp. 107-131.

Chatterjee, A.K. and Muecke, G.K., 1982, Geochemistry and the distribution of uranium and thorium in the granitoid rocks of the Southern Mountain Batholith, Nova Scotia: some genetic and exploration implications, in uranium in granites, Y.T. Maurice (ed.). Geological Survey of Canada, Paper 81-23, pp. 11-17.

Chavez, P.S., Sides, S.C., Anderson, J.A., 1991, Comparison of three different methods to merge multiresolution and multispectral data: Landsat TM and SPOT Panchromatic. Photogrammetric Engineering & Remote Sensing, v. 57, n. 3, pp. 295-303.

Choukroune, P., Gaspais, D. and Merle, O., 1987, Shear criteria and structural symmetry. Journal of Structural Geology, v. 9, pp. 525-530.

Chung, C.F., Rencz, A.N., Zhang, A., Garson, D.F., 1998, Geoscientific data for northeastern Alberta, contribution to Canada-Alberta agreement on mineral development (1992-1995),CD-ROM, Open File 3501. Geological Survey of Canada, Ottawa.

CIE, 1971, Recommendations on uniform color spaces-color difference equations, psychometric colour terms, CIE Publication, 15(E-1.3.1)/(TC-1.3) Supplement 2, pp. 9-12.

CIE, 1986, Colorimetry, 2nd Edition, CIE Publication 15-2 1986 ISBN 3-900-734-00-3, 83 pp.

Clark, D.A., 1997, Magnetic petrophysics and magnetic petrology aids to geological interpretation of magnetic surveys. AGSO Journal of Australian Geology & Geophysics, v. 17, n. 2, pp. 83-104.

Corsini, M., Vauchez, A. and Caby, R., 1996, Ductile duplexing of a continental-scale strike-slip shear zone: example from NE-Brazil. Journal of Structural Geology, v. 18, n. 4, pp. 385-394.

Davis, J.C., 1973, Statistics and Data Analysis in Geology. John Wiley & Sons, New York, 646 pp.

deKemp, E.A., 1998, Variable 3-D geometrical projection of curvilinear geological features through direction cosine interpolation of structural field observations. Computer and Geosciences, v. 24, n. 3, pp. 269-284.

Denham, D., 1997, Airborne geophysics in Australia: the government contribution. AGSO Journal of Australian Geology & Geophysics, v. 17, n. 2, pp. 23-30.

Dickson, B.L., and Scott, K.M., 1997, Interpretation of aerial gamma-ray surveys-adding the geochemical factors. AGSO Journal of Australian Geology & Geophysics, v. 17 n. 2, pp. 187-200.

Dixon, J. and Williams, G., 1983, Reaction softening in mylonites from the Arnaboll thrust Sutherland. Scottish journal of Geology, v. 19, pp. 157-168.

Drury, S.A., 1993, Image interpretation in geology, 2nd ed. Chapman & Hall, London, 283 pp.

Elachi, C., Brown, W.E., Cimino, J.B., Dixon, T., Evans, D.L., Ford, J.P., Saunders, R.S., Breed, C., Masursky, H., McCauley, J.F., Schaber, G., Dellwig, L., England, A., MacDonald, P., Martin-Kaye, P. and Sabbins, F., 1982, Shuttle imaging radar experiment. Science 218, pp. 996-1003.

European Space Agency, 1992, ERS-1 user handbook, Proud, L. and Battrick, B. (eds.), ESA Publication Division, ESA sp-1148, c/o ESTEC, Noordwijk, The Netherlands, 159 pp.

Fabbri, A.G., 1984, Image processing of geological data, New York, Van Nostrand Reinhold, 244 pp.

Fisher, N.I., 1993, Statistical analysis of circular data, University Press, Cambridge, 277 pp.

Fox, W.T., 1967, FORTRAN IV Program for vector trend analysis of directional data. Kansas Geological Survey computer contributions n. 11, 36 pp.

Ford, K.L. and O'Reilly, G.A., 1985, Airborne gamma-ray spectrometric surveys as an indicator of granophile element specialization and associated mineral deposits in the granitic rocks of the Meguma Zone of Nova Scotia, Canada. *in* high heat production (HHP) granites, hydrothermal circulation and ore genesis. The institution of Mining and Metallurgy, London, pp. 113-133.

Frost V.S., Stiles, J.A., Shanmugan, K.S., and Holtzman, J.C., 1982, A model for radar images and its application to adaptive filtering of multiplicative noise, IEEE Trans. Pattern Analysis and Machine Intelligence, v. 7, n. 2, pp. 992-1000.

Gaile, G.L., and Burt, J.E., 1980, Directional statistics, concepts and techniques in modern geography CATMOG 25, 29 pp.

Geological Survey of Canada (1963a - 1963e, 1964a - 1964t) Geophysical Series (Aeromagnetic Maps) 2861G, 2862G, 2863G, 2868G, 2869G, 2870G, 2871G, 2876G, 2877 G, 2878G, 2879G, 2884G, 2885G, 2886G, 2887G, 2892G, 2893G, 2894G, 2895G, 2903G, 2904G, 2905G, 2906G, scale 1 inch: 1 mile; (1964y) 7161G (74M); (1964v), 7159G (74L), scale 1: 250.000.

GEOSOFT 1994, GEOSOFT mapping and processing system, MAGMOD Interactive Magnetic Anomaly Inversion, User manual, Toronto, Canada, 52 pp.

Gibb, R.A., 1979, Slave-Churchill collision tectonics. Nature, v. 271, pp. 50-52.

Gibb, R.A., 1983, Model for suturing of Superior and Churchill plates: an example of double indentation tectonics. Geology, v. 11, pp. 413-417.

Gillespie, A.R., Kahle, A.B., Walker, R.E., 1986, Colour enhancement of highly correlated images. Decorrelation and IHS contrast stretches. Remote Sensing of the Environment, v. 20, pp. 209-235.

Godfrey, J.D. and Langenberg C.W., 1978, Metamorphism in the Canadian Shield of northeastern Alberta, Geological Survey of Canada, Paper 78-10, pp. 129-138.

Godfrey, J.D., 1986, Geology of the Precambrian Shield of northeastern Alberta: Alberta Research Council, Map 1986-1, scale 1:250,000.

Godfrey, J.D. and Langenberg, C.W., 1987, Geology of the Myers-Daly Lakes district, Alberta, Earth Sciences Report 84-6, Alberta Research Council, 30 pp.

References

Goetz, A.F.H. and Rowan, L.C., 1981, Geologic Remote Sensing. Science, v. 211, pp. 781-791.

Goff, S.P., Godfrey, J.D., Holland, J.G., 1986, Petrology and geochemistry of the Canadian Shield of northeastern Alberta. Alberta Research Council Bulletin 51, pp. 1-60.

Goossens, M.A., 1992, Petrogenesis of the mineralized granitic intrusion near Los Santos, Western Spain, and remote sensing and data integration as a tool in regional exploration for granite related mineralization. PhD thesis. Geologica Ultraiectina 89, 164 pp.

Gorte, B. and Koolhoven, W., 1990, Interpolation between isolines based on the Borgefors distance transform. ITC Journal, Special Issue n. 3, pp. 245-247.

Gorte, B., 1994, Tools for advanced image processing and GIS using ILWIS. ITC internal publication n. 24, 60 pp.

Gosh, S.K. and Sengupta, S., 1987, Progressive development of structures in a ductile shear zone. Journal of Structural Geology, v. 9, pp. 277-287.

Grant, J.A., 1998, Ten things textbooks don't tell you about processing and archiving airborne gamma-ray spectrometric data *in* current Research 1998 D. Geological Survey of Canada, Ottawa, pp. 83-87.

Grasso, D.N., 1993, Applications of the IHS color transformation for 1:24,000-scale geologic mapping: a low cost SPOT alternative. Photogrammetric Engineering & Remote Sensing, v. 59, n. 1 pp. 73-80.

Grasty, R.L., Carson, J., Charbonneau, B.W., Holman, P.B., 1984, Natural background radiation in Canada. Bulletin 360. Geological Survey of Canada, Ottawa.

Green, A.A. and Craig, M., 1984, Integrated analysis of image data for mineral exploration, *in* Proceedings of the Third Thematic Conference on Geologic Remote Sensing, 16-19 April, 1996, Colorado Springs, Colorado, USA, pp. 131-137.

Grover, T.W., Pattison, D.R.M., McDonough, M.R., McNicoll, V.J., 1997, Tectonometamorphic evolution of the southern Taltson Magmatic Zone and associated shear zones, northeastern Alberta. The Canadian Mineralogist, v. 35, pp. 1051-1067.

Gundersen, L.C.S., 1991, Radon in sheared igneous and metamorphic rocks. *in* Gundersen, L.C.S., and Wanty, R.B., (*eds.*) Field studies of radon in rocks, soil and water.U.S. Geological Survey Bulletin 1991, pp. 39-50.

Gunn, P.J., 1997, Quantitative methods for interpreting aeromagnetic data: a subjective review. AGSO Journal of Australian Geology and Geophysics, v. 17 n. 2, pp. 105-113.

Hanmer, S., Shaocheng, J., Darrach, M., and Kopf, C., 1991, Tantato domain, northern Saskatchewan: a segment of the Snowbird tectonic zone, in Current research, Part C, Geological Survey of Canada, Paper 91-1C, pp. 121-33.

Hanmer, S. and Passchier, C.W., 1991, Shear-sense indicators: a review. Geological Survey of Canada, Paper 90-17, 71 pp.

Hanmer, S., Bowring, S., van Breemen, O., and Parrish, R., 1992, Great Slave Lake shear zone, NW Canada: mylonitic record of Early Proterozoic continental convergence, collision and indentation.Journal of Structural Geology, v. 14, pp. 757-773.

Harrington, S.E., McLellan, E.L., Siegrist, H.G., 1991, A remote sensing based investigation of geobotanical relationships associated with ultramafic rocks in the Bedivere Lake Region, NW Ontario. Canadian Journal of Remote Sensing, v. 17, n. 2, pp. 72-84.

Harris, J.R., 1991, Mapping of regional structure of eastern Nova Scotia using remotely sensed imagery: implications for regional tectonics and gold exploration. Canadian Journal of Remote Sensing, v. 17, n. 2, pp. 122-136.

Harris, J.R, Murray, R., Hirose, T., 1990, IHS Transform for the integration of Radar imagery and other remotely sensed data. Photogrammetric Engineering & Remote Sensing, v. 56, n. 12, pp. 1631-1641.

Harris, J.R., Bowie, C., Rencz, A.N., Graham, D., 1994, Computer enhancement techniques for the integration of remotely sensed, geophysical, and thematic data for the geosciences. Canadian Journal of Remote Sensing, v. 20, n. 3, pp. 210-221.

Haydn, R., Dalke, G.W., Henkel, J. and Bare, J.C., 1982, Application of the IHS color transform to the processing of multisensor data and image enhancement *in* Proceedings of the International Symposium on RS of Arid and Semi-Arid Lands, pp. 599-607.

Henderson, J.R. and Broome, J., 1990, Geometry and kinematics of Wager shear zone interpreted from structural fabrics and magnetic data. Canadian Journal of Earth Sciences, 27, pp. 590-604.

Hippertt, J.F., 1998, Breakdown of feldspar, volume gain and lateral mass transfer during mylonitization of granitoid in a low metamorphic grade shear zone. Journal of Structural Geology, v. 20, n. 2/3, pp. 175-193.

Hippertt, J.F., 1999, Are S-C structures, duplexes and conjugate shear zones different manifestations of the same scale-invariant phenomenon? Journal of Structural Geology, v. 21, pp. 975-984.

Hoffman, P.F., 1987, Continental transform tectonics: Great Slave Lake shear zone (ca. 1.9 Ga.), northwest Canada. Geology, v. 15, pp. 785-788.

Hoffman, P.F., 1988, United Plates of America: The birth of a craton. Annual Review of Earth and Planetary Sciences, v. 16, pp. 543-603.

Hoffman, P.F., 1989, Precambrian geology and tectonic history of North America; *in* Bally, A.W. and Palmer, A.R., (eds.), The Geology of North America. An overview: Boulder, Colorado. Geological Society of America, v. A, pp. 447- 512.

Horsfall, K.R., 1997, Airborne magnetic and gamma-ray data acquisition. AGSO Journal of Australian Geology & Geophysics, v. 17, n. 2, pp. 23-30.

Hutton, D.H.W., 1996, The 'space problem' in the emplacement of granite, Episodes, Special issue on the geology of granites, v. 19, n. 4, pp. 114-119.

ILWIS 1.4, 1993, The integrated land and water information system: users manual, International Institute for Aerospace Surveys and Earth Sciences, Enschede, 400 pp.

References

Jaques, A.L., Wellman, P., Whitaker, R. and Wyborn, D., 1997, High-resolution geophysics in modern geological mapping. AGSO Journal of Australian Geology & Geophysics. v. 17, n. 2, pp. 159-174.

Kaupp, V.H., Waite, W.P., Derryberry, B.A. and MacDonald, H.C., 1988, Comparative evaluation of like polariation for non-renewable resource exploration, Proceedings, IEEE International geoscience and remote sensing symposium, Michigan, v. 2, pp. 1287-1292.

King, R.W., Kaupp, V.H. and Waite, W.P., 1984, Digital color space transformations *in* Proceedings of IGARSS'84 Symposium,Strasbourg 27-30 August 1984, pp. 649-653.

Kuosmanen, V., 1994, Gold prediction in northeast Finland. *in* Spatial data integration for mineral exploration, resource assessment and environmental studies, a guidebook, IAEA-TECDOC-782, pp. 161-172.

Lang, S. C., Withnall, I.W., Grimes, K.G., Murphy, P.R., Day, R.W., 1990, REGMAP, a computerized geological field data management system, Queensland Department of Mines, Australia, unpublished internal report 6 pp.

Langenberg, C.W. and Ramsden, J., 1980, The geometry of folds in granitoid rocks of northeastern Alberta. Tectonophysics, v. 66, pp. 269-285.

Lavreau, J., and Fernandez-alonso, M., 1991, Correcting airborne radiometric data for water vegetation screening using Landsat Thematic Mapper imagery. Proceedings of the eight Thematic conference on geologic Remote Sensing, Denver, Colorado, USA, 29 April-2 May 1991 (Ann Arbor; ERIM), pp. 439-446.

Lewry, J.F., Sibbald, T.I.I., Schledewitz, D.C.P., 1985, Variation in character of Archean rocks in the western Churchill Province and its significance. *in* Evolution of Archean Supracrustal sequences (L.D. Ayres, P.C. Thurston, K.D. Card & W. Weber, (eds.) Geological Association of Canada, Special Paper. 28, pp. 239-261.

Lillesand, T.M. and Kiefer, R.W. 1994, Remote Sensing and Image Interpretation, third edition, John Wiley & Sons, Inc., 750 pp.

Lowman, P., 1994, Radar geology of the Canadian shield: a 10-year review. Canadian Journal of Remote Sensing, v. 19, n. 4, pp. 198-209.

Luyendyk, A.P.J., 1997, Processing of airborne magnetic data. AGSO Journal of Australian Geology & Geophysics, v. 17, n. 2, pp. 31-38.

Macqueen, R.W., 1997, Exploring for minerals in Alberta: Geological Survey of Canada Geoscience Contributions, Canada-Alberta agreement on mineral development (1992-1995). Geological Survey of Canada, Bulletin 500, 357 pp.

Mather, P.M., Brandt, Tso, and Koch, M., 1998, An evaluation of Landsat TM spectral data and SAR-derived textural information for lithological discrimination in the Red Sea Hills, Sudan. International Journal of Remote Sensing, v. 19, n. 4, pp. 587-604.

Marschallinger, R., 1991, Interface programs to enable full 3-D geologic modelling with a combination of AutoCAD and SURFER. Computer & Geosciences, v. 17, n. 10, pp. 1383-1394.

Martel, C., Flouzat, G., Souriau, A. and Safa, F., 1989, A morphological method of geometric analysis of images: applications to the gravity anomalies in the Indian Ocean. Journal of Geophysical Research, v. 94, n. B2, pp. 1715-1726.

Maurice, Y.T. and Charbonneau, B.W., 1987, U and Th concentration processes in Canadian granitoids their detection by airborne gamma-ray spetrometry and their relationship to granophile mineralization *in* Revista Brasileira de Geociências, v. 17, n. 4, pp. 644-646.

McClay, K., 1987, The mapping of geological structures, Geol. Soc. London Handbook, John Wiley & Sons, New York, 161 pp.

McDonough, M.R., Grover, T.W., McNicoll, V.J., and Lindsay, D.D., 1993, Preliminary report of the geology of the southern Taltson magmatic zone, northeastern Alberta, *in* current research, Part C. Geological Survey of Canada, Paper 93-1C, pp. 221-232.

McDonough, M.R., Grover, T.W., McNicoll, V.J., Cooley, M.A., Schetselaar, E.M. and Robinson, N.N., 1994a, Geology Cornwall Lake, Alberta (74M/10), Geological Survey of Canada, Calgary Open File 2896, scale 1: 50,000.

McDonough, M.R., Cooley, M.A., Schetselaar, E.M., 1994b, Geology Hay Camp, Alberta (74M/11). Geological Survey of Canada, Calgary Open File 2896, scale 1: 50,000.

McDonough, M.R., Grover, T.W., McNicoll, V.J., and Lindsay, D.D., Kelly, K.L. and Guerstein, P.G., 1994c, Geology Tulip Lake, east-half, Alberta (75/M14). Geological Survey of Canada, Calgary, Open File 2904, scale 1: 50,000.

McDonough, M.R., Grover, T.W., McNicoll, V.J., and Lindsay, D.D., Kelly, K.L., and Guerstein, P.G., 1994d, Geology Mercredi Lake, Alberta - Northwest Territories (75/M15). Geological Survey of Canada, Calgary, Open File 2904, scale 1: 50,000.

McDonough, M.R., Grover, T.W., McNicoll, V.J., and Lindsay, D.D., Kelly, K.L. and Guerstein, P.G., 1994e, Revised Geology Andrew Lake, Alberta - Sasketchewan - Northwest Territories (75/M16). Geological Survey of Canada, Calgary, Open File 2905, scale 1: 50,000.

McDonough, M.R.M., McNicoll, V.J. and Schetselaar, E.M., 1995, Age and kinematics of crustal shortening and escape in a two-sided oblique-slip collisional and magmatic orogen, Paleoproterozoic Taltson Magmatic Zone, Northeastern Alberta *in* Ross, G.M., (ed.) LITHOPROBE Alberta Basement Transects Workshop, Lithoprobe Report n. 47, Lithoprobe Secretariat, University of British Columbia.

McDonough, M.R., 1997, Structural controls and age constraints on sulphide mineralization, Southern Taltson Magmatic Zone, northeastern Alberta *in* R.W. Macqueen (ed.), Exploring for minerals in Alberta: Geological Survey of Canada Geoscience contributions, Canada-Alberta agreement on mineral development (1992-1995). Geological Survey of Canada Bulletin 500, Ottawa, pp. 13-30.

McDonough, M.R.M., McNicoll, V.J. and Schetselaar, E.M., 2000, Age and kinematics of crustal shortening and escape in a two-sided oblique-slip collisional and magmatic orogen, Paleoproterozoic Taltson Magmatic Zone, Northeastern Alberta. Canadian Journal of Earth Sciences (*in press*).

References

McLachlan, G.J. 1992, Discriminant Analysis and Statistical Pattern Recognition, New York, Wiley, 300 pp.

McNicoll, V.J., McDonough, M.R., and Grover, T.W. 1994, U-Pb geochronological studies in the southern Taltson magmatic zone, northeastern Alberta. In Report of LITHOPROBE Alberta Basement Transects Workshop, LITHOPROBE Report n. 37, pp. 270-273.

Merriam, D.F. and Harbaugh, J.W., 1964, Trend surface analysis of regional and residual components of geological structure of Kansas, Kansas Geological Survey. Special distribution publication 11, 27 pp.

Merriam, D.F., 1969, Computer Applications in the Earth Sciences. Plenum, New York, 281 pp.

Michael, P.J., 1984, Chemical differentiation of the Cordillera Paine granite (southern Chile) by in situ fractional crystallization. Contributions to Mineralogy and Petrology, v. 87, pp. 179-195.

Milligan and Gunn, 1997, Enhancement and interpretation of airborne geophysical data. AGSO Journal of Australian Geology & Geophysics, v. 17, n. 2, pp. 63-75.

Mussakowski, R., Trowell, N.F., Heather, K.B., 1991, Digital integration of remote sensing and geoscience data for the Goudreau-Lochalsh area, Wawa, Ontario. Canadian Journal of Remote Sensing, v. 17, n. 2, pp. 162-173.

Nash, C., Leeming, P., Kotasek, H., Carey, R., 1996, Integrated interpretation of imaged airborne geophysical survey and remoe sensing data with the aid of vectorised CAD/GIS coverages: Halls Creek mobile Belt, Australia *in* Proceedings of the Eleventh Thematic Conference on Geologic Remote Sensing, 27-29 February, 1996, Las Vegas, Nevada, USA, v. 1, pp. 343-352.

Niblack, W., 1986, An introduction to digital image processing, Prentice/Hall International, London, 215 pp.

Nielsen, P.A., Langenberg, C.W., Baadsgaard, H. and Godfrey, J.,1981, Precambrian metamorphic conditions and crustal evolution, Northeastern Alberta, Canada. Precambrian Research, v. 16, pp. 171-193.

Norwegian Geological Survey, 1992, GBAS, et PD-systen for lagring og bruk av berggrunnsgeologiske feltdata, (in Norwegian) NGU report 92.230.

Paola, J.D. and Schowengerdt, R.A., 1995, A review and analysis of backpropagation neural networks for classification of remotely sensed multi-spectral imagery. International Journal of Remote Sensing, v. 16, n. 16, pp. 3033-3058.

Paradella, W., R., Bignelli, P.A., Veneziani, P., Pietsch, R.W., Toutin, T., 1997, Airborne and spaceborne Synthetic Aperture Radar (SAR) integration with Landsat TM and gamma-ray spectrometry for geological mapping in a tropical rainforest environment, the Carajás Mineral Province, Brazil, International Journal of Remote Sensing, v. 18, n. 7, pp. 1483-1502.

Paradella, W.R., Bignelli, P.A., Veneziani, P, Pietsch, R.W., Toutin, T., 1997, Airborne and spaceborne synthetic aperture radar (SAR) integration with Landsat TM and gamma-ray spectrometry data for geological mapping in a tropical rainforest environment, Carajas Mineral Province, Brazil. International Journal of Remote Sensing, v. 18, n. 7, pp. 1483-1502.

Passchier, C.W. and Trouw, R.A.J., 1996, Microtectonics, Springer-Verlag, Berlin Heidelberg, 289 pp.

Passchier, C.W. and Williams, P.R., 1996, Conflicting shear sense indicators; the problem of non-ideal sections. Journal of Structural Geology, v. 18, n. 10, pp. 1281-1284.

Paterson, S.R., and Fowler, T.K., 1993, Re-examining pluton emplacement processes. Journal of Structural Geology, v. 15, n. 2, pp. 191-206.

Patiño-Douce, A.E. and Johnston, A.D., 1991, Phase equilibria and melt productivity in the pelitic system; implications for the generation of peraluminous granitoids and aluminous granites. Contributions to Mineraology and Petrology, v. 107, pp. 202-218.

Pitcher, W.S., 1993, The nature and origin of granites, Blackie Academic & Professional, Chapman and Hall, Glasgow, 321 pp.

Platt, J.P. and Vissers, R.L.M., 1980, Extensional structures in anisotropic rocks. Journal of Structural Geology, v. 2, pp. 397-410.

Plint, H.E. and McDonough, 1995, M.R. $^{40}Ar/^{39}Ar$ and K-Ar age constraints on shear zone evolution, southern Taltson magmatic zone, northeastern Alberta. Canadian Journal of Earth Sciences, v. 32, pp. 281-291.

Pohl, C., 1996, Geometric aspects of multisensor image fusion for topographic map updating in the humid tropics, Ph.D.-Thesis. ITC publication 39, 159 pp.

Pohl, C. and van Genderen, J.L., 1998, Multisensor image fusion in remote sensing: concepts, methods and applications. International Journal of Remote Sensing, v. 19, n. 5, pp. 823-854.

Press, S.J. 1972, Applied Multivariate Analysis, Holt, Rinehart and Winston inc., 521 pp.

Pristas, R.S. and Herman, G.C., 1997, Overview of New Jersey Geological Survey digital data methods *in* Proceedings of a workshop on digital mapping techniques: methods for geologic map data capture, management and publication. U.S. Geological Survey Open-File report 97-269, pp. 77-82.

Ramsay, J. G. 1967, Folding and fracturing of rocks, McGraw-Hill, New York, 568 pp.

Ramsay, J.G., 1980, Shear zone geometry: a review. Journal of Structural Geology, v. 2, pp. 83-99.

Ramsay, J.G. and Huber, M.I., 1987, Appendix F geological mapping *in* The techniques of modern structural geology, Volume 2: Folds and Fractures, Academic Press, London, pp. 673-684.

Reeves, C.V., Zeil, P.W., Zhou, Y., 1990, Airborne geophysics, image processing and GIS. ITC Journal, 1990-2, pp. 126-136.

Reeves, C.V., Reford, S.W. and Milligan, P.R., 1997, Airborne geophysics: old methods, new images. *in* A.G. Gubbins (ed.) Proceedings of Exploration 97, fourth decennial international conference on mineral exploration, pp. 13-30.

Reeves, C.V., 1998, Continental scale and global geophysical anomaly mapping. ITC Journal 1998-2, pp. 91-98.

References

Reeves, CV., 1998, Geophysical anomaly mapping. ITC Journal, 1998-2, pp. 91-98.

Ripley, B.D., 1996, Pattern Recognition and Neural Networks, Cambridge University Press, Cambridge, 403 pp.

Robertson, P.K. and O'Callaghan, J.F., 1988, The application of perceptual colour spaces to the display of remotely sensed data, IEEE Transaction on geoscience and remote sensing, v. 26, n. 1, pp. 49-59.

Ross, G.M., Parrish, R.R., Villenueve, M.E., and Bowring, S.A., 1991, Geophysics and geochronology of the crystalline basement of the Alberta Basin, western Canada. Canadian Journal of Earth Sciences, v. 28, pp. 512-522.

Rummelhart, D.E. and Williams, R.J., 1986, Parallel Distributed Processing:exploration in microstructures of cognition, v.1. Cambridge, NJ, MIT Press.

Sabbins, F.F. Jr., 1987, Remote Sensing Principles and Interpretation (2nd. ed.), New York, Freeham & Co., 449 pp.

Satterwhite, M.B., Henley, J.P. and Carney, J.M., 1985, Effects of lichen cover on the reflectance of granitic rock surfaces. Remote Sensing of Environment, v. 18, pp. 105-112.

Sawka, W.N. , Chappell, B.W. and Kistler, R.W., 1990, Granitoid compositional zoning by side-wall boundary layer differentiation; evidence from the Pallisade Creek intrusive suite, central Sierra Nevada, California. Journal of Petrology, v. 31, pp. 519-553.

Schetselaar, E.M., 1994, A comparative evaluation on the potential of C-band airborne SAR and Panchromatic SPOT images for geologic mapping in the Archean Hood River Belt, Bathurst Inlet, Northwest Territories. Canadian Journal of Remote Sensing, v. 20, n. 3, pp. 302-316.

Schetselaar, E.M., 1995, Computerized field data capture for geological data integration, proceedings Joint European Conference and Exhibition on Geographical Information Systems, The Hague, pp. 436-441.

Schetselaar, E.M., 1995, Computerized field-data capture and GIS analysis for the generation of cross-sections in 3-D perspective views. Computer and Geosciences, v. 21, n. 5, pp. 687-701.

Schetselaar, E.M. and McDonough, M.R.M., 1996, Shear zone mapping using ERS-1 SAR images of the Paleproterozoic Taltson magmatic zone, Canadian Shield, northeastern Alberta. ITC Journal, 1996-2, pp. 166-175.

Schetselaar. E.M and Rencz, A.N., 1997, Reducing the effects of vegetation cover on radiometric data using Landsat TM data. International Journal of Remote Sensing, v. 18, n. 7, pp. 1503-1515.

Schetselaar, E.M., 1998, Fusion by the IHS transform: should we use cylindrical or spherical coordinates? International Journal of Remote Sensing, v. 19, n. 4, pp. 759-765.

Schetselaar, E.M., Chung, C.F, and Kim, K.E., 2000, Integration of Landsat TM, gamma-ray, magnetic, and field data to discriminate lithological units in vegetated granite-gneiss terrain. Remote Sensing of the Environment, v. 71, pp. 89-105.

Selby, M.J., 1982, Earth's changing surface, Claredon Press, Oxford, 607 pp.

Serra, J., 1982, Image Analysis and Mathematical Morphology, Academic. San Diego, California, 610 pp.

Shelley, D., 1993, Igneous and metamorphic rocks under the microscope, classification, textures, microstructures and mineral preferred orientations, Chapman and Hall, London, 445 pp.

Shettigara, V.K., 1992, A Generalized Component Substitution Technique for Spatial Enhancement of Multispectral Images Using a Higher Resolution Data Set. Photogramettric Engineering & Remote Sensing, v. 58, n. 5, pp. 561-567.

Shi, Z. and Fung, K.B., 1994, A comparison of digital speckle filters. Proceedings IGARSS, August 94, pp. 2129-2133.

Singhroy, V., Slany, R., Lowman, P., Harris, J., and Moon W., 1993, Radarsat and radar geology in Canada. Canadian Journal of Remote Sensing, (special Radarsat issue), v. 19, n. 4, pp. 338-351.

Simpson, C. and Schmid, S.M., 1983, An evaluation of criteria to deduce the sense of movement in sheared rocks. Geological Society of America Bulletin, v. 94, pp. 1281-1288.

Skilbrei, J.R., Skyseth, T. and Olesen, O., 1991, Petrophysical data and opaque mineralogy of high-grade and retrogressed lithologies: implications for the interpretation of aeromagnetic anomalies in Northern Vestranden, Central Norway. Tectonophysics, v. 192, pp. 21-31.

Sprenke, K.F., Wavra, C.S., Godfrey, J.D., 1986, Geophysical expression of the Canadian Shield of northeastern Alberta, Geological Survey Department, Alberta Research Council, Bulletin 52, 54 pp.

Stephens, W.E. and Halliday, A.M., 1980, Discontinuities in the composition surface of a zoned pluton, Criffel, Scotland. Geological Society of America Bulletin, Part I, v. 91, pp. 165-170.

Sullivan, K.N.O., 1991, A map for all reasons: the role of image processing in mineral exploration. Minerals Industry International, Jan. 1991.

Sultan, M., Arvidson, R.E., Duncan, I.J., Stern, R.J. and Kaliouby, B.E., 1988, Extension of the Najd shear system from Saudi Arabia to the Central Eastern Desert of Egypt based on integrated field and Landsat observations. Tectonics, v. 7, n. 6, pp. 1291-1306.

Switzer, P., 1980, Extensions of linear discriminant analysis for statistical classification of remotely sensed satellite imagery. Mathematical Geology, v. 12, n. 4, pp. 367-376.

Tapponier, R., Lacassin, R., Leloup, P.H., Scharer, U., Dalai, Z., Haiwei, W., Xiaohan, L., Shaocheng, J., Lianshang, Z and Jiayou, Z., 1990, The Ailao Shan/Red River metamorphic belt: Tertiary left-lateral shear between Indochina and South China. Nature, v. 343, pp. 431-437.

Telford, W.M., Geldart, L.P., Sheriff, R.E., 1990. Applied Geophysics, 2nd edition, Cambridge University Press, 770 pp.

Theriault, R.J., 1992, Nd isotopic evolution of the Taltson magmatic zone, Northwest Territories, Canada: Insights into Early Proterozoic accretion along the western margin of the Rae Province. Journal of Geology, v. 100, pp. 465-475.

References

Tou, J.T. and Gonzales, R.C., 1974, Pattern Recognition Principles; Addison-Wesley Publishing Co., Inc. London, 78 pp.

Twiss, R.J., and Moores, E.M., 1992, Structural Geology, W.H. Freeman and Co, New York, 532 pp.

Vrabel, J., 1996, Multispectral imagery band sharpening study. Photogrammetric Engineering & Remote Sensing, v. 62, n. 9, pp. 1075-1083.

Watanabe, R.Y., 1965, Petrology of cataclastic rocks of northeastern Alberta, Ph.D.-Thesis. University of Alberta, 219 pp.

Watkins, N.D., 1961, The relative contributions of remanent and induced magnetization in northeastern Alberta. Geophysical Prospecting, v. 9, pp. 421-426.

Welman, P., 1998, Mapping of a granite batholith using geological and remotely sensed data: the Mount Edgar Batholith, Pilbara Craton. Exploration Geophysics, v. 29, pp. 643-648.

White, S.H., Bretan, P.G. and Rutter, E.H., 1986, Fault zone reactivation: kinematics and mechanisms, Philosoph. Trans. Royal Society of London. Series A, v. 317, pp. 81-97.

Wilford, J.R., Bierwith, P.N., Craig, M.A., 1997, Application of airborne gamma-ray spectrometry in soil/regolith mapping and applied geomorphology. AGSO Journal of Australian Geology & Geophysics, v. 17, n. 2, pp. 201-216.

Wyszecki, G. and Styles, W.S., 1982, Color Science: concepts and methods, quantitative Data and Formulae, 2nd. edition, New York, Wiley, 457 pp.

Yésou, H., Besnus, Y., Rolet., J., Pion, J.C., 1993, Merging Seasat and SPOT imagery for the study of geologic structures in a temperate agricultural region. Remote Sensing of Environment, v. 43, n. 3, pp. 265-280.

Yésou, H. and Rolet, J., 1990, Regional mapping of the South Amorican shear zone (Brittany, France) using remotely sensed SPOT imagery. ISPRS Journal of Photogrammetry and Remote Sensing, v. 45, pp. 419-427.

BIBLIOGRAPHY

Journal publications

Schetselaar, E.M., van Dijk, P.M. and Al Fasatwi, A., 1990, Digital image processing of geophysical data using a rater-based GIS., ITC Journal 1990-3, pp. 248-252.

Schetselaar, E.M., 1994, A comparative evaluation on the potential of C-band airborne SAR and Panchromatic SPOT images for geologic mapping in the Archean Hood River Belt, Bathurst Inlet, Northwest Territories, Canadian Journal of Remote Sensing, v. 20, n. 3, pp. 302-316.

Schetselaar, E.M., 1995, Computerized field-data capture and GIS analysis for the generation of cross-sections in 3-D perspective views, Computer and Geosciences, v. 21, n. 5, pp. 687-701.

Schetselaar, E.M. and McDonough, M.R.M., 1996, Shear zone mapping using ERS-1 SAR images of the Paleoproterozoic Taltson magmatic zone, Canadian Shield, northeastern Alberta, ITC Journal 1996-2, pp. 166-175.

Schetselaar, E.M and Rencz, A.N., 1997, Reducing the effects of vegetation cover on radiometric data using Landsat TM data, International Journal of Remote Sensing, v. 18, n. 7, pp. 1503-1515.

Schetselaar, E.M., 1998, Fusion by the IHS transform: should we use cylindrical or spherical coordinates? International Journal of Remote Sensing, v.19, n. 4, pp. 759-765.

Schetselaar, E.M., Chung, C.F, and Kim, K.E., 2000, Integration of Landsat TM, gamma-ray, magnetic, and field data to discriminate lithological units in vegetated granite-gneiss terrain, Remote Sensing of the Environment, v. 71, pp. 89-105.

Schetselaar, E.M., 2000, On preserving spectral balance in image fusion. And its advantages for geological image interpretation. Photogrammetric Engineering and Remote Sensing (submitted).

Schetselaar, E.M., 2000, Mapping the compositional and structural patterns of a granite batholith by integrating gamma-ray spectrometry, Landsat TM and geological data, The Arch Lake granite (1.94 Ga.). International Journal of Remote Sensing (submitted).

McDonough, M.R.M., McNicoll, V.J., and Schetselaar, E.M., 2000, Geochronological and kinematic constraints on crustal shortening and escape in a two-sided oblique-slip colisional and magmatic orogen, Paleoproterozoic Taltson magmatic zone, northeastern Alberta, Canadian Journal of Earth Sciences, special issue LITHOPROBE Alberta Basement Transect (*in press*).

Conference proceedings and reports

Schetselaar, E.M. and Fabbri, A.G., 1994, Data integration and GIS modelling in the Northwest Territories of Canada, in Spatial data integration for mineral exploration, resource assessment and environmental studies, International Atomic Energy Agency, IAEA-TECDOC-782, pp. 136-150.

Schetselaar, E.M., 1995, Computerized field data capture for geological data integration, proceedings Joint European Conference and Exhibition on Geographical Information Systems, The Hague, pp. 436-441.

Schetselaar, E.M. and McDonough, M.R.M., 1995, Integration of ERS-1 SAR and total field aeromagnetic images for the spatial and kinematic characterization of the Charles Lake shear zone, Canadian Shield, northeastern Alberta: a mathematical morphologic approach in Proceedings Geomatics Conference, Ottawa, June 25-27, 1995 Canadian Geomatics CD-ROM.

Schetselaar, E.M., Gardini, C. and Costa, C.H., 1996, Reactivation tectonics in the Sierras Pampeanas: a case study from the Sierra de el Gigante, San Luis, Argentina, 3rd. Dutch Earth Scientific Conference, Veldhoven 2-3, March 1996.

Schetselaar, E.M. and Rencz, A.N., 1997, Reducing the effects of vegetation cover on radiometric data using Landsat TM data *in* Proceedings on the 11th Thematic Conference on applied geologic remote sensing, 27-29 Febuary 1996, Las Vegas, Nevada, USA, v.1 pp. 217-226.

Schetselaar, E.M., and deKemp, E.A., 2000, Image classification from Landsat TM, airborne magnetics and DEM data for mapping Paleoproterozoic bedrock units, Baffin Island, Nunavut, Canada. ISPRSS Amsterdam, July 2000 (*in press*).

Published map (GSC open files)

McDonough, M.R., Grover, T.W., McNicoll, V.J., Cooley, M.A., Schetselaar, E.M. and Robinson, N.N., 1994a, Geology Cornwall Lake, Alberta (74M/10), Geological Survey of Canada, Calgary Open File 2896, scale 1: 50,000.

McDonough, M.R., Cooley, M.A., Schetselaar, E.M., 1994b, Geology Hay Camp, Alberta (74M/11), Geological Survey of Canada, Calgary Open File 2896, scale 1: 50,000.

McDonough, M.R., Grover, T.W., McNicoll, V.J., Cooley, M.A., Schetselaar, E.M., Robinson, N.N., Bednarski, J. 1995, Geology Colin Lake, Alberta-Saskatchewan (74M/9), Geological Survey of Canada, Calgary Open File 3047, scale 1: 50,000.

McDonough, M.R., Grover, T.W., McNicoll, V.J., Cooley, M.A., Schetselaar, E.M, Robinson, N.N., and Bednarski, J. 1996c. Geology, Wylie Lake, Alberta-Saskatchewan (74M/8), Geological Survey of Canada, Map 1951A, 1:50,000 scale.

McDonough, M.R., Grover, T.W., McNicoll, V.J., Cooley, M.A., Schetselaar, E.M., Robinson, N.N., and Bednarski, J. 1996d. Geology, Turtle Lake, Alberta (74M/7), Geological Survey of Canada, Map 1958A, 1:50,000 scale.

CURRICULUM VITAE

Ernst Martinus Schetselaar was born in Dordrecht on February 15, 1963. He completed secondary school (VWO) at the Erasmus College in Zoetermeer in 1982. He studied applied structural geology with sedimentology and exploration geophysics as subsidiary subjects at the faculty of earth sciences of Utrecht University where he received a B.Sc degree in 1985. He did his M.Sc research on the structural geology of the Terena synform, Ossa-Morena zone, Portugal, which leaded to his degree in 1988. In 1990 he started to work at the Institute for Aerospace Survey and Earth Sciences (ITC) in Enschede as technical support officer for the Integrated Land and Water Information System (ILWIS). He joined the Geological Survey Division of ITC as a lecturer in 1992. In 1994 he went for one year to Ottawa, Canada where, in collaboration with the Geological Survey of Canada, the research presented in this thesis was initiated. He became an assistant professor at ITC in 1999.

PLATES

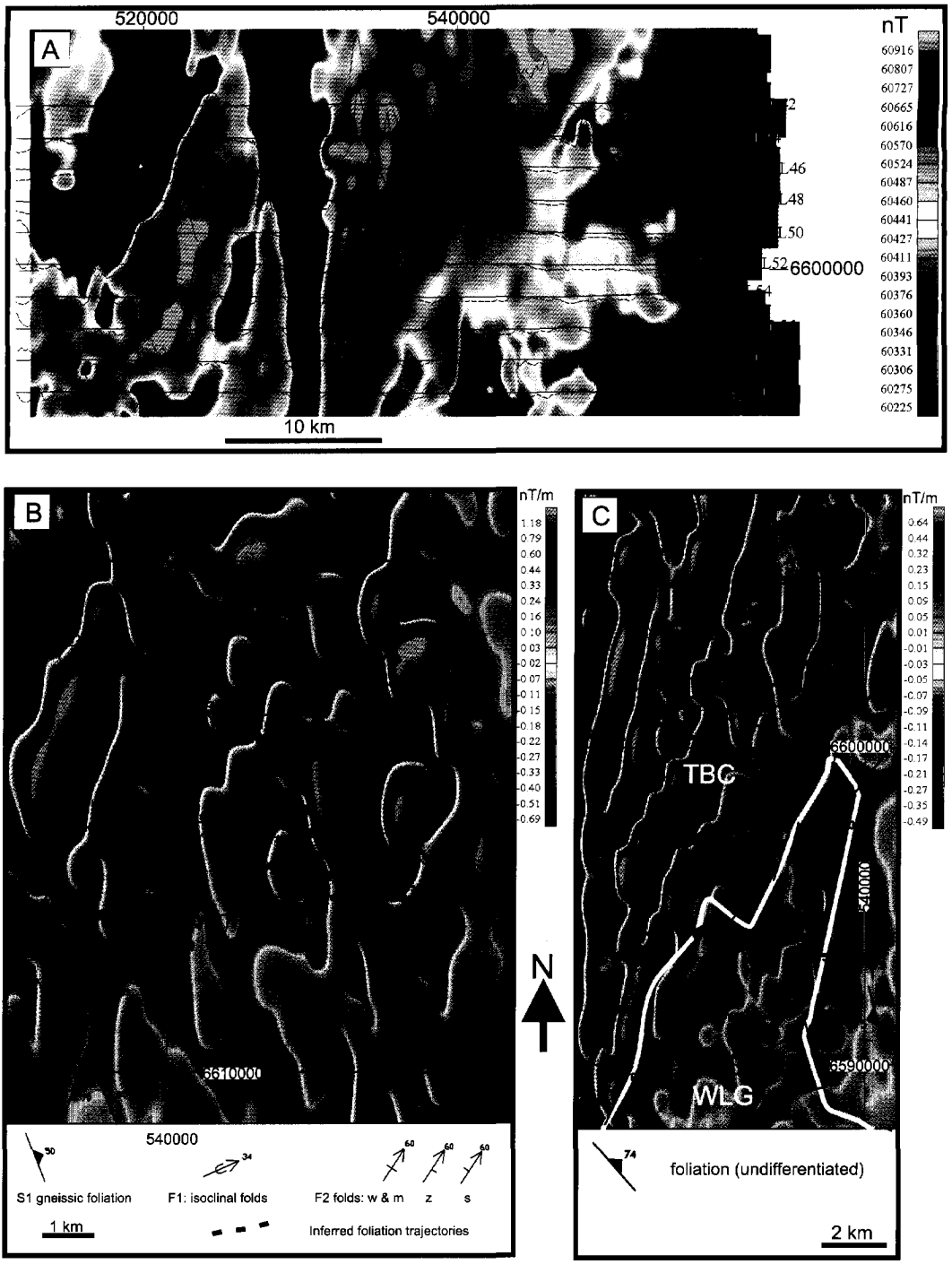

Plate 3.1 Detailed image representations of aeromagnetic data. (A) Total field magnetic data and flight line profiles (base level of profiles = 60500 nT, 1 mm = ca. 75 nT); (B) First vertical derivative magnetic data with overlay of structural elements displaying fold interference patterns (illumination inclination 45°, declination 320°); (C) First vertical derivative magnetic data and foliation data to show the nature of the contact between the Taltson Basement Complex (TBC) and Wylie Lake granitoids (WLG) (illumination inclination 30°, declination 290°).

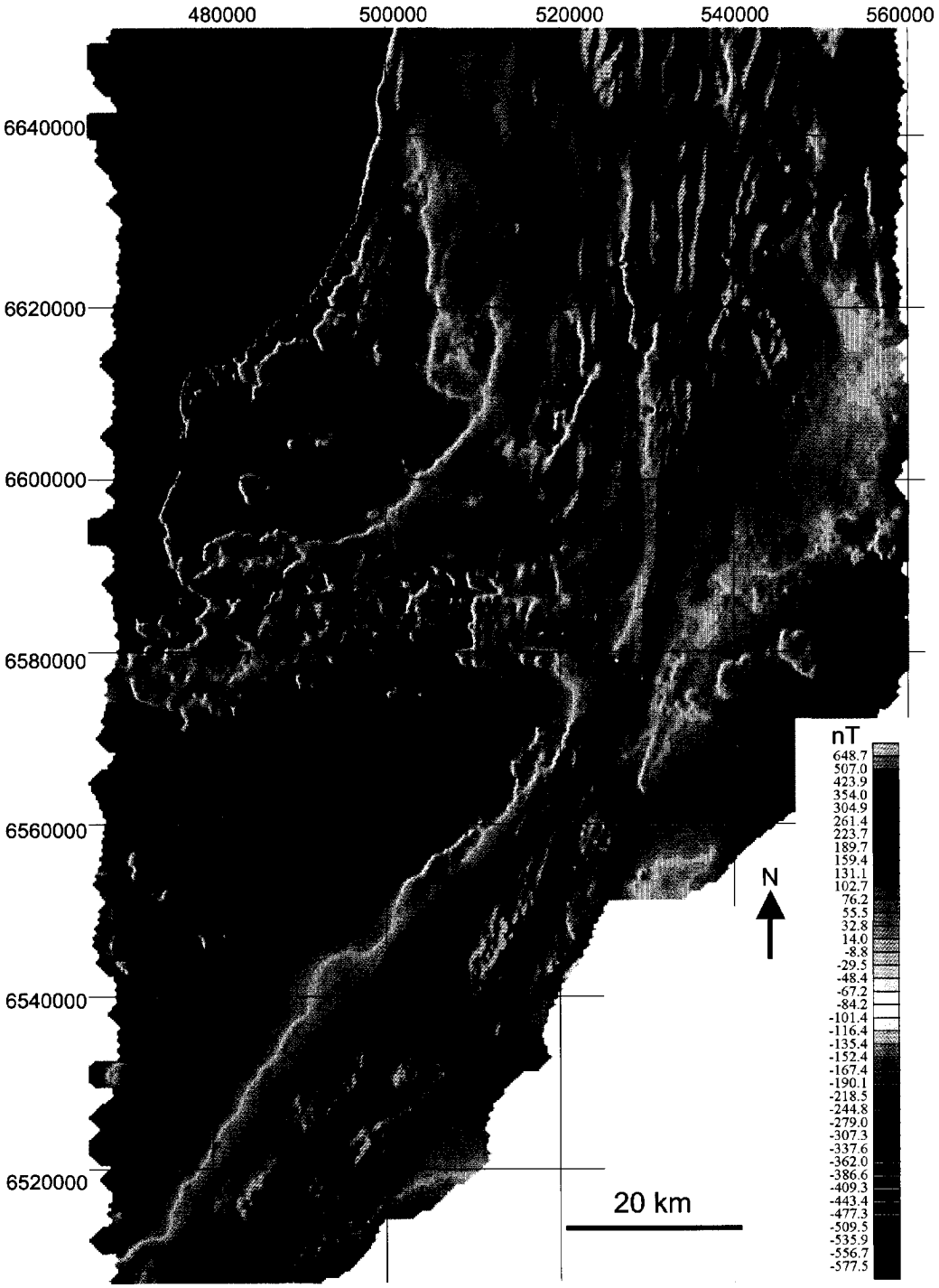

Plate 3.2 Colour-shaded relief representation of total field magnetic data. Hue = histogram quantization of IRGF (datum 1990) subtracted total field magnetic data. Relief shading with illumination azimuth 290° and 30° inclination.

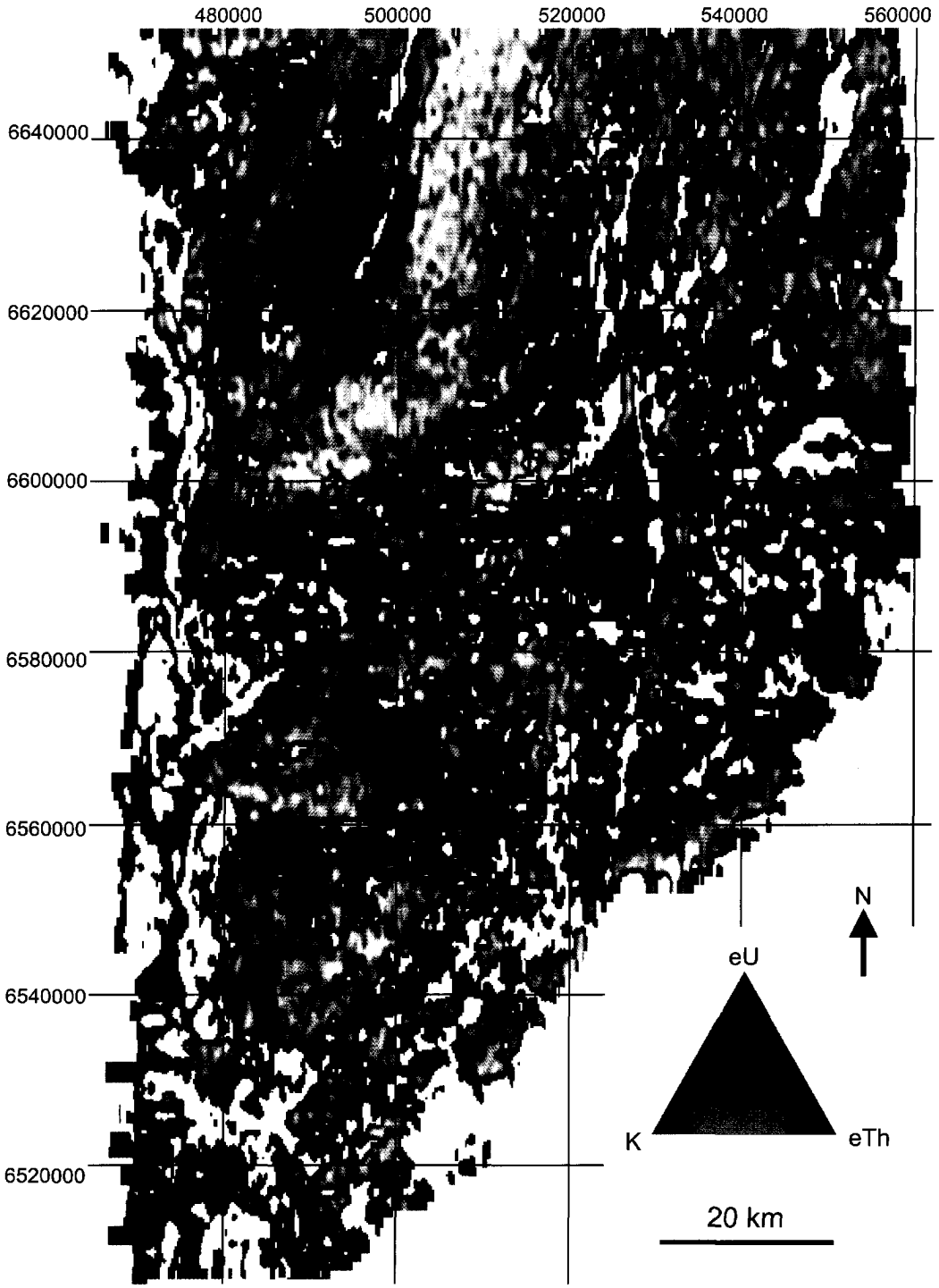

Plate 3.3 Ternary radioelement map of airborne potassium (K), equivalent Thorium (eTh) and equivalent uranium (eU) gamma-ray spectrometry channels. Total count levels below 3 μR/h over lakes and swamps were masked.

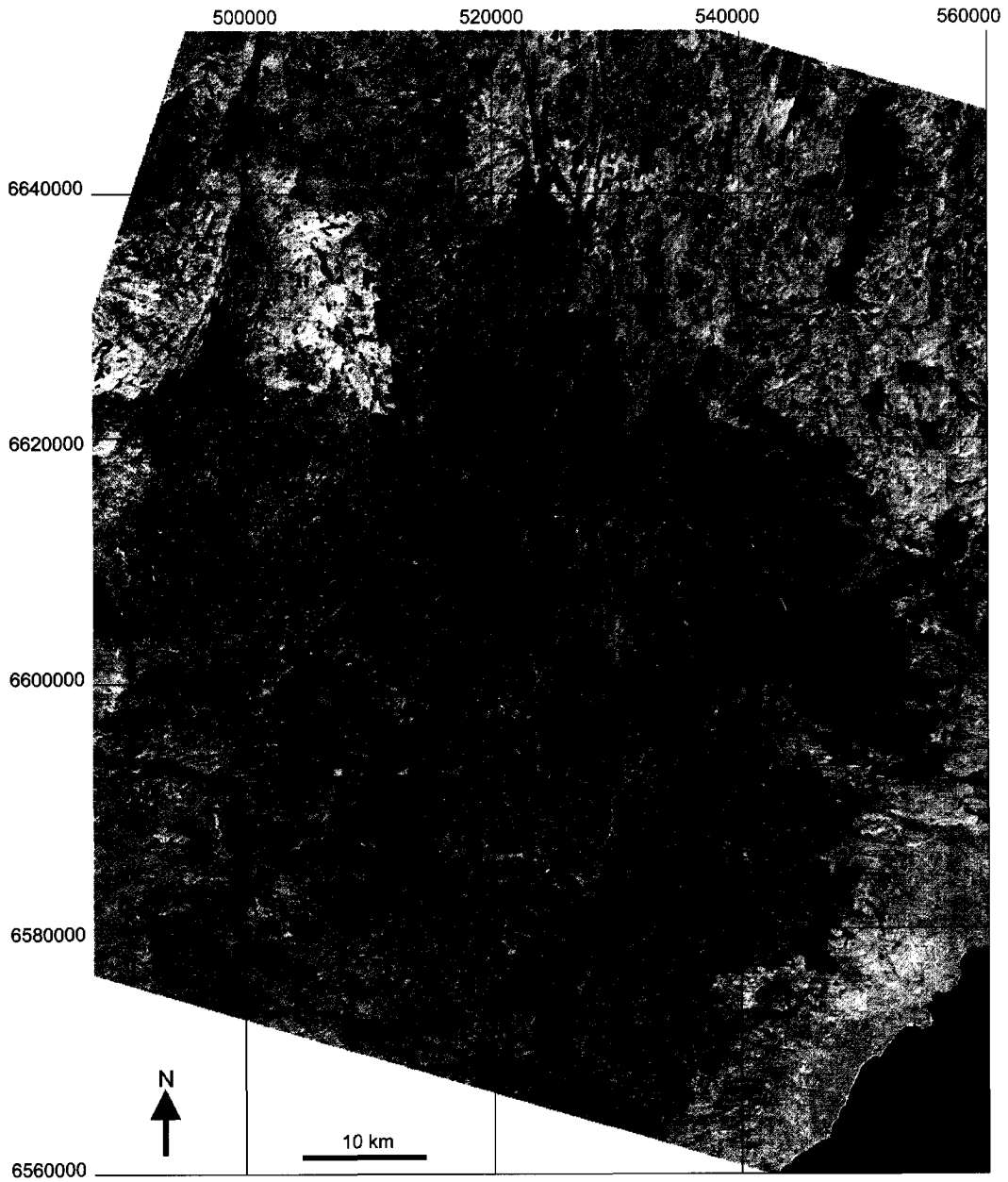

Plate 3.4 Landsat Thematic Mapper colour composite image; TM5 = red, TM4 = green, TM3 = blue.

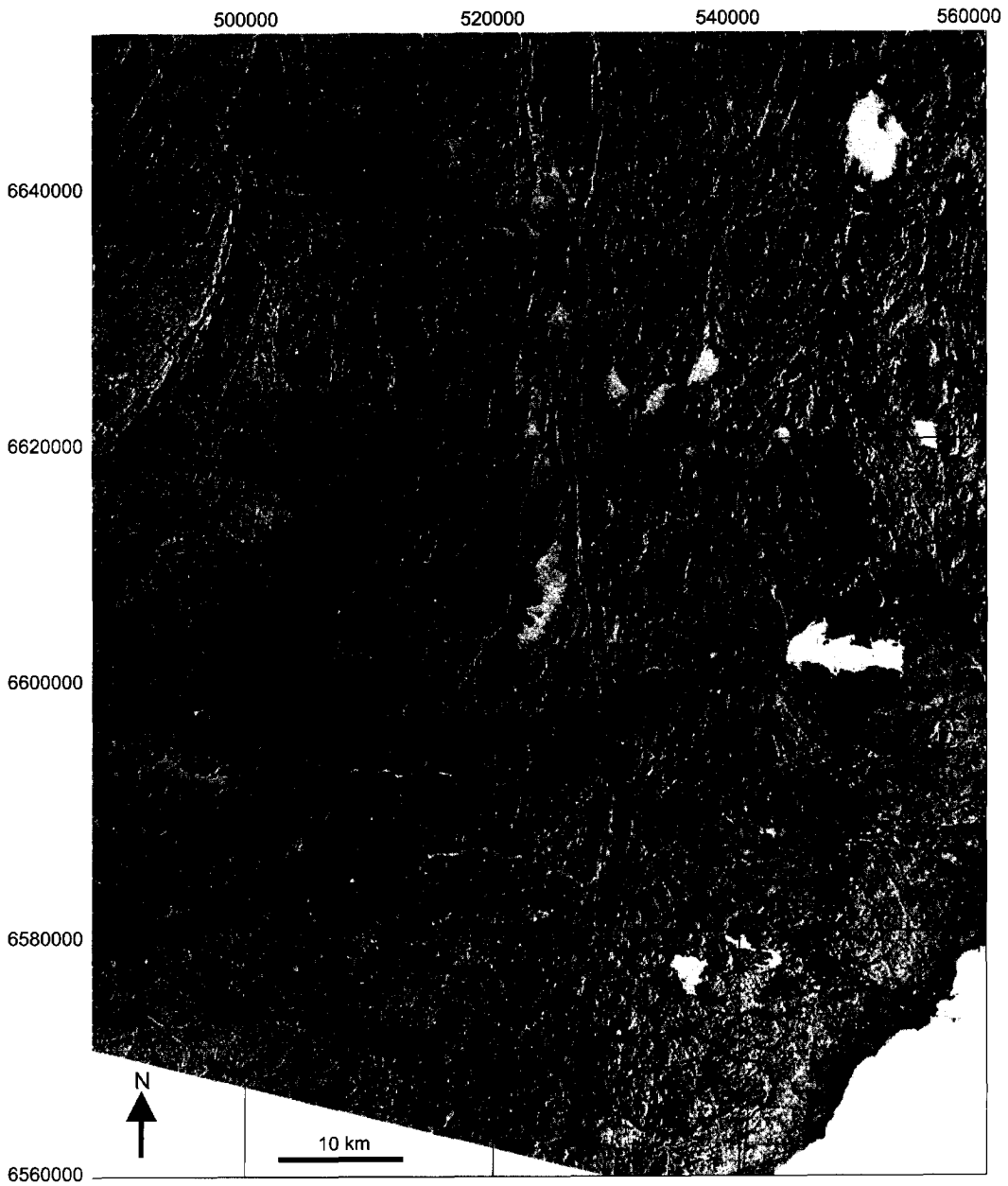

Plate 3.5 ERS-1 scene (east-looking).

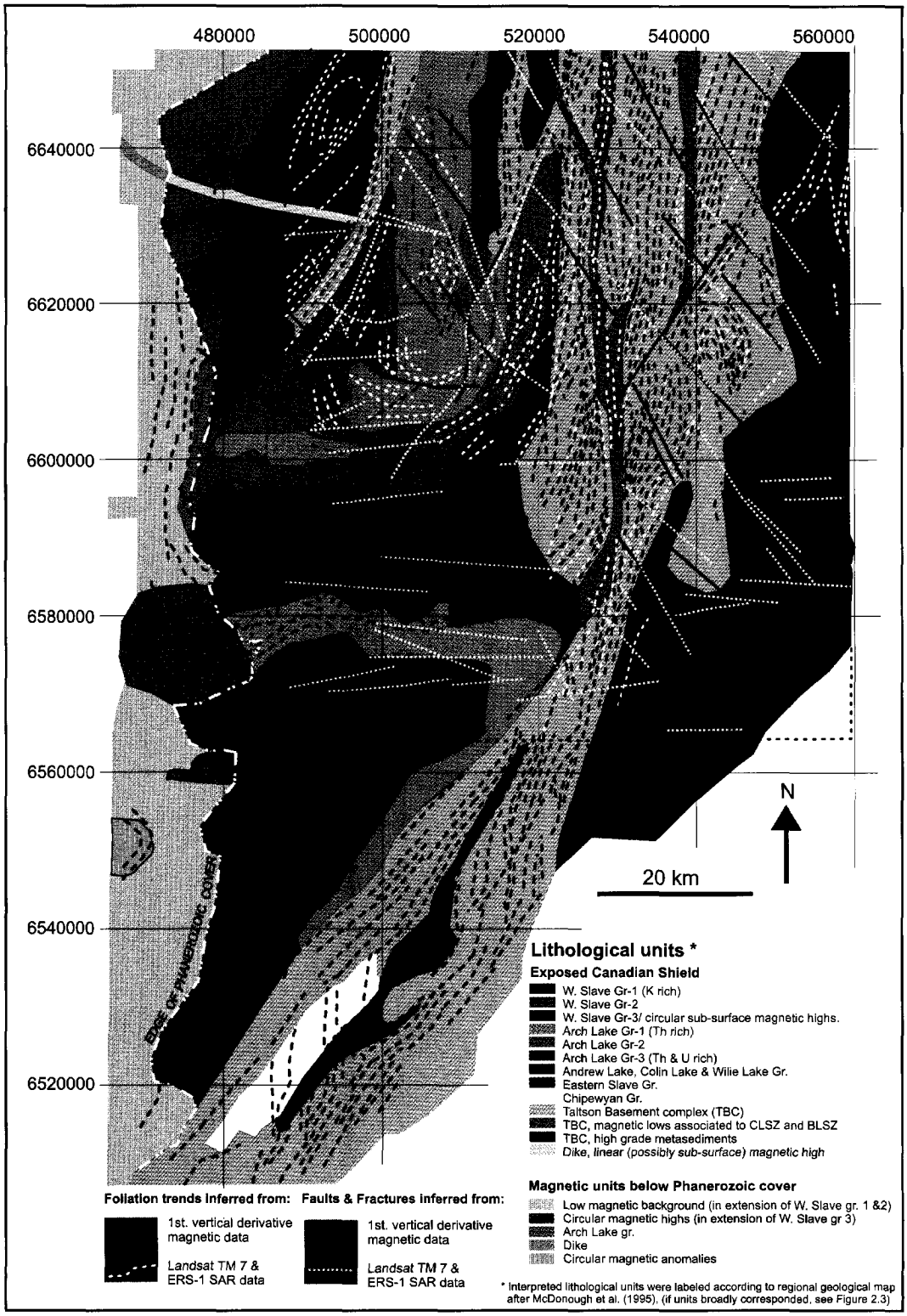

Plate 3. 6 Integrated lithostructural interpretation of gamma-ray spectrometry, Landsat TM, ERS-1, total field and 1st vertical derivative magnetic data.

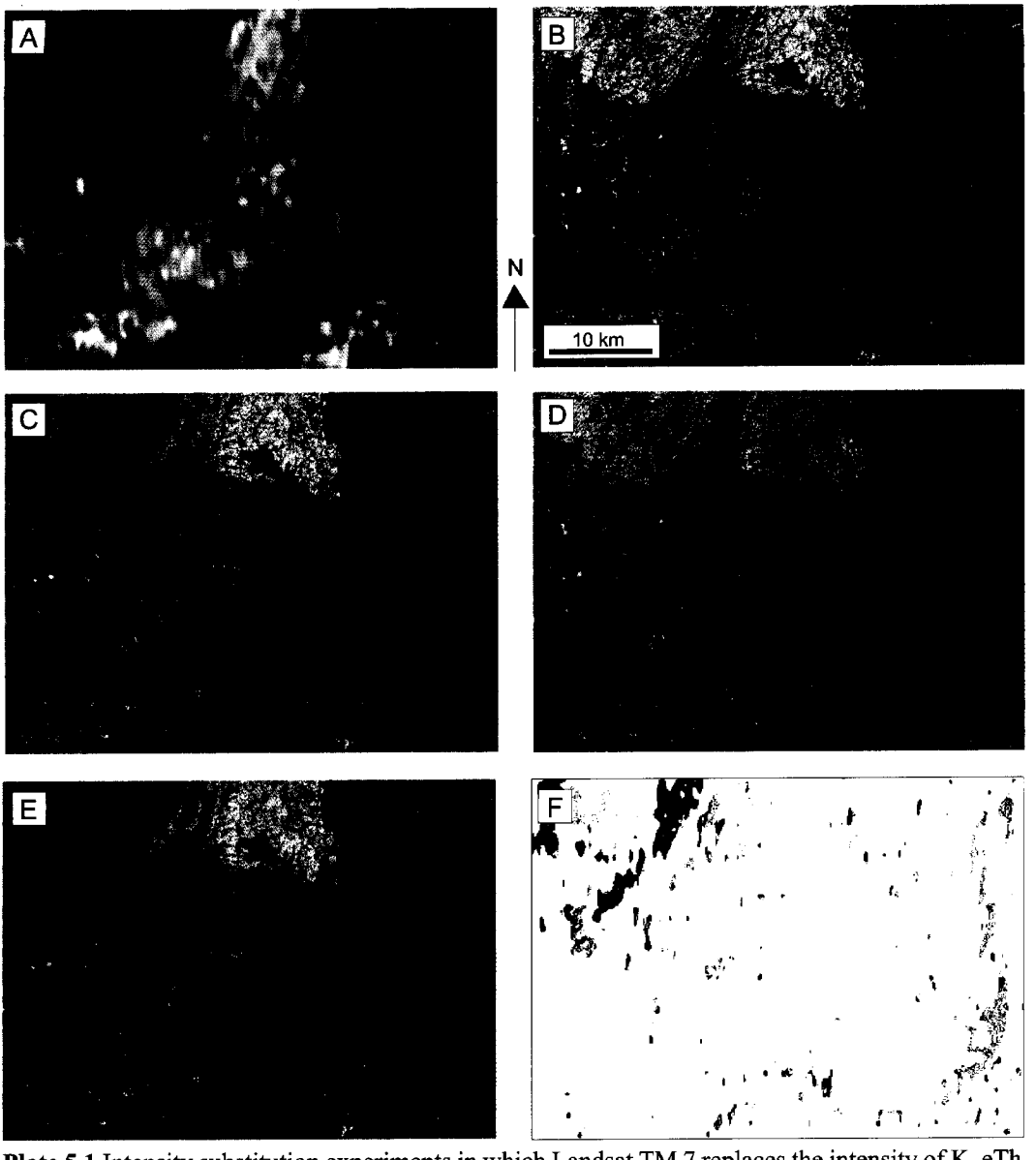

Plate 5.1 Intensity substitution experiments in which Landsat TM 7 replaces the intensity of K, eTh and eU airborne gamma-ray spectrometry grids; (A) colour composite of K (red), eTh (green) and eU (blue); (B) Landsat TM7 ; (C) IHS composite image obtained by hue and saturation invariant intensity substitution; (D) IHS composite image obtained by conventional intensity substitution method. Note hue shift towards green and magenta; (E) as (C) but with saturation enhancement factor of 1.5; (F) over-saturated pixels (5%) obtained from intensity substitution shown in (E).

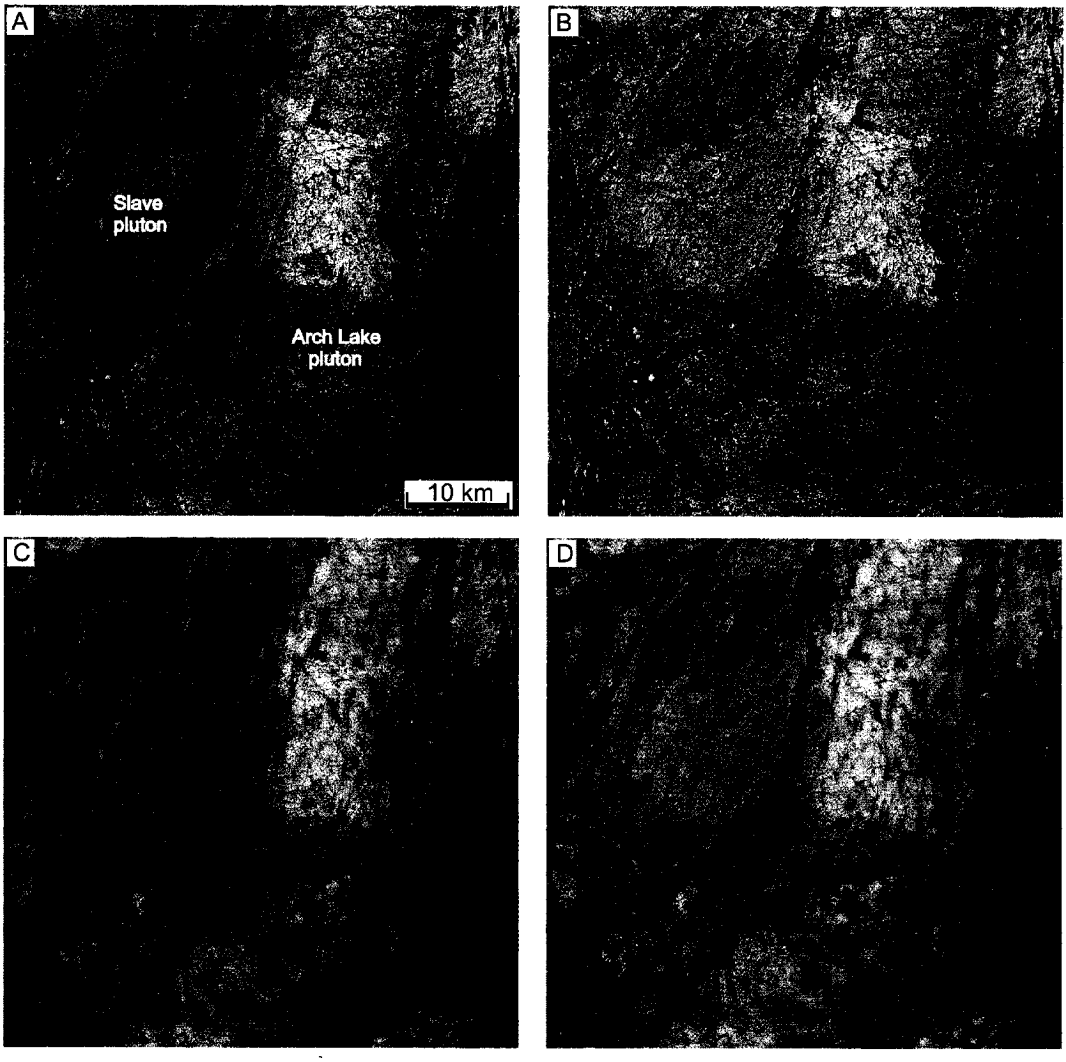

Plate 5.2 Results of intensity substitution experiments to compare spherical and cylindrical IHS transforms; (A) Intensity substitution in which TM7 replaces the intensity of K, eTh and eU airborne gamma-ray spectrometry grids using spherical transform; (B) as (A) using cylindrical transform; (C) as (A) using 50 percent of the original intensity; (D) as (C) using cylindrical transform.

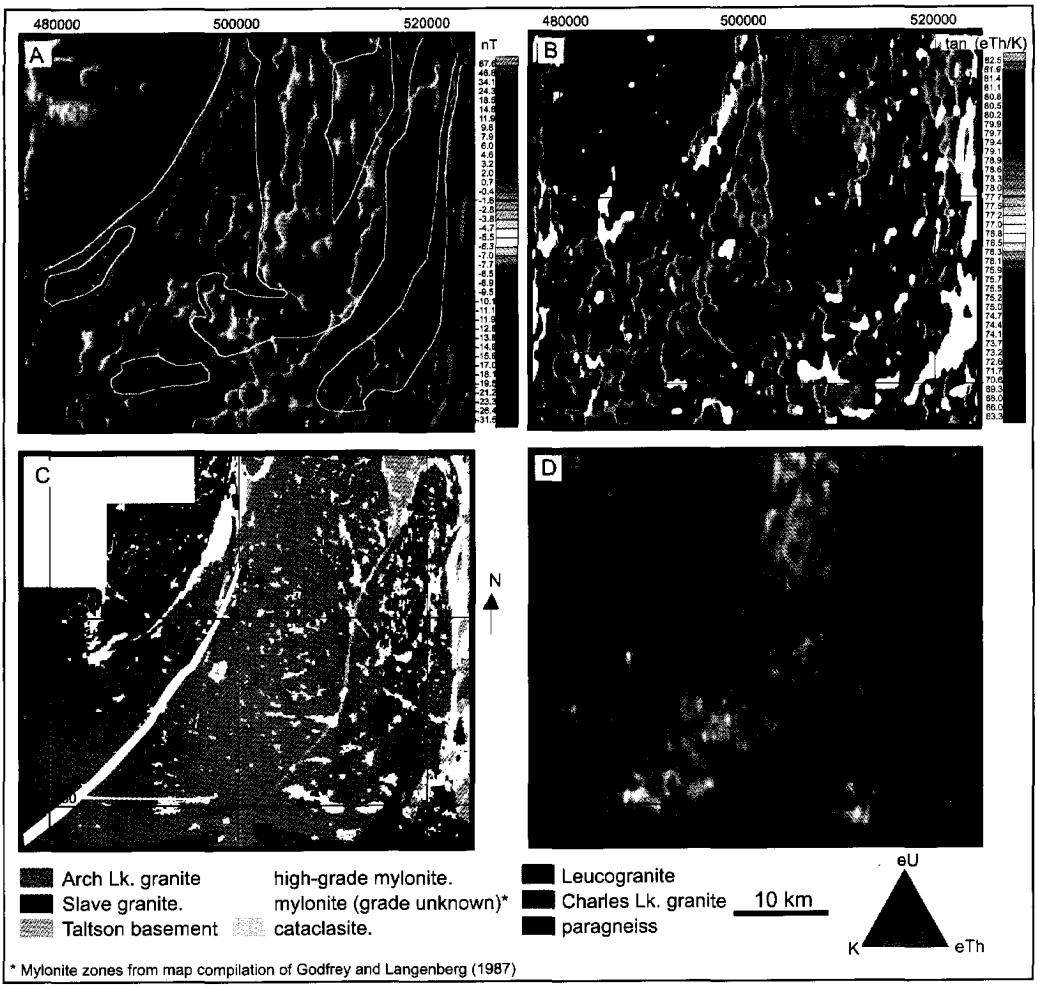

Plate 6.1 Geophysical and geological map compilations of the Arch Lake pluton. (A) relief shaded residual magnetic field. Polygons outlined in white show Th-rich zones inferred from Plate 10 (D); (B) relief shaded representation of eTh/K ratio grid (illumination: azimuth: 290°, inclination, 30°); (C) generalized geological map (after Godfrey and Langenberg (1987) and McDonough *et al.* (1994b); (D) ternary radioelement map. A comparative geological interpretation of the maps is presented in chapter 6.

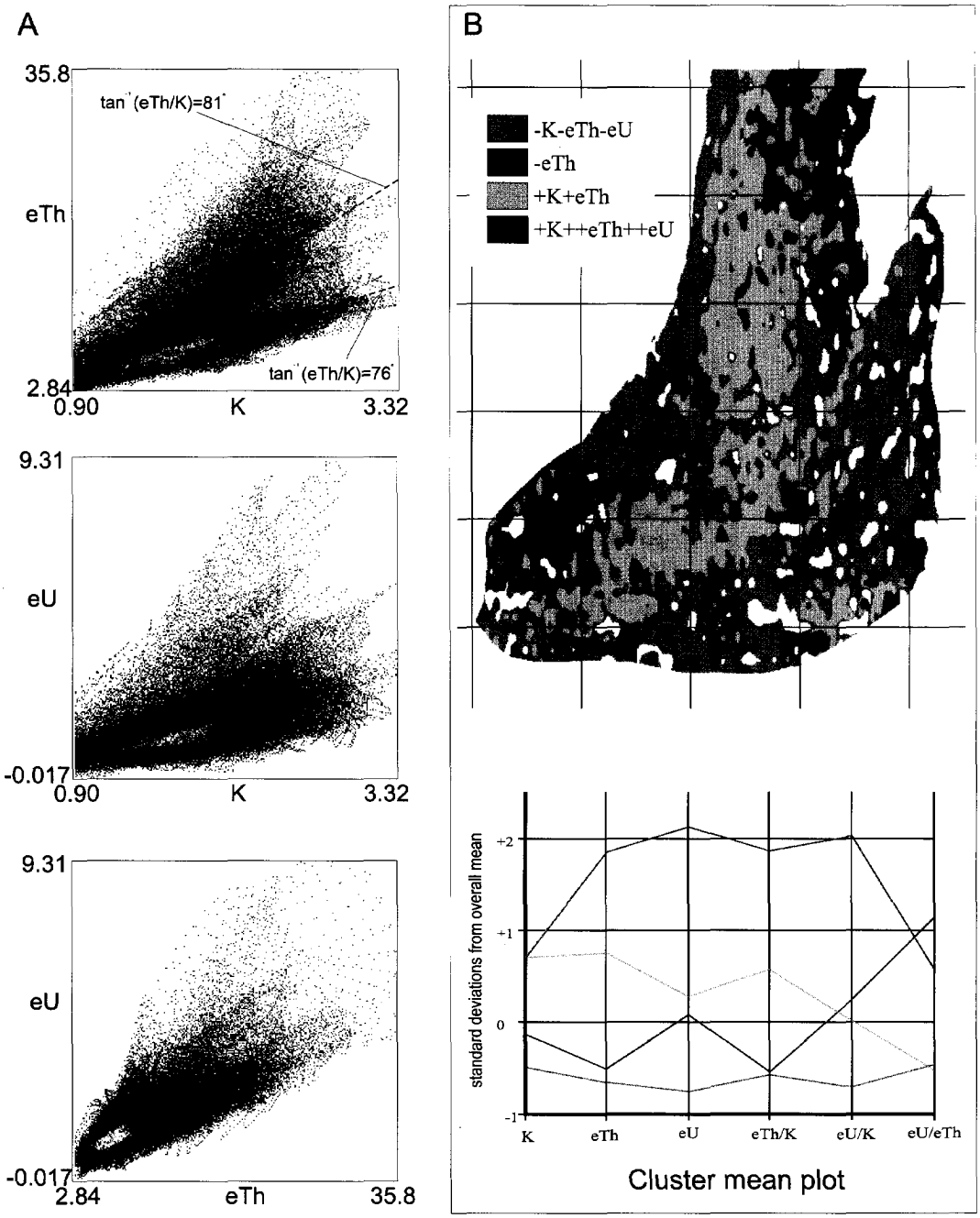

Plate 6.2 (A) Scatter plots of K, eTh, eU image grids over Arch Lake granites; (B) Results of cluster analysis.

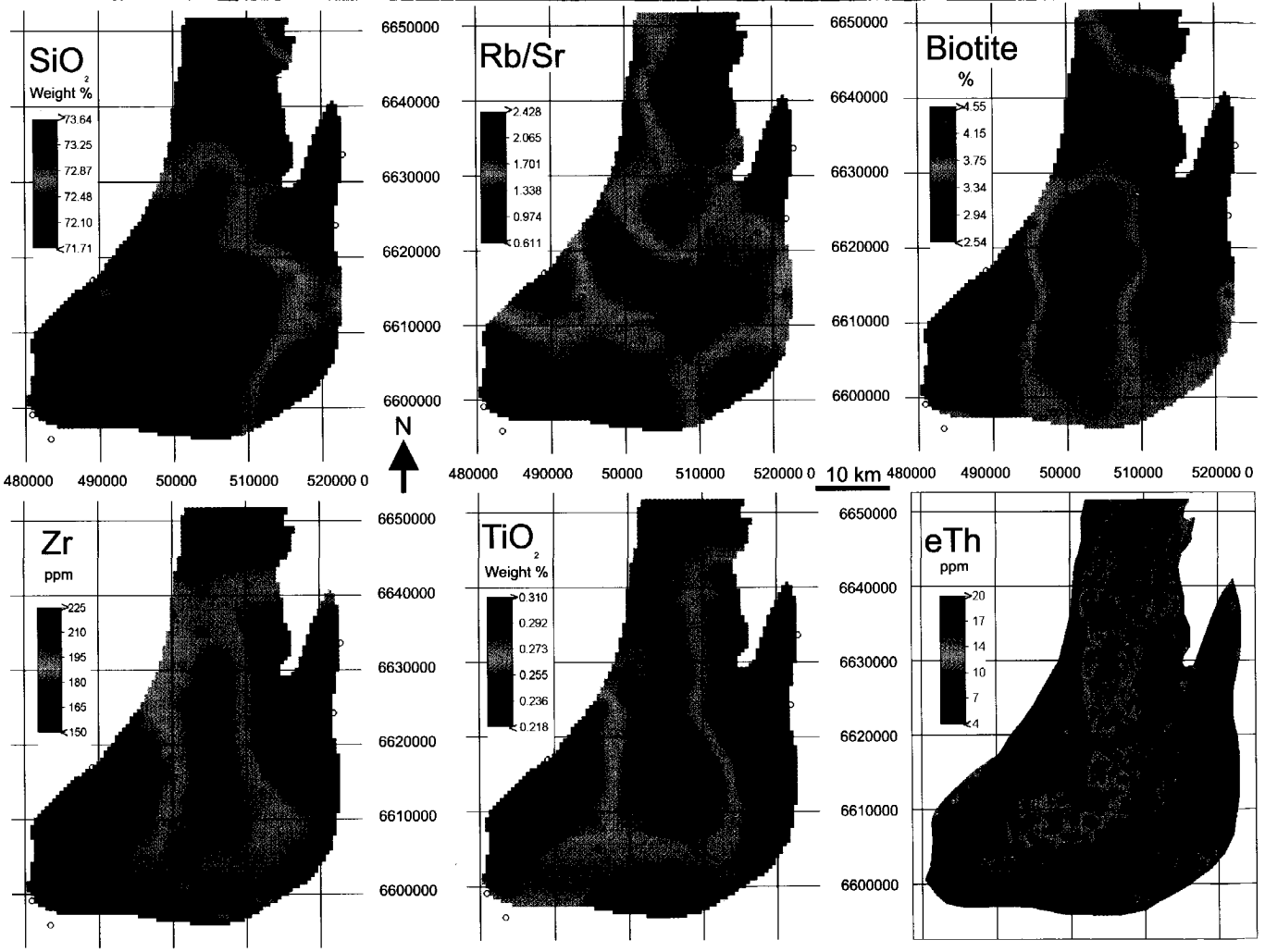

Plate 6.3 Moving average interpolation patterns of SiO_2, Rb/Sr, % biotite, Zr, TiO_2 and airborne eTh grid over Arch Lake granites. Circles indicate sample locations of lithogeochemical data of the Alberta Geological Survey (Goff et al., 1986).

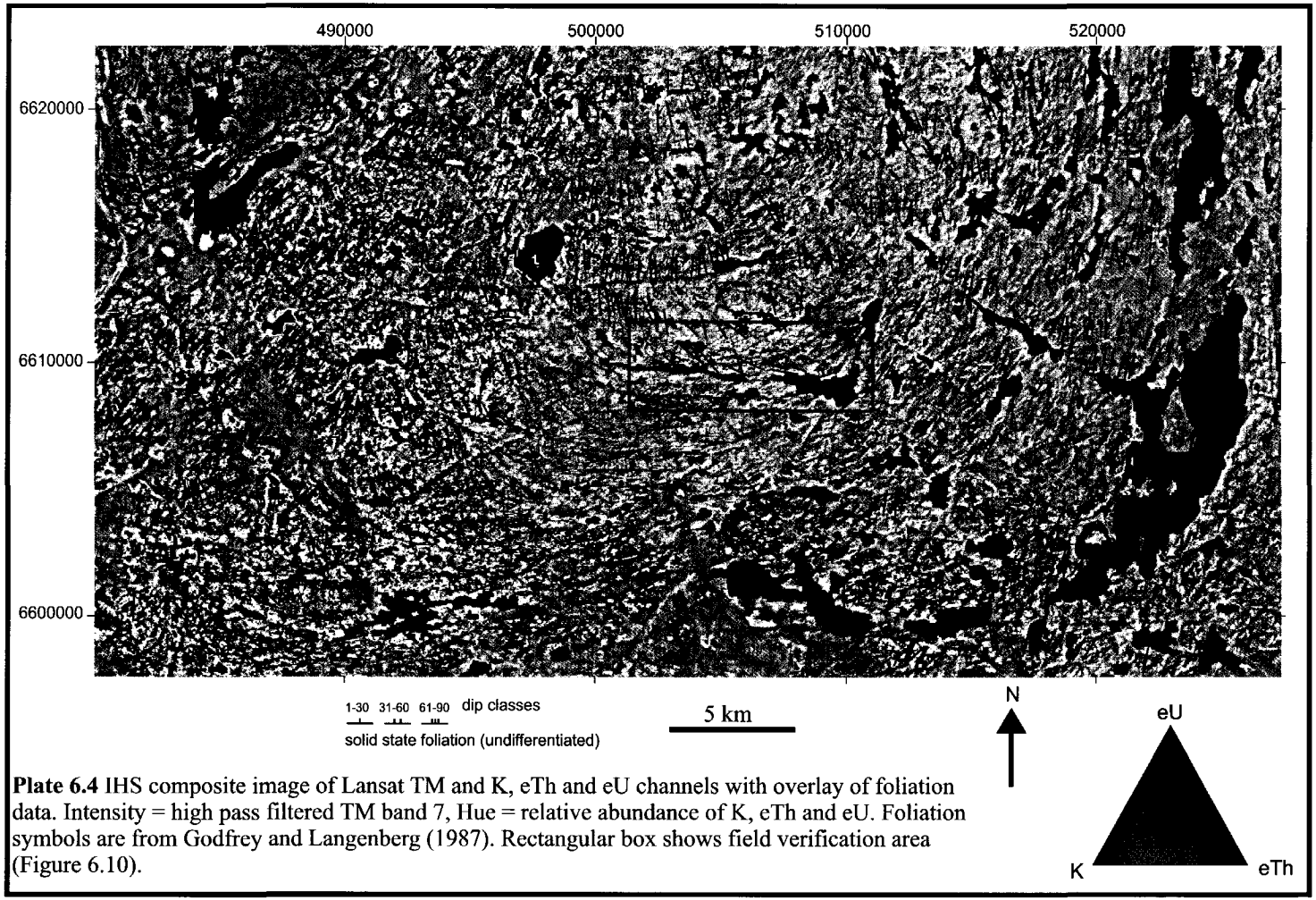

Plate 6.4 IHS composite image of Lansat TM and K, eTh and eU channels with overlay of foliation data. Intensity = high pass filtered TM band 7, Hue = relative abundance of K, eTh and eU. Foliation symbols are from Godfrey and Langenberg (1987). Rectangular box shows field verification area (Figure 6.10).

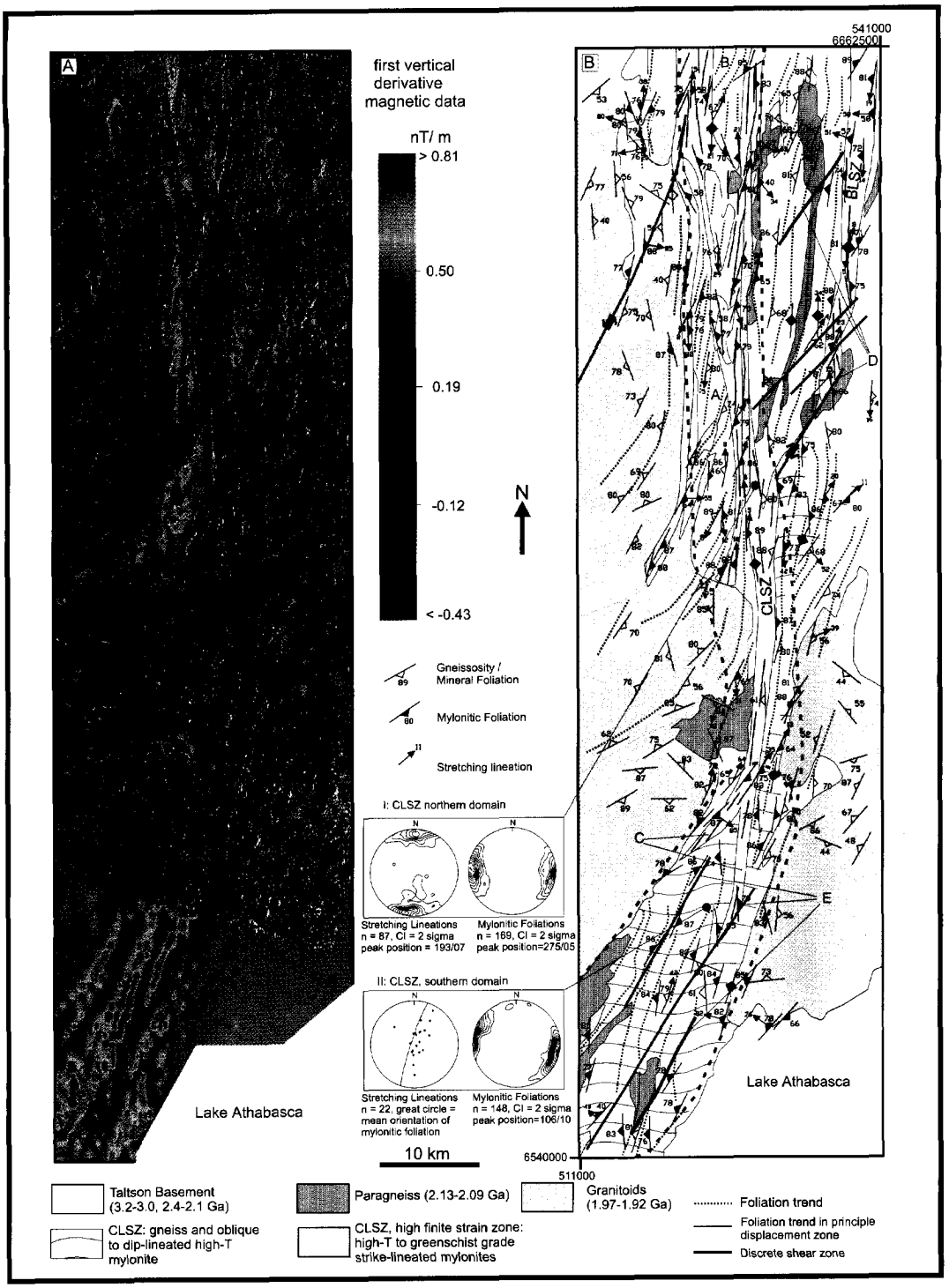

Plate 7.1. (A) IHS composite image of ERS-1 and 1st vertical derivative magnetic data, Intensity (I) = filtered ERS-1 data, hue (H) = 1st vertical derivative magnetic data, saturation (S) = 40% of S_{max}. (B) structural map compilation of Charles Lake shear zone (CLSZ). Structural data along CLSZ from (McDonough *et al.*, 1995); Foliation data in granitoids are mainly from Godfrey and Langenberg (1986(a), 1986(b) and Godfrey (1980a, 1980b, 1984b). Lithological units and geochronology after McDonough *et al.* (1995).

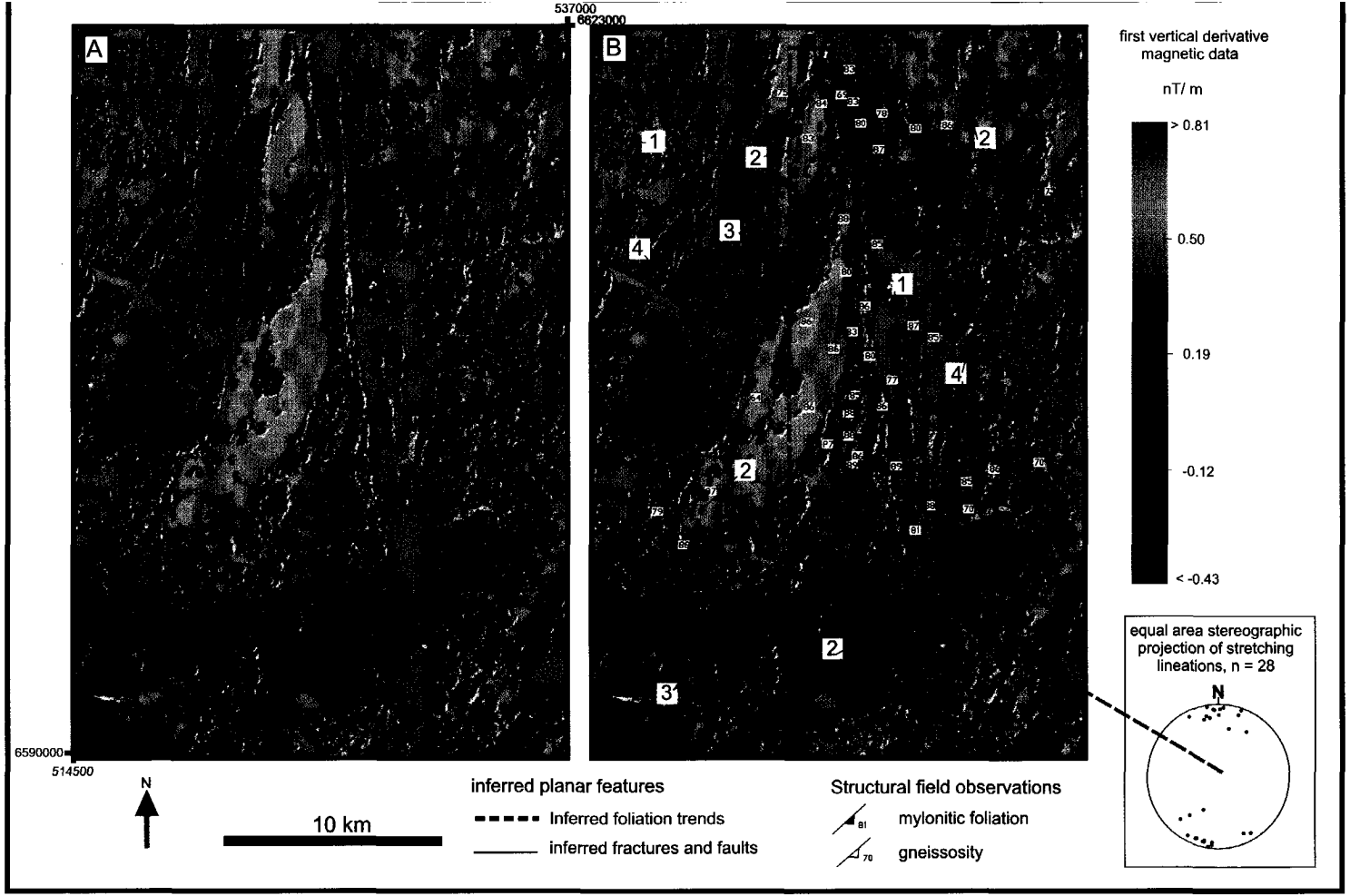

Plate 7.2 (A) IHS integrated image of enhanced ERS-1 and vertical derivative magnetic data. Intensity (I) = enhanced ERS-1 data, Hue (H) = vertical derivative magnetic data, Saturation (S) = 40 % S_{max}. (B) As (A) with overlay of structural field observations and inferred structural features discussed in the text. Inset shows equal area stereographic projection of stretching lineations in central segment of Charles Lake shear zone.

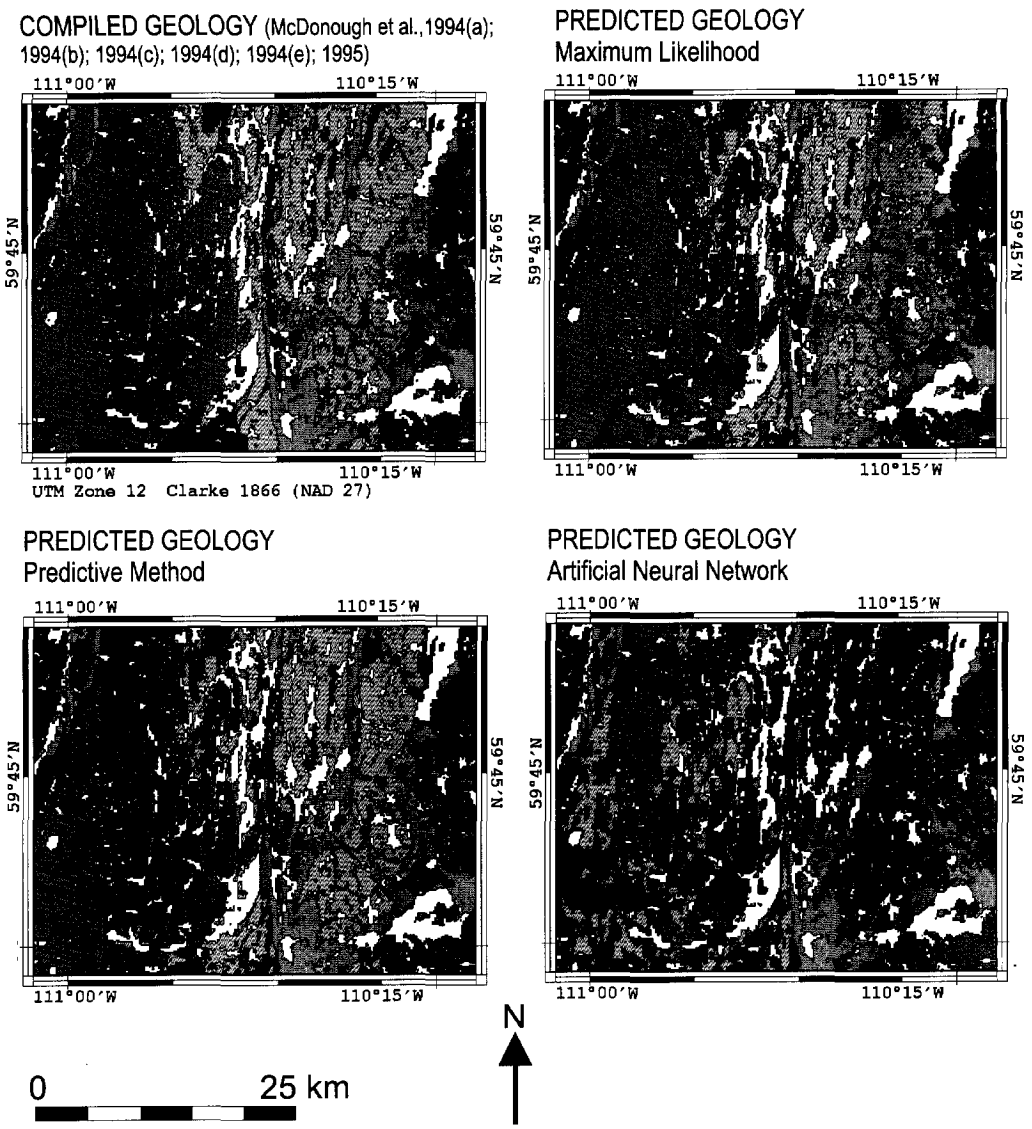

Plate 8.1 Classification results of the training area.

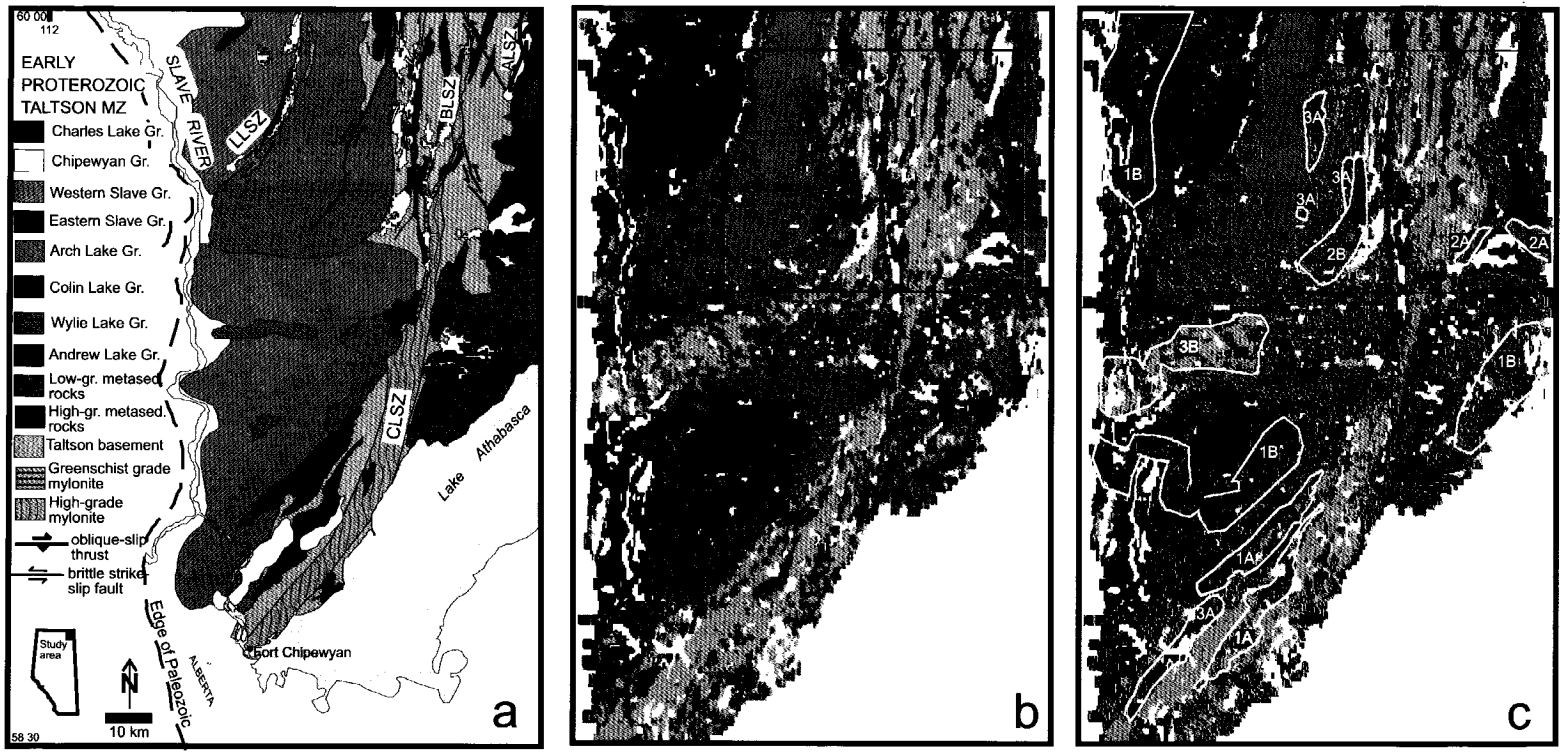

Plate 8.2 General geological map and classification results of the exposed northeastern Alberta Shield. (A) general geological map after McDonough et al (1995); (B) classification obtained with maximum likelihood method; (C) classification obtained with predictive method. Polygons with yellow outline are discrepancies between the geological map (A) and classification patterns discussed in the text. Rectangle shows outline of the training area (plate 8.1).

Author	Year	ITC dissertation no.	ISBN	(Short) Dissertation title
Mr. Akinyede (Nigeria)	1990	1	n.a.	Highway cost modelling and route selection using a geotechnical information system
Mr. Pan He Ping (China)	1990	2	90-9003757-8	Spatial structure theory in machine vision and applications to structural and textural analysis of remotely sensed images.
Mr. G. Bocco Verdinelli (Mexico)	1990	3	n.a.	Gully erosion analysis using remote sensing and geographic information systems: a case study in Central Mexico
Mr. M. Sharif (ITC staff)	1991	4	n.a.	Composite sampling optimization for DTM in the context of GIS
Ms. J. Drummond (ITC staff)	1991	5	n.a.	Determining and processing quality parameters in geographic information systems
Ms. S. Groten (ITC staff)	1991	6	n.a.	Satellite monitoring of agro-ecosystems in the Sahel.
Mr. A. Sharifi (ITC staff)	1991	7	90-6164-074-1	Development of an appropriate resource information system to support agricultural management at farm enterprise level
Mr. D. van der Zee (ITC staff)	1991	8	90-6164-075-X	Recreation studied from above: Air photo interpretation as input into land evaluation for recreation
Mr. C. Mannaerts (ITC staff)	1991	9	90-6164-085-7	Assessment of the transferability of laboratory rainfall-runoff and rainfall - soil loss relationships to field and catchment scales: a study in the Cape Verde Islands
Mr. Ze Shen Wang (China)	1991	10	90-393-0333-9	An expert system for cartographic symbol design
Mr. Zhou Yunxian (China)	1991	11	90-6164-081-4	Application of Radon transforms to the processing of airborne geophysical data.
Mr. M. de Zuviria (Argentina)	1992	12	90-6164-077-6	Mapping agro-topoclimates by integrating topographic, meteorological and land ecological data in a geographic information system: a case study of the Lom Sak area, North Central Thailand
Mr. C. van Westen (ITC staff)	1993	13	90-6164-078-4	Application of Geographic Information Systems to landslide hazard zonation
Mr. Shi Wenzhong (China)	1994	14	90-6164-099-7	Modelling positional and thematic uncertainties in integration of remote sensing and geographic information systems
Mr. R. Javelosa (Philippines)	1994	15	90-6164-086-5	Active Quaternary environments in the Philippine mobile belt.
Mr. Lo King-Chang (China)	1994	16	90-9006526-1	High Quality Automatic DEM, Digital Elevation Model Generation from Multiple Imagery
Mr. S. Wokabi (Kenya)	1994	17	90-6164-102-0	Quantified land evaluation for maize yield gap analysis at three sites on the eastern slope of Mt. Kenya.
Mr. O. Rodriguez (Venezuela)	1995	18	n.a.	Land Use conflicts and planning strategies in urban fringes: a case study of Western Caracas, Venezuela
Mr. F. van der Meer (ITC staff)	1995	19	90-5485-385-9	Imaging spectrometry & the Ronda peridotites

Author	Year	ITC dissertation no.	ISBN	(Short) Dissertation title
Mr. O. Kufoniyi (Nigeria)	1995	20	90-6164-105-5	Spatial coincidence: automated database updating and data consistency in vector GIS
Mr. P. Zambezi (Zambia)	1995	21	n.a.	Geochemistry of the Nkombwa Hill carbonatite complex of Isoka District, north-east Zambia, with special emphasis on economic minerals
Mr. T. Woldai (ITC staff)	1995	22	n.a.	The application of remote sensing to the study of the geology and structure of the Carboniferous in the Calañas area, pyrite belt, SW Spain
Ms. P. Verweij (ITC staff)	1995	23	90-6164-109-8	Spatial and temporal modelling of vegetation patterns: burning and grazing in the Paramo of Los Nevados National Park, Colombia
Ms. C. Pohl (Germany)	1996	24	90-6164-121-7	Geometric Aspects of Multisensor Image Fusion for Topographic Map Updating in the Humid Tropics
Mr. Jiang Bin (China)	1996	25	90-6266-128-9	Fuzzy overlay analysis and visualization in GIS
Ms. G. Metternicht (Argentina)	1996	26	90-6164-118-7	Detecting and monitoring land degradation features and processes in the Cochabamba Valleys, Bolivia. A synergistic approach.
Mr. Hoanh Chu Thai (Vietnam)	1996	27	90-6164-120-9	Development of a Computerized Aid to Integrated Land Use Planning (CAILUP) at regional level in irrigated areas: a case study for the Quan Lo Phung Hiep region in the Mekong Delta, Vietnam
Mr. A. Roshannejad (Iran)	1996	28	90-9009284-6	The management of spatio-temporal data in a national geographic information system
Mr. M. Terlien (AiO)	1996	29	90-6164-115-2	Modelling Spatial and Temporal Variations in Rainfall-Triggered Landslides: the integration of hydrologic models, slope stability models and GIS for the hazard zonation of rainfall-triggered landslides with examples from Manizales, Colombia
Mr. J. Mahavir (India)	1996	30	90-6164-117-9	Modelling settlement patterns for metropolitan regions: inputs from remote sensing
Ms. S. Al-Amir (Syria)	1996	31	90-6164-116-0	Modern spatial planning practice as supported by the multi-applicable tools of remote sensing and GIS: the Syrian case
Mr. M. Pilouk (Thailand)	1996	32	90-6164-122-5	Integrated modelling for 3D GIS
Mr. Duan Zengshan (China)	1996	33	90-6164-123-3	Optimization modelling of a river-aquifer system with technical interventions: a case study for the Huangshui river and the coastal aquifer, Shandong, China
Mr. W.H. de Man (ITC staff)	1996	34	90-9009775-9	Surveys: informatie als norm: een verkenning van de institutionalisering van dorp - surveys in Thailand en op de Filippijnen
Mr. Z. Vekerdy *Hungary)	1996	35	90-6164-119-5	GIS-based hydrological modelling of alluvial regions: using the example of the Kisaföld, Hungary

Author	Year	ITC dissertation no.	ISBN	(Short) Dissertation title
Ms. Luisa Pereira (Portugal)	1996	36	90-407-1385-5	A Robust and Adaptive Matching Procedure for Automatic Modelling of Terrain Relief
Ms. M. Fandino Lozano (Colombia)	1996	37	90-6164-129-2	A Framework of Ecological Evaluation oriented at the Establishment and Management of Protected Areas: a case study of the Santuario de Iguaque, Colombia
Mr. B. Toxopeus (ITC staff)	1996	38	90-6164-126-8	ISM : an Interactive Spatial and temporal Modelling system as a tool in ecosystem management : with two case studies : Cibodas biosphere reserve, West Java Indonesia : Amboseli biosphere reserve, Kajiado district, Central Southern Kenya
Ms. Wang Yiman (China)	1997	39	90-6164-131-4	Satellite SAR imagery for topographic mapping of tidal flat areas in the Dutch Wadden Sea
Ms. Asun Saldana-Lopez (Spain)	1997	40	90-6164-133-0	Complexity of soils and Soilscape patterns on the southern slopes of the Ayllon Range, central Spain: a GIS assisted modelling approach
Mr. T. Ceccarelli (Italy)	1997	41	90-6164-135-7	Towards a planning support system for communal areas in the Zambezi valley, Zimbabwe; a multi-criteria evaluation linking farm household analysis, land evaluation and geographic information systems
Mr. Peng Wanning (China)	1997	42	90-6164-134-9	Automated generalization in GIS
Ms. C. Lawas (Philippines)	1997	43	90-6164-137-3	The Resource Users' Knowledge, the neglected input in Land resource management: the case of the Kankanaey farmers in Benguet, Philippines
Ms. W. Bijker (ITC staff)	1997	44	90-6164-139-X	Radar for rain forest: A monitoring system for land cover Change in the Colombian Amazon
Mr. A. Farshad (ITC staff)	1997	45	90-6164-142-X	Analysis of integrated land and water management practices within different agricultural systems under semi-arid conditions of Iran and evaluation of their sustainability
Mr. B. Orlic (Serbia)	1997	46	90-6164-140-3	Predicting subsurface conditions for geotechnical modelling
Mr. Y. Bishr (Egypt)	1997	47	90-6164-141-1	Semantic Aspects of Interoperable GIS
Mr. Zhang Xiangmin (China)	1998	48	90-6164-144-6	Coal fires in Northwest China: detection, monitoring and prediction using remote sensing data
Mr. R. Gens (Germany)	1998	49	90-6164-155-1	Quality assessment of SAR interferometric data
Mr. J. Turkstra (ITC staff)	1998	50	90-6164-147-0	Urban development and geographical information: spatial and temporal patterns of urban development and land values using integrated geo-data, Villaviciencia, Colombia
Mr. C. Cassells (UK)	1998	51	n.a.	Thermal modelling of underground coal fires in northern China

Author	Year	ITC dissertation no.	ISBN	(Short) Dissertation title
Mr. M. Naseri (Iran)	1998	52	n.a.	Monitoring soil salinization, Iran
Mr. B.G.H. Gorte (ITC staff)	1998	53	90-6164-157-8	Probabilistic Segmentation of Remotely Sensed Images
Mr. Tenalem Ayenew (Ethiopia)	1998	54	90-6164-158-6	The hydrological system of the lake district basin, central main Ethiopian rift
Mr. Wang Donggen (China)	1998	55	90-6864-551-7	Conjoint approaches to developing activity-based models
Ms. M. Bastidas de Calderon (Venezuela)	1998	56	n.a.	Environmental fragility and vulnerability of Amazonian landscapes and ecosystems in the middle Orinoco river basin, Venezuela
Mr. A. Moameni (Iran)	1999	57	n.a.	Soil quality changes under long-term wheat cultivation in the Marvdasht plain, South-Central Iran
Mr. J.W. van Groenigen (The Netherlands)	1999	58	90-6164-156-X	Constrained optimisation of spatial sampling: a geostatistical approach
Ms. Cheng Tao (China)	1999	59	90-6164-164-0	A process-oriented data model for fuzzy spatial objects
Mr. Piotr Wolski (Poland)	1999	60	90-6164-165-9	Application of reservoir modelling to hydrotopes identified by remote sensing
Mr. B. Acharya (Nepal)	1999	61	90-6164-168-3	Forest biodiversity assessment: A spatial analysis of tree species diversity in Nepal
Mr. Ali Akbar Abkar (Iran)	1999	62	90-6164-169-1	Likelihood-based segmentation and classification of remotely sensed images
Mr. T. Yanuariadi (Indonesia)	1999	63	90-5808-082-X	Sustainable Land Allocation: GIS-based decision support for industrial forest plantation development in Indonesia
Mr. Mohamed Abu Bakr (Sudan)	1999	64	90-6164-170-5	An Integrated Agro-Economic and Agro-Ecological Framework for Land Use Planning and Policy Analysis
Ms. M. Eleveld (The Netherlands)	1999	65	90-6461-166-7	Exploring coastal morphodynamics of Ameland (The Netherlands) with remote sensing monitoring techniques and dynamic modelling in GIS
Ms. Yang Hong (China)	1999	66	90-6164-172-1	Imaging Spectrometry for Hydrocarbon Microseepage
Mr. Félix Mainam (Cameroon)	1999	67	90-6164-179-9	Modelling soil erodibility in the semiarid zone of Cameroon
Mr. Mahmoud Bakr (Egypt)	2000	68	90-6164-176-4	A Stochastic Inverse-Management Approach to Groundwater Quality
Ms. S. Zlatanova (Bulgaria)	2000	69	90-6164-178-0	3D GIS for Urban Development
Mr. Wilber K. Ottichilo (Kenya)	2000	70	90-5808-197-4	Wildlife Dynamics: An Analysis of Change in the Masai Mara Ecosystem
Mr. Nuri Kaymakci	2000	71	90-6164-181-0	Tectono-stratigraphical Evolution of the Cankori Basin (Central Anatolia, Turkey)
Ms. Rhodora Gonzalez	2000	72	90-5808-246-6	Platforms and Terraces: Bridging participation and GIS in joint-learning for watershed management with the Ifugaos of the Philippines